

Current Studies on Electrical-Electronics and Communication Engineering

Editör
HASAN ÜZMUŞ

BIDGE Publications

Current Studies on Electrical-Electronics and Communication
Engineering

Editor: Dr. Öğr. Üyesi Hasan ÜZMUŞ

ISBN: 978-625-6707-08-5

Page Layout: Gözde YÜCEL

1st Edition:

Publication Date: 25.12.2023

BIDGE Publications,

All rights of this work are reserved. It cannot be reproduced in any way without the written permission of the publisher and editor, except for short excerpts to be made for promotion by citing the source..

Certificate No: 71374

Copyright © BIDGE Publications

www.bidgeyayinlari.com.tr - bidgeyayinlari@gmail.com

Krc Bilişim Ticaret ve Organizasyon Ltd. Şti.

Güzeltepe Mahallesi Abidin Daver Sokak Sefer Apartmanı No: 7/9 Çankaya /
Ankara



Contents

Contents	4
Nmea Protocol Compliance Recommendation for Ship Bridge Electronic Devices	8
Ali Sinan ÇABUK.....	8
A Comparative Performance Analysis of GPS Receiver Position Estimation Methods	43
Nurullah GÜRCAN.....	43
Özgür ERTUĞ.....	43
Mosaicing of Non-Overlapping Images Using Deep Learning Based Homography Estimation	61
Ali Batuhan YELLİ.....	61
Gökhan Koray GÜLTEKİN	61
Disease Diagnosis and Determination of Various Emotional States and Behaviors in Model Animals with Artificial Intelligence (Visual Processing, Machine and Deep Learning).....	86

Emre AYDEMİR.....	86
İnci BİLGE.....	86
Stap Radar Signal Processing for Real-World Clutter Environments	98
Necmi Serkan TEZEL	98
Advancements in Brain Tumor Classification Using ResNet-50: Exploring Activation Functions and Batch Size Influence.....	131
Ahmet SOLAK.....	131
Production of Commonly Used Components in the Cathode Active Substance of Lithium-Ion Cells by Enrichment with Graphene Derivatives	154
Bırayda Alparslan.....	154
Ekin ASLAN	154
Comparison of Nonlinear Twin Motor Multi Inputs Multi Output System with Metaheuristic Optimization Methods of The Parameters of Different Controllers	173
Ali Can ÇABUKER	173
M. Nuri ALMALI.....	173
İshak PARLAR.....	173
Real-time Measurement of CO Gas Released During Laser Cutting of Wood using MQ-7 Sensor	208
Çağatay ERSİN	208
Mehmet GÜNEŞ	208
Design of Servo Motor Positioning Application for Android Phone with Arduino Nano 33 IoT on Simulink	224
Erdem İLTEN.....	224
Metin DEMİRTAS	224

Haris CALGAN.....	224
Design of Robotics Educational Material For Teaching English Color Concepts in Preschool.....	241
Mehmet GÜNEŞ	241
Çağatay ERSİN	241
Single Phase Inverter Square Wave Inverter and PWM Control Circuit.....	253
Metin DEMİRTAS	253
A Two-Port MIMO Patch Antenna at 28 GHz for mm-Wave Communication.....	272
Cem GÜLER	272
Sena Esen BAYER KESKİN	272

CHAPTER I

Nmea Protocol Compliance Recommendation for Ship Bridge Electronic Devices

Ali Sinan ÇABUK

Introduction

Maritime transportation and ship industry have been the focus of attention of all countries for centuries. A large proportion of international trade is realized by maritime transport. The shipbuilding industry is a rapidly developing sector depending on its transportation capacity. Maritime transportation is widely preferred because it is cheap and allows the transportation of large tonnages of cargo at once (Atamer, 2017). Around 80% of global commerce in terms of capacity and excessive 70% in terms of value is conducted through maritime transportation (UNCTAD, 2020a). Due to reasons such as carrying more load at a time and being less costly and effective transportation, is attracting more attention. International maritime trade is an industry that is rapidly increasing by 2019. Maritime trade routes, which include developing countries and

between industrially strong countries and developing countries, have become more important over time and constituted 60.9% of world trade in 2019 (UNCTAD, 2020b; Taşdelen et al., 2022).

Since December 2019, the novel coronavirus, Covid-19, emerging from in Wuhan, China, has swiftly disseminated to numerous countries worldwide. The World Health Organization (WHO) described the outbreak as a "pandemic" with the decision dated March 11, 2020. Thus, it increased the global risk level to "very high". At the same time, an "International Public Health Emergency" was declared due to the pandemic (Şahiner and Özel, 2020). The maritime industry, like all sectors, has been significantly and adversely impacted by the Covid-19 epidemic.

According to the United Nations Conference on Trade and Development (UNCTAD) data, with the pandemic, it has been reported that the annual growth rate of international maritime trade will change by -4.1% in 2020 and 4.8% in 2021 (UNCTAD, 2020:2). However, it appears that international maritime trade will be negatively affected in 2021 and beyond due to the economy being negatively affected by supply and demand shocks due to the UNCTAD Covid-19 pandemic.

The most important element of maritime trade is ships. The shipping industry has undergone substantial changes due to the profound impact of the Covid-19 pandemic. The pandemic has negatively affected the shipping industry in terms of logistics, production and workforce.

Due to the pandemic, countries have closed their borders for a long time. Thus, trade between countries was disrupted. With the pandemic, ship commercial travel and port activities have been severely restricted. Due to restrictions, ship sailings have been canceled and operations at ports have slowed down and in some cases stopped. This has led to supply chains being disrupted and commercial products unable to be transported on time. This contraction in maritime trade has made ship crew health and safety a major concern. Strict protocols have been implemented to reduce

the risk of infection and transmission on ships. Quarantine rules and tests have become mandatory for ship personnel and passengers during travels (Grzelakowski, 2022). This has caused flights and logistics processes to become more complex. Due to the impact of the pandemic on maritime trade, the shipbuilding sector was also negatively affected in this process. Ship manufacturing, maintenance and services were also affected by the epidemic. Shipbuilding companies have had to slow down work to keep up with the balance of supply and demand due to the pandemic. The measures taken in shipyards caused a decrease in the number of workers and delays in production processes. In addition, disruptions in the international supply chain have caused difficulties in obtaining the materials required for ship construction. It has been observed that the ship sector, which carries out container transportation as shown in Figure 1, has been much more affected by the pandemic process.



Figure 1. Container Ship

Despite the difficulties noted in foreign trade due to the pandemic, the shipbuilding industry has sought various solutions to adapt to the pandemic. Digitalization and automation are becoming more accepted in the shipping industry. Remote working opportunities have enabled the maintenance and repair processes to be managed effectively. Additionally, during the pandemic, the

cruise industry has made progress in adopting more sustainable practices. Steps such as turning to cleaner energy sources, reducing carbon emissions and adopting environmentally friendly technologies have been taken towards the sector becoming more environmentally friendly and sustainable in the future.

In 2019, the shipping industry grappled with a global financial crisis, aggravated by an oversupply of ships compared to the demand. Ocean carriers and charter ship owners came to understand that the concept of larger vessels and 'economy of scale' lacked significance without a careful balance between supply and demand. To address plummeting freight rates and cope with dwindling cargo volumes in early 2020, they promptly instituted a buying freeze to regulate capacity. Ship builders experienced a months-long drought in new orders as a result. This realization, though belated, was a crucial decision aimed at rescuing an entire industry that had evolved into a sizable predicament resembling a snowball gaining momentum downhill.

The lifespan of the vessels had to increase; shipowners started to saving money to be able to survive in the market. They reduced to renew their main bridge navigation equipment and not following updated technology which increase efficiency and safety at sea.

On the vessels there is many different types of navigation and communication products. Each equipment maker has own protocol and own standards. Therefore, shipping companies are not willing to modernize their equipment on board, because of high compatibility costs and replacements takes long time.

It is especially problematic for ships with old technology to communicate with other devices that have new technological bridges and ship electronics. The fact that maritime trade came to a halt with the Covid 19 pandemic has slowed down new ship manufacturing and almost brought it to a halt. Therefore, the re-acceleration of maritime trade after the pandemic has revealed the shortage of ships.

Thus, the navigation times of technologically old ships have increased.

The biggest deficiency of ships with old technology is the lack of data traffic based on The National Marine Electronics Association (NMEA) standard, which can be called the electronic backbone of the ship. The term "electronic devices on vessels" encompasses a diverse array of equipment and systems employed across various maritime applications. These devices play critical roles in navigation, communication, safety, and operational aspects of the vessel. Electronic devices on board can be summarized as Radar Systems, Global Positioning System (GPS), Automatic Identification System (AIS), Electronic Chart Display and Information System (ECDIS), Communication Systems, Automatic Pilot System, Engine Monitoring Systems, Weather Monitoring Systems, Alarm and Monitoring Systems and Entertainment and IT Systems. These electronic devices are crucial for modern vessels, enhancing safety, efficiency, and navigational accuracy while also facilitating effective communication and operational management on the ship. They contribute significantly to the overall functionality and safety of maritime operations. It is a major deficiency that old ships have analog navigation devices and other electronic devices do not generate signals compatible with the NMEA system. Adaptation of the old system to the new system is important.

Ship Electronics

Electronic systems on ships play a critical role in modern shipping and perform a number of important functions as given in Figure 2. These systems increase the safety of ships, increase operational efficiency and ensure the safety of the crew. It is also critical to improving efficiency and competitiveness in the shipping industry. Electronic devices on the ship's bridge and other units perform very important tasks in both navigation and stand-by situations. Electronic systems increase ship safety.



Figure 2. Bridge on Ship (Riviera Maritime, 2023)

Ensuring onboard security involves measures to prevent collisions using navigation systems like radar, the Global Positioning System (GPS), and the Automatic Identification System (AIS). Additionally, it entails safeguarding the ship's crew through systems such as fire detection and emergency signal systems. Another important unit in ship electronic systems is navigation systems. Navigation helps ships determine their location, plan their route, and reach their destination safely. Accurate navigation is provided by systems such as electronic maps and GPS. Another electronic system is engine control systems. These are electronic systems such as fuel management systems and autopilot systems. Engine control systems help improve the ship's operational efficiency. These systems optimize fuel consumption and reduce the ship's costs. The most important electronic system on ships is the communication systems. The term ship communications covers electronic systems such as Very High Frequency (VHF), High Frequency (HF), Ultra High Frequency (UHF) radios and satellite communication systems to meet communication needs such as communication between ships, communication with shore stations and emergency calls. In addition to the navigation, communication and security systems that are mandatory on ships, it includes

electronic systems for the crew's comfort. Electronic systems on ships provide entertainment systems, internet access, communication tools and other services to increase the living comfort of the crew (Aghamirbaha et al., 2022).

Ship electronics encompass a broad range of electronic systems and devices specifically designed for use on ships and vessels. Ship electronics can be divided into sections as follows:

Navigation Systems:

Positioning studies at sea were previously carried out by traditional methods, such as compass and speed information, and astronomical observations, evaluated according to time. Nowadays, depending on the developments in technology, classical position detection systems and radars have begun to be used together. Distance measurements have been made by taking advantage of the propagation properties of electromagnetic waves with technological developments and the locations of marine vessels have begun to be determined by using backward or forward estimation methods with these measured distances (Fukuda et al., 2021). Due to the disruptions in the transit system, the GPS (Global Positioning System) satellite system was developed and has started to operate at full capacity today.

This includes Global Positioning System (GPS), Electronic Chart Display and Information System (ECDIS), radar, and Automatic Identification System (AIS), used for determining the vessel's position, plotting courses, and avoiding collisions as given in Figure 3.



Figure 3. Navigation System on Ship (Marcom, 2023)

The Global Positioning System (GPS) is a satellite-based navigation system that furnishes precise position information, allowing ships to ascertain their precise location in terms of latitude and longitude. It allows vessels to navigate with precision and reliability. Radar systems use radio waves to detect other vessels, landmasses, and obstacles in the vicinity. ECDIS displays electronic navigational charts and integrates information from various navigational sensors. It replaces traditional paper charts and provides real-time navigation information, aiding in route planning and course monitoring. AIS transponders exchange data with nearby vessels and shore stations, providing information such as the ship's identity, position, course, and speed. It enhances situational awareness and assists in collision avoidance. Compasses and Gyrocompasses are other important equipment of navigation system in ship. Traditional magnetic compasses and more modern gyrocompasses help determine the ship's direction and heading, especially useful in case of electronic failures.

Communication Equipment:

Communication equipment on ships comprises a range of electronic systems and devices designed to facilitate communication between vessels, as well as between the ship and external entities such as shore stations or other maritime authorities as given in Figure 4. These systems are crucial for maintaining operational efficiency, safety, and coordination during maritime voyages. Very High Frequency (VHF) radios, Medium and High-Frequency (MF/HF) radios, satellite communication systems (Inmarsat, VSAT), and Global Maritime Distress and Safety System (GMDSS) equipment for ship-to-ship and ship-to-shore communication.



Figure 4. *Communication Equipment on Ship (Marinegyaan, 2023)*

VHF radios are widely used for short-range communication between ships and between ships and shore. They are effective for general voice communication, distress signaling, and receiving weather updates. MF/HF radios are capable of longer-range communication. They are used for communication over greater distances, especially when out of VHF range, and are vital for long-distance distress signaling. Satellite Communication Systems such as Inmarsat and VSAT provide long-range satellite communication, enabling ships to communicate globally for voice, data, and internet connectivity (Zalewski, 2020). These systems are crucial for remote areas or when conventional communication means are unavailable. GMDSS equipment comprises emergency distress beacons, satellite-

based emergency position-indicating radio beacons (EPIRBs), search and rescue transponders (SARTs), and NAVTEX systems. These are dedicated to maritime distress communication and search and rescue operations. Radio Telex and Telemetry Systems enable the transmission of data via radio waves and are used for sending and receiving telex messages, as well as operational data transmission.

Engine Control and Monitoring Systems:

Engine control and monitoring systems on ships are critical components that oversee and manage the performance, operation, and health of a vessel's propulsion system. These systems employ a series of electronic devices and software to control and monitor the ship's engines, ensuring optimal functionality and efficiency. There are engine performance control, fuel management systems, engine health monitoring, propulsion system control, emission control and remote monitoring and diagnostics in engine control and monitoring system as given in Figure 5.



Figure 5. Engine Control and Monitoring Systems on Ship (Marine Inbox, 2023)

Engine performance control systems manage and optimize the performance of the ship's engines, regulating parameters such as fuel consumption, power output, and engine speed to maintain efficient operation. Fuel management systems related to engine performance control system. They monitor and manage the fuel consumption of the engines, ensuring that the ship operates within optimal fuel efficiency ranges, thus reducing costs and environmental impact. Engine health monitoring systems continuously monitor and assess the condition of the engines, detecting and alerting the crew about any irregularities or potential issues. This includes temperature, pressure, vibration, and other critical engine parameters. Propulsion system control, including the engine's power delivery to the propeller, ensuring smooth and efficient vessel movement. Some advanced systems aid in managing and controlling the ship's emissions, ensuring compliance with environmental regulations by optimizing engine performance and reducing harmful emissions. Remote monitoring and diagnostics are other important system for engine performance system. Many systems provide the capability for remote monitoring and diagnostics. This allows for shore-based engineers or technical support teams to access real-time data and provide remote assistance in case of technical issues or engine abnormalities.

Entertainment and IT Systems:

Entertainment and IT systems on ships are designed to provide a range of services and facilities to enhance the overall experience and functionality for both the crew and passengers on board. These systems encompass various electronic devices and technologies aimed at providing entertainment, communication, and operational support. Onboard internet, satellite TV, computers, and connectivity as given Figure 6 for crew welfare and operational purposes.

Internet and satellite connection are very important on ships. Internet connectivity is providing internet access to crew and passengers for communication, browsing, and accessing online

services. This connectivity often involves satellite communication systems to ensure connectivity, even in remote areas. Satellite TV systems is offering entertainment through satellite-based television services, providing access to various channels and programs for crew and passengers. WiFi Networks for crew and passenger use, enabling wireless connectivity for personal devices like smartphones, tablets, and laptops.



Figure 6. Entertainment and IT Systems on Ship (Actia, 2023)

IT infrastructure and support is managing the ship's information technology infrastructure, including servers, storage, and networking equipment, and providing IT support for maintenance and troubleshooting.

Weather Monitoring Equipment:

Devices such as anemometers, barometers, thermometers, and other sensors to monitor weather conditions for safe navigation and operational planning as given Figure 7.



Figure 7. Weather Monitoring Equipment on Ship (Nomadic Research Labs, 2023)

Weather monitoring equipment on ships comprises a set of instruments and devices specifically designed to collect, measure, and track various meteorological conditions and environmental parameters while at sea. These instruments play a vital role in safeguarding the vessel, crew, and cargo by delivering real-time weather data. These are anemometers, barometers, thermometers and hygrometers, weather radar and weather satellites and receivers. Anemometers measure wind speed and direction. Wind data is crucial for navigation, especially during severe weather conditions. Barometers measure atmospheric pressure, which is a key indicator of weather changes. A drop in pressure might signify an approaching storm or rough weather conditions. Thermometers and Hygrometers instruments measure temperature and humidity levels. They help in assessing weather conditions and provide information for crew comfort and cargo handling. Weather Radar systems aid in detecting precipitation, storms, and potentially hazardous weather patterns, allowing the crew to navigate around severe weather areas. Ships often utilize weather satellite data and receivers to receive weather forecasts, updated weather charts, and real-time information about atmospheric conditions.

Security and Surveillance Systems:

The shipping industry is one of the main carriers of international trade. However, ensuring the safety of goods transported by sea has become a major priority for ship owners and operators. Ships sailing at sea may face theft, piracy, terrorist attacks and other security threats. Therefore, ship security alert systems are a critical security measure used to keep ship personnel and cargo safe. CCTV cameras, access control systems, and other security measures for onboard safety and security. Security and surveillance systems on ship is as shown in Figure 8.



Figure 8. Security and Surveillance Systems on Ship (Wiley B2B Publisher, 2023)

Alarm and Monitoring Systems:

Systems that provide alarms and monitor various ship conditions, such as fire detection, gas detection, and bilge alarms, ensuring the safety and integrity of the vessel as given Figure 9.

Fire detection systems on ships are designed to identify and alert crew members to the presence of a fire in its early stages, allowing for prompt response and mitigation. These systems typically include smoke detectors, heat detectors, and flame detectors strategically placed in various areas of the ship, including engine rooms, accommodation spaces, and cargo holds. When smoke, elevated temperatures, or flames are detected, the system triggers alarms and may also activate fire suppression systems such as sprinklers or fire extinguishing agents.

Gas detection systems are crucial for identifying the presence of hazardous gases in different areas of the ship. This is essential for preventing explosions, ensuring crew safety, and protecting the environment. Gas detectors are specialized devices that can detect specific gases such as methane, carbon monoxide, hydrogen sulfide, and others. They are often placed in locations where gas leaks are most likely to occur, such as in engine rooms or cargo spaces. If a dangerous level of gas is detected, the system will activate alarms and may also trigger ventilation systems or shut off the supply of the specific gas to prevent further leakage.

The bilge is the lowest compartment on a ship's hull, and it's designed to collect water that enters the ship. Bilge alarms are used to monitor the water level in the bilge, helping to prevent flooding and ensuring the ship remains stable. Bilge alarms consist of sensors or float switches located in the bilge, connected to an alarm panel on the bridge or another central location on the ship. If the water level in the bilge rises beyond a safe level, the bilge alarm is triggered, alerting the crew to a potential flooding situation. Crew members can then take appropriate action to pump out the water and address the issue.



Figure 9. Fire, Gas and Bilge Alarm Systems on Ship (Sea Navigation and Automation, 2023)

Sonar and Echo Sounders:

Equipment used for depth sounding, fish finding, and underwater mapping. Sonar is a technology that utilizes sound waves to identify and pinpoint objects beneath the water's surface, as illustrated in Figure 10. It is commonly used for navigation, communication, and underwater target detection, including submarines, fish, and the seafloor. A typical sonar system consists of a transmitter, which emits sound waves (ping), and a receiver, which detects the echo of the sound waves bouncing off objects. The time taken for the sound waves to return provides information about the distance and direction of the object. There are various types of sonar, including passive sonar and active sonar. Sonar can be used for navigation, obstacle avoidance, and submarine detection.



Figure 10. Sonar and Echo Sounders (Hydro International Magazine, 2023)

Echo sounders, also known as depth sounders or sounders, are specialized sonar devices primarily used for measuring the depth of water beneath a ship. They are essential for safe navigation and avoiding underwater obstacles. An echo sounder emits a sound pulse downward, and when it reaches the seafloor, the echo returns to the transducer. The duration it takes for the echo to return is employed in determining the water's depth. The depth information is typically displayed on a screen or gauge on the ship's bridge, allowing the crew to monitor the water depth in real-time. This information helps in determining the safe passage of the ship and avoiding shallow or hazardous areas.

Ship data communication adaptation

Ship data communication refers to the exchange of information between various systems and devices on a ship using communication technologies. With technological advancements, modern ships are outfitted with an array of systems that produce, gather, and employ data for navigation, safety, control, and monitoring purposes. Ship data communication enables these

systems to share information with each other, enhancing the overall efficiency, safety, and operational capabilities of the vessel.

One of the retrofit processes on ships is related to electrical systems connected to the ship's main engine with a data-driven process controller (Giannoutsos and Manias, 2015; Sulligoi et al., 2016). There are various retrofit studies on sensors, which are an important part of ship electronic systems. There are systems that improve diagnostic capability with wireless sensors and do not provide a cost-effective retrofit solution for legacy systems (Ong and Thompson, 2011). Typically, these types of retrofits are about optimizing maintenance schedules and reducing costly downtime. Systems with simple functions such as Dynamic Underwater Positioning Systems (Lemieszewski et al., 2021), geographical positions (Hemminghaus et al., 2021) can be specified from this type of retrofit solutions.

As it can be understood from these studies, there are not many studies on retrofit of ship bridge electronic devices. The old technology found in most old ships was abandoned to its fate and forced to be replaced with new ones, which is a costly solution. In 2020, with the Covid-19 pandemic in the world, it has become mandatory to increase the duration of use of ships. Due to the decrease in production power as a result of both the global economic crisis and the pandemic. For these reasons, it is imperative that the obsolete technology on old ships be made to keep up with new electronic devices. If old electronics device as communication on ship can modernization or retrofit like adapted NMEA protocol, it will have the ability to communicate with all old-new ship bridge devices. The new device can be exchanged non-standardized old data protocols to new updated technology protocols. This will reduce the cost of system replacement and shortening replacement process. As an illustration, each vessel is equipped with a gyrocompass system, a vital mandatory component that indicates true north. This gyrocompass system is interconnected with the autopilot, radars, ECDIS, and various other navigation equipment. If this compass makes errors, vessel will head to wrong destination, radars will not

show correctly the targets, and this can cause accidents in the sea. Gyrocompass systems has many components, like repeaters, data units, additional displays etc. For changing compass, you need to change all of side equipment, if your old autopilot does not support new gyrocompass protocol you need to change your autopilot as well, if your radar does not support your new gyrocompass protocol you need to change your radar as well. This all equipment has natural connections therefore we need to have data exchange unit in between which will save a lot of costs and time.

It is important that the electronic systems on the ship communicate with each other. This communication system can be thought of as the data backbone of the ship. Devices operating based on a common protocol send data to each other over a communication data line. The important point here is that the devices connected to the data line are connected to a common communication protocol. NMEA protocol was developed by the "US National Marine Electronics Association" and provides communication between many types of electronic devices used in maritime and military fields, such as sonar, anemometer, top compass, autopilot and GPS receivers, and is used in devices that define more than one data at a time. It is a serial communication based protocol used. In this standard, communication is based on ASCII. It is possible to show the NMEA protocol on a ship or any other marine vessel as shown in Figure 11.

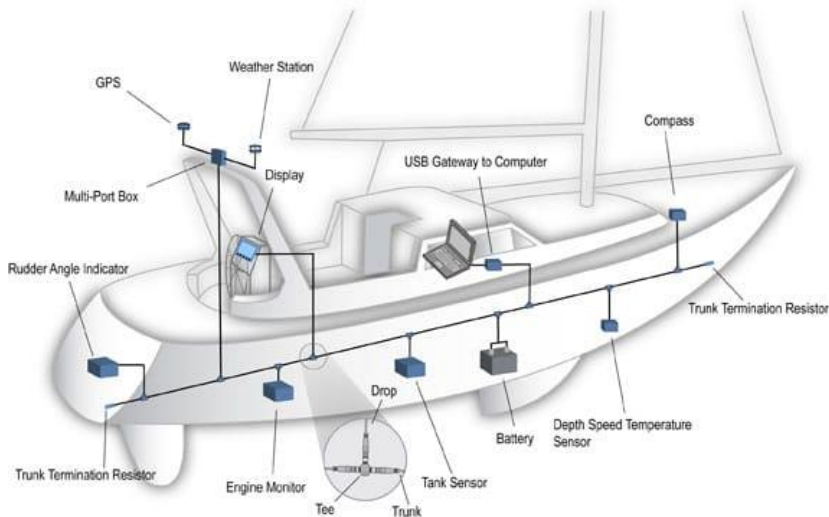


Figure 11. NMEA protokol on Ship (Sea and Land Yacht Works, 2023)

The NMEA introduced its first international interfacing standard, NMEA 0183, which remains in use and recognized today. Initially launched in 1983, it continues to receive regular updates over 30 years later. Following this, the NMEA released the NMEA 2000 as the second international standard in 2001. In the last decade, NMEA 2000 has emerged as the primary standard for leisure marine vessels. Currently, the NMEA OneNet® working group is in the beta test phase for a new standard designed to complement NMEA 2000. This standard aims to facilitate the safe sharing of data over Ethernet. The interface called NMEA 0183 is a simple 3-wire serial communication interface similar to the RS232 SERIAL INTERFACE in computers. It can be installed between two devices. To connect more than two devices, transfer is made through the devices or distributor devices called multiplexers can be used. The speed is slow, but for several device connections this is not a problem. As seen in Figure 12, it is a simple, therefore trouble-free and reliable system.

NMEA 2000, on the other hand, is newer, with its daisy chain connection structure, similar to the ethernet network connection in computers, where many devices are connected to each other as a network at the same time as plug-and-play, with features such as speed, physical connection features and the connection of the connected devices through a separate electrical supply. It has a more advanced and modern interface. It is a version of the CAN BUS systems that Bosh firm used in automobiles in the 1980s and was transferred to the marine world in order to provide both speed and ease of connection with the proliferation of electronic devices on boats.

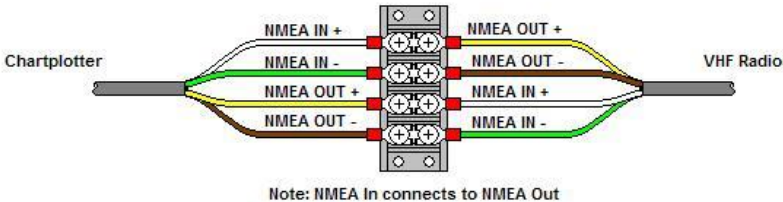


Figure 12. NMEA line (Gemi trafik, 2023)

NMEA 2000 network, as seen in Figure 11, has parts such as “spur”, which is distributed to the devices via T connectors over the backbone, a terminator at the beginning and end of the backbone, and 12V DC supply input at certain points of the line.

Many bridge electronic devices on technologically old ships cannot read the NMEA message and cannot send the message sentence appropriate to the data line used. Therefore, understanding the NMEA sentence is important for ship electronics. NMEA output messages contain the information in Table 1.

Table 1. NMEA message (SiRF Technology, Inc., 2007)

Message	Description
GGA	Time, position and fix type data
GLL	Latitude, longitude, UTC time of position fix and status
GSA	GPS receiver operating mode, satellites used in the position solution, and DOP values
GSV	Number of GPS satellites in view satellite ID numbers. elevation, azimuth. & SNR values
MSS	Signal-to-noise ratio, signal strength. frequency. and bit rate from a radio-beacon receiver
RMC	Time. date, position, course and speed data
VTG	Course and speed information relative to the ground
ZDA	PPS timing message (synchronized to PPS)
150	OK to send message
151	GPS Data and Extended Ephemeris Mask
152	Extended Ephemeris Integrity
154	Extended Ephemeris ACK

NMEA sentence contains information package, especially GGA data. The meaning of the GGA sentence is as shown in Table 2.

A "Position Fix Indicator" refers to a specific parameter in NMEA sentences that provides information about the quality of the GPS or Global Navigation Satellite System (GNSS) position fix. This indicator helps users assess the reliability and accuracy of the position data provided by their navigation equipment. The Position Fix Indicator is typically represented by a single-digit numeric code within NMEA sentences. Position Fix Indicator information is as in Table 3.

Table 2. NMEA GGA data format (SiRF Technology, Inc., 2007)

Name	Unit	Description
Message 1D		GGA protocol header
UTC Time		hhmmss.sss
Latitude		ddmm.mmmm
N/S Indicator		N=north or S=south
Longitude		dddmm.mmmm
EAV Indicator		E=cast or W=west
Position Fix Indicator		
Satellites Used		Range 0 to 12
HDOP		Horizontal Dilution of Precision
MSL Altitude	meters	
Units	meters	
Geoid Separation	meters	Geoid-to-ellipsoid separation. Ellipsoid altitude = MSL Altitude + Geoid Separation.
Units	meters	
Age of Diff. Com	sec	Null fields when DGPS is not used
Diff. Ref. Station ID		
Checksum		
<CR> <LF>		End of message termination

Table 3. NMEA GGA data format (SiRF Technology, Inc., 2007)

Value	Description
0	Fix not available or invalid
1	GPS SPS Mode, fix valid
2	Differential GPS, SPS Mode, fix valid
3-5	Not supported
6	Dead Reckoning Mode, fix valid

The specific values and their meanings may vary depending on the NMEA sentence and the type of navigation equipment. Users can interpret the Position Fix Indicator to understand the current status of the GPS or GNSS fix. For example, a code of "1" indicates a standard autonomous GPS fix, while higher values like "4" or "5"

suggest more precise fixes, often associated with differential or RTK positioning. Understanding the Position Fix Indicator is crucial for mariners and navigators to assess the reliability of the positioning information provided by their GPS or GNSS receivers, especially in situations where accuracy is critical, such as maritime navigation

An example of a GGA sentence as NMEA is as follows.

```
$GPGGA,002153.000,3342.6618,N,11751.3858,W,1,10,1.2,27.0,  
M,-34.2,M,,0000*5E
```

This package is the GPS location information package, which is one of the most frequently used packages as it contains latitude, longitude and time information. The packet starts with the '\$' character and ends with the checksum. Between these two characters are all other relevant data. A comma is placed between two different data to separate them. The first data of the packet indicates the type of incoming packet. So it indicates what data is in this package. In the NMEA protocol, each message begins with the GP prefix and is followed by a suffix that completes the relevant packet. For the message above, this structure is "GP + GGA". The format of the package is: \$GPGGA,hhmmss.ss,llll.ll,a,yyyy.yy,a,x,xx,x.x,x.x,M,x.x,M,x.x,xxxx*hh and contains 15 data. If the data specified in the standard is not included in the incoming package or is not used on that device, that section is left blank. This situation is reflected in the package as "M,-34.2,M,,0000*5E". The data between two adjacent commas here means that the data was not sent to this device (13th data). Since the standard defines what information each packet will contain and in what order, the "parse" process of the received packet is carried out accordingly. The meaning of the specified sample NMEA sentence is as in Table 4.

Table 4. NMEA GGA example (SiRF Technology, Inc., 2007)

Message	Description	Message	Description
SGPGGA	Message 1D	1.2	HDOP
002153.000	UTC Time	27.0	MSL Altitude
3342.6618	Latitude	M	Units
N	N/S Indicator	-34.2	Geoid
			Separation
11751.3858	Longitude	M	Units
W	EAV Indicator	0000	Diff. Ref.
			Station ID
1	Position Fix Indicator	*5E	Checksum
10	Satellites Used		

If the NMEA sentence is output as GLL—Geographic Position- Latitude/Longitude, it has the meanings in Table 5.

Table 5. NMEA GLL data format (SiRF Technology, Inc., 2007)

Name	Description
Message 1D	GLL protocol header
Latitude	ddmm.mmmm
N/S Indicator	N=north or S=south
Longitude	dddmm.mmmm
E/W Indicator	E=east or W=west
UTC Time	hhmmss.sss
Status	A=data valid or V=data not valid
Mode	A=Autonomous. D=DGPS. E=DR (Only present in NMEA v3.00)
Checksum	
<CR> <LF>	End of message termination

An example of the GLL sentence appearing at the output as a NMEA sentence is as given below.

\$GPGLL,3723.2475,N,12158.3416,W,161229.487,A,A*41

The meaning of the specified sample NMEA sentence is as in Table 6.

Table 6. NMEA GLL example (SiRF Technology, Inc., 2007)

Message	Description
SGPGLL	GLL protocol header
3723.2475	ddmm.mmmm
N	N=north or S=south
12158.3416	dddmm.mmmm
W	E=east or W=west
161229.487	hhmmss.sss
A	A=data valid or V=data not valid
.1	A=Autonomous. D=DGPS. E=DR (Only present in NMEA v3.00)

NMEA input messages enable the management of the evaluation receiver when operating in NMEA protocol mode. Once the receiver is switched to NMEA mode, certain messages can be employed to command it. NMEA is a set of communication protocols widely used in the marine industry to enable the exchange of information between different marine electronic devices, such as GPS receivers, chartplotters, autopilots, and other navigation and communication equipment. NMEA sentences typically consist of alphanumeric characters and contain specific information about various parameters, such as position, speed, course, depth, and more. These sentences are transmitted between devices in a standard format, allowing for interoperability and compatibility among different manufacturers' equipment.

For example, an NMEA input message could contain a sentence such as GGA (Global Positioning System Fix Data), offering details about altitude, longitude, latitude and GPS fix quality. Another prevalent NMEA sentence is RMC (Recommended Minimum Navigation Information), encompassing crucial navigation data like latitude, date, time, speed over ground, course over ground and longitude. When we refer to NMEA input messages in the context of a ship, it means that the ship's navigation or communication equipment is receiving these NMEA-formatted

messages from various onboard sensors and systems. This information is crucial for navigation, safety, and situational awareness. The ship's electronic systems can process and display this data on navigation displays, radar screens, or other relevant interfaces, providing the crew with real-time information about the ship's position and other navigational parameters. NMEA input messages and their description are as in Table 7.

Table 7. NMEA Input Messages (SiRF Technology, Inc., 2007)

Message	Name	Description
100	Set Serial Port	Set PORT A parameters and protocol
101	Navigation initialization	Parameters required for start using X/Y/Z ¹
102	Set DGPS Port	Set PORT B parameters for DGPS input
103	Query/Rate Control	Query standard NMEA message and/or set output rate
104	LLA Navigation initialization	Parameters required for start using Lat/Lon/Alt"
105	Development Data On/Off	Development Data messages On/Off
106	Select Datum	Selection of datum used for coordinate transformations
107	Proprietary	Extended Ephemeris Proprietary message
108	Proprietary	Extended Ephemeris Proprietary message
110	Extended Ephemeris Debug	Extended Ephemeris Debug
200	Marketing Software Configuration	Selection of Marketing Software Configurations
MSK	MSK Receiver Interface	Command message to a MSK radio-beacon receiver

The input NMEA sentence related to navigation and its meaning are as in Table 8.

Table 8. NMEA Navigation Initialization Data Format (SiRF Technology, Inc., 2007)

<i>Name</i>	<i>Unit</i>	<i>Description</i>
<i>Message ID</i>		<i>PSRF101 protocol header</i>
<i>ECEF X</i>	<i>meters</i>	<i>X coordinate position</i>
<i>ECEF Y</i>	<i>meters</i>	<i>Y coordinate position</i>
<i>ECEF Z</i>	<i>meters</i>	<i>Z coordinate position</i>
<i>Clk Offset</i>	<i>11/</i>	<i>Clock Offset of the Receiver¹</i>
<i>Time Of Week</i>	<i>sec</i>	<i>GPS Time Of Week</i>
<i>Week No</i>		<i>GPS Week Number</i>
<i>Channel Count</i>		<i>Range 1 to 12</i>
<i>Reset Cfg</i>		<i>See Table 9</i>
<i>Checksum</i>		
<i><CR> <LF></i>		<i>End of message termination</i>

The reset configuration in the navigation data format is as given in Table 9.

Table 9. NMEA Navigation Reset Configuration (SiRF Technology, Inc., 2007)

Decimal	Description
01	Hot Start— All data valid
02	Warm Start—Ephemeris cleared
03	Warm Start (with Init)—Ephemeris cleared, initialization data loaded
04	Cold Start—Clears all data in memory
08	Clear Memory— Clears all stored information in the memory and restores the receiver to its original factory settings.

The navigation sample input NMEA sentence is as follows.

```
$PSRF101,-2686700,-
4304200,3851624,96000,497260,921,12,3*1C
```

The meaning of the specified navigation sample input NMEA sentence is as given in Table 10.

Table 10. NMEA Navigation Input Example (SiRF Technology, Inc., 2007)

Message	Description
SPSRF101	PSRF101 protocol header
-2686700	X coordinate position
-4304200	Y coordinate position
3851624	Z coordinate position
96000	Clock Offset of the Receiver
497260	GPS Time Of Week
921	GPS Week Number
12	Range 1 to 12
3	See Table 10 and Table 11

There are communication protocols subject to the NMEA standard, especially bridge devices. The basic operation of the digital interface device is to provide the electrical data of devices communicating in the NMEA-0183 standard, generally carried by two cables (as Tx+, Tx- or Tx, GND), as input to other devices. Accurate, complete and timely transmission of protocol sentences is critical for the communication of devices. It is to establish networks that enable bridge devices to exchange data with each other for the specified adaptation of technologically old ships. Therefore, the electronic device that will perform NMEA conversion is of critical importance to connect the bridge navigation and communication devices on every ship.

Ensuring NMEA protocol compliance for ship bridge electronic devices that have old technology analog electronic systems or do not have NMEA protocol should be as shown in Figure 13.

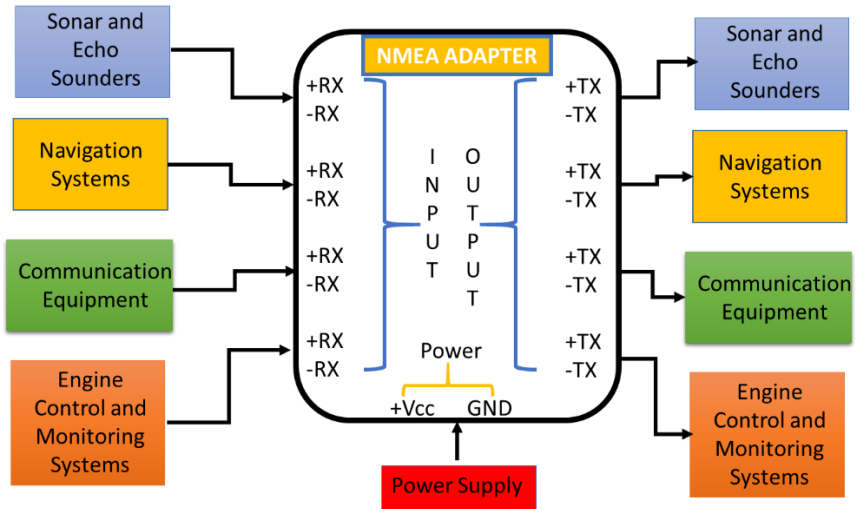


Figure 13. Ship Electronic System Adaptation

In implementing the proposed ship electronics adaptation system, careful consideration should be given to data communications. The communication protocols of the devices connected to the input and output terminals must be determined and the conversion is made accordingly.

The primary communication choice on the bridge is RS-422, alternatively referred to as TIA/EIA-422. This technical standard, established by the Electronic Industries Alliance, outlines the electrical characteristics of a digital signal circuit. The differential signal is capable of transmitting data at speeds of up to 10 Mbit/s and can be conveyed over cables spanning lengths of up to 1500 meters. Differentially, data can be exchanged between -6 V and +6 V at most and between -2 V and +2 V at least. +2 V to +6 V corresponds to zero (0) in the binary number system. Between -2V and -6V corresponds to one (1) in the binary number system. At the same time, the RS422 standard supports high data rates while allowing line impedances of up to 50 ohms.

Another crucial data communication standard is RS-232, a term in telecommunications denoting a standard for serial

communications transmission that was initially introduced in 1960. It officially defines the signals exchanged between data terminal equipment, such as a computer terminal, and data circuit termination equipment or data communications equipment, like a modem. The most recent iteration of this standard is TIA-232-F, which details the interface between the data terminal and data circuit termination equipment using serial binary data interchange, and was published in 1997. RS-232 has found widespread use in computer serial ports.

The RS-232 standard establishes voltage levels that correspond to logic and represent the logical zero levels employed in data transmission and control signal lines. Applicable signals span from +3 to +15 volts or -3 to -15 volts concerning the "Common Ground" (GND) pin. Therefore, the interval between -3 and +3 volts does not constitute a valid RS-232 level. In the case of data transmission lines (TxD, RxD, and their equivalent secondary channels), a negative voltage represents logic, and the signal condition is termed "space." A positive voltage indicates logic zero, also known as the "mark" signal condition. Control signals demonstrate opposing polarities; the positive voltage represents the asserted or active state while the negative voltage represents the asserted or inactive state. Request to send (RTS), available to send (CTS), data terminal ready (DTR), and dataset ready (DSR) are examples of control lines.

Furthermore, electronic devices with digital interface used in maritime navigation and radio communication systems should comply with specific international standards, such as IEC 60945, IEC 61162-1 and IEC 61162-2. IEC 60945, also known as "Marine navigation and radio communications equipment and systems - General requirements - Test methods and required test results," establishes the global standard for devices intended for use in marine navigation and radio communication. This standard defines the minimum performance requirements, test methods, and results necessary for devices to successfully pass tests related to marine navigation and radio communication equipment and systems. IEC 61162-1, entitled "Marine Navigation and Radiocommunication

Equipment and Systems - Digital Interfaces - Part 1: Single Speaker and Multiple Listeners," establishes the communication interface for marine navigation and radio communication equipment and systems. Finally, the IEC 61162-2 document, entitled "Marine navigation and radiocommunication equipment and systems - Digital interfaces - Part 2: Single speaker and multiple listeners, High-Speed transmission," specifies the communication protocols for high-speed marine navigation and radio communication equipment and systems.

The structure that will provide ship bridge electronic device adaptation must also meet certain requirements. In order to change the incoming NMEA sentences, a microcontroller that could operate at standard data rates (up to 34800 baud rate, 8 data bits) should be preferred. For such a software model, the timing of sentences is also extremely important. If a microcontroller is to be used, there must be a power circuit on the printed circuit board that will properly meet the voltage needs of the microcontroller, depending on the model used. The microcontroller must be developed to work compatible with embedded software. The software must be able to detect NMEA sentences, extract important data (such as location information from GPS) within the sentence, and create an NMEA sentence by combining the data.

References

Actia Group (2023) (22.09.2023
<https://newsroom.actia.com/en/actia-de-mexico-is-venturing-into-a-new-market-far-removed-from-its-usual-customers>).

Aghamirbaha, E., Toloei, A., Hossein, M. Roknabadi, A. (2022). Analysis of marine navigation methods and systems, *20th International conference of iranian aerospace*, Tehran, Iran.

Atamer, K. (2017). Deniz Ticareti Hukuku. Cilt I, 164-165.

Fukuda, G., Hatta, D., Guo, X. & Kubo, N. (2021) Performance Evaluation of IMU and DVL Integration in Marine Navigation, *Sensors*, 21, 1056.

Gemi trafik (2023) (12.10.2023
<https://www.gemitrafik.com/nmea-0183-2000/>)

Giannoutsos S. V. & Manias S. N. (2015) A Data-Driven Process Controller for Energy-Efficient Variable-Speed Pump Operation in the Central Cooling Water System of Marine Vessels, *IEEE Transactions on Industrial Electronics*, vol. 62, no. 1, pp. 587-598. doi: 10.1109/TIE.2014.2317456,

Grzelakowski, A.S. (2022). The Covid 19 Pandemic – Challenges for Maritime Transport and Global Logistics Supply Chains, *The International Journal on Marine Navigation and Safety of Sea Transportation*, 16(1), 71-77. doi: 10.12716/1001.16.01.07

Hemminghaus C., Bauer J., Wolsing K. (2021) SIGMAR: Ensuring Integrity and Authenticity of Maritime Systems using Digital Signatures, *2021 International Symposium on Networks, Computers and Communications (ISNCC)*, Dubai, United Arab Emirates, pp. 1-6, doi: 10.1109/ISNCC52172.2021.9615738

Hydro International Magazine (2023) (10.10.2023
<https://www.hydro-international.com/content/news/wassp-announces-solutions-to-improve-sounder-and-sonar-systems>)

Lemieszewski, Łukasz, et al. (2021) The Spoofing Detection of Dynamic Underwater Positioning Systems (DUPS) Based on Vehicles Retrofitted with Acoustic Speakers, *Electronics*, 10.17: 2089

Marcom Marine Communications Limited (2023), (11.09.2023 <https://marcomusa.net/navigation/>)

Marinegyaan Online Marine Encyclopedia (2023) (17.09.2023 <https://marinegyaan.com/what-are-regulations-requirements-for-communication-equipments-as-per-solas/>)

Marine Inbox (2023) (17.09.2023 <https://marineinbox.com/marine-exams/engine-control-of-modern-low-speed-two-stroke-marine-diesel-engine/>)

Nomadic Research Labs (2023) (02.10.2023 <https://microship.com/ship-weather-station/>)

Ong M. & Thompson H. A. (2011) Challenges for wireless sensing in complex engineering applications, *IECON 2011 - 37th Annual Conference of the IEEE Industrial Electronics Society*, Melbourne, VIC, Australia, 2011, pp. 2106-2111, doi: 10.1109/IECON.2011.6119633

Riviera Maritime (2023) (11.09.2023 <https://www.rivieramm.com/news-content-hub/news-content-hub/bridge-systems-selected-for-lng-carriers-for-arctic-lng--2-60264>)

Sea & Land Yacht Works (2023) (10.10.2023 <https://www.seaandlandyachtworks.com/post/nmea-2000-basics>)

Sea Navigation and Automation Pte. Ltd. (2023) (05.10.2023 <https://snamarine.com.sg/product/>)

SiRF Technology, Inc. (2007) (12.10.2023 <https://www.sparkfun.com/datasheets/GPS/NMEA%20Reference%20Manual-Rev2.1-Dec07.pdf>)

Sulligoi G., Vicenzutti A., Arcidiacono V. & Khersonsky Y. (2016) Voltage Stability in Large Marine-Integrated Electrical and Electronic Power Systems, *IEEE Transactions on Industry Applications*, vol. 52, no. 4, pp. 3584-3594. doi: 10.1109/TIA.2016.2544833

Şahiner, D.D. ve Özer, L. (2020). Turkey: Denizcilik Sektörü ve Korona Virüs (COVID-19) Önlemler. <https://www.mondaq.com/turkey/marine-shipment/910858/denizcilik-sektrve-korona-virs-covid-19-nlemleri>

Taşdelen S., Köç Bakacak P., Taşdelen U. (2022) Effect of Covid-19 Pandemic on Sea Freight: The Case of Turkey, *Journal of Marine and Engineering Technology (JOINMET)* 2(2), 111-121.

UNCTAD (2020). World seaborne trade, e-Handbook of Statistics. <https://stats.unctad.org/handbook/MaritimeTransport/WorldSeaborneTrade>

UNCTAD (2020) Review of Maritime Transport 2020. New York: United Nations Publications.

Zalewski, P. (2020) Integrity Concept for Maritime Autonomous Surface Ships' Position Sensors, *Sensors*, 20, 2075.

Wiley B2B Publisher (2023) (02.10.2023 <https://www.git-security.com/news/integration-navigation-and-surveillance-systems-boats-qatar>)

CHAPTER II

A Comparative Performance Analysis of GPS Receiver Position Estimation Methods

Nurullah GÜRCAN¹
Özgür ERTUĞ²

Introduction

The estimation of the receiver's position primarily depends on GPS satellite positions and pseudoranges. Receivers acquire GPS satellite positions from broadcasted navigation message. Satellite positions are stored as Keplerian parameters in navigation message, so the receiver converts these parameters to Cartesian coordinates which takes Earth center as origin point. Pseudoranges, which indicates travel time of signal between each visible GPS satellite and receiver are measured and calculated at receiver side. As a result, pseudorange equations consist of satellite positions and pseudorange measurements as the same number of visible satellites are obtained.

¹ Nurullah Gürçan, MSc Student, Gazi University, Electrical Electronics Engineering

² Özgür Ertuğ, Prof. Dr., Gazi University, Electrical Electronics Engineering

Equation (1) shows pseudorange equation for one satellite. τ_j represents pseudorange measurement of j^{th} satellite. (x_j, y_j, z_j) mentions satellite coordinates of j^{th} satellite as x, y and z axes, respectively. $(x_u, y_u, z_u, \delta b_u)$ terms are four unknowns of equation which represent x, y, z axes coordinates of receiver, and receiver clock bias, respectively. c is speed of light and ε is other error correction terms which affect position accuracy due to previously mentioned error sources.

$$\tau_j = \sqrt{(x_j - x_u)^2 + (y_j - y_u)^2 + (z_j - z_u)^2} + \delta b_u \cdot c + \varepsilon. \quad (1)$$

Except for ε , which can be calculated using some methods, there are four unknowns for calculating receiver position which are $(x_u, y_u, z_u, \delta b_u)$. Since pseudorange is measured by subtracting transmit time of signal from satellite and receiving time to receiver, both satellite and receiver have to use common clock. While satellites have atomic clock made of Rubidium and Cesium, receiver clocks are inexpensive and lack the precision required for sensitive measurements. Therefore, receiver clock bias compared to GPS system clock is an unknown for receiver and it must be solved to better estimate of receiver position. To calculate all four unknowns, at least four different pseudorange equations are needed. In other words, at least four different GPS satellites are needed to determine receiver position.

GPS satellite constellation is well designed to serve simultaneously all the Earth surface at any time and a receiver in an open environment can observe at least six satellite. A receiver may observe up to twelve satellites at the same time over 24 hours period (Ochieng, et al., 2002). This means that the receiver must deal with up to twelve pseudorange equations in consideration four unknowns to solve receiver position. This situation leads to not obtaining an

exact solution and such of these problems are defined as overdetermined systems in literature (Raquet, 2013: 66).

Nevertheless, different methods are developed to estimate most probable solution. In this study, estimation results by the least square, the weighted least square and the multilateration methods are compared by means of their position accuracies. Exponential and sigma models are used individually to set weight matrix in weighted least squares method and their result are presented separately. Observation and navigation RINEX (Receiver Independent Exchange Format) files from open platform are used as data sources (CDDIS DAAC, 2023a; CDDIS DAAC, 2023b). This open platform has measurements from stationary GPS receiver stations which their coordinates are known accurately and shared as “approximate position” in RINEX observation files, so that coordinate has taken as reference receiver position to find positional deviation of the results obtained from different position estimation algorithms. RINEX files are resolved in a MATLAB code, then code is utilized to compare mentioned position estimation algorithms (Mahooti, 2019). The sigma-modeled weighted least square method demonstrated its superiority among other algorithms by estimating position with lowest average error for same data.

Receiver Position Estimation Methods

While GPS receiver has satellite positions and pseudorange measurements, it would be so handy if more precise position accuracy of overdetermined problem is obtained by just doing math. This provides us to improve quality of receiver position accuracy with no cost. How position estimation is processed by three methods is investigated in this section.

Least Square Method

The method of least squares provides an approximate solution for overdetermined systems. If this method is applied to the equations in the system, the sum of the squares of the resulting error

amounts is the smallest possible value for the system's solution. Thus, the error amounts are distributed with the lowest possible share to all equations, resulting in an approximate solution set.

The method of least squares is only applied to linear systems. Since the pseudorange equations are not linear, linearization processes are required to apply this method.

As the first step of the linearization process, an estimate is made for the receiver's position. The estimated receiver's position is expressed as the estimated position in the x-axis (\hat{x}_u), in the y-axis (\hat{y}_u), in the z-axis (\hat{z}_u), and the estimated time difference ($\widehat{\delta b}_u$) in Equation (2).

$$\widehat{\alpha}_u = (\hat{x}_u, \hat{y}_u, \hat{z}_u, \widehat{\delta b}_u)^T. \quad (2)$$

According to this estimate, the pseudorange equation can be written as follows. This equation is a function of the $\widehat{\alpha}_u$ matrix which is expressed in Equation (3).

$$\tau_j = f(\alpha_u) = f(x_u, y_u, z_u, \delta b_u). \quad (3)$$

The relationship between estimated and the real receiver's position is expressed with the Equation (4, 5). α_u represents the real position of the receiver, $\widehat{\alpha}_u$ represents the estimated position of the receiver, and $\Delta\alpha$ represents the difference between the real position and the estimated position of the receiver. α_u is consist of actual user position in the x-axis (x_u), in the y-axis (y_u), in the z-axis (z_u), and actual time difference (δb_u) in Equation (5).

$$\alpha_u = \Delta\alpha + \widehat{\alpha}_u. \quad (4)$$

$$\alpha_u = (x_u, y_u, z_u, \delta b_u)^T. \quad (5)$$

When this equation is expressed as a function, it will appear as Equation (6, 7):

$$\tau_j = f(\alpha_u) = f(\Delta\alpha + \hat{\alpha}_u). \quad (6)$$

$$f(x_u, y_u, z_u, \delta b_u) = f([\Delta x + \hat{x}_u] + [\Delta y + \hat{y}_u] + [\Delta z + \hat{z}_u] + [\Delta\delta b + \hat{\delta b}_u]). \quad (7)$$

The real receiver's position can be expressed as the estimated position, the estimated position difference, and the error difference. Based on this, the function is expanded as a Taylor series in Equation (8). Terms of higher orders are denoted as *HOT*.

$$f(\Delta\alpha + \hat{\alpha}_u) = f(\hat{\alpha}_u) + \frac{d(f(\Delta\alpha))}{d\alpha} \cdot f(\Delta\alpha) + HOT. \quad (8)$$

In the Taylor series expansion, terms of second order and higher are neglected. Since the matrix of the difference between the estimated receiver's position and the real receiver's position consists of four unknowns, its derivative is taken partially which is expressed in Equation (9, 10, 11, 12, 13, 14).

$$f(\Delta\alpha + \hat{\alpha}_u) = f(\hat{\alpha}_u) + \frac{\partial(f(\Delta x))}{\partial \hat{x}_u} \cdot \Delta x_u + \frac{\partial(f(\Delta y))}{\partial \hat{y}_u} \cdot \Delta y_u + \frac{\partial(f(\Delta z))}{\partial \hat{z}_u} \Delta z_u + \frac{\partial(f(\Delta\delta b))}{\partial \delta \hat{b}_u} \cdot \Delta\delta b_u. \quad (9)$$

$$\frac{\partial(f(\Delta x))}{\partial \hat{x}_u} = \frac{(x_j - \hat{x}_u)}{r_j}. \quad (10)$$

$$\frac{\partial(f(\Delta y))}{\partial \hat{y}_u} = \frac{(y_j - \hat{y}_u)}{r_j}. \quad (11)$$

$$\frac{\partial(f(\Delta z))}{\partial \hat{z}_u} = \frac{(z_j - \hat{z}_u)}{r_j}. \quad (12)$$

$$\frac{\partial(f(\Delta\delta b))}{\partial \delta \hat{b}_u} = \frac{(\delta b_j - \delta \hat{b}_u)}{r_j}. \quad (13)$$

$$r_j = \sqrt{(x_j - \hat{x}_u)^2 + (y_j - \hat{y}_u)^2 + (z_j - \hat{z}_u)^2}. \quad (14)$$

When the calculated partial derivatives are used, the estimated pseudorange equation will appear as in Equation (15).

$$\Delta\delta b_u = \hat{\tau}_j + \frac{x_j - x_u}{r_j} \cdot \Delta x_u + \frac{y_j - y_u}{r_j} \cdot \Delta y_u + \frac{z_j - z_u}{r_j} \cdot \Delta z_u + \frac{\delta b_j - \delta b_u}{r_j}. \quad (15)$$

When the fractional terms are shown as a single term, the equation will be as Equation (16, 17).

$$\Delta\tau_j = a_{xj} \cdot \Delta x_u + a_{yj} \cdot \Delta y_u + a_{zj} \cdot \Delta z_u + a_{\delta bj} \cdot \Delta\delta b_u. \quad (16)$$

$$\Delta\tau_j = \tau_j - \hat{\tau}_j. \quad (17)$$

As seen, instead of the pseudorange equation, another equation is created with only the coefficients of the unknowns. When calculating the receiver's position, as many equations as the number of visible satellites will emerge.

Linear equations are equations that can be expressed as Equation (18). If the pseudorange equations are to be expressed in this form, they will appear as Equation (19, 20, 21, 22).

$$A \cdot x = B. \quad (18)$$

$$A = \begin{bmatrix} a_{x1} & a_{y1} & a_{z1} & a_{\delta b1} \\ a_{x2} & a_{y2} & a_{z2} & a_{\delta b2} \\ a_{x3} & a_{y3} & a_{z3} & a_{\delta b3} \\ \vdots & \vdots & \vdots & \vdots \\ a_{xj} & a_{yj} & a_{zj} & a_{\delta bj} \end{bmatrix}. \quad (19)$$

$$x = (\Delta x_u, \Delta y_u, \Delta z_u, \Delta\delta b_u)^T. \quad (20)$$

$$B = (\Delta\tau_1, \Delta\tau_2, \Delta\tau_3, \dots, \Delta\tau_j)^T. \quad (21)$$

If there are four equations, a common solution set is found. If there are more than four equations, this system is an overdetermined system. In this case, the method of least squares can be used.

First, the transpose of matrix A is multiplied on both sides of the equation as Equation (22). This operation makes the matrix sizes on both sides of the equation equal, and four equations for four unknowns are obtained.

$$A^T \cdot A \cdot x = A^T \cdot B. \quad (22)$$

$$A^T = \begin{bmatrix} a_{x1} & a_{x2} & a_{x3} & \dots & a_{xj} \\ a_{y1} & a_{y2} & a_{y3} & \dots & a_{yj} \\ a_{z1} & a_{z2} & a_{z3} & \dots & a_{zj} \\ a_{\delta b1} & a_{\delta b2} & a_{\delta b3} & \dots & a_{\delta bj} \end{bmatrix}. \quad (23)$$

Using the remaining four equations, the four unknowns are solved as Equation (24, 25, 26, 27).

$$b_{11} \cdot \Delta x_u + b_{12} \cdot \Delta y_u + b_{13} \cdot \Delta z_u + b_{14} \cdot \Delta \delta b_u = a_{x1} \cdot \Delta \tau_1 + a_{x2} \cdot \Delta \tau_2 + a_{x3} \cdot \Delta \tau_3 + \dots \quad (24)$$

$$b_{21} \cdot \Delta x_u + b_{22} \cdot \Delta y_u + b_{23} \cdot \Delta z_u + b_{24} \cdot \Delta \delta b_u = a_{y1} \cdot \Delta \tau_1 + a_{y2} \cdot \Delta \tau_2 + a_{y3} \cdot \Delta \tau_3 + \dots \quad (25)$$

$$b_{31} \cdot \Delta x_u + b_{32} \cdot \Delta y_u + b_{33} \cdot \Delta z_u + b_{34} \cdot \Delta \delta b_u = a_{z1} \cdot \Delta \tau_1 + a_{z2} \cdot \Delta \tau_2 + a_{z3} \cdot \Delta \tau_3 + \dots \quad (26)$$

$$b_{41} \cdot \Delta x_u + b_{42} \cdot \Delta y_u + b_{43} \cdot \Delta z_u + b_{44} \cdot \Delta \delta b_u = a_{\delta b1} \cdot \Delta \tau_1 + a_{\delta b2} \cdot \Delta \tau_2 + a_{\delta b3} \cdot \Delta \tau_3 + \dots \quad (27)$$

As can be seen, the calculated values here are the values in the $\Delta\alpha$ matrix representing the difference between the real receiver's position and the estimated receiver's position. In the method of least squares, when pseudorange equations emerge, the center of the Earth can be assumed as the initial estimate for the receiver's position. As a result of this estimate, another estimate closer to the real receiver's position is obtained by adding the $\Delta\alpha$ value to the estimate. In this way, in a few iterations, much closer estimates to the real receiver's position will be put forward.

Weighted Least Square Method

The solution set obtained in the least squares method simply takes the average of the measured values. In the weighted method, on the other hand, the aim is to increase the influence of reliable measurements on the solution set (Simon, 2006: 82).

Weighted least squares uses same idea with least square method. Only difference in algorithm is adding weights to Equation (22). Formula used in weighted least squares is given in Equation (28). Weighting is performed by multiplying both sides by R^{-1} which is inverse of covariance matrix. After this calculation, rest of the process is same as least square method.

$$A^T \cdot R^{-1} \cdot A \cdot x = A^T \cdot R^{-1} \cdot B. \quad (28)$$

A covariance matrix is constructed based on the variance value as shown in Equation (29). Variance values are determined by exponential and sigma weighting models which are covered in (Li and Muqing, 2009). Both of weighting models take SNR (signal to

noise ratio) values of each satellite as weights of observation. More SNR value is considered as more reliable observation.

$$R = \text{diag}(\sigma_1^2, \sigma_2^2, \dots, \sigma_j^2). \quad (29)$$

In the exponential-modeled weighted least square method, variance values are calculated as Equation (30) where s_j is j^{th} covariance matrix and a, b, k is model parameters. Different values of model parameters are tested in (Li and Muqing, 2009) and $a = 0$, $b = 1$ and $k = 0.3$ is determined as optimal condition for exponential model.

$$s_j = a + b \cdot e^{k \cdot (\min(\text{SNR}) - \text{SNR}_j)}. \quad (30)$$

In sigma-modeled weighted least square method, variance values are calculated as Equation (31). Different values of model parameters are tested in (Li and Muqing, 2009) and $a = 0$ and $b = 1.e5$ is determined as optimal condition for sigma model.

$$s_j = \sqrt{a + b \cdot 10^{(-\text{SNR}_j)/10}}. \quad (31)$$

The sum of weighted factors is normalized by Equation (32) and weights to be used in Equation (28) are obtained.

$$\sigma_j^2 = s_j / \left(\prod_{j=1}^N s_j \right)^{1/N}. \quad (32)$$

Similar to the least squares method, in the case of the receiver's initial estimate, the center of the Earth is assumed, and after a few iterations, very close estimates to the actual receiver position are determined.

Multilateration Method

Global positioning systems are generally designed to calculate the receiver's position using a trilateration method. To do this, three satellite distances to receiver are calculate. Three different spheres are created which their center is located at each satellite and their radius is the distance between each satellite to receiver. Three spheres give two intersection point. The point near the Earth is accepted as receiver position as trilateration method. In everyday use scenarios, receivers obtain distances from more than three satellites. Therefore, a common intersection point may not be obtained for more than three spheres, so receiver position cannot be provided. With the multilateration method, an algebraic estimate for the receiver's position is provided without the need for an iteration (Bancroft, 1985).

If number of observed satellites is only four and nonexistence of other errors, multilateration method brought forward by Bancroft gives true position. For more than four satellites, Moore-Penrose pseudoinversion should be implemented to get more accurate solution (Bedin, 2022).

In this method, $n \times 4$ data matrix consists of satellite positions and pseudorange is constructed as Equation (33, 34). a_j represents data matrix of j^{th} satellite. S matrix keeps data matrixes of observed satellites.

$$S = (a_1, a_2, a_3, \dots, a_n)^T. \quad (33)$$

$$a_j = (x_j, y_j, z_j, \tau_j)^T. \quad (34)$$

Bancroft utilize Minkowski sum to implement a solution for overdetermined problem. Formulation of Minkoswki is shown in Equation (35). It is applied to data matrixes of all observed satellites and construct r matrix as Equation (36, 37). r_j represents half of Minkowski sum for j^{th} satellite.

$$\langle a, b \rangle = a_1 \cdot b_1 + a_2 \cdot b_2 + a_3 \cdot b_3 - a_4 \cdot b_4. \quad (35)$$

$$r_j = \langle a_j, a_j \rangle / 2. \quad (36)$$

$$r = (r_1, r_2, r_3, \dots, r_n)^T. \quad (37)$$

H matrix of generalized inverse function is calculated as Equation (38). If so, any weight is known, this H matrix can be modified with weights. However, it is not covered in this study.

$$H = (S^T \cdot S)^{-1} \cdot S^T. \quad (38)$$

E , F and G coefficients are calculated as Equation (39, 40, 41). u and v parameters are defined in Equation (42, 43). i_0 identity matrix to calculate u shown in Equation (44).

$$E = \langle u, u \rangle. \quad (39)$$

$$F = \langle u, v \rangle - I. \quad (40)$$

$$G = \langle v, v \rangle. \quad (41)$$

$$u = H \cdot i_0. \quad (42)$$

$$v = H \cdot r. \quad (43)$$

$$i_0 = (I, I, I, \dots, I)^T. \quad (44)$$

E , F and G coefficients used to calculate roots of λ which is in Equation (45).

$$E \cdot \lambda^2 + 2 \cdot F \cdot \lambda + G = 0. \quad (45)$$

Equation (45) provides two roots for λ which are $\lambda_{1,2}$. Using these roots, $y_{1,2}$ column vectors in Equation (46) is calculated.

$$y_{1,2} = \lambda_{1,2} \cdot u + v. \quad (46)$$

The vector y gives x user position and b receiver clock offset as Equation (47). Although there are two solutions for Equation (47), actual solution can be determined by checking the user position solution via pseudorange equation in Equation (1).

$$y^T = (x^T - b)^T. \quad (47)$$

Method And Test Result

Position estimation methods require satellite positions in view and pseudorange measurements of each satellite to receiver.

RINEX data format provides this information. RINEX files is commonly accepted as a standard and various institution in the world is present their hourly or daily datasets in this format. We acquired satellite positions from RINEX navigation file and pseudorange measurements from RINEX observation file (CDDIS DAAC, 2023a; CDDIS DAAC, 2023b).

RINEX navigation file stores ephemeris data which is broadcasted in the same content from all satellites. Ephemeris data is structure of satellite positions in all GPS orbits and this data uses Keplerian parameters to define satellite positions. Since ephemeris data is accepted to be valid for two minutes, RINEX navigation file keeps ephemeris data within two minutes period. It should not be forgotten that before defining these parameters to position estimation algorithms, correction of Earth rotation must be performed to satellite positions.

RINEX observation file stores pseudorange measurements for visible satellites to user along with some error corrections measurements to compensate errors like ionospheric and tropospheric delays. In the header area of observation file, executive institution of stationary GPS station provides receiver position as “Approximate position XYZ”. This position is accepted as true reference value for the output of three different position estimation methods under investigation.

MATLAB code of (Mahooti, 2019) is used to read RINEX files with some corrections and additions by us like making it suitable to read RINEX 3 observation files. For multilateration method, MATLAB code of (Aaron T. Becker's Robot Swarm Lab, 2023) is provided to implement the method. The code firstly performs ionospheric and tropospheric corrections to pseudorange measurements following by correction of Earth rotation to satellite positions. Then, we implement our code which includes three different position estimation methods and their comparison of reference receiver position. Code is made flexible to perform as much as the number of desired epochs.

To present at this paper, observation and navigation RINEX files from AMC400USA station of IGS network is chosen. Both files are generated on the date of 04.01.2023 and observation file contains information of 30 seconds period while navigation file has two minutes period (CDDIS DAAC, 2023a; CDDIS DAAC, 2023b).

For least square and weighted least square methods, five iterations are performed for each measurement. SNR values which are taken as weight are obtained from S1 and S2 parameters of observations file.

Figure 1 shows comparison of three different position estimation methods for 3000 seconds. Since each observation is made within 30 seconds, totally 100 measurements are compared in Figure 1.

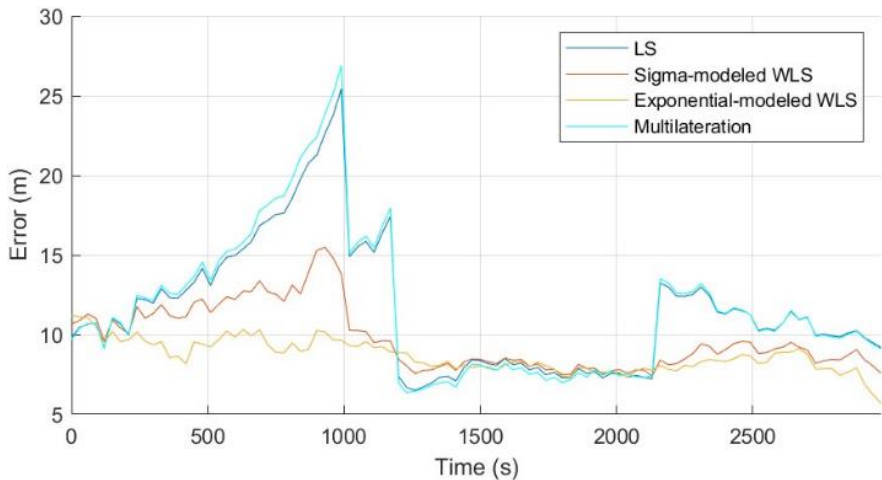


Figure 1. Mean position error of three different position estimation methods

Table 1 shows errors of each method after averaging over 100 samples. It includes mean error in addition to separately calculated X, Y and Z axis.

Table 1. Comparison of position errors of different three methods

	Mean Error (m)	X Axis Error (m)	Y Axis Error (m)	Z Axis Error (m)
Least Square Method	11.54	11.94	10.76	13.99
Exponential-modeled Weighted Least Square Method	8.66	9.92	6.14	9.77
Sigma-modeled Weighted Least Square Method	9.72	11.06	7.05	3.82
Multilateration Algebraic Method	11.69	11.82	11.42	15.56

As seen mean error in “Table 1”, exponential modeled weighted least square method provided least position error.

Conclusions

In this paper, three different position estimation methods are compared to investigate which one of them provides better position accuracy. A MATLAB code is used to read RINEX files and make calculations. Effectiveness of three different position estimation methods is compared by using real measurements. The results shows that exponential modeled weighted least square method which provides best estimate among others yields 8.66 meters error on average over 100 measurements which are sampled 30 seconds intervals.

References

Aaron T. Becker's Robot Swarm Lab. (2023). Multilateration Algebraic GPS Equations (S. Bancroft Method). (1.0.3). MATLAB Central File Exchange. Retrieved September 17, 2023, from <https://www.mathworks.com/matlabcentral/fileexchange/87744-multilateration-algebraic-gps-equations-s-bancroft-method>

Bancroft, S. (1985, January). An Algebraic Solution of the GPS Equations. *IEEE Transactions on Aerospace and Electronic Systems*(AES-21), pp. 56-59. doi:10.1109/TAES.1985.310538

Bedin, D. A. (2022). Positioning by Pseudorange Measurements Using the Bancroft Method: Approaches to the Description of the Nonlinear Error Distribution. *29th Saint Petersburg International Conference on Integrated Navigation Systems (ICINS)*, (pp. 1-4). Saint Petersburg, Russian Federation. doi:10.23919/ICINS51784.2022.9815398

Crustal Dynamics Data Information System (CDDIS DAAC). (2023). Daily 30-second observation data on January 31,2023 from AMC400USA station. Greenbelt, MD, USA: International GNSS Service (IGS). Retrieved October 3, 2023, from <https://cddis.nasa.gov/archive/gnss/data/daily/2023/004/23o/>

Crustal Dynamics Data Information System (CDDIS DAAC). (2023). Daily navigation data on January 31,2023 from AMC400USA station. Greenbelt, MD, U.S.A: International GNSS Service (IGS). Retrieved September 3, 2023, from <https://cddis.nasa.gov/archive/gnss/data/daily/2023/004/23n>

Li, J., & Muqing, W. (2009). The Improvement of Positioning Accuracy with Weighted Least Square Based on SNR. *5th International Conference on Wireless Communications, Networking and Mobile Computing*, (pp. 1-4). Beijing, China. doi:10.1109/WICOM.2009.5302600

Mahooti, M. (2019, November 26). GPS Receiver Position. (1.1.1.0). Retrieved September 7, 2023, from

<https://www.mathworks.com/matlabcentral/fileexchange/56730-gps-receiver-position>

Ochieng, W., Sauer, K., Cross, P., Sheridan, K., Lannelongue, S., Ammour, N., & Petit, K. (2002, December). Integrity Mechanisms for GPS Satellites within the GALILEO Architecture. *Journal of Geospatial Engineering*, pp. 95-110.

Raquet, J. (2013). *Calculation of GPS PNT Solution*. Trieste: Workshop on GNSS Data Application to Low Latitude Ionospheric Research.

Simon, D. (2006). *Optimal State Estimation: Kalman, H ∞ , and Nonlinear Approaches*. John Wiley & Sons. doi:10.1002/0470045345

CHAPTER III

Mosaicing of Non-Overlapping Images Using Deep Learning Based Homography Estimation

Ali Batuhan YELLİ¹
Gökhan Koray GÜLTEKİN²

1.Introduction

Image mosaicing is the process of combining multiple images to create a high-resolution, panoramic image with a wider FOV (Inampudi, 1998: 1). Examples of areas where image mosaicing is used include satellite imaging, medical imaging, virtual imaging and games, mobile applications, underwater surveillance etc.

¹ Msc Student, Ankara Yıldırım Beyazıt Üniversitesi., Elektrik Elektronik Mühendisliği,
Orcid: 0000-0002-4636-5879

² Assist. Prof., Ankara Yıldırım Beyazıt Üniversitesi, Elektrik Elektronik Mühendisliği,
Orcid: 0000-0003-2895-7042

The image mosaicing process consists of feature matching, registration and seam removal stages. A well mosaiced image should be high resolution and smooth-edged. Image mosaicing methods in the literature can be grouped into two; the traditional methods and learning-based methods.

Traditional methods aim to combine images with overlapping area. Traditional methods consist of registration and blending stages. Registration expresses the geometric transformation between image pairs by feature matching.

In the registration stage, geometric transformation estimation is made and images are aligned according to the reference image. The most general case of the transformation is the so called homography. Homography is a matrix with 8 unknowns that contains information about rotation, translation and scaling between a pair of images. In the image registration phase, firstly, feature extraction is performed for two images. Then, the common features in the overlap area of these images are matched. After the feature matching process, the transformation matrix is extracted between the images. Some errors may occur after combining images according to the transformation matrix. Misalignment and ghosting are examples of these errors. To eliminate these errors, blending is performed. Geometric transformation is a method often used when aligning images with a certain common overlap area.

2D homography estimation (or projective transformation) is a frequently used method in computer vision. Homography is a method used in systems, especially at planar scenes, in situations where objects are far away and in scenes with rotational motion. Two images rotating around the camera center can be associated with each other by homography, thus creating a panoramic image. Homography is widely used in SLAM algorithms especially in ORB-SLAM, augmented reality fields and camera calibration. In traditional methods, homography estimation consists of 2 stages. These are corner estimation and robustness. Robustness is provided by the random sample consensus (RANSAC) (Hartley and

Zissermann, 2003) method. After a transformation matrix is extracted in the homography process, it is checked with RANSAC whether this matrix matches the feature matches on a line and the unmatched matches are eliminated.

CNN (Convolutional Neural Network) based methods have become widespread recently thanks to their feature extraction capabilities. These methods are used in areas such as object tracking, depth estimation, semantic segmentation, optical flow, voice recognition algorithms etc.

CNN has also started to be used in the field of image mosaicing. Additionally, homography estimation can be made with Deep Convolutional Neural Network method. As shown in **Hata! Başvuru kaynağı bulunamadı**. Figure 1, HomographyNet is a deep neural network that can estimate the homography matrix between two images.

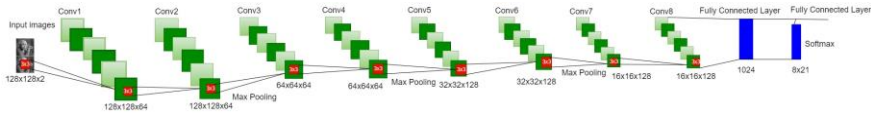


Figure 1 - Deep Image Homography Estimation (HomographyNet).

Studies in the field of image mosaicing are generally stitch pairs of images with a common overlap area. In this article, we describe our stitching method for pairs of images that do not have a common overlap area.

We used homography as a basis for this mosaicing process and use a deep learning-based method. When creating a dataset for pairs of images that do not have overlapping areas, we cut a pair of images on a large image so that one image ends where the other image begins. We used only translation while using the homography method in these image pairs that do not include rotation and scaling between them. We trained a deep homography network according to the amount of translation in the horizontal and vertical axes between

the image pairs, then stitched the image pairs that have non-overlap area in the test process.

In summary, our method; allows pairs of images that have non-overlapping area to be stitched with horizontal and vertical translation information (without rotation and scaling) using a homography matrix. We perform this mosaicing process with a deep learning-based method.

Related Work

This paper presents a learning based homography solution for image mosaicing. Hence, related work section includes previous works related to image mosaicing with traditional methods and deep image mosaicing with learning-based methods.

Image Mosaicing with Traditional Methods

Image Mosaicing is the process of stitching image pairs that have an overlapping area on the 3D scene plane (Capel, 2004). Mosaicing can be applied in scenes where images are associated with planar homography (Gosh et al., 2012). If the images show no parallax effect, i.e., the scene is planar, or the camera rotates only around its optical center (Azzari et al., 2008).

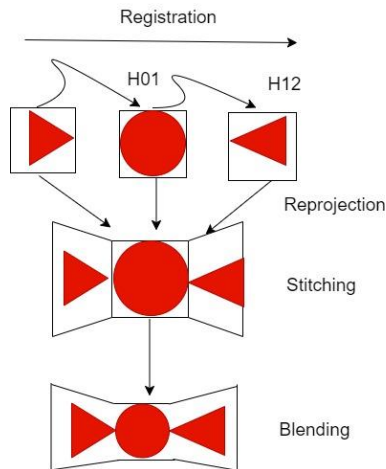


Figure 2 - Traditional image mosaicing steps. H refers to the homography matrix between image pairs (Capel,2004)

As seen in Figure 2, image mosaicing in traditional methods is done with different image processing algorithms, respectively: registration, reprojection, stitching, and blending (Ghosh and Kaabouch, 2016). Image registration and blending are two important parameters that affect performance in the mosaicing process.

In the registration stage, a geometric transformation is estimated between pairs of images in the same plane. Then according to the geometric transformation, the target image and reference image are aligned to each other. As shown in Figure 3 **Hata! Başvuru kaynağı bulunamadı.**, registration based mosaicking algorithms in the literature include two different categories: spatial domain-based or frequency domain-based (Ghosh and Kaabouch, 2016). Spatial domain-based image mosaicing divided into two: area-based and feature-based mosaicing.

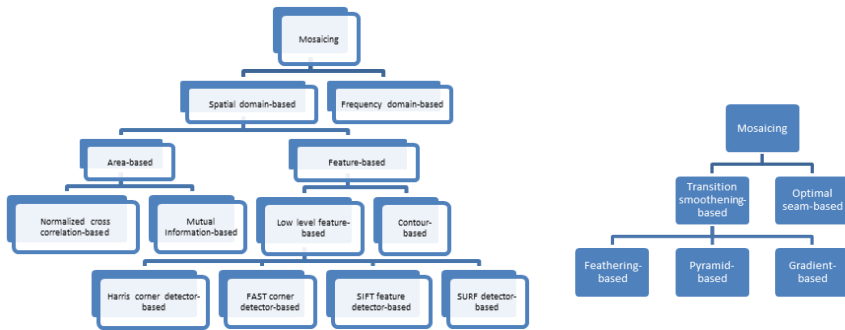


Figure 3 - Classification based on registration(left) and blending(right) methods.

Area-based image mosaicing divided into two groups: Normalized Cross Correlation (NCC) based and Mutual Information (MI) based mosaicing. NCC based method calculates similarity between the “windows” in the two images for each displacements defined as (Szeliski, 2007). Nasibov et al. (Nasibov et al., 2009)

developed a mosaicing algorithm that is more sensitive to illumination differences with a brightness correction matrix.

Berberidis et al (Berberidis and Karybali, 2002) proposed an iterative algorithm for spatial cross correlation. Thus, the displacement between image pairs were calculated and a faster algorithm was presented. In (Miranda-Luna et al., 2008), Luna et al. compute similarity between image pairs with MI. In addition, they presented a faster algorithm using a stochastic gradient optimization. To increase the computation speed, Dame et.al. (Dame and Marchand, 2011) proposed a fast algorithm using a B-spline function for normalized mutual probability density.

Frequency-domain based image mosaicing algorithms require computation in order to find the optimal transformation parameters between a pair of images.

Blending algorithms are used in mosaicing algorithms to increase efficiency and make a good visual combination. With blending algorithms, the brightness and color transitions in the images are optimized. Thus, problems such as misalignment, ghosting, and camera exposure differences that may arise in mosaic images can be eliminated.

Image mosaicing algorithms can be grouped as shown in Figure 3, based on the image blending methods as transition smoothing-based and optimal-seam based (Ghosh and Kaabouch, 2016).

Transition-smoothing based mosaicing algorithms are applied to overlapping regions of images and provide seamless transition. These algorithms are divided into 3: feathering, pyramid and gradient-based blending algorithms. Feather-based algorithms perform blending by averaging the pixel values in the common area of image pairs (Jain et al., 2012). As an example, the study of Levin et al (Levin et al., 2004). can be given. Pyramid-based algorithms provide a more efficient method by converting input images into bandpass pyramids (Xiong and Turkowski, 1998). Xiong et al

proposed a pyramid-based method (Xiong, 2009). Gradient-based algorithms provide a method of mosaicing by blending gradients of images. An example of gradient-based algorithms is the study of Szeliski et al (Szeliski et al., 2011).

Optimum seam-based mosaicing algorithms try to provide a seamless transition by searching for the most appropriate seam at the points where the images stitch. Examples of optimal seam-based algorithms include a modified difference region method in (El-Saban et al., 2011), an algorithm based on watershed segmentation and graph cutting optimization in (Gracias et al., 2009), and Dynamic programming and gray relational analysis-based methods in (Wen and Zhou, 2008).

Deep Image Mosaicing

Learning-based image mosaicing methods are divided into view-fixed and view-free methods (Nie et al., 2021). View-fixed methods are used in specific areas such as autonomous driving (Wang et al., 2020), (Lai et al., 2019), surveillance videos (Li et al., 2019). While end-to-end networks are proposed in these studies, images are not stitched from arbitrary viewpoints. In view-free methods, images can be stitched from arbitrary viewpoints using CNNs. In some studies, CNN's have also been used for feature detection (Hoang et al., 2020), (Shi et al., 2020). According to the first complete learning-based method (Nie et al., 2020), images with arbitrary viewpoints can be stitched in three stages: homography estimation, spatial transformation and content refinement. In addition to this method, the resolution limitation is removed with an edge-preserving deep image stitching method and significant improvement in performance achieved in real scenes (Nie et al., 2020).

Since we use the homography method in this study, we will also describe the studies on deep homography. In the first proposed deep homography method (DeTone et al., 2016), a homography matrix was estimated using a VGG style network (Simonyan and Zisserman, 2014) corresponding to eight displacement of the four

vertices of the image. Nguyen et al. presented the first unsupervised deep homography method (Nguyen et al., 2018) using effective unsupervised loss in addition to this architecture (DeTone et al., 2016). Zhang et al. (Zhang et al., 2020) proposes a content-aware unsupervised network, contributing to SOTA performance in small-baseline deep homography. In another study (Le et al., 2020), using image pyramids, multi-scale features were detected and homography estimation was performed.

Methodology

In this paper, we study mosaicing images that have a non-overlap area with a learning-based method. We provide this mosaicing process with the homography method. We train our network according to the homography matrix between pairs of images in our dataset. The non-overlap image mosaicing process explains of 3 steps homography estimation, network architecture and loss function, respectively.

Homography Estimation

Rotation, translation and scale information between two images are expressed by the homography matrix.

$$\begin{pmatrix} u' \\ v' \\ 1 \end{pmatrix} = \begin{pmatrix} H_{11} & H_{12} & H_{13} \\ H_{21} & H_{22} & H_{23} \\ H_{31} & H_{32} & H_{33} \end{pmatrix} \begin{pmatrix} u \\ v \\ 1 \end{pmatrix} \quad (1)$$

The homography maps $[u, v]$, the pixels in the left image, to $[u', v']$, the pixels in the right image, and scale is one. The homography matrix is divided into submatrices as rotation and translation. $[H_{11} \ H_{12} ; H_{21} \ H_{22}]$ submatrices represent the rotational terms and $[H_{13} \ H_{23}]$ is the translational displacement.

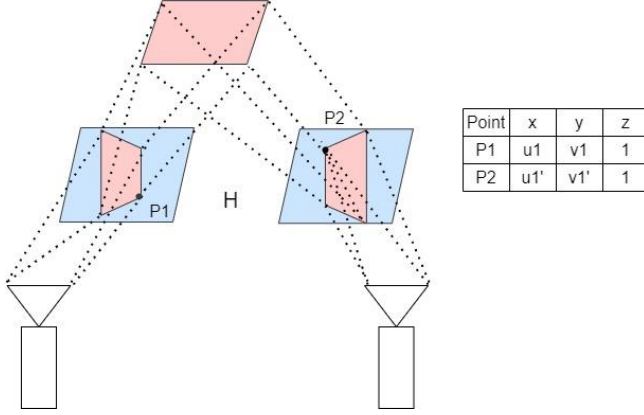


Figure 4 - 4-point parametrization

As shown in Figure 4, 4-point parameterization can be used to express the coordinate difference between the vertices in two images. 4-point parameterization is used in traditional homography estimation methods (Baker et al., 2006) and is also suitable for deep homography estimation methods. For example, if $\Delta_{u1} = u1' - u1$ be the u-displacement for the first corner, the 4-point parameterization in homography is formulated as follows (D. DeTone, 2016):

$$H_{4point} = \begin{pmatrix} \Delta_{u1} & \Delta_{v1} \\ \Delta_{u2} & \Delta_{v2} \\ \Delta_{u3} & \Delta_{v3} \\ \Delta_{u4} & \Delta_{v4} \end{pmatrix} \quad (2)$$

If the coordinate changes in the horizontal and vertical axes between the image pairs are known, H_{4point} can easily convert to homography matrix. This can be defined as the direct linear transform (DLT) algorithm (Hartley and Zissermann, 2003).

In our study of non-overlap image mosaicing, there is no rotational and scaling difference between the image pairs. Therefore, we only use the translational terms in the horizontal and vertical axis in training and testing processes.

While creating the dataset, firstly $p=(x,y)$ point is selected in a large I image and a 320×240 image is cut from the beginning of this point. Let's call this image patch A. Then, a random amount of translation is generated for the horizontal and vertical axis so that there is no overlap between the images. These translation values are summed with the coordinates of the p point and a new $p=(x+tx,y+ty)$ point is created. A new 320×240 image is cut from the beginning of the p point, which is called patch B. The coordinate difference between the 4 vertices of the A and B images is expressed as H_{AB} with the 4-point parameterization (Figure 5). The dataset creation phase will be explained more descriptively in section 0.

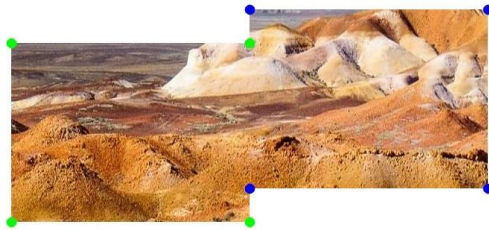


Figure 5 - Dataset Creating

Network Architecture

At this stage, we create a network that generates homography output. Our network has a structure similar to the VGGNet architecture in Figure 1 (Simonyan and Zisserman, 2014)0. It uses 3×3 convolutional blocks in addition to BatchNorm and RELU. Two input images feed a network, causing it to produce a homography matrix. In our network, the input images are grayscale and $128 \times 128 \times 2$ in size as in VGGNet. VGGNet is a Deep Convolutional Neural Network that enables homography estimation between image pairs. We use a total of 8 convolutional layers in the architecture, with 1 max pooling layer (2×2 , stride 2) after every 2 convolutional layers. The first 4 of the 8 convolutional layers have 64 filter numbers and the last 4 have 128 filter numbers. After the last 2 convolutional layers, we use 2 fully connected layers. After the final

convolutional layer and the following first fully connected layer with 1024 units, a dropout with probability 0.5 is applied.

While our network architecture has the same architecture as HomographyNet until the last layer, in the last layer we use a regression network (DeTone et al., 2016) 0 instead of a classification network(Figure 6).

The regression network uses Euclidean loss(L2) and 8 numbers at the end of the training process. This network, which is simple in formulation, may not always be used because it is not based on a certainty.

The formula of loss function in regression network:

$$\text{Loss:Euclidean(L2)} = \sqrt{px^2 + qx^2} \tag{3}$$

The classification network uses a quantization scheme. In addition to this scheme, it uses cross-entropy loss because it has a softmax in the last layer. It is more useful to use on image pairs that contain rotational changes. We do not use the classification network because our study doesn't include rotational changes. De tone et al. in their study they created a final layer with 168 output neurons using 21 quantization boxes for each of 8 output dimensions.

The formula of loss function in classification network:

$$\text{Loss:Cross-Entropy} = - \sum_x p(x) \log q(x) \tag{4}$$

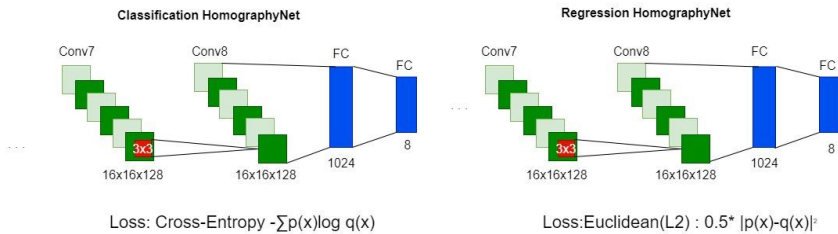


Figure 6 - Classification Network vs Regression Network

Loss Function

While training our deep neural network, we use the Euclidean loss function (L2) at the end of the training process. The Euclidean loss function (L2) we use is expressed as follows.

$$Loss: (L2) = \sqrt{\sum (H_{gt} - H_{network})^2} \quad (5)$$

H_{gt} : Ground truth of homography matrix between image pairs.

$H_{network}$: The homography matrix produced by our network in the training process.

The general formula of homography matrix is:

$$H = \begin{matrix} H_{11} & H_{12} & H_{13} \\ H_{21} & H_{22} & H_{23} \\ H_{31} & H_{32} & H_{33} \end{matrix} \quad (6)$$

Since our study does not include rotational difference, the rotational terms(H_{11} , H_{12} , H_{21} , H_{22}) will be taken as 0. We also accept 1 as the scale(H_{33}). Therefore, while formulating the loss function, we actually only train according to the difference between the translation(H_{13} , H_{23}) values.

Dataset Preparation

Image mosaicing studies in the literature stitch images with overlapping areas. Since mosaicing has not been done before for non-overlapping images, we used plain image datasets with fewer edges and features to train the network more easily. So, we trained and tested our deep homography estimation algorithm with Kaggle's dataset containing landscape images (Arnaud58, 2020). This dataset includes mountain, desert, sea, island and beach landscape images (Figure 7).



Figure 7 - Some examples of Kaggle landscape dataset images (left). Some images of our dataset (right).

While creating training, validation and testing set from Kaggle’s landscape image datasets, we first resized all images to 1280x960 pixels. Then, from this large image, we created by randomly cutting 2 input images that have non-overlapping area, and stitch from the horizontal or vertical axis. (see right image in Figure 7). The corner points of image A are shown in green, and the corner points of image B are shown in blue. Thus, a large dataset was created for image pairs that have non-overlap area. Our dataset contains 500000 image pairs for training and 5000 image pairs for validation and testing.

Experiments

Implementation Details

We trained our network for about 120 hours using the Intel Iris Xe Graphics GPU that using stochastic gradient descent (SGD) with momentum of 0.9. We basically set the learning rate to 0.005 and multiplied it to 0.1 after every 30,000 iterations. While the algorithm was trained with a total of 90,000 iterations, the batch size was chosen as 64.

While creating the dataset for training, we used Kaggle’s landscape dataset (Arnaud58, 2020), which includes desert, mountain, beach, island, sea images. Among these images, we cut the 320x240 image pairs that have non-overlap area, as we explained

in section 0 and converted the images to grayscale. In this way, we have created 500,000 image pairs for training. We resized these grayscale image pairs to 128x128 before inputting them into the homography estimation network in Figure 1.

When creating image pairs that have non-overlap area from the horizontal or vertical axis, we define some corner-displacement amount between them. The corner-displacement amount is the horizontal or vertical pixel difference between the points where the images stitch. While creating the data set in our algorithm, this displacement amount was randomly selected to be a maximum of 32 pixels. For example, in the Figure 8, the corner-displacement amount for the image pairs whose corners are marked in green and blue is defined as the pixel difference on the horizontal axis between the green and blue corners in the red box. The corner-displacement amount for Figure 8 is approximately 20 pixels.

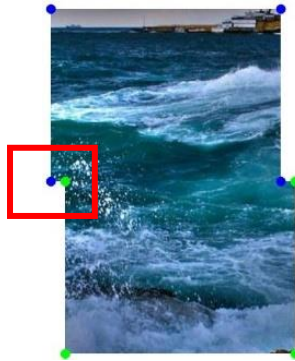


Figure 8 - Corner displacement between the image pairs. The green corner inside the red box is the upper left corner of the reference image. The blue corner is the lower left corner of the target image. The pixel difference between these 2 corners is defined as the corner-displacement.

Experimental Configuration

In this section, we will explain the performance of our Deep Homography estimation network with different experiments. We

will compare the performance of our algorithm on images with different corner-displacement amounts and different amounts of Gaussian noise, respectively.

5.2.1. Testing at Different Corner-Displacement Amounts.

In section 0, we explained that when testing our algorithm, we set a random corner displacement value. In order to examine the variation of the performance of our network according to the amount of corner displacement, we train our network by only changing the amount of corner displacement, provided that the parameters such as GPU, number of iterations and training time remain constant. Below we describe the results when we train our mesh to have a maximum vertex displacement of 32 and 96, respectively.

To measure the performance of our network, we take the median of the error values on the horizontal and vertical axes. In addition, we can observe the performance of our algorithm by plotting the average corner position errors on the horizontal and vertical axis. Table 1 shows the variation of the median of corner position errors in the horizontal and vertical axes for the maximum corner-displacement of 32 and 96 pixels.

Table 1 - Error analysis in x and y axis according to different corner-displacement amounts.

Max. Corner-displacement (pixel)	\bar{X} (pixel)	\bar{Y} (pixel)
32	1	1
96	2	2

\bar{X} : Median of corner position errors along x axis. \bar{Y} : Median of corner position

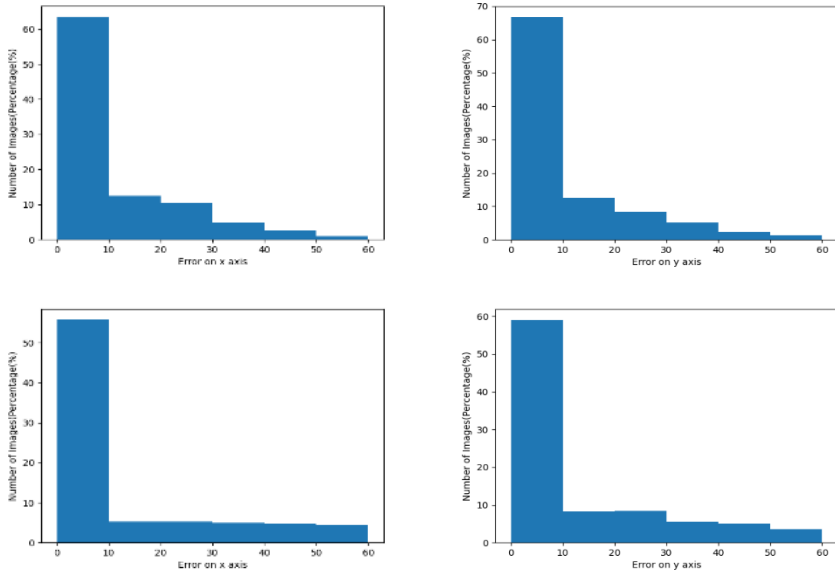


Figure 9 - Percentage histogram graphs on horizontal and vertical axis for maximum corner-displacement of 32 and 96 pixels respectively.

In Figure 9 the percentile histogram graph of the corner position errors on the horizontal and vertical axis relative to the maximum corner-displacement of 32 and 96 pixels, respectively, is given. According to this figure, the network gives better performance when the amount of corner-displacement is reduced. However, in both cases the median of the corner position errors is less than 2 pixels which means that most of the images are stitched very accurately.

5.2.2. Testing at Different Amounts of Gaussian Noise.

In this section, we tested our network with images containing different amount of Gaussian noise without changing other parameters such as maximum vertex-displacement amount, training time, GPU etc. Table 2 shows the variation of the median of corner position errors in the horizontal and vertical axes for the different

gaussian noise with different variances. As we can see from the table, the performance of the network decreases as the amount of gaussian noise increases.

Table 2. Error analysis in horizontal and vertical axis according to different gaussian-noise.

Variance (pixel)	\bar{X} (pixel)	\bar{Y}
0	1	1
0.001	45	2
0.005	83	-
0.1	88	-

\bar{X} : Median of corner position errors along x axis. \bar{Y} : Median of

Results

Our network has been tested for 5000 image pairs that have no overlap area. In the test process, we set the maximum corner-displacement amount to 32 and our test set does not contain gaussian noise. As a result of this test applied to 320x240 image pairs, the median of the errors in the horizontal and vertical axes is 1 pixel. Contrary to the studies in the literature mosaicing overlapping images, our method yielded successful results in non-overlapping images.

In the previous section, we also explained the variation of the performance of our network according to the amount of corner-displacement and gaussian noise. When we increase the maximum corner-displacement amount to 96, the performance of our network has decreased a little and the median of the corner position errors in both axes is 2. We anticipate that this amount of error can be reduced by training our network more. As we explained in section 0, the performance of our homography estimation network decreases dramatically in images containing Gaussian noise. Example visual results from these experiments are presented in Figure 10, Figure 11.

The left image in Figure 10, we show some visual results for pairs of images that do not contain gaussian noise and have

displacements up to a maximum of 32 pixels. The visual results show that our method gives an overall good performance. Our method can sometimes make mistakes in pairs of images that contain too many or too few edges. The right image in Figure 10, we have sampled some visual results for corner-displacements up to a maximum of 96 pixels. When the corner-displacement amount increases, the error rate of our method has increased because it is necessary to train the network more. Figure 11 shows some visual results for image pairs containing gaussian noise. The images show, from left to right, the stitching results of pairs of images with ground truth, gaussian noise with variance of 0, 0.01, 0.05, and 0.1. According to the results, as the variance value increases, the amount of error increases.



Figure 10 - *Stitching results for image pairs with corner-displacements up to 32 pixels (left) and up to 96 pixels (right) without noise.*

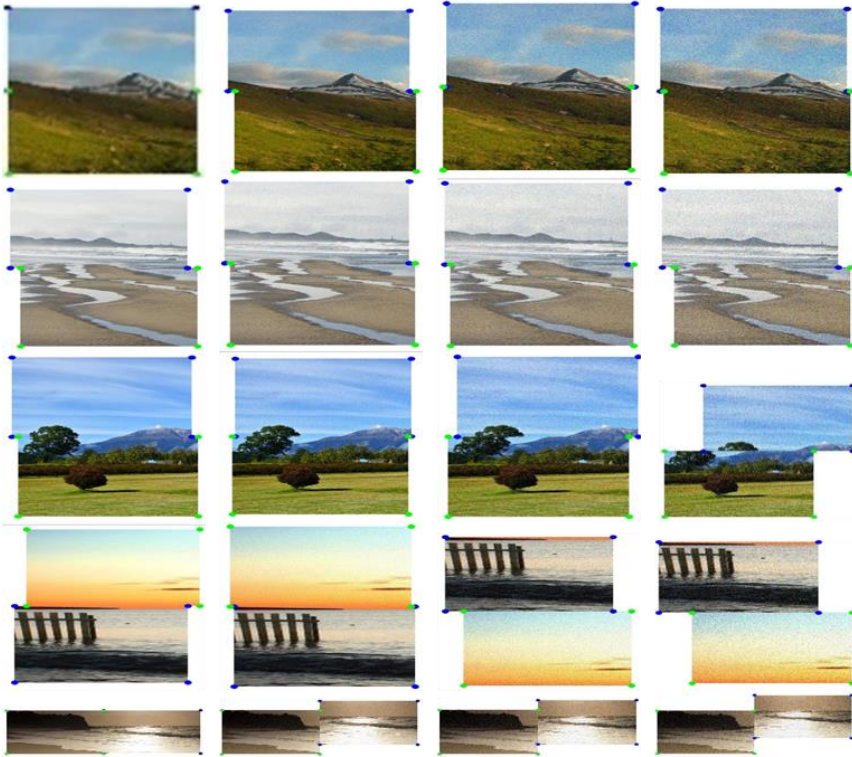


Figure 11 - Stitching results for image pairs with gaussian noise. Ground truth, variance values of 0.001 and 0.005 and 0.1, respectively.

Conclusion

In this study, we presented a deep learning based image mosaicing method. Unlike the studies in the literature that stitching images with overlapping areas, our method stitch images that have non-overlapping areas. We performed this process with a deep learning-based method and used a network that generates a homography matrix according to the amount of translation between image pairs that do not have rotation difference and scale change. We generated a custom dataset by clipping images from a Kaggle's landscape dataset. The network is trained and tested using this dataset under different scenarios including different displacement

amounts and different noise levels. Our method showed a successful performance up to a large amount of displacements. However, the performance drops dramatically with increasing noise since there is no common regions in images and the weak features learned by the network are corrupted with noise. The performance of the method may be increased by training with a larger dataset including noisy images.

References

Inampudi, R. B. (1998, July). Image mosaicing. In IGARSS'98. Sensing and Managing the Environment. 1998 IEEE International Geoscience and Remote Sensing. Symposium Proceedings.(Cat. No. 98CH36174) (Vol. 5, pp. 2363-2365). IEEE.

Hartley, R., & Zisserman, A. (2003). Multiple view geometry in computer vision. Cambridge university press.

Capel, D. (2004). Image mosaicing. In Image Mosaicing and super-resolution (pp. 47-79). London: Springer London.

Ghosh, D., Park, S., Kaabouch, N., & Semke, W. (2012, May). Quantitative evaluation of image mosaicing in multiple scene categories. In 2012 IEEE International Conference on Electro/Information Technology (pp. 1-6). IEEE.

Azzari, P., Di Stefano, L., & Mattoccia, S. (2008). An evaluation methodology for image mosaicing algorithms. In Advanced Concepts for Intelligent Vision Systems: 10th International Conference, ACIVS 2008, Juan-les-Pins, France, October 20-24, 2008. Proceedings 10 (pp. 89-100). Springer Berlin Heidelberg.

Joshi, H., & Sinha, K. (2013). A survey on image mosaicing techniques. International Journal of Advanced Research in Computer Engineering & Technology (IJARCET), 2(2), 365-369.

Szeliski, R. (2007). Image alignment and stitching: A tutorial. Foundations and Trends® in Computer Graphics and Vision, 2(1), 1-104.

Nasibov, A., Nasibov, H., & Hacizade, F. (2009, September). Seamless image stitching algorithm using radiometric lens calibration for high resolution optical microscopy. In 2009 Fifth International Conference on Soft Computing, Computing with Words and Perceptions in System Analysis, Decision and Control (pp. 1-4). IEEE.

Berberidis, K., & Karybali, I. (2002, September). A new efficient cross-correlation based image registration technique with improved performance. In 2002 11th European Signal Processing Conference (pp. 1-4). IEEE.

Miranda-Luna, R., Daul, C., Blondel, W. C., Hernandez-Mier, Y., Wolf, D., & Guillemin, F. (2008). Mosaicing of bladder endoscopic image sequences: Distortion calibration and registration algorithm. *IEEE Transactions on Biomedical Engineering*, 55(2), 541-553.

Dame, A., & Marchand, E. (2011, September). Video mosaicing using a mutual information-based motion estimation process. In 2011 18th IEEE International Conference on Image Processing (pp. 1493-1496). IEEE.

Jain, D. K., Saxena, G., & Singh, V. K. (2012, May). Image mosaicing using corner techniques. In 2012 International Conference on Communication Systems and Network Technologies (pp. 79-84). IEEE.

Levin, A., Zomet, A., Peleg, S., & Weiss, Y. (2004). Seamless image stitching in the gradient domain. In *Computer Vision-ECCV 2004: 8th European Conference on Computer Vision, Prague, Czech Republic, May 11-14, 2004. Proceedings, Part IV 8* (pp. 377-389). Springer Berlin Heidelberg.

Xiong, Y., & Turkowski, K. (1998, October). Registration, calibration and blending in creating high quality panoramas. In *Proceedings Fourth IEEE Workshop on Applications of Computer Vision. WACV'98 (Cat. No. 98EX201)* (pp. 69-74). IEEE.

Xiong, Y. (2009, December). Eliminating ghosting artifacts for panoramic images. In 2009 11th IEEE International Symposium on Multimedia (pp. 432-437). IEEE.

Szeliski, R., Uyttendaele, M., & Steedly, D. (2011, April). Fast poisson blending using multi-splines. In 2011 IEEE

International Conference on Computational Photography (ICCP) (pp. 1-8). IEEE.

El-Saban, M., Izz, M., Kaheel, A., & Refaat, M. (2011, September). Improved Optimal Seam Selection Blending for Fast Video Stitching of Videos Captured from Freely Moving Devices, Image Processing (ICIP). In 2011 18th IEEE International Conference, Brussels (pp. 11-14).

Gracias, N., Mahoor, M., Negahdaripour, S., & Gleason, A. (2009). Fast image blending using watersheds and graph cuts. *Image and Vision Computing*, 27(5), 597-607.

Wen, H., & Zhou, J. (2008, December). An improved algorithm for image mosaic. In 2008 International Symposium on Information Science and Engineering (Vol. 1, pp. 497-500). IEEE.

Nie, L., Lin, C., Liao, K., Liu, S., & Zhao, Y. (2021). Unsupervised deep image stitching: Reconstructing stitched features to images. *IEEE Transactions on Image Processing*, 30, 6184-6197.

Wang, L., Yu, W., & Li, B. (2020, June). Multi-scenes image stitching based on autonomous driving. In 2020 IEEE 4th Information Technology, Networking, Electronic and Automation Control Conference (ITNEC) (Vol. 1, pp. 694-698). IEEE.

Lai, W. S., Gallo, O., Gu, J., Sun, D., Yang, M. H., & Kautz, J. (2019). Video stitching for linear camera arrays. arXiv preprint arXiv:1907.13622.

Li, J., Zhao, Y., Ye, W., Yu, K., & Ge, S. (2019). Attentive Deep Stitching and Quality Assessment for 360° Omnidirectional Images. *IEEE Journal of Selected Topics in Signal Processing*, 14(1), 209-221.

Hoang, V. D., Tran, D. P., Nhu, N. G., Pham, T. A., & Pham, V. H. (2020). Deep feature extraction for panoramic image stitching. In *Intelligent Information and Database Systems: 12th Asian Conference, ACIIDS 2020, Phuket, Thailand, March 23–26, 2020*,

Proceedings, Part II 12 (pp. 141-151). Springer International Publishing.

Shi, Z., Li, H., Cao, Q., Ren, H., & Fan, B. (2020). An image mosaic method based on convolutional neural network semantic features extraction. *Journal of Signal Processing Systems*, 92, 435-444.

Nie, L., Lin, C., Liao, K., Liu, M., & Zhao, Y. (2020). A view-free image stitching network based on global homography. *Journal of Visual Communication and Image Representation*, 73, 102950.

Nie, L., Lin, C., Liao, K., & Zhao, Y. (2020). Learning edge-preserved image stitching from large-baseline deep homography. *arXiv preprint arXiv:2012.06194*.

DeTone, D., Malisiewicz, T., & Rabinovich, A. (2016). Deep image homography estimation. *arXiv preprint arXiv:1606.03798*.

Simonyan, K., & Zisserman, A. (2014). Very deep convolutional networks for large-scale image recognition. *arXiv preprint arXiv:1409.1556*.

Nguyen, T., Chen, S. W., Shivakumar, S. S., Taylor, C. J., & Kumar, V. (2018). Unsupervised deep homography: A fast and robust homography estimation model. *IEEE Robotics and Automation Letters*, 3(3), 2346-2353.

Zhang, J., Wang, C., Liu, S., Jia, L., Ye, N., Wang, J., ... & Sun, J. (2020). Content-aware unsupervised deep homography estimation. In *Computer Vision–ECCV 2020: 16th European Conference, Glasgow, UK, August 23–28, 2020, Proceedings, Part I 16* (pp. 653-669). Springer International Publishing.

Le, H., Liu, F., Zhang, S., & Agarwala, A. (2020). Deep homography estimation for dynamic scenes. In *Proceedings of the IEEE/CVF conference on computer vision and pattern recognition* (pp. 7652-7661).

Baker, S., Datta, A., & Kanade, T. (2006). Parameterizing homographies. Robotics Institute, Pittsburgh, PA, Tech. Rep. CMU-RI-TR-06-11.

[Online].

Available:

<https://www.kaggle.com/datasets/arnaud58/landscape-pictures>

CHAPTER IV

Disease Diagnosis and Determination of Various Emotional States and Behaviors in Model Animals with Artificial Intelligence (Visual Processing, Machine and Deep Learning)

Emre AYDEMİR¹
İnci BİLGE²

Introduction

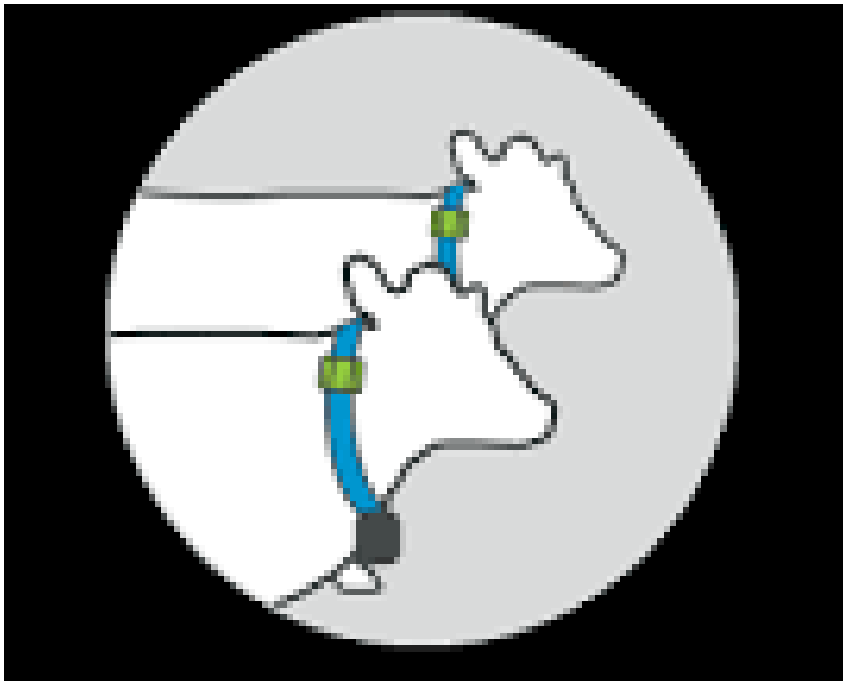
Emotion a reaction of a model animal to external stimuli. Physiological features such as voice, blood pressure, facial expression, body posture, and brain waves are used to describe these emotions (Manstead, 2008). These features; data obtained with the help of devices such as microphones, various tracking devices, and

¹ Akdeniz Üniversitesi, Ziraat Fakültesi, Zootečni Bölümü, Antalya/Türkiye, aydemir1825@gmail.com, ORCID NO: 0000-0002-2451-8248

² Mehmet Akif Ersoy Üniversitesi, Elektrik ve Enerji Bölümü, Burdur/Türkiye, aydemir1825@gmail.com, ORCID NO: 0000-0002-0194-2759

cameras can be converted into numerical data thanks to interfaces (Driscoll et al., 2007; Hare et al., 2010; Huet al., 2014; Wichakam and Vateekul, 2014; Koyasu and Nagasawa, 2019). Artificial intelligence is one of the biggest factors that play a role in converting these features into digital data.

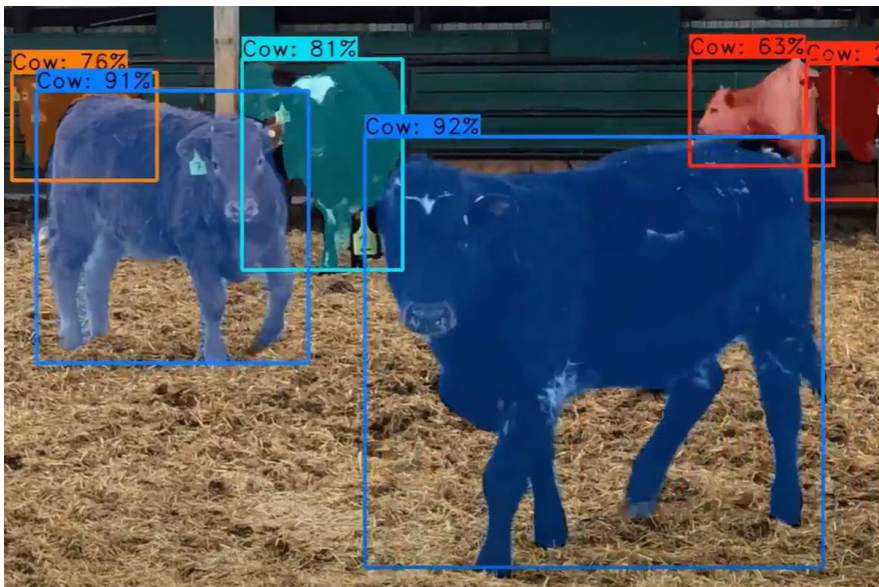
With the increasing use of artificial intelligence around the world, it has been integrated into various fields. Especially; use is becoming increasingly widespread in fields such as health, engineering and animal husbandry, and it provides easy access to reliable information. Obtaining this information includes deep learning and machine learning, which are sub-branches of artificial intelligence. With these methods, it easy to monitor the health, nutrition and behavior of animals.



Especially with the help of artificial intelligence, model animal welfare, health, disease detection and classification, productivity and performance monitoring, herd management,

applied treatment monitoring, trace and record analysis, epidemiology, herd health, population monitoring, determination of zoonotic diseases, individual animal behavior, animal interaction, provides information on various topics such as nutritional monitoring and emotional state.

To obtain this information, various wearable sensors, functional near-infrared spectroscopy measurements, multi-mode sensors, biometric sensors, video and thermal imaging cameras, microphones and functional near-infrared spectroscopy sensors, skin impedance sensors, digital twin modeling, heterogeneous, multi-mode, biometric sensors, respirometers (breathing rate), heart rate meters, accelerometers (body movement) and optical sensors are used.



In this way, it helps to obtain information about the psychological and physiological state of the model animal (Luo and Chong 2020; Prince 2012; Molini-Avejonas et al. 2015).



Visual Processing

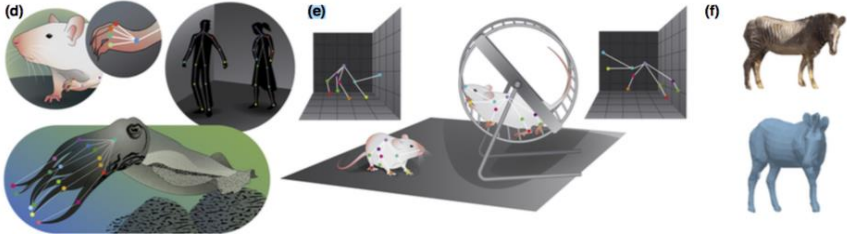
Image processing takes place as a result of taking images of animals with the help of various devices such as cameras and evaluating them, then processing them on the computer and converting them into digital data (Luo and Chong 2020).

The images obtained at the end of this process are defined, classified and interpreted. In this way, it helps to obtain information about the chemical, physiological and psychological conditions of the model animal. In addition, it is also used in situations such as identifying various diseases in animals, monitoring estrus, and determining productivity and performance characteristics (Rhody, 2021).

Deep Learning

Artificial intelligence and deep learning software use algorithm data to transform input data into output data. Algorithms are software consisting of a sequence of instructions. They vary depending on the desired output result from the input data. Image

processing, face and voice recognition are among the main subject areas of deep learning (Steinberg, Shamir and Boag, 2006)



Deep learning method; helps to accurately and quickly predict the behavior, geometric configuration of body parts and posture of the model animal (Dell et al. 2014; Gomez-Marin et al. 2014; Camomilla et al. 2018; Mathis and Mathis 2020).

Machine Learning

Machine learning an important subfield of artificial intelligence. The algorithms used here carry out a specific task by learning from patterns in the data. Any of a spectrum of machine learning algorithms, including supervised, semi-supervised, and unsupervised algorithms, constitutes a specific task and its associated data (Noorbakhsh-Sabet et al. 2019; Awaysheh et al. 2019; Cui et al. 2020).



Especially; image and voice recognition, natural language processing, medicine and health, finance, marketing and sales, production and logistics, security, fraud detection, environmental science, weather and climate forecasting, robotics and computer games, brain and machine interface, model emulation, It is widely used in many fields such as hydrological forecasts and air quality (Janiesch et al. 2021).

Algorithms of machine learning

Thanks to machine learning algorithms, it can help classify various behaviors from accelerometer data such as drinking water, licking, estrus, rubbing, scratching and sniffing (Vehkaoja et al. 2022; Chambers et al. 2021). Unsupervised machine learning methods can be used to identify genetic patterns in different species. In common diseases in animals, detection of cross-species patterns in different diseases and phenotypes is used in zoonotic and infectious disease modeling (Goursot et al. 2018; Grandin 2018; Jorquera-Chavez et al. 2019). Moreover; in in silico trials based on machine learning models, virtual animals receive a virtual treatment and observations yield datasets about patient sensitivities and

responses. This offers an alternative to traditional clinical trials (Goursot et al. 2018; Grandin 2018; Jorquera-Chavez et al. 2019).

Machine learning model choice

Model selection is made depending on the type of data to be analyzed and the desired task or output. Most readers are familiar with basic statistical parameter estimates (mean and SD) for describing and analyzing 1D data and basic correlation analysis and regression modeling. Machine learning algorithms that produce output can be thought of as complex regression modeling. More complex data analysis and modeling are often required for 2D and higher dimensional data. Analysis of image data with machine learning has grown significantly over the past decade, fueled by faster computers and image-based neural networks, the most common form of which is a convolutional neural network (CNN) (Krizhevsky et al. 2012-2017; Yamashita et al. 2018)

Machine Learning Methods

Machine learning basically divided into four basic methods. These methods; supervised machine learning, unsupervised machine learning, semi-supervised machine learning and reinforcement machine learning.

- **Supervised Machine Learning**

Supervised machine learning algorithm a process that consists of a training data set. This algorithm primarily focuses on estimation and estimation problems (Marsland, 2015). It frequently preferred especially in the field of medicine, cancer diagnosis, handwriting recognition, speech recognition applications, face recognition, medical imaging, e-mail security applications, number and letter recognition applications (Rashidi, et al. 2019).

- **Unsupervised Machine Learning**

Unsupervised machine learning; is used to obtain information from data or to reveal hidden patterns in data (Ma and Sun, 2020). The extracted features have key information about the real data and can be used and interpreted as input in further analysis. Especially; it used for diagnosis in the field of health.

- **Semi-Supervised Machine Learning**

It covers both unsupervised and supervised machine learning algorithms. It an algorithm that uses a small number of labeled data as well as a large number of unlabeled data. Especially; widely used in disease diagnosis.

- **Reinforcement Machine Learning**

Reinforcement machine learning; in particular, is an algorithm of data obtained based on trial-and-error, input/output information. Generally; used in many different areas in daily life such as automation, navigation, robot control, automatic driving (Pandey, Niwaria and Chourasia, 2019).

Some studies done

In a study conducted on pet animals; Eunbee et al. (2021) reported that with the help of artificial intelligence, 481 of 500 cases were analyzed technically successfully. In another similar study, Thiago et al. (2021) tried to detect pleural effusion in the chest radiographs of dogs by using artificial intelligence algorithms in diagnostic radiology. In their study results, they detected the presence of pleural effusion with 88.7% accuracy ($P < 0.05$). In conclusion; they stated that they found statistically significant results in the diagnostic interpretation of chest radiographs. This shows that artificial intelligence has been successfully applied in the field of animal health. Garbey et al.(2007), Pavlidis et al. (2012) and Cho et al. (2019) reported that the results of the studies conducted by animals were determined by using thermal imaging channels

(Thermography) for various physiological activities such as respiration, sweating, and cardiovascular responses. In another study, Suresh et al. used video recordings obtained from dogs as model animals. (2019), Ahuja (2019) and Noah (2020) declared that they achieved successful results from the application of artificial intelligence in disease diagnosis, diagnosis and treatment.

References

Awaysheh A, Wilcke J, Elvinger F, Rees L, Fan W, Zimmerman KL. Review of medical decision support and machine-learning methods. *Vet Pathol.* 2019;56(4):512–525. doi:10.1177/0300985819829524

Camomilla V, Bergamini E, Fantozzi S, Vannozzi G: Trends supporting the in-field use of wearable inertial sensors for sport performance evaluation: a systematic review. *Sensors* 2018, 18(3):873.

Cui S, Tseng HH, Pakela J, Ten Haken RK, El Naqa I. Introduction to machine and deep learning for medical physicists. *Med Phys.* 2020;47(5):e127–e147. doi:10.1002/mp.14140

Dell AI, Bender JA, Branson K, Couzin ID, de Polavieja GG, Noldus LPJJ, Pérez-Escudero A, Perona P, Straw AD, Wikelski M et al.: Automated image-based tracking and its application in ecology. *Trends Ecol Evol* 2014, 29(7):417-428.

Driscoll CA, Menotti-Raymond M, Roca AL, Hupe K, Johnson WE, Geffen E, Harley EH, Delibes M, Pontier D, Kitchener AC, Yamaguchi N, O'Brien SJ, Macdonald DW (2007) The near eastern origin of cat domestication. *Science* 317:519–523

Gomez-Marin A, Paton JJ, Kampff AR, Costa RM, Mainen ZF: Big behavioral data: psychology, ethology and the foundations of neuroscience. *Nat Neurosci* 2014, 17(11):1455.

Goursot, C.; Döpjan, S.; Kanitz, E.; Tuchscherer, A.; Puppe, B.; Leliveld, L.M.C. Assessing animal individuality: Links between personality and laterality in pigs. *Curr. Zool.* 2018, 65, 541–551.

Grandin, T. *Livestock Handling and Transport*, 5th ed.; CABI: Wallingford, UK, 2019; p. 485.

Hare B, Rosati A, Kaminski J, Brauer J, Call J, Tomasello M (2010) The domestication hypothesis for dogs' skills with human

communication: a response to Udell et al. (2008) and Wynne et al. (2008). *Anim Behav* 79(2):e1–e6 ISSN 0003-3472

Hu, Y., Hu, S., Wang, W., Wu, X., Marshall, F.B., Chen, X., Hou, L., Wang, C. (2014) Earliest evidence for commensal processes of cat domestication. *Proc Natl Acad Sci USA* 7 111(1):116–120. doi:10.1073/PNAS1311439110

Janiesch, C., Zschech, P., & Heinrich, K. (2021). Machine learning and deep learning. *Electronic Markets*, 31(3), 685-695.

Jorquera-Chavez, M.; Fuentes, S.; Dunshea, F.R.; Jongman, E.C.; Warner, R. Computer vision and remote sensing to assess physiological responses of cattle to pre-slaughter stress, and its impact on beef quality: A review. *Meat Sci.* 2019, 156, 11–22.

Koyasu, H., and Nagasawa, M. (2019). Recognition of directed-gaze from humans in cats. *Jpn. J. Anim. Psychol.* 69, 2–3.

Krizhevsky A, Sutskever I, Hinton GE. ImageNet classification with deep convolutional neural networks. In: *Advances in Neural Information Processing Systems*. Vol 25. Curran Associates Inc; 2012.

Ma, L., & Sun, B. (2020). Machine learning and AI in marketing-Connecting computing power to human insights. *International Journal of Research in Marketing*, 37(3), 481-504.

Manstead, A. S. R., *Psychology of Emotions*, Sage Publications Ltd, 89, 2008.

Marsland, S. (2015). *Machine learning: An algorithmic perspective*. New York: CRC Press.

Mathis, M.W., Mathis, A. (2020). Deep learning tools for the measurement of animal behavior in neuroscience. *Current Opinion in Neurobiology*, 60, 1–11. doi:10.1016/j.conb.2019.10.008

Noorbakhsh, N., Zand, R., Zhang, Y., Abedi, V. Artificial intelligence transforms the future of healthcare. *Am J Med.* 2019;132(7):795–801. doi:10.1016/j.amjmed.2019.01.017

Pandey, D., Niwaria, K., & Chourasia, B. (2019). Machine learning algorithms: A Review. *Machine Learning*, 6(2),916-923.

Rashidi, H.H., (2019). Artificial intelligence and machine learning in pathology: The present landscape of supervised methods. *Academic pathology*, 6, 1-17.

RHODY, H., “SIMG-782 Introduction to Digital Image Processing”, Rochester Institute of Technology: <https://www.cis.rit.edu/class/simg782/> adresinden alındı, (Erişim Tarihi: 16.06.2021)

Steinberg, B.Z., Shamir, A. and Boag, A. (2006) “Two-dimensional Green’s function theory for the electrodynamics of a rotating medium.,” *Physical review. E, Statistical, nonlinear, and soft matter physics*, 74(1 Pt 2), p. 016608. Available at: <https://doi.org/10.1103/PhysRevE.74.016608>.

Wichakam, I. and Vateekul, P., 2014. An evaluation of feature extraction in EEG- based emotion prediction with support vector machines, 11 International Joint Conference on Computer Science and Software Engineering, 106 – 110

CHAPTER V

Stap Radar Signal Processing for Real-World Clutter Environments

Necmi Serkan TEZEL¹

Introduction

Space-time adaptive processing (STAP) is well-established in the academic literature as a method for significantly improving the detection of slow-moving ground or low-altitude targets using an airborne radar (Klemm, 2002; Guerci, 2014). STAP can be divided into two steps: adaptation and filtering. Although the filtering step is very straightforward for a given covariance matrix using the whitened matched filter, in practise, this matrix is not known and must be estimated from the training data. The training and updating of the clutter covariance matrix are key factors in the implementation and effectiveness of any STAP system. In both sidelooking-looking monostatic and bistatic environments, the usual impediment to

¹ Prof. Dr., Karabük University, Faculty of Engineering, Department of Electric-Electronic Engineering, Karabük, Türkiye, ORCID No: [0000-0002-9452-677X](https://orcid.org/0000-0002-9452-677X), E-mail:nstezel@karabuk.edu.tr

performance, namely clutter inhomogeneity, is further complicated by the range dependent nature of the clutter ridge in the angle-Doppler plane induced by the physical geometry of the aircraft. In general, the non-stationarity of the clutter covariance matrix with range is due to a combination of two effects: (i) inhomogeneity of ground scatterers themselves; (ii) range dependence of the clutter ridge in the angle-Doppler plane. This non-stationarity leads to significant errors in the estimated clutter covariance matrix and results in a widening of the STAP filter clutter notch: causing the returns from relatively low-velocity targets to be heavily suppressed or even to go undetected. Our work in this area is inspired by practical constraints and directed towards what might be called "small STAP", where the number of spatial channels is small and the array is uniform.

Traditionally, the training data used for estimation of the covariance matrix is assumed to share the same statistics as the test data and be homogeneous along the range direction, when a more accurate training data model is considered, statistical properties of this data may change along the range direction. For example, when the nonhomogeneous earth surface composed of different parts such as forest, rocky soil, sand, sea etc. is modeled. Reflectivity is range dependent.

In this report, we model the clutter signal for scatterers given by a specified probability density function (pdf) and correlation obtained by a memoryless nonlinear transformation (MNLT) (Tough & Ward, 1999). We evaluate the performance of STAP algorithms based on estimation of the covariance matrix called as two data set (TDS) (Klemm, 2002; Guerci, 2014), single data set (SDS) (Aboutanios and Mulgrew, 2007) and Hybrid (Aboutanios&Mulgrew, 2007). Performance measures are compared against optimum STAP in terms of improvement factor loss plots.

Reconstruction of scatterers on the ground

In order to model radar clutter, it is necessary to model ground reflectivity in an appropriate way. Scatterers on the ground are depicted in Figure 1.

There are a total $M_s \cdot N_s$ scatterers on the ground located equally in the x and y directions with dx and dy distances respectively. Each scatterer is defined by its location and reflectivity as $r_{mn} = (x_{mn}, y_{mn})$ and $\mu_{mn} = \gamma_{mn} e^{i\phi_{mn}}$ respectively. The location of the first scatterer is given by $r_{11} = (x_1, y_1)$. Therefore, r_{mn} , the position of a particular scatterer, is defined as, \mathbf{r}

$$\begin{aligned} \mathbf{r}_{mn} &= (x_1 + (n-1)dx, y_1 - (m-1)dy) \\ &= (x_{mn}, y_{mn}) \end{aligned} \quad (1)$$

The phase of the each scatterer ϕ_{mn} is an uncorrelated random variable and uniformly distributed on the interval $[-\pi, \pi]$.

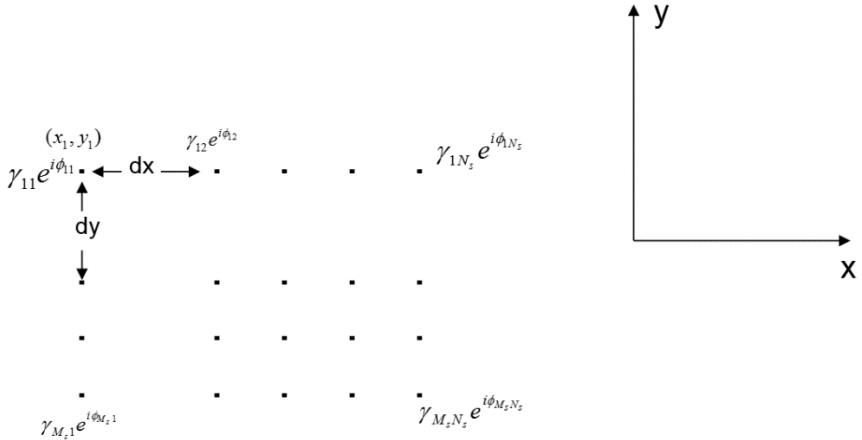


Figure 1. Definition of scatterers on the ground.

Our aim is to reconstruct the amplitude of the reflectivity γ_{mn} with a desired probability density function $p(x)$ and correlation $c(k,l)$ where $c(k,l) = E\{\gamma_{(m-k)(n-l)}\gamma_{mn}\}$ is the amplitude correlation of scatterers γ_{mn} and $\gamma_{(m-k)(n-l)}$. This is accomplished by using a memoryless nonlinear transformation (MNL) (Tough and Ward, 1999). The block diagram of the MNL method is depicted in Figure 2.

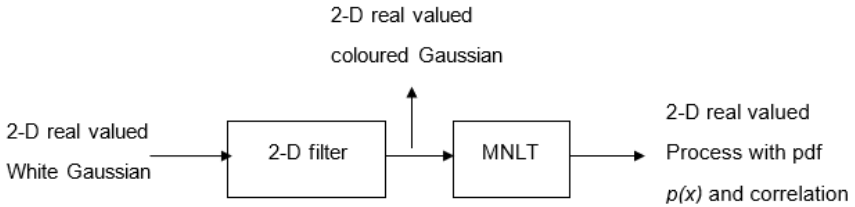


Figure 2. MNL method for obtaining process for given pdf and correlation.

By using the MNL method, it is possible to obtain any probability density function (pdf). In order to control correlation, a 2-D finite impulse response (FIR) filter is designed such that desired correlation $c(k,l)$ on the output process can be obtained. This can be achieved by using spectral factorization.

Given a desired $c(k,l)$, $-K \leq k \leq K$, $-L \leq l \leq L$, correlation of the output of a 2-D filter has to be,

$$r(k,l) = c(k,l) / \sigma_\gamma^2 \quad (2)$$

where σ_γ^2 is variance of process whose probability density function is $p(x)$. Fourier transform of $r(k,l)$ is given by

$$Y(f_x, f_y) = \sum_{k=-K}^K \sum_{l=-L}^L r(k, l) \exp(i2\pi f_x k / (K + 1)) \exp(i2\pi f_y l / (L + 1)) \quad (3)$$

$$f_x = 0, 1, \dots, K; \quad f_y = 0, 1, \dots, L$$

A process whose power spectral density given by $Y(f_x, f_y)$ can be produced by filtering the white Gaussian process by a 2-D filter whose transfer function is

$$H(f_x, f_y) = \sqrt{Y(f_x, f_y)} \quad (4)$$

The 2-D filter impulse response can be obtained as

$$h(m, n) = \frac{1}{(K + 1)(L + 1)} \sum_{f_x=0}^K \sum_{f_y=0}^L H(f_x, f_y) \exp(i2\pi m f_x / (K + 1)) \exp(i2\pi n f_y / (L + 1)) \quad (5)$$

$$m = 0, 1, \dots, K; \quad n = 0, 1, \dots, L$$

The output of the filter can be expressed by the convolution of the white Gaussian input process and impulse response of the filter as

$$y(m, n) = \sum_{p=0}^K \sum_{q=0}^L h(p, q) x(m - p, n - q) \quad (6)$$

As an example, we constructed gamma distributed amplitude data with a specified correlation. One realization of this process is depicted in Figure 3. In order to verify our method, the probability density function and correlation of this realization is measured and compared with the designed pdf and correlation. As seen from Figure 4, good agreements are observed between measured and designed pdf and correlation.

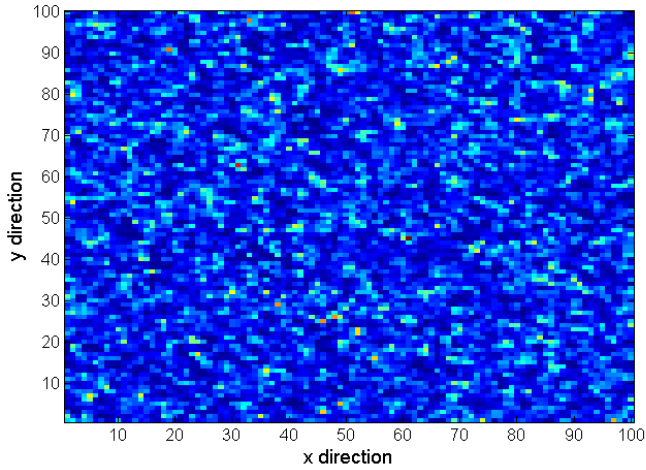


Figure 3. One realization of process with gamma distribution and specified correlation.

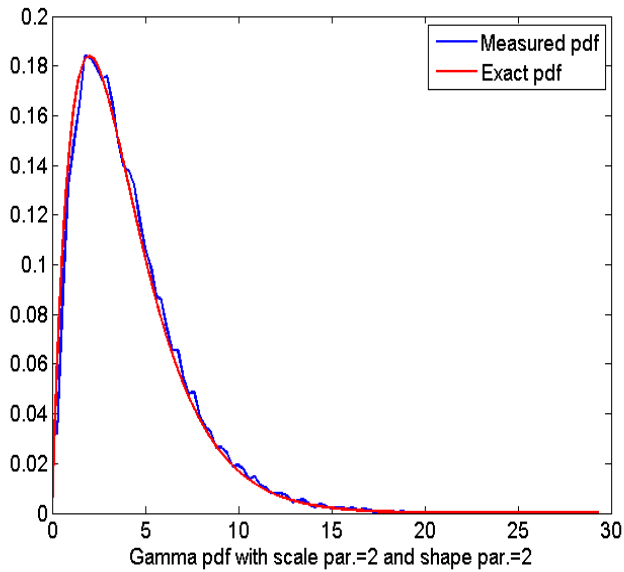


Figure 4. Designed and measured pdf and correlation.

$k \backslash l$	-1	0	1
-1	17.06	18.93	17.60
0	19.73	24.00	19.73
1	17.60	18.93	17.06

Designed correlation $c(k,l)$

$k \backslash l$	-1	0	1
-1	17.29	18.80	17.61
0	19.49	24.22	19.49
1	17.61	18.80	17.29

Measured correlation $c(k,l)$

Modeling of radar clutter and target signal

Let's suppose that the platform moves along the y direction with velocity v_p and height H (Figure 5). The radar system transmits rectangular shaped waveforms with power P_t and pulse duration τ and carrier frequency f_c and pulse repetition frequency $\text{PRF}=1/T$ through the transmit antenna with gain pattern $G_t(\hat{k})$ where \hat{k} is the unit pointing vector. The radar system has N identical receive channel whose phase centers are separated distance at a d to each other and effective aperture $A_e(\hat{k})$. Let's suppose that the radar transmits M coherent pulses with PRF and collects their echoes with N channels located along the flight direction.

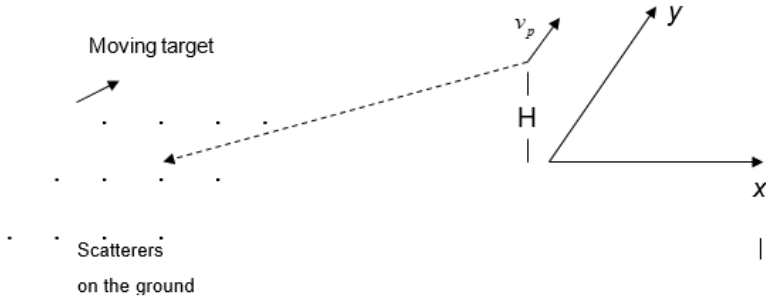


Figure 5. Radar signal acquisition geometry.

The received clutter signal, after being down converted, match filtered and sampled in fast time with rate $f_s = 1/\tau$ can be expressed as

$$s_c(n, m, t) = \sum_{p=1}^{M_s} \sum_{q=1}^{N_s} \alpha_{pq} W(t\tau - 2R_{pq}/c) \exp(i2\pi n(d/\lambda)(y_{pq})/R_{pq}) \exp(i2\pi m(2v_p T/\lambda)(y_{pq})/R_{pq}) \quad (7)$$

$m=1,2,\dots,M; \quad n=1,2,\dots,N; \quad t=1,2,\dots,F$

where $R_{pq} = \sqrt{H^2 + x_{pq}^2 + y_{pq}^2}$ is the range of a scatterer on the ground, c is velocity of light, $F = T/\tau$ is total number of range gates on fast time direction, $\lambda = c/f_c$ is wavelength, $W(t)$ is waveform after match filtering given by

$$W(t) = \begin{cases} 1 - \frac{|t|}{\tau}, & -\tau < t < \tau \\ 0, & \text{else} \end{cases} \quad (8)$$

α_{pq} is the complex amplitude factor obtained by using the radar range equation,

$$\alpha_{pq} = \frac{\mu_{pq}}{4\pi R_{pq}^2} \sqrt{P_t G_t(\hat{k}_{pq}) A_e(\hat{k}_{pq})} \quad (9)$$

Therefore, for the given geometric scenario, radar operation parameters and scatterer distribution on the ground, it is possible to obtain the radar clutter signal by using (7). In the STAP literature, although the radar signal in a specific range gate is a matrix, it is transformed to column vector by stacking the columns of this matrix, In this case, clutter signal is represented as

$$s_c(n + (m-1)N, t) = \sum_{p=1}^{M_s} \sum_{q=1}^{N_s} \alpha_{pq} W(t\tau - 2R_{pq}/c) \exp(i2\pi m(d/\lambda)(y_{pq}/R_{pq})) \exp(i2\pi m(2v_p T/\lambda)(y_{pq}/R_{pq})) \quad (10)$$

More compactly, eq. (10) can be expressed as

$$s_c(t) = \sum_{p=1}^{M_s} \sum_{q=1}^{N_s} \alpha_{pq} W(t\tau - 2R_{pq}/c) u_{pq} \quad (11)$$

where u_{pq} is column vector with size (MNx1) describing the signal from individual scatterer on ground. This vector represents the snapshot signal of scatterer whose index is defined by p and q . Since radar signal acquisition is assumed to be linear, the clutter signal is defined as the superposition of all signals from scatterers on ground.

The received target signal, after being down converted, match filtered and sampled in fast time can be expressed as

$$s_T(n + (m-1)N, t) = A \exp(i2\pi m(d/\lambda)(y_T)/R_T) \exp(i(4\pi m/\lambda)((v_p - v_T)y_T - v_T x_T)/R_T) \delta(t - t_T) \quad (12)$$

Where v_{Ty} and v_{Tx} are velocity of target along y and x direction respectively, x_T and y_T are x and y coordinate of the target, $R_T = \sqrt{H^2 + x_T^2 + y_T^2}$ is range of the target and t_T is the range gate that contains the target signal. In this assumption, the target signal occupies only a single range gate and no range straddle loss exists. A is the amplitude of the target obtained from radar range equation

$$A = \frac{1}{4\pi R_T^2} \sqrt{P_t G_t(\hat{k}_T) A_e(\hat{k}_T) \sigma} \quad (13)$$

Receiver noise is modeled by

$$s_n(n + (m-1)N, t) = (\sigma_n / \sqrt{2})(x + iy) \quad (14)$$

Where x and y are zero mean statistically independent gaussian distributed random variables with a variance of one. Noise samples are assumed to be uncorrelated from pulse to pulse, channel to channel and range gate to range gate, Therefore, its correlation is

$$E\{s_n(p, t) \cdot s_n^*(p', t')\} = \sigma_n^2 \delta(p - p') \delta(t - t') \quad (15)$$

STAP principles and clutter inhomogeneity

Given received data $x(t)$ in a test range gate t , the STAP signal processor has to decide from one of two hypothesis,

$$\begin{aligned} x(t) &= s_c(t) + s_n(t), & H_0 : t \text{ arg et absence} \\ x(t) &= s_T(t) + s_c(t) + s_n(t), & H_1 : t \text{ arg et present} \end{aligned} \quad (16)$$

The well known solution of the this problem is given by the whitened matched filter operation

$$y_t = \left| w_t^H x(t) \right| \quad (17)$$

where

$$w_t = R_t^{-1} s_T \quad (18)$$

The filter output y_t is then compared with a defined threshold to decide whether or not a target is present. Where R_t is unknown covariance matrix of the range gate t defined by

$$R_t = E\left\{ (s_c(t) + s_n(t))(s_c(t) + s_n(t))^H \right\} = E\left\{ s_c(t)s_c(t)^H \right\} + E\left\{ s_n(t)s_n(t)^H \right\} = R_c^{(t)} + \sigma_n^2 I \quad (19)$$

Given the scatterers on the ground and the radar operation parameters, it is possible to calculate exactly the clutter covariance matrix,

$$\begin{aligned} R_c^{(t)} &= E\left\{ s_c(t)s_c(t)^H \right\} = E\left\{ \sum_{p=1}^{M_r} \sum_{q=1}^{N_r} \alpha_{pq} W(t\tau - 2R_{pq}/c) u_{pq} \sum_{p'=1}^{M_r} \sum_{q'=1}^{N_r} \alpha_{p'q'}^* W(t\tau - 2R_{p'q'}/c) u_{p'q'}^H \right\} = \\ &E\left\{ \sum_{p=1}^{M_r} \sum_{q=1}^{M_r} \sum_{p'=1}^{M_r} \sum_{q'=1}^{N_r} \alpha_{pq} \alpha_{p'q'}^* u_{pq} u_{p'q'}^H W(t\tau - 2R_{pq}/c) W(t\tau - 2R_{p'q'}/c) \right\} = \\ &\sum_{p=1}^{M_r} \sum_{q=1}^{M_r} \sum_{p'=1}^{M_r} \sum_{q'=1}^{N_r} E\left\{ \alpha_{pq} \alpha_{p'q'}^* \right\} u_{pq} u_{p'q'}^H W(t\tau - 2R_{pq}/c) W(t\tau - 2R_{p'q'}/c) = \sum_{p=1}^{M_r} \sum_{q=1}^{N_r} \left| \alpha_{pq} \right|^2 u_{pq} u_{pq}^H W^2(t\tau - 2R_{pq}/c) \end{aligned} \quad (20)$$

In order to obtain (20), we use the result of phase decorrelation given as

$$\begin{aligned}
E\{\alpha_{pq}\alpha_{p'q'}^*\} &= \frac{P_t}{(4\pi)^2 R_{pq}^2 R_{p'q'}^2} \sqrt{G_t(\hat{\kappa}_{pq})A_s(\hat{\kappa}_{pq})G_t(\hat{\kappa}_{p'q'})A_s(\hat{\kappa}_{p'q'})} E\{\mu_{pq}\mu_{p'q'}^*\} = \\
&= \frac{P_t}{(4\pi)^2 R_{pq}^2 R_{p'q'}^2} \sqrt{G_t(\hat{\kappa}_{pq})A_s(\hat{\kappa}_{pq})G_t(\hat{\kappa}_{p'q'})A_s(\hat{\kappa}_{p'q'})} \{\gamma_{pq}\gamma_{p'q'}^*\} E\{\exp(i\phi_{pq})\exp(i\phi_{p'q'})\} = \\
&= \frac{P_t}{(4\pi)^2 R_{pq}^2 R_{p'q'}^2} \sqrt{G_t(\hat{\kappa}_{pq})A_s(\hat{\kappa}_{pq})G_t(\hat{\kappa}_{p'q'})A_s(\hat{\kappa}_{p'q'})} \{\gamma_{pq}\gamma_{p'q'}^*\} \delta(p-p')\delta(q-q') = \\
&= \frac{P_t G_t(\hat{\kappa}_{pq})A_s(\hat{\kappa}_{pq})}{(4\pi)^2 R_{pq}^4} |\gamma_{pq}|^2 \delta(p-p')\delta(q-q') = |\alpha_{pq}|^2 \delta(p-p')\delta(q-q')
\end{aligned} \tag{21}$$

This follows from the phase decorrelation assumption on the scatterers despite the fact that their amplitudes are correlated.

In normal radar operation, the covariance matrix is unknown and has to be estimated during the flight. Usually, the covariance matrix is estimated by using snapshots from other range gates, known as training samples, as seen from Figure 6 using

$$\hat{R}_t = \frac{1}{K} \sum_{\substack{p=t-K/2 \\ p \neq k}}^{t+K/2} x(p)x^H(p) \tag{22}$$

In this assumption, the clutter signal is assumed to be statically independent and identically distributed. Otherwise, the covariance matrix estimation becomes biased. It is obviously seen from (20) that the exact covariance matrix can change from range gate to range gate. The received data $x(p)$ from range gate p is the realization of a Gaussian process whose covariance matrix R_p can be factorized by Cholesky decomposition

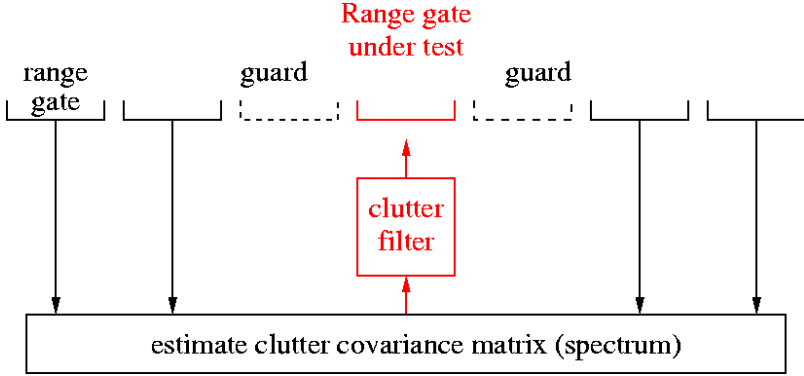


Figure 6. Estimation of covariance matrix using fast time samples.

$$R_p = D_p^H D_p \quad (23)$$

Therefore $x(p)$ can also be produced by

$$x(p) = D_p^H n \quad (24)$$

where n is a vector of complex independent Gaussian numbers with covariance matrix I

Substituting (24) into (22), one gets,

$$\hat{R}_t = \frac{1}{K} \sum_{\substack{p=t-K/2 \\ p \neq k}}^{t+K/2} D_p^H n n^H D_p \quad (25)$$

Performing the expectation operator on both side

$$E\{\hat{R}_t\} = \frac{1}{K} \sum_{p=-t-K/2}^{t-K/2} D_p^H E\{mm^H\} D_p = \frac{1}{K} \sum_{p=-t-K/2}^{t-K/2} D_p^H D_p = \frac{1}{K} \sum_{p=-t-K/2}^{t-K/2} R_p \neq R_t \quad (26)$$

Since $E\{\hat{R}_t\} \neq R_t$, it can be concluded that estimation is biased, and yields at best the average of the covariance matrices.

As seen from (20), given the scatterers amplitude on the ground, it is possible to exactly evaluate the covariance matrix. One possible way to model scatterers distribution on the ground is to use SAR image. Therefore, we can assume amplitude of each pixel on SAR image represent the amplitude of the scatterer on the pixel location on the ground.

In order to investigate clutter heterogeneity and its effect on STAP performance, it is assumed that scatterers on the ground is represented by the SAR image. The use of SAR images in this way represents an intermediate step between stochastic modeling of the clutter and the use of directly measured STAP data. It offers the possibility of more realistic clutter simulation for a specific scenario than stochastic modeling and more flexibility than using measured data in that radar parameters and look directions can be varied using a single SAR image.

The concept of STAP clutter modelling using SAR data is depicted in Fig.7. The direction of flight is depicted by the blue arrow on the right hand side. Antenna channels on the STAP system are aligned along the flight direction, i.e. a side looking geometry. The amplitude, phase and location of the scatterers on the ground are represented by amplitude, phase and location of each pixel of the SAR image. The size of the SAR image is 1476x1784 and its resolution is 1mx1m. The STAP system parameters are given in Table 1. In order to estimate the covariance matrix of the clutter, the STAP clutter signal is obtained from 5 spatial channels and 120 slow time samples using a sliding window snapshot vector

constructed from a matrix of 5 spatial and 10 time samples. An estimate of the covariance matrix is obtained by averaging the outer product of these snapshot vectors over each range gate. After obtaining the clutter covariance matrix of each range gate, an FFT is used to evaluate the clutter spectrum. These are shown in Fig. 7 for range gates 85 and 87.

As seen from Fig.7, although the distance between two range gates is very small, their clutter ridges are completely different. This situation known as clutter heterogeneity causes over nulling or under nulling the clutter. The former causes signal loss where as the latter causes increasing false alarm rate. In order to investigate the effect of clutter heterogeneity further, we have to evaluate the estimation loss because of the unknown covariance matrix. For any value of the weights w , SINR at the output of the filter can written as,

$$SINR = \frac{|w^H s|^2}{w^H R w} \quad (27)$$

The optimum weights can be expressed as $w_{opt} = R^{-1} s$, and performing optimum filtering by using optimum weights in (27), one can obtain optimum SINR given by

$$SINR_{opt} = s^H R^{-1} s \quad (28)$$

Since the exact covariance matrix is unknown and has to be estimated, weights are obtained as $w = \hat{R}^{-1} s$ and SINR is

$$SINR = \frac{|s^H \hat{R}^{-1} s|^2}{s^H \hat{R}^{-1} R \hat{R}^{-1} s} \quad (29)$$

Therefore, we have a loss given by

$$L = \frac{SINR}{SINR_{opt}} = \frac{|s^H \hat{R}^{-1} s|^2}{s^H \hat{R}^{-1} R \hat{R}^{-1} s} \frac{1}{s^H R^{-1} s} \leq 1 \quad (30)$$

Loss for method called as SMI based on estimation of covariance matrix given by (22) is investigated for clutter region described SAR image given by Fig.7. Since all algorithms perform well for detection of targets apart from clutter ridge, we consider the average loss for detection of targets for all angles and doppler region for $[-PRF/10, PRF/10]$. The average loss via using the neighboring range gates to the estimate covariance matrix is depicted in Fig.8.

Table 1. STAP system parameters.

Channel Number	5
Pulse Number	10
Velocity of platform	188m/s
Height of platform	500m
Pulse Reputation Frequency (PRF)	2500
Pulse Waveform	100ns rectangular pulse
Carrier Frequency	1 GHz
Clutter to Noise Ratio (CNR)	40dB
Array Geometry	Linear side looking
Transmit Pattern	Isotropic
Receive Pattern of each channel	Isotropic

As seen from Figure 8, because the clutter statistics change from range gate to range gate, increasing the number of training range samples to estimate the covariance matrix does not necessarily improve performance and even can decrease the performance. In order to gain insight about the range variation of the clutter, we investigate the reflectivity variation of scatterers along the ground range direction for cross range of 600m in the SAR image of Figure

7. As seen from Figure 9, the reflectivity of scatterers changes dramatically along the range direction even for small distances.

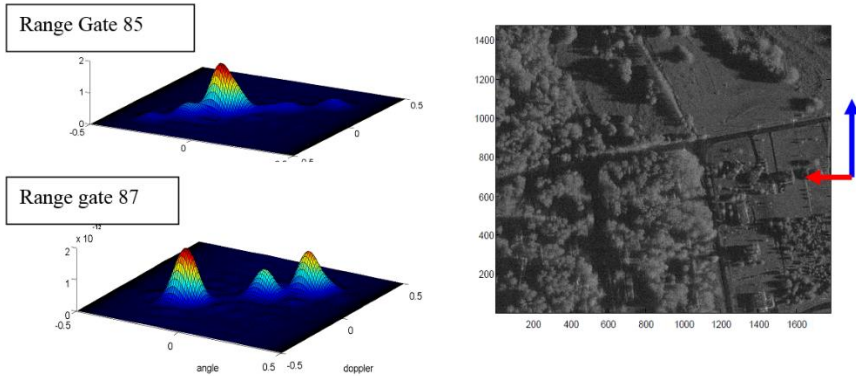


Figure 7. Clutter heterogeneity.

It can be concluded that a STAP system based on SMI is not good method for heterogeneous clutter. Therefore, new methods that deal with clutter heterogeneity are developed such as the Hybrid STAP method (Guerci, 2014).

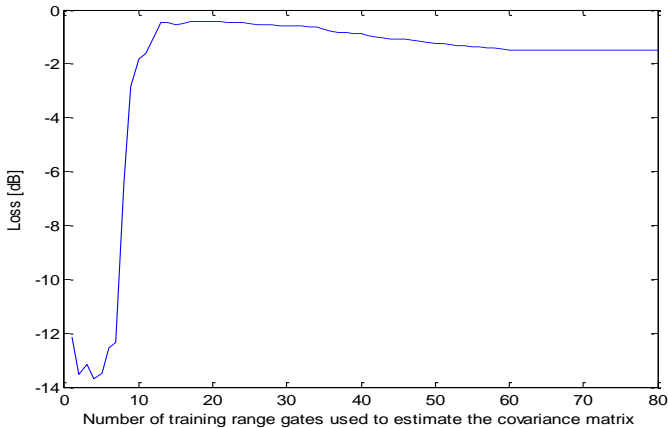


Figure 8. Estimation loss via number of range samples to estimate covariance matrix for region modeled by SAR image.

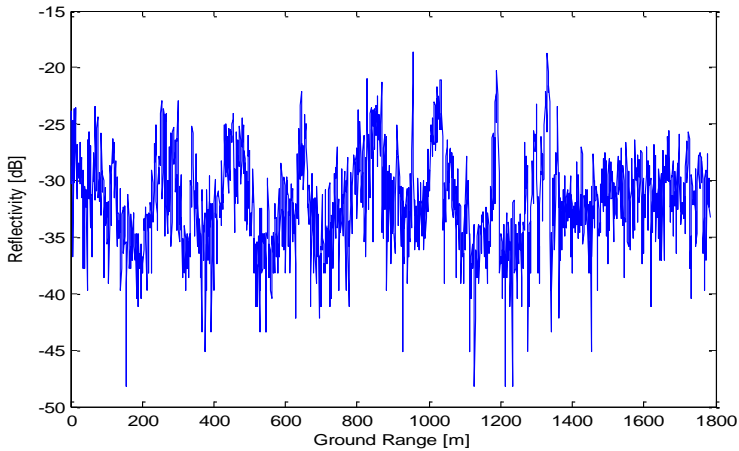


Figure 9. Reflectivity distribution of scatterers along range for cross range 600 m.

Hybrid STAP method

We address the problem of radar target detection under clutter heterogeneity using the new Hybrid STAP method. Traditional approaches, designated as the two-data set (TDS) algorithms, require a training data set in order to estimate the interference covariance matrix as given by (16). This training data is usually drawn from range gates adjacent to the cell under test as depicted in Fig.6 that are deemed to be statistically homogeneous with it. When the training data exhibits statistical heterogeneity with respect to the test data, the TDS detectors suffer from degradation in their performance as depicted in Fig.8 for clutter region described by SAR image. The single-data set (SDS) detectors have been proposed to deal with this problem by operating solely on the test data. In this report, we present performance of a general hybrid approach (Aboutanios and Mulgrew, 2007) that combines the SDS and TDS algorithms as depicted in Figure 10 and Figure 11, taking the degree of heterogeneity into account. Both the SDS and TDS detectors are special cases of the more general Hybrid formulation. We use the

generalized inner product (GIP) as a heterogeneity measure. We assess performance of Hybrid method for clutter region described by simulated scatterer with specified pdf and correlation.

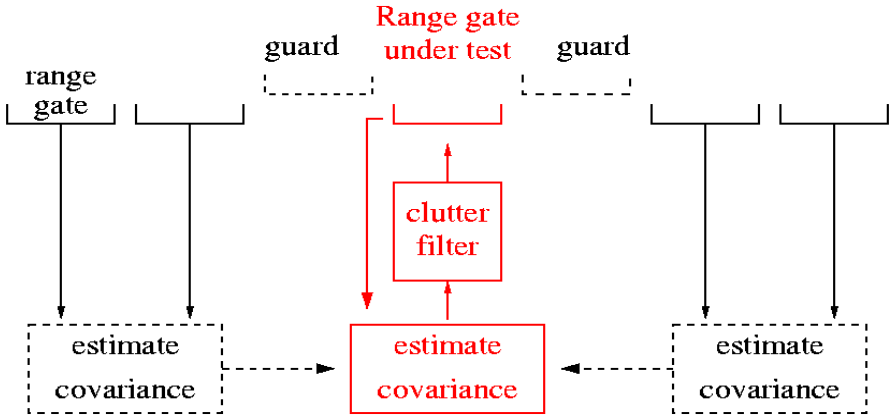


Figure 10. Estimation of covariance matrix by Hybrid method.

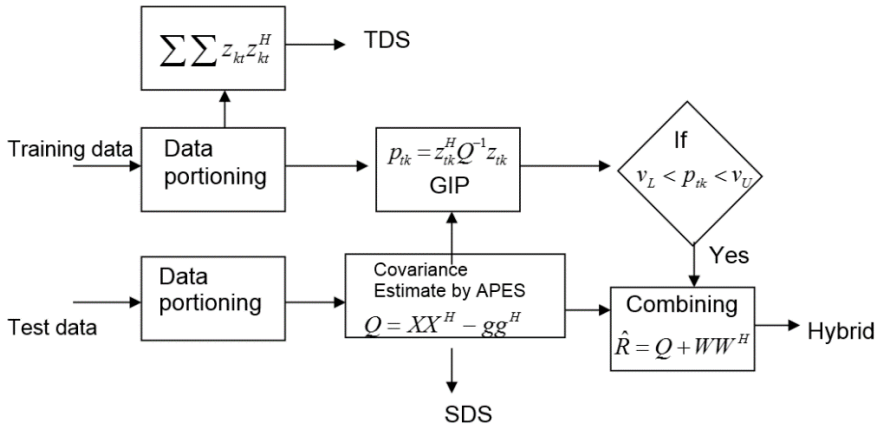


Figure 11. Covariance matrix estimation methods for STAP.

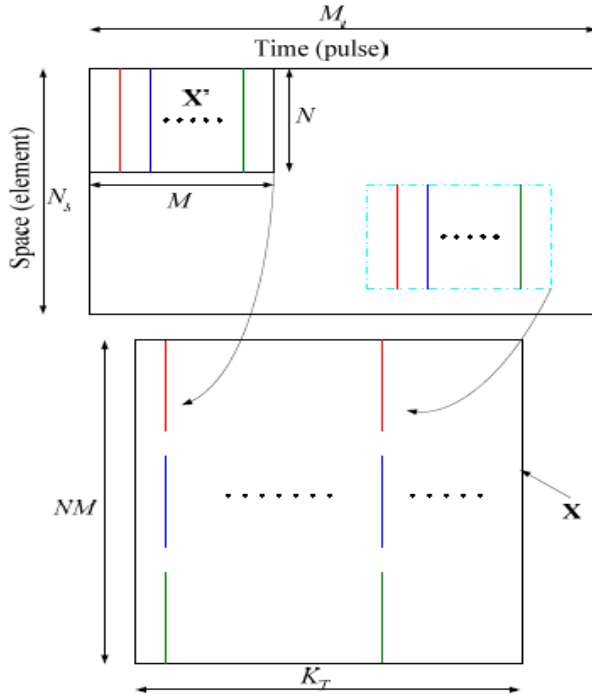


Figure 12. Data portioning in one range cell.

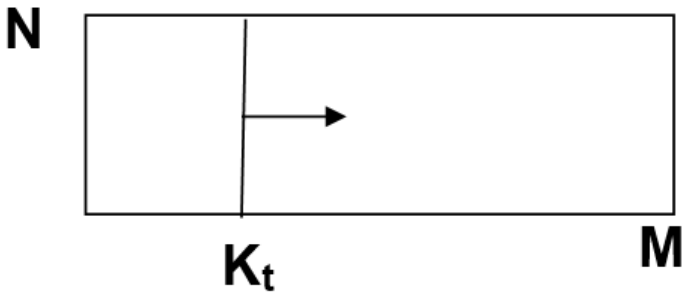


Figure 13. Data collection in one range cell for $N_s = N$.

Hybrid STAP method can be summarized as;

Estimate the covariance matrix of test cell by using amplitude and phase estimate of sinusoid (APES) algorithm (Glentis, 2008) as depicted in Figure 12 and Figure13 by

$$Q = XX^H - gg^H \quad (31)$$

Measure the homogeneity of training data snapshots z_{tk} by using GIP by

$$p_{tk} = z_{tk}^H Q^{-1} z_{tk} \quad (32)$$

where z_{tk} is the snapshot from k^{th} snapshot, obtained by data portioning as depicted Fig. 11, of range gate t . If $v_L < p_{tk} < v_U$, include these snapshots to have better estimate of covariance matrix by

$$\hat{R} = Q + W^H W \quad (33)$$

where W is a matrix whose columns are snapshots obtained from train range gates that satisfy homogeneity condition. SDS algorithm obtains $\hat{R} = Q$, whereas TDS algorithm obtains $\hat{R} = C^H C$ where C a matrix is whose columns snapshots are obtained from train range gates. Detailed explanation of Hybrid STAP method can be found (Guerci, 2014).

Simulation results

We evaluate the performance of SDS, TDS and Hybrid algorithms by five simulated examples. Scatterers on ground are modeled by Rayleigh distribution with parameter $\sigma = 10$ and

correlation of scatterers is depicted as Figure 14. Radar operation parameters are

- Sidelooking only;
- Rectangular shaped waveform
- Range resolution=21m
- CNR=30dB
- SCR=-20dB
- Number of channels = 5
- Channel spacing= $\lambda / 2$
- Processed pulse number=128
- Training range gates number=40
- Transmit beam is pencil shaped
- Upper limit of GIP for homogeneity decision $\nu_u=1.339$
- Lower limit of GIP for homogeneity decision $\nu_l=0.747$

	Case 1	Case 2	Case 3	Case 4	Case 5
Platform velocity (m/s)	35	70	150	280	280
PRF (kHz)	8	16	20	40	40
Carrier frequency (GHz)	10, 17	10, 17	10, 17	10, 17	10
Stand of range (km)	11	11	11	11	80
Altitude (km)	1	1	1	1	8
Antenna beamwidth (deg)	6.8, 4	6.8, 4	6.8, 4	6.8, 4	6.8

In order to investigate the effect of carrier frequency on the performance of algorithms, the simulations are performed for 10 GHz and 17 GHz carrier frequency. It is assumed that reflectivity of scatterers do not change with carrier frequency.

TDS, SDS and Hybrid STAP algorithms are compared based on loss given by

$$L = \frac{SINR}{SINR_{opt}} = \frac{|s^H \hat{R}^{-1} s|^2}{s^H \hat{R}^{-1} R \hat{R}^{-1} s} \frac{1}{s^H R s} \leq 1 \quad (34)$$

In all cases, we also evaluate the optimum improvement factor (IF) given by

$$IF_{opt} = \frac{SINR_{out}}{SINR_{in}} = \frac{s^H R^{-1} s}{s^H s} trace(R) \quad (35)$$

Therefore, it can be shown that IF for any method can be expressed as

$$IF = IF_{opt} L \quad (36)$$

All result are evaluated for one angle corresponding to transmit antenna main lobe direction.

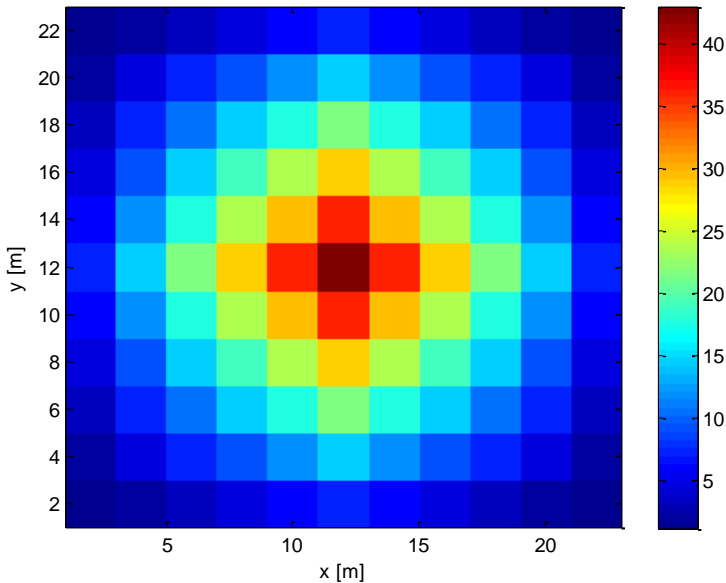


Figure 14. Correlation of the scatterers on the ground.

Case 1

The results for case 1 are illustrated in Figures 15, 16 and 17 are typical of the format used to compare the 3 algorithms at the two carrier frequencies. Figure 17 is a comparison of the theoretical performance of the STAP systems operating at these two frequencies in terms of the improvement factor (IF) in the look direction. The improvement factor is the signal to clutter-plus-noise gain between the input and output of the STAP filter. As the Doppler frequency tends towards zero (the clutter ridge), the improvement factor degrades as is to be expected. The 10 GHz system gives better optimum performance than 17 GHz system because, transmit antenna gain in 17 GHz system higher than those in 10 GHz that result in more clutter power density in clutter ridge. Although, 10 GHz system produces larger doppler width with less clutter density

than those in 17GHz system, if target signal is separated from clutter ridge, STAP can discriminate the target signal very well.

Figures 15 and 16 show the algorithm losses with respect to the optimum performance at the two carrier frequencies. With reference to Figure 15 and Figure 16, the SDS algorithm has the poorest performance. This is to be expected since it uses the least amount of training data i.e. a single range gate and dependent training data because of data portioning method given in Figure 13. The TDS algorithms do better in general but incurs a large loss near the clutter ridge. The Hybrid algorithm effectively combines data from the range gate under test with the neighboring range gates to produce the best performance. Because of the statistical nature of the problem, it is possible to obtain different performance loss even if we consider exactly same cases.

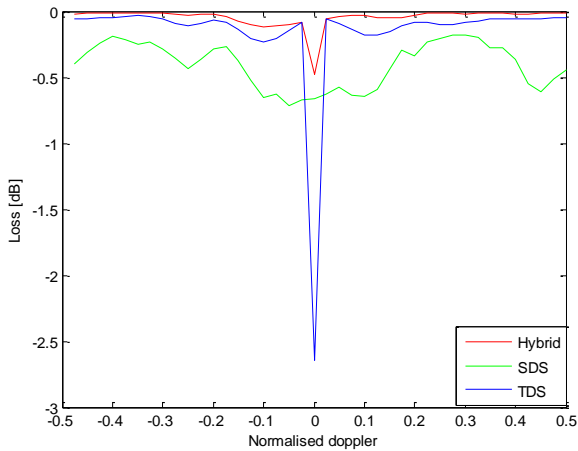


Figure 15. Performance loss of the methods for case 1 and 10 GHz carrier frequency.

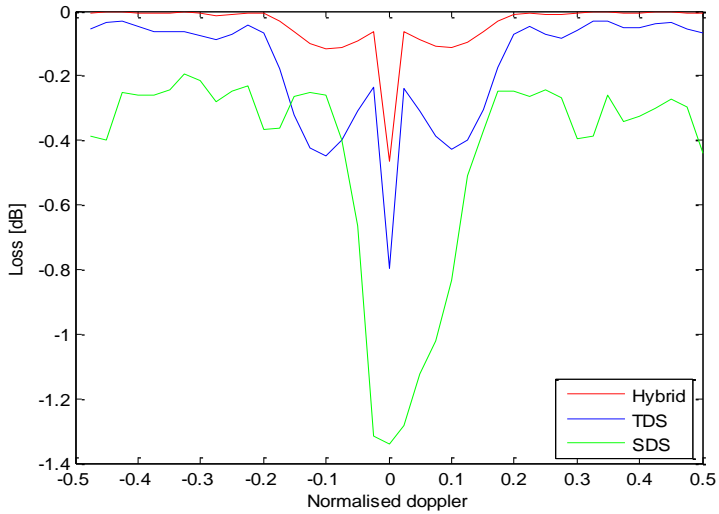


Figure 16. Performance loss of the methods for case 1 and 17 GHz carrier frequency.

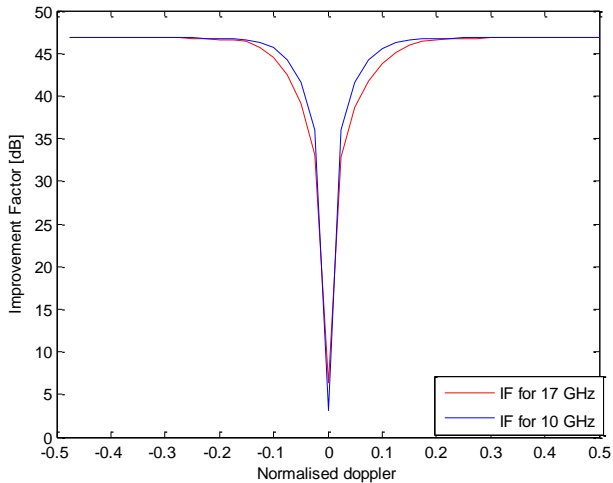


Figure 17. Optimum improvement factor of case 1 for 10 GHz and 17 GHz carrier frequencies.

Case 2

The results for case 2 are illustrated in Figures 18, 19 and 20 are typical of the format used to compare the 3 algorithms at the two carrier frequencies. Figure 20 is a comparison of the theoretical performance of the STAP systems operating at these two frequencies in terms of the improvement factor (IF) in the look direction. As the Doppler frequency tends towards zero (the clutter ridge), the improvement factor degrades as is to be expected again. The 10 GHz system gives better optimum performance than 17 GHz system because, transmit antenna gain in 17 GHz system higher than those in 10 GHz that result in more clutter power density in clutter ridge. Although, 10 GHz system produces larger doppler width with less clutter density than those in 17GHz system, if target signal is separated from clutter ridge, STAP can discriminate the target signal very well.

Figures 18 and 19 show the algorithm losses with respect to the optimum performance at the two carrier frequencies. With reference to Figure 18 and Figure 19, the SDS algorithm has the poorest performance again. This is to be expected since it uses the least amount of training data i.e. a single range gate and dependent training data because of data portioning method given in Figure 13. The TDS algorithms do better in general but incurs a large loss near the clutter ridge. The Hybrid algorithm effectively combines data from the range gate under test with the neighboring range gates to produce the best performance. As seen from Figure 19, SDS algorithm can do better than Hybrid algorithm. This can be explained by statistical nature of problem, Hybrid algorithm can choose non homogeneous data with non zero probability.

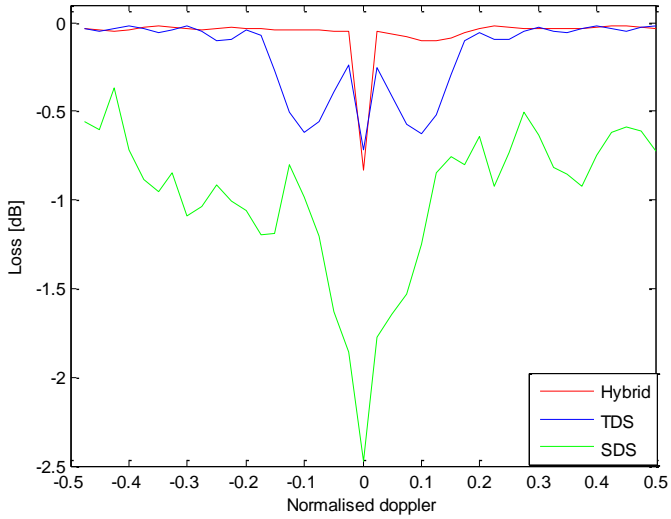


Figure 18. Performance loss of the methods for case 2 and 10 GHz carrier frequency.

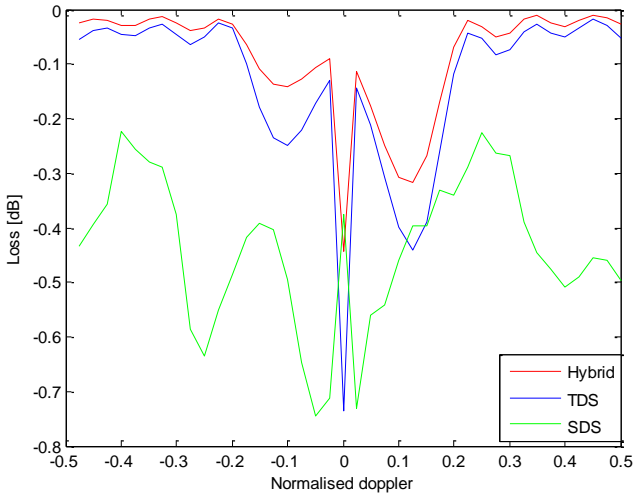


Figure 19. Performance loss of the methods for case 2 and 17 GHz carrier frequency.

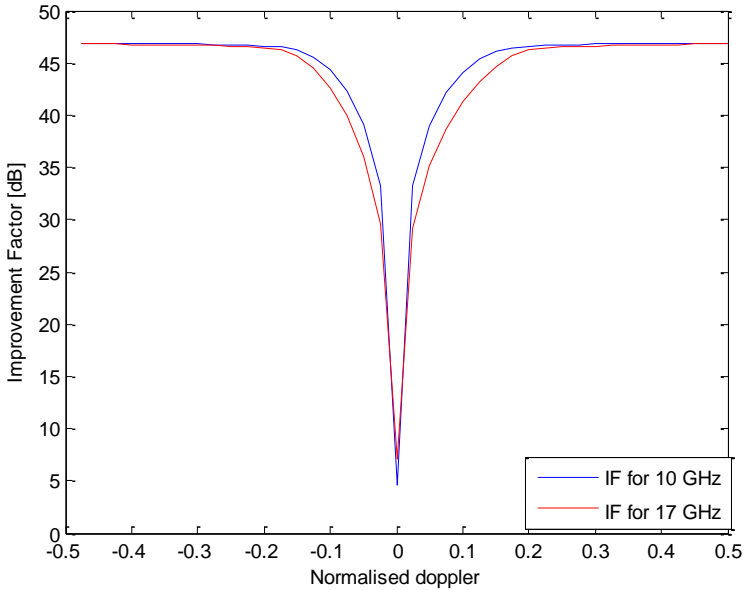


Figure 20. Optimum improvement factor of case 2 for 10 GHz and 17 GHz carrier frequencies.

Case 3

The results for case 3 are illustrated in Figures 21, 22 and 23 are typical of the format used to compare the 3 algorithms at the two carrier frequencies. Figure 23 is a comparison of the theoretical performance of the STAP systems operating at these two frequencies in terms of the improvement factor (IF) in the look direction. As the Doppler frequency tends towards zero (the clutter ridge), the improvement factor degrades as is to be expected again. The 10 GHz system gives better optimum performance than 17 GHz system. Because, transmit antenna gain in 17 GHz system higher than those in 10 GHz that result in more clutter power density in clutter ridge. Although, 10 GHz system produces larger doppler width with less clutter density than those in 17GHz system, if target signal is

separated from clutter ridge, STAP can discriminate the target signal very well.

Figures 21 and 22 show the algorithm losses with respect to the optimum performance at the two carrier frequencies. With reference to Figure 22 and Figure 23, the SDS algorithm has the poorest performance. This is to be expected since it uses the least amount of training data i.e. a single range gate and dependent training data because of data portioning method given in Figure 13. The TDS algorithms do better in general but incurs a large loss near the clutter ridge. The Hybrid algorithm effectively combines data from the range gate under test with the neighboring range gates to produce the best performance. It is also observed that SDS algorithm can do better than Hybrid algorithm. This can be explained by statistical nature of problem, Hybrid algorithm can choose non homogeneous data with non zero probability.

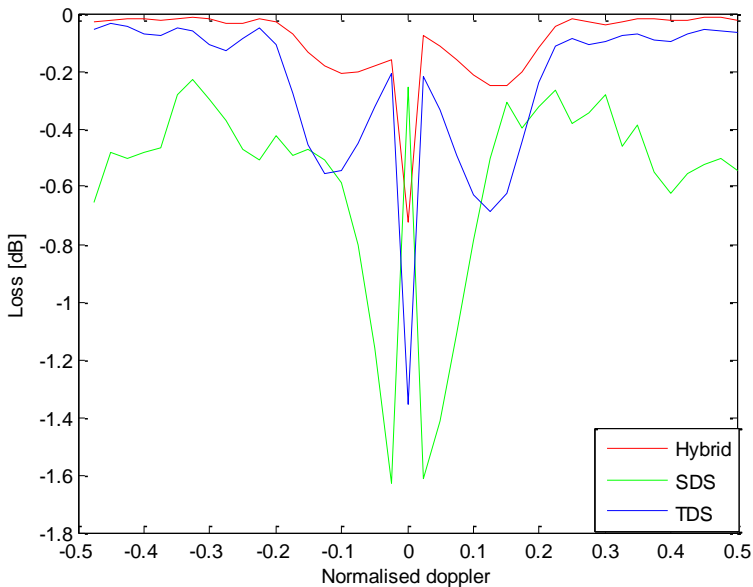


Figure 21. Performance loss of the methods for case 3 and 10 GHz carrier frequency.

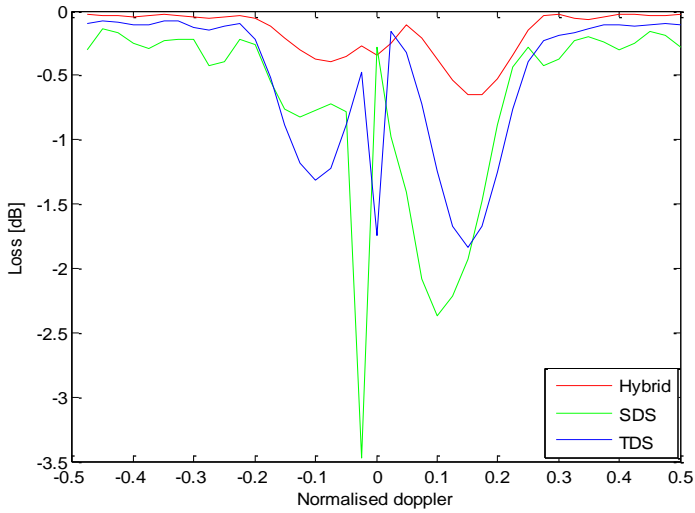


Figure 22. Performance loss of the methods for case 3 and 17 GHz carrier frequency.

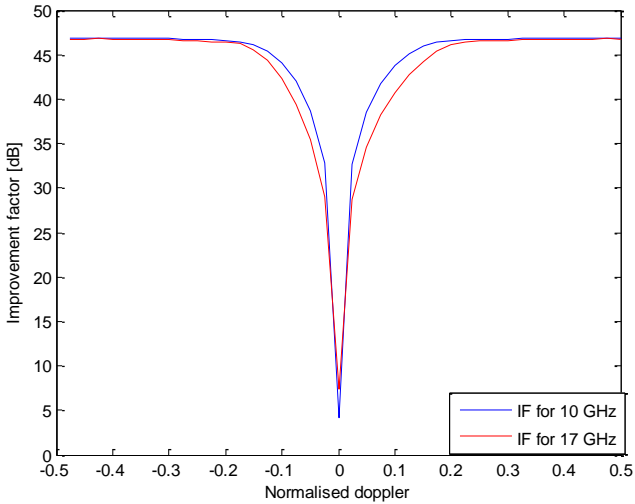


Figure 23. Optimum improvement factor of case 3 for 10 GHz and 17 GHz carrier frequencies.

Although Hybrid method gives better performance than TDS and SDS methods, Hybrid method needs more computational operations than TDS and SDS methods. Because of the statistical nature of the problem, it is possible to obtain different performance loss even if we consider same cases.

Conclusions

In this report, we introduce application of the MNLT method for modeling scatterer reflectivity on the ground. By using the MNLT, it is possible to construct a reflectivity distribution for a given pdf and correlation. Traditionally, the training data used for estimation of the covariance matrix is assumed to share the same statistics as the test data and be homogeneous along the range direction, when a more accurate training data model is considered, statistical properties of this data may change along the range direction. For example, when the nonhomogeneous earth surface composed of different parts such as forest, rocky soil, sand, sea etc. is modeled, the reflectivity is range dependent. On the other hand, it is reasonable to consider that scatterers can have some degree of correlation on the ground. This correlation property of scatterers is also observable in SAR images.

We evaluate the performance of STAP algorithms based on the estimation of the covariance matrix in the two data set (TDS) (Klemm, 2002; Guerri, 2014), single data set (SDS) (Aboutanios and Mulgrew, 2007) and Hybrid algorithms. Performance measures are compared against the optimum STAP in terms of improvement factor loss plots. As seen from the figures, the Hybrid method usually performs better than TDS and SDS methods. The SDS and Hybrid method provide new ideas for the estimation of covariance matrix for heterogeneous environments when homogeneous training data is not available.

References

Aboutanios, E., & Mulgrew, B. (2007). A generalised hybrid STAP approach for radar target detection in heterogeneous clutter. submitted to the IEEE Transactions on Aerospace And Electronic Systems, 2006 14th European Signal Processing Conference, 04-08 September 2006, Florence, Italy.

Glentis, G. O. (2008). A fast algorithm for APES and Capon spectral estimation. IEEE Transactions on Signal Processing, 56(9), 4207-4220.

Guerci, J. R. (2014). Space-time adaptive processing for radar. (Second Edition). Boston/London:Artech House.

Klemm, R. (2002). Principles of space-time adaptive processing. (second ed.), IEE Radar, Sonar, Navigation and Avionics 12, London: IEE Press.

Tough, R. J. A., & Ward, K. D. (1999). The correlation properties of gamma and other non-Gaussian processes generated by memoryless nonlinear transformation. Journal of Physics D: Applied Physics, 32(23), 3075.

CHAPTER VI

Advancements in Brain Tumor Classification Using ResNet-50: Exploring Activation Functions and Batch Size Influence

Ahmet SOLAK¹

Introduction

Brain tumors are a complex and diverse group of neoplasms that pose significant challenges in the field of oncology. Accurate classification of brain tumors is crucial for personalized therapeutic strategies and prognostic assessments due to their heterogeneity in terms of histology, molecular characteristics, and clinical behavior (DeAngelis, 2001). Accurate classification of brain tumors is crucial for personalized therapeutic strategies and prognostic assessments due to their heterogeneity in terms of histology, molecular characteristics, and clinical behavior. Therefore, a nuanced approach

¹ Res. Asst. Dr., Konya Technical University, Department of Electrical and Electronics Engineering

to diagnosis and treatment planning is necessary. Accurate classification of brain tumors is crucial for personalized therapeutic strategies and prognostic assessments due to their heterogeneity in terms of histology, molecular characteristics, and clinical behavior (Herholz, Langen, Schiepers, & Mountz, 2012). Understanding the different types of brain tumors is essential for customizing interventions to the unique characteristics of each case. Primary brain tumors originate within the central nervous system and are traditionally classified based on factors such as cell type, grade, and location. Gliomas, meningiomas, and pituitary tumors are just a few examples of the diverse spectrum of brain neoplasms. In addition, molecular diagnostics have refined classifications, revealing distinct subtypes with varied clinical implications. Precise classification is significant because it directly impacts treatment decisions. Different tumor types respond differently to therapies, and accurately identifying and classifying these entities informs the selection of appropriate therapeutic modalities. Additionally, the advent of targeted therapies and immunotherapies has highlighted the importance of understanding the molecular signatures associated with specific tumor types at a granular level (Perkins & Liu, 2016).

Medical imaging is crucial in brain tumor classification. Radiological techniques, such as magnetic resonance imaging (MRI) and computed tomography (CT), provide valuable insights into tumor morphology and localization. However, the complexity of tumor phenotypes often exceeds the interpretative capacities of conventional imaging alone. Therefore, advanced computational methods, particularly machine learning and deep learning approaches, are necessary.

This scholarly paper investigates the crucial role of accurate brain tumor classification, emphasizing the nuanced diversity of tumor types and the evolving significance of computational models in augmenting classification precision. The study centers on an in-depth examination of the ResNet-50 architecture, with the goal of refining methodologies for brain tumor classification. The goal is to improve the accuracy of diagnostic procedures and therapeutic

decision-making. Advanced technologies are seen as a crucial factor in navigating the complex landscape of brain tumor heterogeneity, leading to personalized and effective patient care. Subsequent sections of this chapter provide a detailed exposition of the methodology employed, experimental designs, and the discernible impact of different activation functions and batch sizes on the performance of ResNet-50 in brain tumor classification. This study aims to provide a significant contribution to the understanding and treatment of brain tumors, with the ultimate goal of improving the quality of life for those affected by these complex medical conditions.

Methodology

This section will provide comprehensive information about the dataset used for the study, describe the architectural features of the ResNet-50 network and explain the activation functions used in the experimental framework.

Dataset

This study utilized a dataset characterized by the presence of four distinct classes: glioma, meningioma, pituitary, and non-tumor samples ("Brain Tumor MRI Dataset, "). Detailed information on the distribution of images among these classes during the training, validation, and testing phases is presented in Table 1. The tabulated data provides a comprehensive overview of the dataset segmentation strategy by explaining the relevant image quantities assigned to each class.

Figure 1 presents representative examples of MRI scans falling within the scope of the aforementioned classes to facilitate the visual understanding of the dataset. These visual illustrations serve not only as visual aids but also contribute to the qualitative understanding of various anatomical features summarized by different tumor categories and the non-tumor class. These detailed class-based distributions and visual representations form the basis for further

discussions on the performance and effectiveness of the ResNet-50 model in the context of brain tumor classification.

Table 1. Distribution of dataset images for train, validation, and test

Class	Train	Validation	Test
Glioma	1123	198	300
Meningioma	1139	200	306
Pituitary	1239	218	300
Non-tumour	1355	240	405

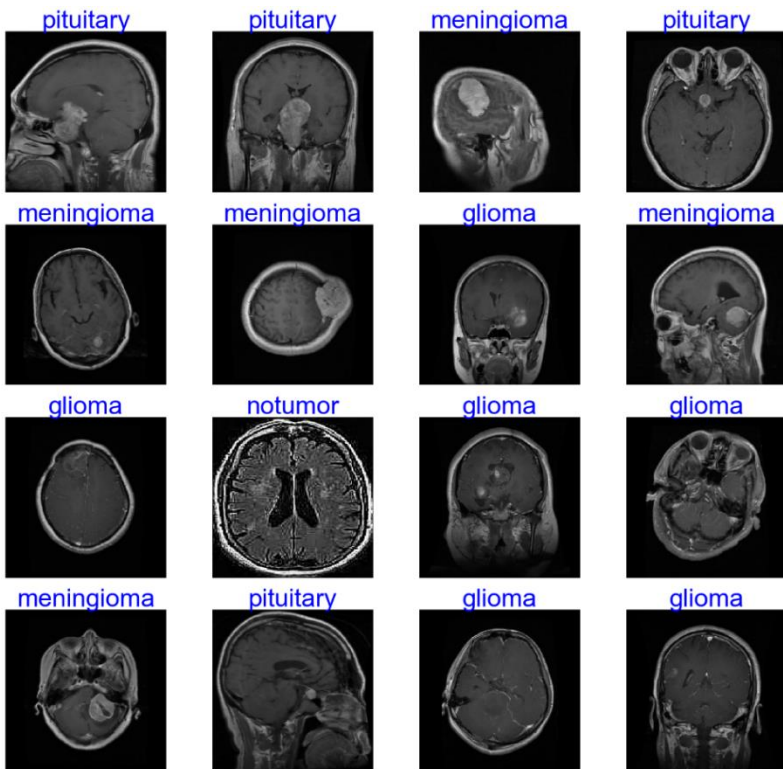


Figure 1. Sample images from the classes in the dataset

ResNet-50 Architecture

The ResNet-50 architecture is a significant advancement in deep convolutional neural networks (CNNs). It was introduced in the 2016 paper 'Deep Residual Learning for Image Recognition' (He, Zhang, Ren, & Sun, 2016). The architecture addresses the challenge of training extremely deep networks by incorporating residual learning blocks. ResNet-50 is a network that consists of 50 layers and uses residual blocks to mitigate the vanishing gradient problem.

Each block includes convolutional layers, batch normalization, and rectified linear unit (ReLU) activations. The innovation of ResNet-50 lies in the inclusion of skip connections or shortcuts, which allow for the direct flow of information from one layer to subsequent layers. ResNet-50 addresses the degradation problem encountered in very deep networks by enhancing the training process through residual learning.

The fundamental concept of residual learning involves the addition of shortcut connections. In traditional networks, the output of a layer is directly passed to the subsequent layer. However, ResNet-50 employs residual blocks where the input is added to the output. ResNet-50 uses residual mapping to simplify optimization and aid convergence in deep networks. To optimize computational efficiency, it employs a bottleneck architecture within its residual blocks, which includes 1x1, 3x3, and 1x1 convolutions to reduce the dimensionality of input feature maps before and after the 3x3 convolutional layer. This design choice balances computational efficiency without sacrificing representational power. This is followed by fully connected layers for the final classification. The architecture ends with a global average pooling layer, which condenses spatial dimensions to a single value per feature map, providing a compact and informative representation for classification. The ResNet-50 architecture is presented in Figure 2.

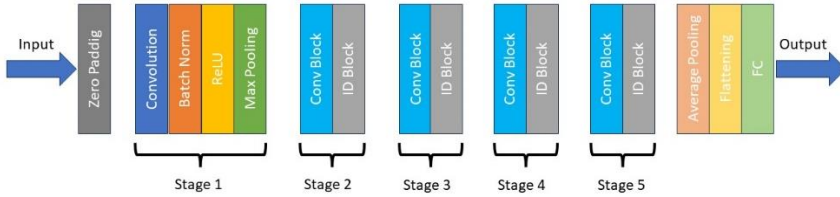


Figure 2. ResNet-50 Architecture

Activation Functions

Activation functions are key components within neural networks, imparting nonlinearity to individual neurons and allowing the model to learn complex patterns. Among the widely used activation functions, the Rectified Linear Unit (ReLU) (Agarap, 2018) stands out. ReLU introduces nonlinearity by setting negative values to zero, expressed mathematically as (1). While ReLU's simplicity facilitates efficient training and mitigates the vanishing gradient problem, it is susceptible to the "dying ReLU" problem, where neurons become inactive during training.

A more recent entrant in the activation function space is the Gaussian Error Linear Unit (GELU) (Hendrycks & Gimpel, 2016). GELU introduces smooth nonlinearity by applying the Gaussian cumulative distribution function to the input. Mathematically, GELU is defined as (2). GELU has demonstrated improved performance over ReLU in certain scenarios, especially in deeper networks and more complex tasks.

The Parametric Rectified Linear Unit (PReLU) (He, Zhang, Ren, & Sun, 2015) is an extension of ReLU that addresses the dying ReLU problem. PReLU allows learning a small slope for negative values during training, expressed as (3) where α is a learnable parameter. This adaptability of the negative slope mitigates the "dying ReLU" problem by allowing gradients to flow during backpropagation even for negative inputs.

$$f(x) = \max(0, x) \tag{1}$$

$$f(x) = 0.5x * (1 + \tanh(\sqrt{\frac{2}{\pi}} * (x + 0.044715x^3))) \quad (2)$$

$$f(x) = \max(\alpha x, x) \quad (3)$$

In this study, the three activation functions ReLU, GELU, and PReLU were selected to investigate their impact on brain tumor classification using the ResNet-50 architecture. ReLU, which is a basic and computationally efficient choice, is contrasted with GELU, which introduces a smooth nonlinearity, and PReLU, which addresses the "dying ReLU" problem. The study aims to discern the performance nuances of these activation functions in the specific context of medical image analysis, where precise feature extraction is paramount.

Figure 3 shows visual representations of the ReLU, GELU, and PReLU activation functions. The graphs illustrate the mathematical formulations of these functions and provide visual insight into their shapes and nonlinear characteristics. These visualizations serve to enhance the academic discourse on the pros and cons of each activation function, thus contributing to a comprehensive understanding of their applicability in neural network architectures.

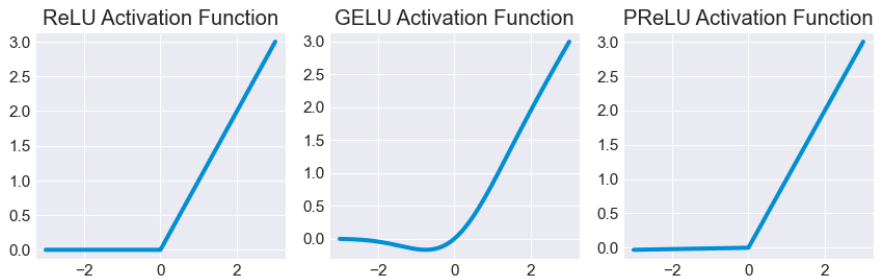


Figure 3. Activation Function Characteristics

Batch Size

Batch size is a critical hyperparameter in neural network training that affects the efficiency and effectiveness of the learning process. In the context of stochastic gradient descent (SGD) optimization algorithms, which are widely used in neural network training, batch size refers to the number of training examples used in a single iteration. This parameter represents a trade-off between computational efficiency and model generalization. Smaller batch sizes, such as 16 or 32, allow for more frequent updates of model weights, but may exhibit increased variability in learning, resulting in noisy updates. Conversely, larger batch sizes, such as 64, allow for smoother convergence by providing a more stable estimate of the gradient, but at the cost of increased computational complexity (Smith, Kindermans, Ying, & Le, 2017).

Choosing an appropriate batch size is a critical aspect of neural network training, affecting both the speed of convergence and the quality of the learned model. A reasonable choice takes into account the available computational resources, the size of the training dataset, and the inherent characteristics of the data. Smaller batch sizes are often preferred when dealing with limited computational resources or large datasets, as they allow for more frequent weight updates and faster convergence. However, larger batch sizes can be advantageous in scenarios where computational resources are plentiful, as they take advantage of parallelism and can lead to more stable convergence. The importance of selecting an optimal batch size lies in achieving a delicate balance between efficient model training and the production of a well-generalized model capable of robust performance on unseen data. Exploring different batch sizes allows researchers and practitioners to understand the nuances of this hyperparameter and tailor its selection to the specific characteristics of the dataset and computational infrastructure at hand.

Experimental Design

Careful consideration was given to various components in the experimental design of this brain tumor classification neural network study using the ResNet-50 architecture. The dataset, which includes glioma, meningioma, pituitary, and non-tumor samples, was selected to ensure representativeness and diversity. Preprocessing steps, including normalization and augmentation, were implemented to improve model generalization.

The ResNet-50 architecture, chosen for its proven effectiveness in image classification, was configured with specific hyperparameters. The transparency of these choices facilitates interpretability and reproducibility. The study extends to the exploration of activation functions (ReLU, GELU, PReLU) and batch sizes (16, 32, 64) to reveal their impact on classification performance and training dynamics.

The delineation of training and evaluation protocols was done with meticulous precision, including careful partitioning of the dataset into training, validation, and test sets. In addition, extensive details regarding the choice of optimizer, number of epochs, and learning rates were specified to ensure methodological rigor. In this particular context, a predefined set of hyperparameters was used, with the number of epochs fixed at 100, the Adam optimizer selected, and the data size standardized to 150x150 pixels. The initial learning rate was set to 0.001 and an adaptive learning rate strategy was implemented. Specifically, the learning rate was reduced by ten percent when no significant progress was observed over successive epochs to optimize convergence.

In evaluating the classification performance, a judicious selection of performance metrics was made to align with the research objectives. The selected metrics included accuracy (4), precision (5), recall (6), and F1 score (7) (Powers, 2020). These metrics were explicitly tailored to quantify the success of the model in accurately categorizing instances. The notation used in these metrics, denoting

True Positive (TP), True Negative (TN), False Positive (FP), and False Negative (FN), was applied consistently throughout the equations. This methodological refinement ensures a robust evaluation framework that promotes a nuanced understanding of the model's effectiveness in the specific context of brain tumor classification using the ResNet-50 architecture.

$$Accuracy = \frac{TP+TN}{TP+TN+FP+FN} \quad (4)$$

$$Precision = \frac{TP}{TP+FP} \quad (5)$$

$$Precision = \frac{TP}{TP+FN} \quad (6)$$

$$F1\ score = 2 * \frac{Precision*Recall}{Precision+Recall} \quad (7)$$

Results

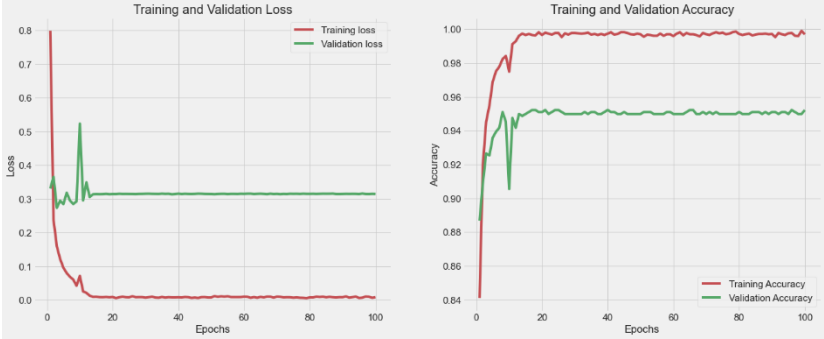
The results derived from the conducted experimental efforts encapsulate a thorough evaluation of the efficacy of the ResNet-50 architecture in the domain of brain tumor classification. Following the meticulous execution of the predefined experimental design, the performance of the model was rigorously examined across different activation functions and batch sizes. As part of the study, certain layers within the model, excluding the classification layer, were frozen, and a novel classification block was added to the framework in the final stages. The evaluation included an assessment of the model's performance with respect to different activation functions introduced in the added block and different batch sizes used during the training phase. The following section elucidates the results of these evaluations, with particular emphasis on the nuanced effects observed within each activation function, which are meticulously presented under individual headings.

As a contribution to the academic discourse, it is pertinent to note that freezing certain layers in the model, except the classification layer, while adding a new classification block is a strategic approach often used in transfer learning scenarios. This

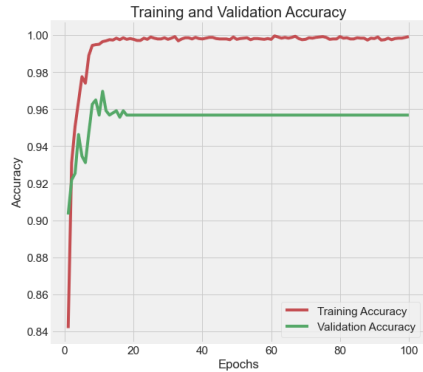
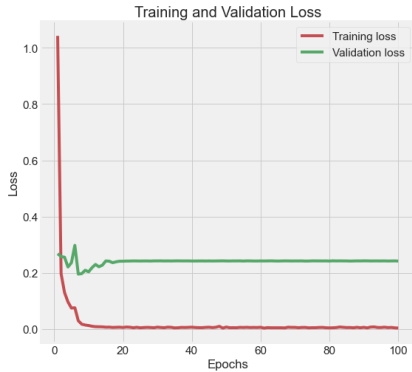
method allows the pre-trained features in the frozen layers to retain their knowledge, optimizing the model's adaptability to the specific task at hand, in this case brain tumor classification. In addition, the deliberate separation of results under different headings not only facilitates a systematic presentation, but also emphasizes the methodological rigor applied in evaluating the impact of different activation functions on the model's performance. This level of granularity in reporting contributes to the transparency and interpretability of the experimental results.

Results with ReLU on Classification Performance

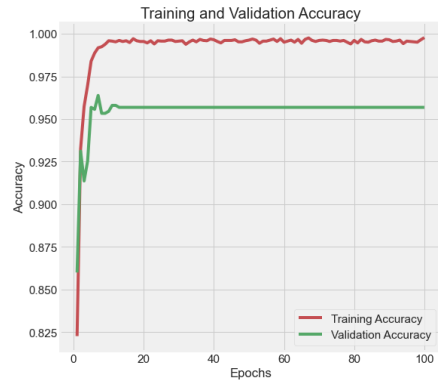
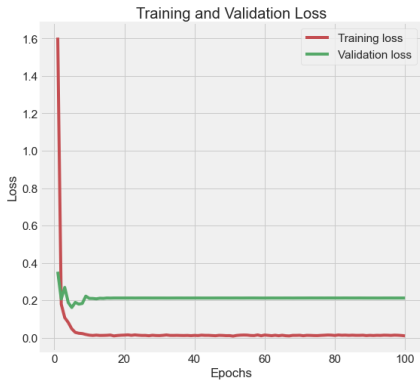
In the studies conducted using the ReLU activation function, the performance of both ReLU and different batch sizes were examined. Accordingly, the training and validation accuracy and loss plots obtained during the training phase are shown in Figure 4 for each batch size. Upon close examination of both graphs, a discernible pattern emerges that shows a consistent reduction in loss and simultaneous increase in accuracy as the number of batches increases. This observation leads to the assertion that a batch size of 64 yields the most favorable results during both the training and validation phases.



(a)



(b)



(c)

Figure 4. Training and validation loss-accuracy graphs were generated using the ReLU activation function. a) Batch size 16, b) Batch size 32 c) Batch size 64

The evaluation of trained models on test images is a critical aspect in assessing the overall validity and generalizability of the model. In this study, the evaluation process involved providing each network with test images using the Rectified Linear Unit (ReLU) activation function. The subsequent analysis involved examining the performance of the models using established performance metrics, the results of which are meticulously presented in Table 2. To enhance the interpretability of the results, confusion matrices are

also presented in Figure 5. These matrices provide a detailed visualization of the classification results, delineating the correct classifications, the misclassifications, and the specific categories into which the misclassifications occurred.

Table 2. Evaluation metrics results for test images on using ReLU activation function.

	Batch Size 16			Batch Size 32			Batch Size 64		
	Precision	Recall	F1 score	Precision	Recall	F1 score	Precision	Recall	F1 score
Glioma	0.98	0.93	0.95	0.97	0.92	0.95	0.99	0.91	0.95
Meningioma	0.92	0.93	0.92	0.91	0.92	0.92	0.90	0.94	0.92
No tumor	0.99	0.99	0.99	0.99	1	0.99	0.99	1	0.99
Pituitary	0.96	0.99	0.98	0.97	0.98	0.98	0.96	0.98	0.97

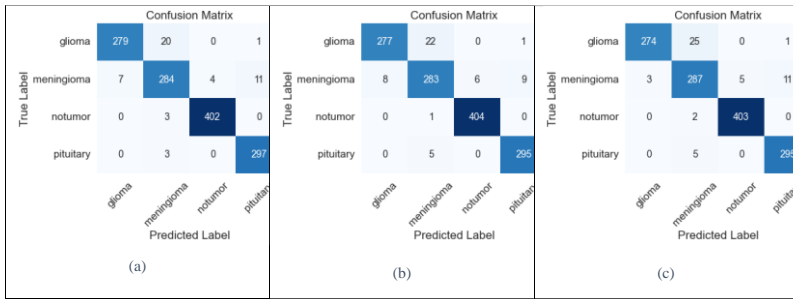


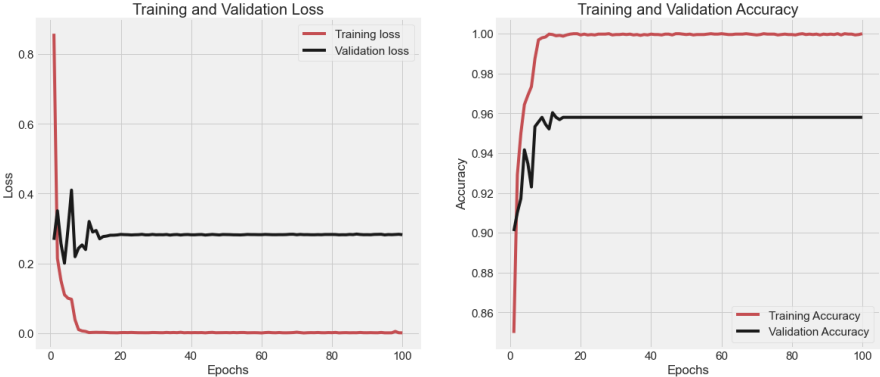
Figure 5. Confusion matrixes of test images using the ReLU activation function. a) Batch size 16, b) Batch size 32 c) Batch size 64

A careful examination of the results presented in Table 2 reveals that marginal differences of one or two percent persist across the scenarios evaluated. As a result, it is difficult to provide definitive commentary on the test results. However, a more nuanced understanding can be gained by examining the provided confusion matrices shown in Figure 5. These matrices provide insight into the numerical magnitude of misclassifications and reveal variations in misclassification prevalence across classes. In particular, optimal classification performance is seen for images assigned to no tumor class, where the model shows incorrect predictions for as few as

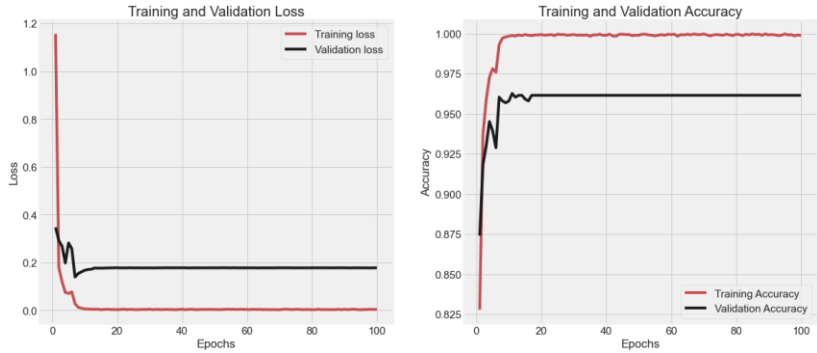
three images. Conversely, the glioma class is particularly challenging, showing the worst classification performance of all models. This observation suggests a consistent struggle to accurately classify glioma instances. Additionally, a notable trend emerges when considering the collective test images - increasing the batch size appears to correlate positively with improved overall classification results.

Results with PReLU on Classification Performance

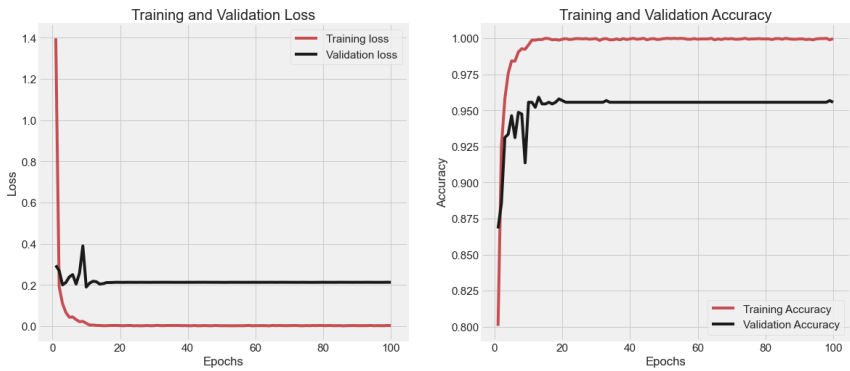
PReLU differs from ReLU by addressing the "dying neuron" problem through its unique treatment of the negative region. A comparative investigation was conducted by subjecting both activation functions to identical training procedures in order to identify potential advantages or disadvantages in the context of brain tumor classification studies. Figure 6 shows the graphical representations of the loss and accuracy metrics derived throughout the training and validation phases, providing a visual representation of the performance dynamics associated with PReLU in contrast to ReLU.



(a)



(b)



(c)

Figure 6. Training and validation loss-accuracy graphs were generated using the PReLU activation function. a) Batch size 16, b) Batch size 32 c) Batch size 64

Examination of the training and validation results shown in Figure 6 for the PReLU activation function reveals optimal results when using a batch size of 32. However, in order to strengthen the accuracy and reliability of the study, an evaluation of the model performance on test images is of paramount importance. The results derived from each model during the testing phase are meticulously presented in Table 3. At the same time, confusion matrices were constructed to numerically illustrate both correct and incorrect classifications, providing a comprehensive visualization of the

classification results. These matrices are thoughtfully detailed and visually presented in Figure 7.

Table 3. Evaluation metrics results for test images on using PReLU activation function.

	Batch Size 16			Batch Size 32			Batch Size 64		
	Precision	Recall	F1 score	Precision	Recall	F1 score	Precision	Recall	F1 score
Glioma	0.99	0.91	0.95	0.98	0.95	0.96	0.98	0.93	0.95
Meningioma	0.90	0.95	0.92	0.93	0.93	0.93	0.93	0.93	0.93
No tumor	0.99	0.99	0.99	0.99	1	0.99	0.99	0.99	0.99
Pituitary	0.97	0.98	0.98	0.96	0.99	0.98	0.96	0.99	0.98

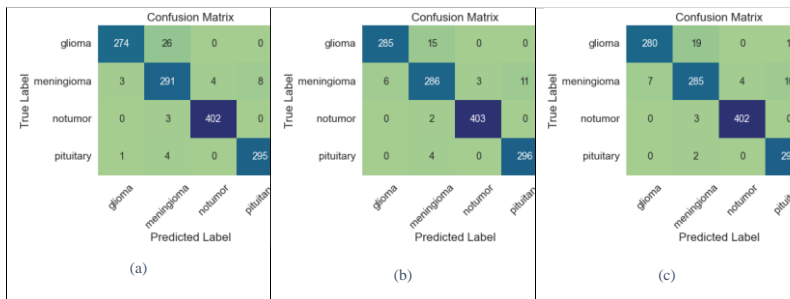


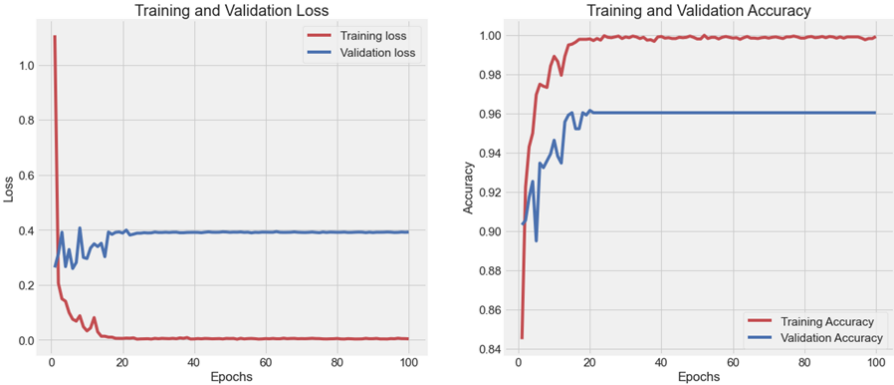
Figure 7. Confusion matrixes of test images using the ReLU activation function. a) Batch size 16, b) Batch size 32 c) Batch size 64

Evident from both the tabulated information in Table 3 and the graphical representation in Figure 7, the model configured with a batch size of 32 exhibited superior performance in the classification of test images, demonstrating fewer misclassifications than its counterparts. This notable efficacy extended across not only the testing phase but also the training and validation phases, highlighting its consistent robustness. A granular examination of the classification performance on a class-specific basis reveals that the model excelled in accurately classifying non-tumor images, followed closely by the pituitary class. In contrast, the glioma class

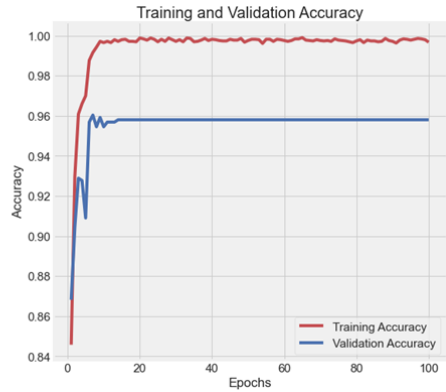
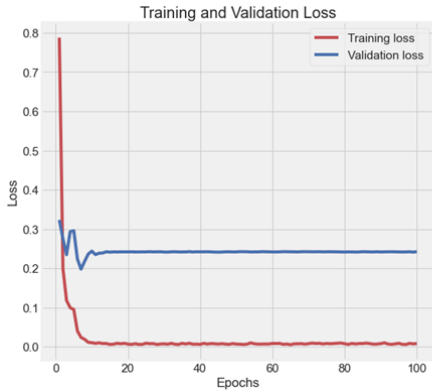
exhibited the least favorable classification outcomes, representing the most challenging category for the model. These discernments contribute to a nuanced understanding of the model's strengths and weaknesses, elucidating its performance differentials across distinct classes in the task of brain tumor classification.

Results with GELU on Classification Performance

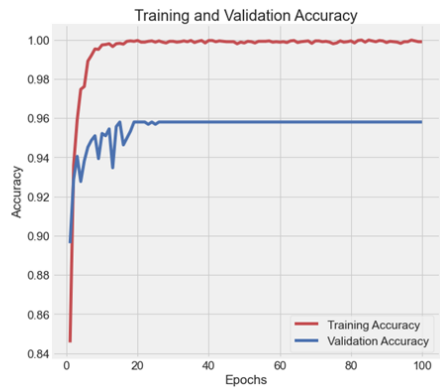
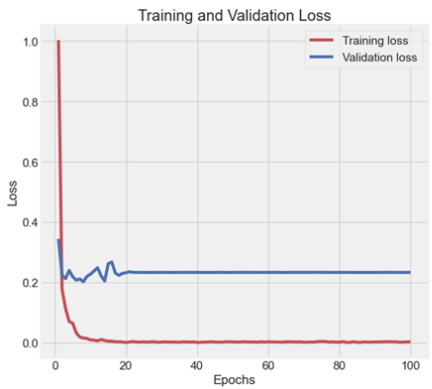
In the final phase of the investigation, training operations were performed using GELU activation function in the domain of biomedical engineering. Specifically, the salient feature that distinguishes the GELU activation function from ReLU type functions is its inherent smooth transition property. Following the initial training with alternative activation functions, an extensive iteration of the training process was performed, this time integrating the GELU activation function. The graphical representations of the training and validation metrics, including loss and accuracy, resulting from these training sessions for each specified batch size are shown in Figure 8.



(a)



(b)



(c)

Figure 8. Training and validation loss-accuracy graphs were generated using the GELU activation function. a) Batch size 16, b) Batch size 32 c) Batch size 64

As evident from the training and validation plots, optimal outcomes were discerned when employing the GELU activation function, particularly when a batch size of 16 was selected. To ensure the robustness and generalizability of the trained models, the evaluation of their performance on test images assumes paramount significance. In this context, Table 4 provides a comprehensive summary of precision, recall, and F1 score metrics derived from

assessments conducted on the test image set. Furthermore, Figure 9 offers detailed confusion matrices, delineating the instances of both correct and incorrect classifications for each distinct batch size.

Table 4. Evaluation metrics results for test images on using GELU activation function.

	Batch Size 16			Batch Size 32			Batch Size 64		
	Precision	Recall	F1 score	Precision	Recall	F1 score	Precision	Recall	F1 score
Glioma	0.98	0.94	0.96	0.98	0.92	0.95	0.98	0.93	0.96
Meningioma	0.92	0.94	0.93	0.90	0.93	0.92	0.92	0.95	0.93
No tumor	0.99	0.99	0.99	0.99	0.99	0.99	1	1	1
Pituitary	0.97	0.98	0.98	0.96	0.98	0.97	0.97	0.99	0.98

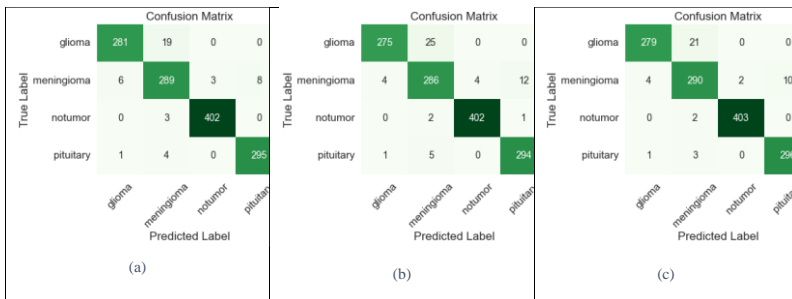


Figure 9. Confusion matrixes of test images using the GELU activation function. a) Batch size 16, b) Batch size 32 c) Batch size 64

Examination of both the tabulated results and the confusion matrix clearly demonstrate optimal results when using batch sizes of 16 and 64 during the testing phase. The performance differences between the different classes show a remarkable ability to classify non-tumor images, followed by pituitary, meningioma and glioma. In particular, the extensive training scheme using the GELU activation function highlights that batch size 16 yields the best performance during the training and validation phases. Furthermore,

batch sizes 16 and 64 show commendable performance during the testing phase, illustrating the robustness and generalizability of the model across different batch sizes.

Discussion

As part of this investigation, the training phase was meticulously executed to discern the impact of different activation functions and batch sizes on the classification of brain tumors using the ResNet-50 architecture. The results of these investigations clearly show that both training and validation accuracy rates consistently exceed 95% across all activation functions considered. During the testing phase, analogous commendable results are manifested, as evidenced by assessments encompassing precision, recall, F1 score, and confusion matrices. Notably, the model that achieves the most robust performance in the testing phase emerges from training instances where the PReLU activation function and a batch size of 32 were judiciously selected.

An intriguing facet of the investigation relates to batch size evaluation, revealing that different batch size values exhibit superior performance depending on the chosen activation function. A closer look at the individual image classes during the testing phase reveals that the classification of non-tumor images is excellent, while gliomas are the most difficult class to classify accurately. These findings provide a nuanced understanding of the interplay between activation functions, batch sizes, and the classification of specific tumor classes, enriching the understanding of ResNet-50's efficacy in brain tumor classification.

Conclusion

In conclusion, this study provided a systematic exploration of the ResNet-50 architecture for brain tumor classification, delving into the nuanced effects of different activation functions and batch sizes. The results highlight the commendable accuracy rates achieved during both the training and validation phases, exceeding the 95% threshold for all activation functions considered. In

particular, the PReLU activation function coupled with a batch size of 32 yielded the most robust test performance, highlighting the importance of careful hyperparameter selection in model training.

Investigation of batch size dynamics revealed remarkable variability in performance depending on the chosen activation function, highlighting the intricate relationship between architectural choices and training dynamics. Careful evaluation of tumor classes in the testing phase revealed varying degrees of classification difficulty, with non-tumor images demonstrating superior classification performance, contrasted with the challenges posed by glioma classification, marking it as the most difficult class to accurately discriminate.

The contributions of this study extend beyond numerical results, providing a nuanced understanding of ResNet-50's efficacy in brain tumor classification. The insights gained from variations in activation function and batch size not only enrich our understanding of model behavior, but also provide avenues for future research and optimization. As the field of medical image analysis continues to advance, the insights gained from this study pave the way for more informed decisions when deploying deep learning architectures for the complex task of brain tumor classification.

References

- Agarap, Abien Fred. (2018). Deep learning using rectified linear units (relu). arXiv preprint arXiv:1803.08375.
- Brain Tumor MRI Dataset. Retrieved from <https://www.kaggle.com/datasets/masoudnickparvar/brain-tumor-mri-dataset>
- DeAngelis, Lisa M. (2001). Brain tumors. *New England journal of medicine*, 344(2), 114-123.
- He, Kaiming, Zhang, Xiangyu, Ren, Shaoqing, & Sun, Jian. (2015). Delving deep into rectifiers: Surpassing human-level performance on imagenet classification. Paper presented at the Proceedings of the IEEE international conference on computer vision.
- He, Kaiming, Zhang, Xiangyu, Ren, Shaoqing, & Sun, Jian. (2016). Deep residual learning for image recognition. Paper presented at the Proceedings of the IEEE conference on computer vision and pattern recognition.
- Hendrycks, Dan, & Gimpel, Kevin. (2016). Gaussian error linear units (gelus). arXiv preprint arXiv:1606.08415.
- Herholz, Karl, Langen, Karl-Josef, Schiepers, Christiaan, & Mountz, James M. (2012). Brain tumors. Paper presented at the Seminars in nuclear medicine.
- Perkins, Allen, & Liu, Gerald. (2016). Primary brain tumors in adults: diagnosis and treatment. *American family physician*, 93(3), 211-217B.
- Powers, David MW. (2020). Evaluation: from precision, recall and F-measure to ROC, informedness, markedness and correlation. arXiv preprint arXiv:2010.16061.

Smith, Samuel L, Kindermans, Pieter-Jan, Ying, Chris, & Le, Quoc V. (2017). Don't decay the learning rate, increase the batch size. arXiv preprint arXiv:1711.00489.

CHAPTER VII

Production of Commonly Used Components in the Cathode Active Substance of Lithium-Ion Cells by Enrichment with Graphene Derivatives

**Birayda Alparslan¹
Ekin ASLAN²**

Introduction

Humanity's continuous progress in the fields of technology and industry has increased the demand for energy. A significant portion of this growing energy need is met through the use of fossil fuels. It is important to remember that fossil fuel reserves are limited. Additionally, the combustion of fossil fuels releases harmful gases into the atmosphere, causing serious damage to the ozone layer and

¹ Student, Kayseri University, Department of Electrical and Electronics Engineering, brayda.alparslan@gmail.com, ORCID: 0009-0009-3566-7204

² Ekin Aslan, Assoc. Prof, Kayseri University, Department of Electrical and Electronics Engineering, ekinaslan@kayseri.edu.tr, ORCID: 0000-0003-0933-7796

the environment. Various efforts towards environmentally friendly, clean, and sustainable energy sources have gained importance.

In this context, the development of lithium-ion (Li-ion) batteries has generated excitement, especially in the field of energy storage. With their efficiency, high specific capacities, and high voltages, Li-ion batteries continue to evolve over time. Li-ion batteries fall under the category of rechargeable batteries. Unlike rechargeable batteries with different chemical compositions, Li-ion batteries experience minimal capacity loss when fully discharged and then fully recharged. The shelf life of Li-ion batteries is also high. If there is no charge-discharge cycle, their chemical nature results in slow degradation, leading to minimal capacity loss. However, in cases of overcharging, there is a noticeable loss in capacity.

In 1991, Sony combined Goodenough's cathode and a carbon anode in the world's first commercial rechargeable Li-ion battery. The result was a blockbuster breakthrough overnight. In addition to boosting battery sales, Sony also resolved an issue related to handheld video cameras, one of its leading electronic products (LeVine, 2015).

Li-ion cells can be produced in various shapes, as illustrated in Figure 1. This diversity has allowed for a wide range of applications. In Figure 1(a), the cell is marked as cylindrical, in Figure 1(b), it is prismatic, in Figure 1(c), it is button-shaped, and in Figure 1(d), there are designs for flat and thin cells.

Bellcore researchers introduced polymer electrolytes to the liquid Li-ion system. They developed the first reliable and practical rechargeable Li-ion high-power energy (HPE) cell, which significantly differs from traditional coin, cylindrical, or prismatic cell configurations and is called plastic lithium-ion (PLiON). The flexibility, elasticity, and lightness provided by this thin-film battery technology, as shown in Figure 1(d), have been commercially developed since 1999.

It offers numerous potential advantages for the trend of electronic miniaturization (Tarascon and Armand, 2011).

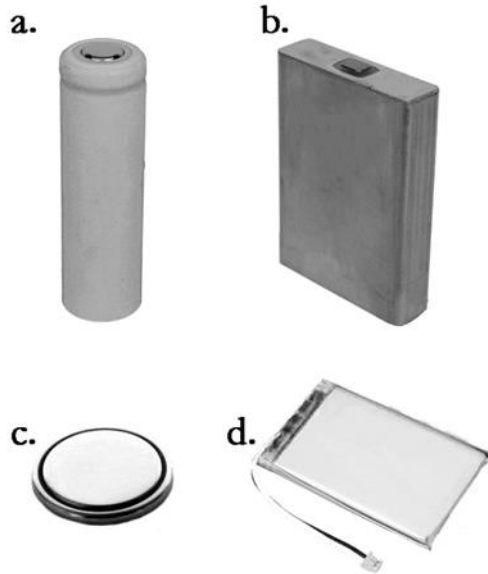


Figure 1. Various geometric shapes of manufactured Li-ion batteries: a) Cylindrical cell, b) prismatic cell, c) button cell, d) flat and thin cell

To the present day, it is the most popular battery technology worldwide. The reason for this is its high-performance and long-lasting solutions in every field requiring batteries, coupled with ease of use. The global Lithium-Ion Battery Market was valued at 65.9 billion USD in 2021, and it is expected to reach 273.8 billion USD by 2030, with a Compound Annual Growth Rate (CAGR) of 19.3%, according to estimates. (Sengüler, 2023).

The components found in layers within Li-ion batteries are fundamentally as follows: cathode, anode, electrolyte, and separator. The positive electrode is the cathode, and the negative electrode is the anode. These electrodes are separated from each other by a separator. Electrolyte is used to facilitate ion transfer between the electrodes. Lithium ions are mobile, and this is explained as follows:

during the charging of the battery, an ion movement from the cathode to the anode is observed, and conversely, if there is an ion flow from the anode to the cathode, a discharge condition is observed in the battery.

In lithium batteries, the negative electrode, which is the anode, is lithium metal itself. The anode is the negative pole during discharge and the positive pole during charging. Lithium has a molecular weight of 6.941 g/mol and a theoretical capacity of 3860 mAhg¹. In the initial research on Li-ion batteries in the 1970s, lithium metal was used as the anode (Whittingham, 1976).

Indeed, lithium metal anodes have challenges related to the formation of dendrites on the electrode surface (Kominato et al., 1997:471-475). Due to this disadvantage of lithium, commercial graphite has started to be used as an anode material. Graphite provides a stable structure to the anode, ensuring capacity retention. Graphite anodes are still widely used in the industry.

The electrolyte is defined as a solution containing a salt and solvents, forming the third essential component of a battery, with the first two components being the anode and cathode (Tarascon and Armand, 2011).

The separator is placed between the anode and cathode. A good separator should have high ionic conductivity, negligible electrical conductivity, and a chemically stable structure that does not dissolve in the electrolyte.

The positive electrode, which is the cathode, and the negative electrode, which is the anode, can have different chemical compositions. When looking at the gravimetric and volumetric energy densities of rechargeable cells, it can be observed in Figure 2 that cells with both higher gravimetric and volumetric energy density are Li-ion cells.

Figure 2 is a comparison of different battery technologies in terms of volumetric and gravimetric energy density. Globally, the sales share of portable Ni-Cd, Ni-MH, and Li-ion batteries is 23%,

14%, and 63%, respectively. The use of lead-acid batteries is generally limited to starting, lighting, and ignition (SLI) or backup applications in automobiles, while Ni-Cd batteries remain the most suitable technologies for high-power applications, such as power tools. (Tarascon and Armand, 2011).

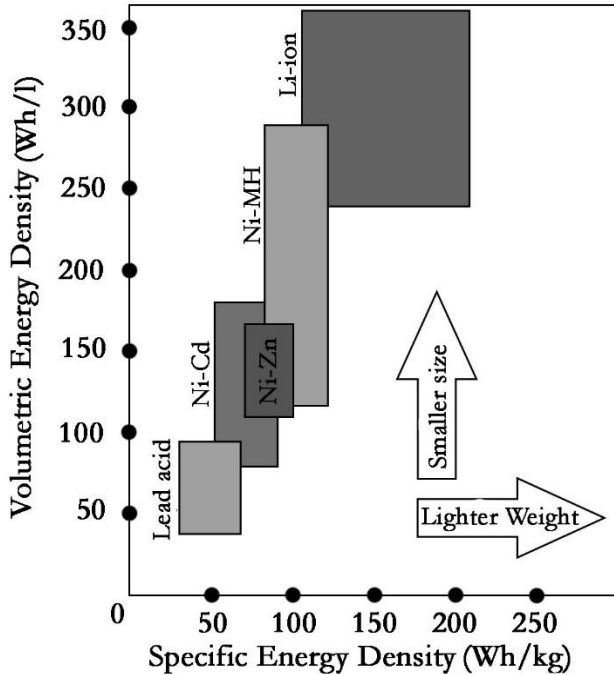


Figure 2. Comparison of rechargeable batteries in terms of gravimetric and volumetric energy density (Ouyang et al., 2017).

Several types of rechargeable batteries have been developed and practically used, such as lead-acid (Pb-acid) batteries, nickel-cadmium (Ni-Cd) batteries, nickel-metal hydride (Ni-MH) batteries, and Li-ion batteries (Kang et al., 2014).

The most well-known cathode electrodes include layered LiCoO_2 , spinel-structured LiMn_2O_4 , olivine-structured LiFePO_4 , layered

$\text{LiNi}_{0.8}\text{Co}_{0.15}\text{Al}_{0.05}\text{O}_2$ (NCA) and layered $\text{LiNi}_x\text{Mn}_y\text{Co}_z\text{O}_2$ (NMC). In contemporary applications, NCA and NMC cathode materials stand out due to their high energy density among these cathode materials.

The NMC cathode is a commonly used and reliable cathode in the market. Of course, research is being conducted for cathodes with better performance because the NMC cathode electrode faces the challenge of rapid capacity degradation in the later stages of charge-discharge cycles over time.

Today, there is considerable interest in using graphene to modify cathode materials because it significantly enhances the conductivity of cathode materials (Zhou et al., 2011).

In this study, efforts were made to increase the capacity of the NMC cathode electrode and address potential issues within the battery. Initially, high-purity and homogeneous NMC powder were produced using the sol-gel process. In the next stage, reduced graphene oxide (rGO) synthesis was carried out using the modified Hummers method. Various binders and conductive carbon (c-black) were added to convert the produced NMC powders and rGO materials into electrodes, completing the cathode preparation process.

Additionally, the large specific surface area of graphene facilitates Li-ion adsorption and diffusion, leading to a reduction in charging time and an increase in power output (Rao et al., 2011:2966-2972). K. Jiang et al. reported that the electrochemical performance of the RGO/NMC mixture can be clearly improved by directly processing rGO and NMC together using a milling method. They also reported that by directly mixing RGO and NMC in alcohol at a temperature of 80 °C, the electrochemical performance of the RGO/NMC compound is much better (K. Jiang et al., 2012).

Method

Li-NMC Powder Production

NMC powder has been produced through the sol-gel process. The starting materials include lithium acetate dihydrate $\text{Li}(\text{CH}_3\text{COO})\cdot 2\text{H}_2\text{O}$, nickel acetate $(\text{Ni}(\text{CH}_3\text{COO})_2\cdot 4\text{H}_2\text{O})$, manganese acetate $(\text{Mn}(\text{CH}_3\text{COO})_2\cdot 4\text{H}_2\text{O})$, and cobalt acetate $(\text{Co}(\text{CH}_3\text{COO})_2\cdot 4\text{H}_2\text{O})$. The material and quantity ratios are shown in Table 1.

Table 1. Material and Quantity Ratios for NMC Powder Production

Materials	Amount ($\text{Li}_{1,2}\text{Ni}_{1,2}\text{Co}_{0,08}\text{Mn}_{0,52}\text{O}_2$)
$\text{Li}(\text{CH}_3\text{COO})\cdot 2\text{H}_2\text{O}$	7.344 g
$\text{Ni}(\text{CH}_3\text{COO})_2\cdot 4\text{H}_2\text{O}$	2.986 g
$\text{Mn}(\text{CH}_3\text{COO})_2\cdot 4\text{H}_2\text{O}$	5.390 g
$\text{Co}(\text{CH}_3\text{COO})_2\cdot 4\text{H}_2\text{O}$	0.849 g
Pure water	140 ml
Citric acid	23.055 g

The ingredients are dissolved in distilled water and stirred in the same beaker. To chelate the mixture, $\text{C}_6\text{H}_8\text{O}_7$ (citric acid) is added, and after complete dissolution, HN_4OH (ammonium hydroxide) is added until the pH reaches 9. The mixture is stirred using a magnetic stirrer with a heating system and achieves a gel-like consistency in approximately 5 hours. The obtained gel is poured into a sapphire concave-shaped glass (watch glass) and subjected to a thermal treatment at 100°C for 24 hours. This process eliminates unwanted volatiles from the gel. The dried gel, made from agate, is thoroughly ground in a mortar until it becomes a fine powder. The powdered mixture is transferred into an alumina crucible and subjected to another heat treatment. This process begins at room temperature, reaches 500°C within 5 hours, and is held at 500°C for 5 hours. Subsequently, it is further raised to 850°C within

the next 5 hours and maintained at 850°C for approximately 8 hours to induce crystallization. The powder is left to cool on its own. Finally, the resulting powder undergoes another grinding process to obtain NMC powder.

Synthesis of Reduced Graphene Oxide

Graphene oxide was synthesized using the modified Hummers method, and graphite was used in the synthesis process. The list of material quantities is provided in Table 2.

Table 2. *Material and Quantity Table for GO Synthesis Using the Hummers Method*

Materials	Amount
Graphite powder	2.50 g
NaNO ₃	1.25 g
H ₂ SO ₄ (%95-97)	60 ml
KMnO ₄	7.50 g
Pure water	370 ml
HNO ₃	125 ml
H ₂ O ₂ (%30 concentrated)	5 ml
HCL	200 ml
Hydrazine hydrate	20 ml

A mixture is prepared with 2.50 grams of graphite powder in a 3:1 ratio of HNO₃ and H₂SO₄ in a 125 mL volume. The solution is stirred with a magnetic stirrer for 3 hours, and a washing process with distilled water is carried out until the pH becomes neutral. Once the desired pH is achieved, the material is dried in an oven at 80°C for 12 hours. The material undergoes heat treatment in an ash furnace at 850°C for 120 seconds. Subsequently, it is mixed with a solution containing 1.25 grams of NaNO₃ in 60 mL of sulfuric acid using a

magnetic stirrer for 3 hours. The material is placed in an ice bath at 0°C, and controlled cooling is applied. Then, 7.50 grams of KMnO_4 is added gradually, ensuring that the temperature does not exceed 20°C. The material is returned to the magnetic stirrer and stirred until a viscous structure is obtained. Slowly, 120 mL of distilled water is added drop by drop to the material. To maintain the temperature below 98°C during this process, distilled water supplementation is carefully controlled. It is kept at 98°C for an additional 15 minutes. Afterward, the material is stirred for another 30 minutes on the magnetic stirrer. To achieve a greenish-yellow color in the solution, 5 mL of H_2O_2 is added and stirred. At the end of the stirring process, the solution is placed in a 250 mL distilled water and stirred for 24 hours. The obtained material is washed with 200 mL of HCl and rinsed with distilled water until the pH of the main material becomes neutral. The final material is dried in an oven at 60°C. Graphene oxide synthesized using the modified Hummers method is reduced by ultrasonication for 15 minutes in a solution containing 5.6 mL of hydrazine hydrate (anhydrous, 98%) and distilled water. The solution is filtered through vacuum filtration to obtain reduced graphene oxide (rGO).

Electrode Preparation Process

"In order to facilitate a meaningful comparison of test results for an rGO-supported battery, two different cathode electrodes have been prepared. The first cathode electrode is labeled as 'rGO-supported NMC,' while the second cathode electrode is labeled as 'NMC' electrode."

"The amount of NMC is determined to be 1 gram, equivalent to 80% of the cathode's mass. According to this ratio, rGO is used in a weight percentage of 7%, equivalent to 87.5 mg, C-Black in a weight percentage of 3%, equivalent to 37.5 mg, PVDF (Polyvinylidene fluoride) binder, and NMP (a solution of N-methyl-2-pyrrolidinone) in a weight percentage of 10%. 6.25 ml of NMP and 2.082 grams of PVDF are used. In the 2.082 grams of PVDF

solution, 125 mg of pure PVDF is present, resulting in a purity ratio of 5.99%. The remaining NMP evaporates at the end of the process."

Table 3 . Material and Quantity Table Used for the Improved Electrode Preparation Process

Materials	Mass ratio	Amount
NMC	%80	1 g
rGO	%7	87.5 mg
C-Black	%3	37.5 mg
PVDF	%10	2.082 g (%5.99 purity 125 mg)
NMP	-	6.25 ml

PVDF and NMP are placed in a magnetic stirrer, and rGO is added. The mixture is stirred at a speed of 1000 rpm for 2 hours, followed by the addition of NMC, which is also stirred at 1000 rpm for another 2 hours. After this process, a total of 4 cycles consisting of 15 minutes of ultrasonication and 5 minutes of magnetic stirring are performed. A homogeneous mixture is obtained. Subsequently, C-Black is added and stirred at 1000 rpm for 2 hours using a magnetic stirrer. The mixture undergoes a 30-minute ultrasonication process, followed by another 30 minutes of stirring at 1000 rpm using a magnetic stirrer. The prepared mixture is held in a vacuum oven at 120°C for 12 hours until it gels. Once it reaches the desired consistency, the mixture is coated onto aluminum foil using the Doctor Blade method, with a coating thickness set at 57 μm . The thickness of the applied aluminum foil is determined to be 15 μm , resulting in a total thickness of 72 μm . It is then returned to the vacuum oven for complete drying, where it is kept at 120°C for another 12 hours. After removal from the oven, it is pressed at 10 MPa pressure, resulting in a cathode thickness measured at 45 μm . When adding the 15 μm thickness of the aluminum foil, the total thickness becomes 60 μm . Since a CR2032 coin-type cell is used in

the experiment, the cathode is cut into precise disks with a diameter of 1.5 cm using a disk cutter.

"In order to comprehensively understand the efficacy of the conducted experiment during the testing phase, a cathode electrode was prepared using classical methods. For this purpose, the amount of NMC was determined to be 1 gram, equivalent to 80% of the cathode's mass. According to this ratio, the weight percentage of C-Black was set at 10%, corresponding to 125 mg, and the weight percentage of PVDF (Polyvinylidene fluoride) binder was also set at 10%, amounting to 125 mg. The amount of NMP, a non-volatile substance absent from the cathode by mass, was determined to be 6.25 ml."

Table 4. *Material and Quantity Table Used for the Standard Electrode Preparation Process*

Materials	Mass ratio	Amount
NMC	%80	1 g
C-Black	%10	125 mg
PVDF	%10	2.082 g (%5.99 purity 125 mg)
NMP	-	6.25 ml

"PVDF and NMP are placed into a magnetic stirrer, and NMC is added. The mixture is stirred at a speed of 1000 rpm for 2 hours. After this process, a total of 2 cycles, consisting of 15 minutes of ultrasonication and 5 minutes of magnetic stirring each, are performed. A homogeneous mixture is obtained. Subsequently, C-Black is added and stirred at 1000 rpm for 2 hours using a magnetic stirrer. The mixture undergoes a 20-minute ultrasonication process, followed by another 20 minutes of stirring at 1000 rpm using a magnetic stirrer. The prepared mixture is held in a vacuum oven at 110°C for 12 hours until it gels. Once it reaches the desired consistency, the mixture is coated onto aluminum foil using the

Doctor Blade method, with a coating thickness set at 50 μm . The thickness of the applied aluminum foil is determined to be 15 μm , resulting in a total thickness of 65 μm . It is then returned to the vacuum oven for complete drying, where it is kept at 120°C for another 12 hours. After removal from the oven, it is pressed at 10 MPa pressure, resulting in a cathode thickness measured at 29 μm . When adding the 15 μm thickness of the aluminum foil, the total thickness becomes 44 μm . Due to the use of a CR2032 coin-type cell in the experiment, the cathode is cut into precise disks with a diameter of 1.5 cm using a disk cutter."

Cell Production

The battery shutdown process is carried out in a controlled environment with oxygen and humidity levels below 0.01 ppm. To enable the shutdown process of a CR2032-sized battery, a rolled cathode has been punched. The materials of the battery placed between the upper case and lower case are shown in Figure 3.

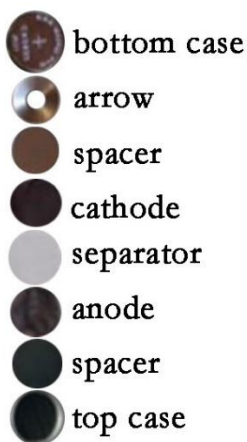


Figure 3. Components of the Manufactured Button Cell

The cathode material, cut to the appropriate dimensions for a CR2032-sized battery, is placed inside the bottom cover of the battery. A separator is added, and 1 mL of LiPF_6 electrolyte is dripped. The electrolyte is dripped between both the cathode and the

separator, and the anode and the separator. All the components inside the sealed battery are shown in Figure 3 in sequence. A lithium plate and a spring are inserted. The top cover is closed, and the inside of the battery is placed in a compression mold to ensure airtightness and is thoroughly compressed.

Characterization Analyzes

XRD analysis

The X-ray diffraction (XRD) analysis of the produced powder was conducted using Cu K α radiation with a wavelength (λ) of 1.54056 Å on the Rigaku Miniflex XRD device. The scanning range is between 10° and 80° (2 θ), and the scanning rate is 2°/min. The results are shown in Figure4.

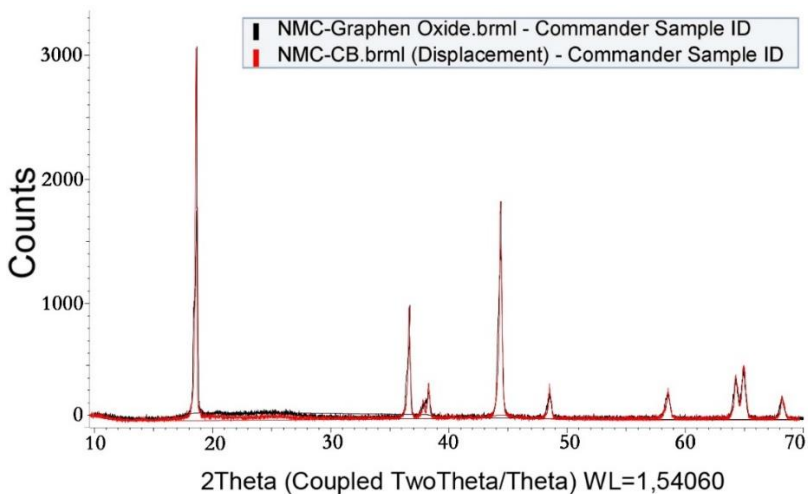


Figure 4. Displays the XRD results of synthesized NMC powders and rGO+NCM.

The X-ray diffraction (XRD) results of rGO obtained by the Hummers method and NMC c-black cathode electrode prepared through conventional methods are shown in Figure 4. As seen in the

graph, there are similar sharp peak points at $2\theta=18^\circ$, $2\theta=36^\circ$, $2\theta=38^\circ$, $2\theta=44^\circ$, $2\theta=48^\circ$, $2\theta=59^\circ$, and $2\theta=64^\circ$.

Electrochemical Tests

All electrochemical tests were conducted at room temperature using a battery analysis device within a voltage range of 2-4.8 V. The applied current values for cycling tests were 20 mA/g for the first 2 cycles during formation, and then consistently 25 mA/g. In rate tests, the applied current values were 25 mA/g (0.1C), 50 mA/g (0.2C), 125 mA/g (0.5C), 250 mA/g (1C), 500 mA/g (2C), and 25 mA/g (0.1C), respectively. Button cells were prepared and cycled at each current value to test their performance at different speeds.

Results

XRD Results

When examining the two cathode electrodes prepared in the experiment on the graph, it is observed that the peak diffraction points are consistent. This is a positive indication (Bajaj et al., 2002:773-787). Using the Scherrer equation given in Equation 1, the number of layers can be calculated according to Equation 2 based on the crystal size and the d-spacing between planes (Tiyek and Bozdoğan, 2008:116-120).

$$t_c = \frac{\kappa \cdot \lambda}{\beta \cos \theta} \quad (1)$$

$$\text{Number of layers} = t_c/d \quad (2)$$

Here, t_c is crystal thickness, κ is Scherer constant, λ is the wavelength, β is peak half height width, θ is Bragg angle, and d is the distance between planes.

In this experiment, peak broadening was observed in all XRD patterns depicting the layered cathode material synthesized at various calcination temperatures. The results suggest that the graphene surface treatment has no adverse effect on the crystalline structure (He et al., 2014:2568-2572).

Electrochemical Test Results

The prepared NMC and rGO+NMC cathodes were assembled into button cells, and galvanostatic tests were conducted at a rate of 0.1C within the voltage range of 2V to 4.8V. These tests aimed to determine the charge and discharge capacities of the produced button cells based on voltage and cycle numbers. The measurements provided information about the electrochemical performance of the rGO+NMC cathode. The results are presented in Figure 5. Here, Figure 5(a) shows the discharge capacities of two different cathodes at different rates and cycles while Figure 5(b) represents the capacity values based on the number of cycles.

a.

		DChg-mAh/g-RGO	DChg-mAh-NMC		
C Y C L E	0	161,71	149,47	0,1 C	C R A T E
	10	155,29	145,5	0,2 C	
	20	118,11	136,92	0,5 C	
	40	89,65	123	1 C	
	60	62,25	102	2 C	

b.

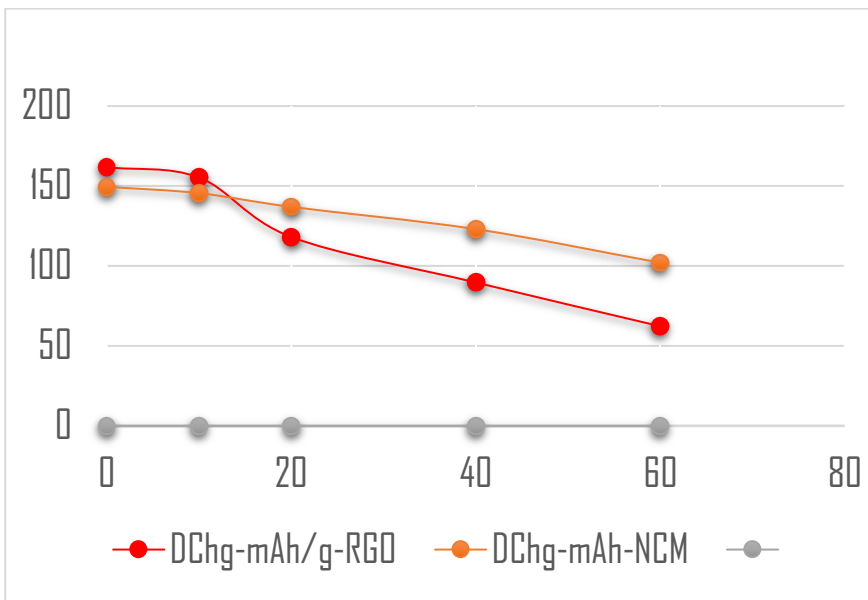


Figure 5. a) Discharge capacities of two different cathodes at different rates and cycles b) Capacity values based on the number of cycles.

The close interaction between NMC particles and graphene sheets is responsible for the higher capacity, improved cycle stability, and enhanced rate capability of RGO/NMC composite cathode materials. Initially, graphene sheets wrapped around NMC act as spacers between particles, providing a large specific surface area that can offer more pathways for Li^+ migration. This, in turn, reduces the time required for Li^+ to migrate between the cathode and electrolyte.

The graphene sheets with high conductivity coating on NMC enable rapid electron transfer, allowing them to exhibit resistance against high discharge rates. The graphene sheets surrounding NMC provide more electrochemically active intercalation lithium sites than a high-conductivity three-dimensional graphene sheet network (He et al., 2014).

Within the scope of this study, the production of layered reduced graphene oxide (rGO) using a different manufacturing method, along with the synthesis of sub-micron NMC cathode electrodes, was successfully carried out to produce rGO+NMC composite electrodes. Battery performance tests have been completed. The results indicate that the electrochemical performance of NMC, when wrapped with rGO, is enhanced.

Conclusion

The subject of this study is the enrichment of NMC cathode material by enriching it with both electrochemical and redundant graphene bands. In this context, nano-sized NMC is produced. Then, a higher performance cathode material is produced by integrating NMC and graphene with a different chemical process. Thus, a lithium ion battery design with a higher capacity can be presented to the literature.

References

Bajaj, P., Sreekumar, T. V., & Sen, K. (2002). Structure development during dry–jet–wet spinning of acrylonitrile/vinyl acids and acrylonitrile/methyl acrylate copolymers. *Journal of applied polymer science*, 86(3), 773-787.

He, J. R., Chen, Y. F., Li, P. J., Wang, Z. G., Qi, F., & Liu, J. B. (2014). Synthesis and electrochemical properties of graphene-modified $\text{LiCo}_{1/3}\text{Ni}_{1/3}\text{Mn}_{1/3}\text{O}_2$ cathodes for lithium ion batteries. *RSC Advances*, 4(5), 2568-2572.

Jiang, K. C., Wu, X. L., Yin, Y. X., Lee, J. S., Kim, J., & Guo, Y. G. (2012). Superior hybrid cathode material containing lithium-excess layered material and graphene for lithium-ion batteries. *ACS applied materials & interfaces*, 4(9), 4858-4863.

Kang, J., Yan, F., Zhang, P., & Du, C. (2014). Comparison of comprehensive properties of Ni-MH (nickel-metal hydride) and Li-ion (lithium-ion) batteries in terms of energy efficiency. *Energy*, 70, 618-625.

Kominato, A., Yasukawa, E., Sato, N., Ijuuin, T., Asahina, H., & Mori, S. (1997). Analysis of surface films on lithium in various organic electrolytes. *Journal of power sources*, 68(2), 471-475.

Ouyang, L., Huang, J., Wang, H., Liu, J., & Zhu, M. (2017). Progress of hydrogen storage alloys for Ni-MH rechargeable power batteries in electric vehicles: A review. *Materials Chemistry and Physics*, 200, 164-178.

Rao, C. V., Reddy, A. L. M., Ishikawa, Y., & Ajayan, P. M. (2011). $\text{LiNi}_{1/3}\text{Co}_{1/3}\text{Mn}_{1/3}\text{O}_2$ -graphene composite as a promising cathode for lithium-ion batteries. *ACS Appl. Mater. Interfaces*, 3(8), 2966-2972.

Tarascon, J.-M., Armand, M., 2001. Issues and challenges facing rechargeable lithium batteries. *Nature*, 414(6861): 359-367.

Tıyrek, İ., & Bozdoğan, F. (2008). Poliakrilonitril Lif Üretiminde Koagülasyon Banyo Sıcaklığının Lif İyapısına Etkisinin Geniř Aı X-Iřınları Difraksiyonu İle İncelenmesi. *Journal of Textile & Apparel/Tekstil ve Konfeksiyon*, 18(2).

Url-1, <https://qz.com/338767/the-man-who-brought-us-the-lithium-ion-battery-at-57-has-an-idea-for-a-new-one-at-92>, accessed: 20.10.2023.

Url-2, <https://temizenerji.org/2023/04/10/temiz-enerji-hedefleri-ile-kuresel-lityum-iyon-pil-pazari-2030a-kadar-2738-milyar-dolara-ulasacak/>, accessed: 18.11.2023.

Whittingham, M.S., 1976. The role ternary phases in cathode reaction. *Journal of The Electrochemical Society*, 123(3): 315-320.

Zhou, X., Wang, F., Zhu, Y., & Liu, Z. (2011). Graphene modified LiFePO₄ cathode materials for high power lithium ion batteries. *Journal of Materials Chemistry*, 21(10), 3353-3358.

CHAPTER VIII

Comparison of Nonlinear Twin Motor Multi Inputs Multi Output System with Metaheuristic Optimization Methods of The Parameters of Different Controllers

Ali Can ÇABUKER¹
M. Nuri ALMALI²
İshak PARLAR³

Introduction

TRMS is a nonlinear system with two degrees of freedoms (2-DOF). The behavior of TRMS is similar to a helicopter, but the aerodynamic forces are controlled by varying the speed of the DC

¹ Van Yuzuncu Yil University, Faculty of Engineering, Department of Electrical-Electronics Engineering, 60080, Van Türkiye alicancabuker@gmail.com, ORCID: 0000-0003-2011-2117

² Van Yuzuncu Yil University, Faculty of Engineering, Department of Electrical-Electronics Engineering, 60080, Van Türkiye mna1@yyu.edu.tr, ORCID: 0000-0003-2763-4452

³ Van Yuzuncu Yil University, Faculty of Engineering, Department of Electrical-Electronics Engineering, 60080, Van Türkiye ishakarparlar@yyu.edu.tr, ORCID: 0000-0002-3383-8091

motors. DC motors drive two propellers. The controller of the system adjusts the amount of voltage supplied to the DC motors to provide the desired values in the yaw and pitch positions. The counter weight fixed to the beam. This weight provides a stable balance position. In TRMS, DC motors are named as main motor and tail motor. When TRMS and helicopter are compared in general terms, it cannot fly like a helicopter and does not include cyclic control (Chalupa et al., 2015; Huu et al., 2016; Castillo et al., 2020). The purpose of the nonlinear controller methods used for the TRMS system is to increase robustness of the system by minimizing the effects of external disturbances such as wind encountered in natural life and the uncertainty of the TRMS system itself (Zeghlache S et al., 2020). It also adjusts its position with controllers that increase the robustness of the system (Tiwalkar et al., 2017). For TRMS methods, there are metaheuristic methods inspired by herd communities of animals to find control coefficients such as FOPID and PID (Mihaly et al., 2021). Algorithms such as particle swarm optimization algorithm, ant colony algorithm, bee colony algorithm, gray wolf optimization and dragonfly algorithm are optimization algorithms based on animal and swarm behaviors (Allouani et al., 2011; Rezoug et al., 2014; Meraihi et al., 2020; Khalaf et al., 2020; Kumar et al., 2021; Azar et al., 2020; Norsahperi et al., 2020). Traditional and classical optimization methods are not sufficient for solving high-dimensional, nonlinear, hybrid problems. Also, these algorithms are categorized by algorithm type (for example, physics-based, human based swarm based and evolutionary,) nature inspired and non-nature inspired, population based, and single solution based. These metaheuristic algorithms create computational paradigms used to solve complex optimization problems (Rajabi Moshtaghi et al., 2021; Abdel-Basset et al., 2018) In this study, the response of metaheuristic algorithms on a nonlinear system such as TRMS has been wondered. Therefore, examining the output responses of the system by trying various algorithms has been our main motivation. When the performances of different metaheuristic algorithms with different controllers are compared in detail, the crucial aspects of the

study can be explained as follows: The stability of the system was tested by examining the performance of metaheuristic algorithms on controllers in detail, When the output responses of the yaw and pitch angles are examined, it has been determined that it is more difficult to find a controller coefficient for pitch angle than for yaw angle, Considering the existing algorithms in the literature, it was seen that they were comparable and applicable with four different metaheuristic algorithms and three different controller methods. The fuzzy logic method was found to work with metaheuristic algorithms to reduce coupling dynamics in pitch and yaw angles. The remainder of the manuscript is arranged into several sections. Firstly, the general dynamic structure and mathematical equations of the TRMS system are introduced. The types of metaheuristic algorithms used for the TRMS system are presented in section 3. Control methods and block diagrams are given in detail. Cost functions, performance analyses, and graphs are given in the following sections with comparative tables and figures. Finally, results of the study were interpreted in detail, and suggestions for future scope were presented.

Material and Method

TRMS General Description and Mathematical Model

The TRMS system, which is a helicopter prototype and developed by Feedback Instruments in order to work on the control of the helicopter, which is one of the aircraft, has two DC motors, horizontal and vertical angles. The dynamic equivalent model of the TRMS system is given in Figure 1.

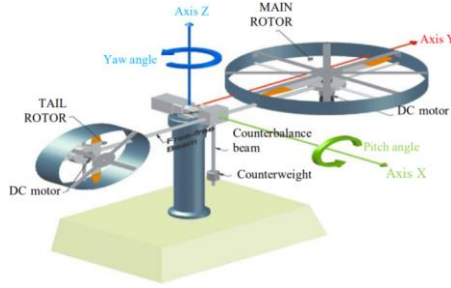


Figure 1. Dynamic equivalent model of TRMS system

The transfer function of the system is obtained by using the state space model in the Matlab/Simulink package program. It can be deduced that there are two transfer functions, yaw and pitch (Chaudhary et al., 2019). The transfer functions for the pitch and yaw planes of the TRMS system can be expressed as:

$$TF_{pitch} = \frac{1.359}{s^3 + 0.997s^2 + 4.786s + 4.278} \quad (1)$$

$$TF_{yaw} = \frac{3.6}{s^3 + 6s^2 + 5s} \quad (2)$$

The motor used for the main propeller controls the vertical flight of the TRMS, while the motor used for the tail propeller controls the horizontal flight of the TRMS.

Types of Metaheuristic Algorithms

The Dragonfly Algorithm

The Dragonfly algorithm inspired metaheuristic optimization algorithms and allowed the development of other optimization types. The dragonfly algorithm was created based on the behavior of dragonflies in nature. Dragonflies, which have about 3000 species in nature, become quite predatory and predatory when they are adults.

Dragonflies, which have hunting and predatory features, live in flocks in nature. In Figure 2, behavioral descriptions of dragonfly insect swarms are shown.

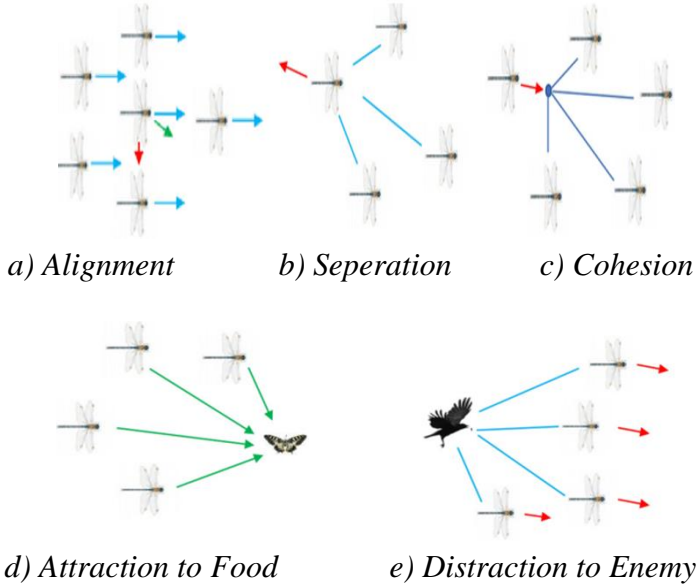


Figure 2. Behavior descriptions of dragonfly insect swarms

(Meraihi Y et. al., 2020)

The alignment, cohesion, separation, distraction to enemy and attraction to food situations in the behavior descriptions of the dragonfly algorithm are the determinants of the movements of the particles of the algorithm and the algorithm's reaching its goal. Artificial dragonflies, including these determinants, can be computer generated. The mathematical expression of artificial dragonflies is given in equation.

$$\Delta P_i^{t+1} = (s.S_i + a.A_i + c.C_i + f.F_i + e.E_i) + w.\Delta P_i^t \quad (3)$$

In equation 3, \mathbf{a} is alignment weight, \mathbf{s} is separation weight, \mathbf{c} is harmony weight, \mathbf{f} is food factor, and \mathbf{e} is an enemy factor. $\mathbf{S}_i, \mathbf{A}_i, \mathbf{C}_i, \mathbf{F}_i$, and \mathbf{E}_i indexed expressions, indicate individual separation, alignment, harmony, food, and enemy factors in computer simulation instant iterations (Chaudhary Mirjalili et al., 2016; Eröz et al., 2019; Hammouri et al., 2020). The algorithm has a specific flow diagram in computer-generated codes as in every algorithm.

In this flowchart, a random dragonfly population is created and the algorithm is run during a certain iteration. In these iterations, the data is constantly updated to reach the target. The stages of this flowchart are shown in Figure 3 (Meraihi et al., 2020).

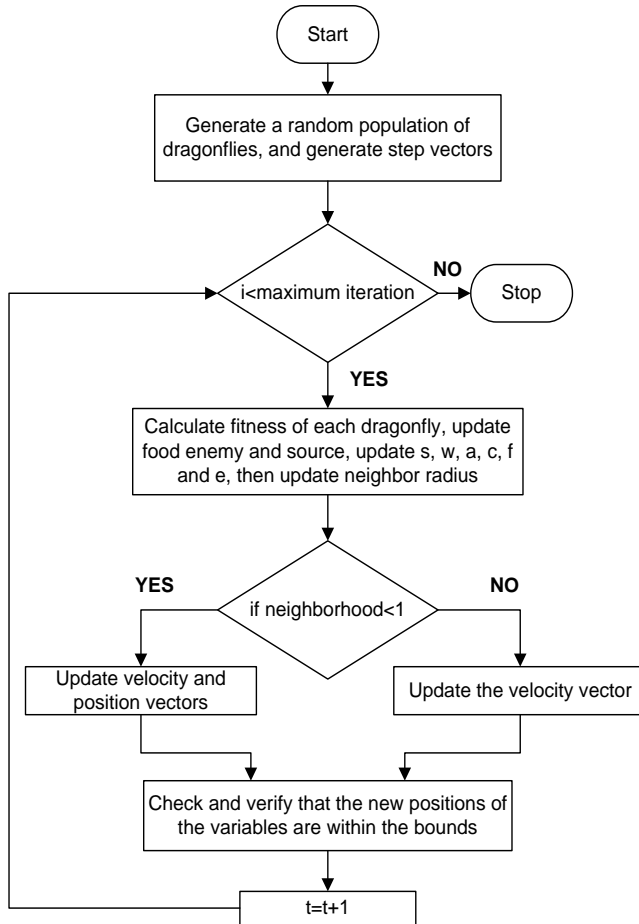


Figure 3. Behavior descriptions of dragonfly insect swarms

The dragonfly algorithm opens up a wide range of applications in optimization problems. Engineering fields such as power and energy systems, medical systems, and audio and video processing are among these applications. There are also single-objective problems, binary dragonfly algorithm, multi-objective, and hybrid versions of the dragonfly algorithm (Alshinwan et al., 2021; Rahman et al., 2021).

Genetic Algorithm

Living things can make some changes in their bodies to adapt to their environment. These changes are called adaptations. Genetic algorithm has stages such as natural selection, crossover, and mutation that living things go through during the adaptation process. These processes are provided by changes in the genotypes and phenotypes of living things. The changes that living things experience are important in terms of adapting to environmental factors. Individuals who cannot adapt to environmental factors cannot transfer their genes to the next generations through natural selection. Thus, the best individuals emerge in animal herds (Katoch et al., 2021; Lambora et al., 2019; Sohail et al., 2021). A general structure for the genetic algorithm is given in Figure 4.

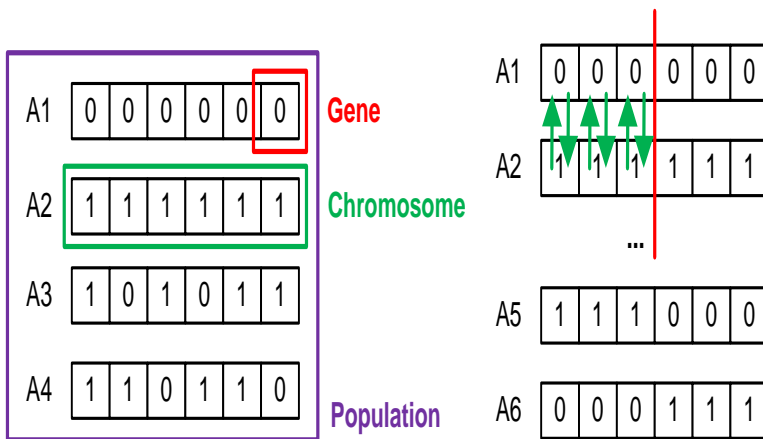


Figure 4. Genetic algorithm structure (Sohail A et. al., 2021)

In a genetic algorithm, living things live as a population. Chromosomes are in the cellular structure of these living things, and there are genes in these chromosomes. Here genes are encoded in chromosomes. This coding creates the genotypes and phenotypes of each individual. The genetic algorithm, like other metaheuristic algorithms has a flow diagram. The flow diagram of the genetic algorithm is given in Figure 5.

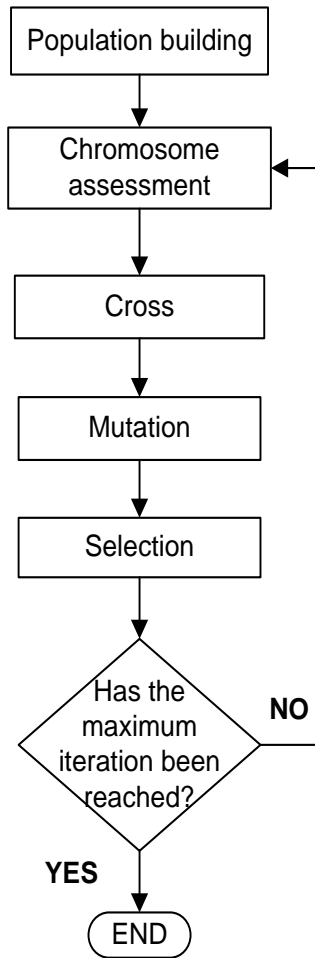


Figure 5. Genetic algorithm flow diagram

It means the creation of genes in the chromosomes in the population creation part of the flow diagram of the genetic algorithm. Genes are created using binary values, consisting of 0 and 1. These genes are placed in the chromosomes so that the population is obtained, each of which gives an individual.

In the chromosome evaluation in the flow chart, the suitability of the generated chromosomes to the desired conditions is

tested. Then the crossover process is started. In the crossover process, the genes of two different chromosomes are mixed, and new chromosomes are obtained without losing their properties completely. This crossover process can be performed as a single-point and multi-point (Karaköse, 2022). In the mutation stage, some genes in the chromosomes undergo mutation. The mutation can be carried out at a certain rate. This ratio is in the range of 0-1.

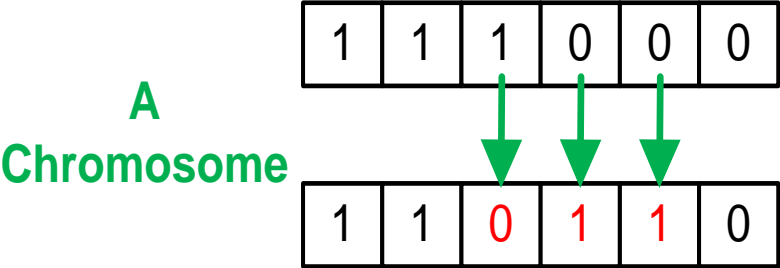


Figure 6. Mutation in genetic algorithm

Selection is performed in the last step before testing maximum number of iterations. At this stage, people to be matched are selected using methods such as the roulette wheel and the tournament method, as in Figure 7.

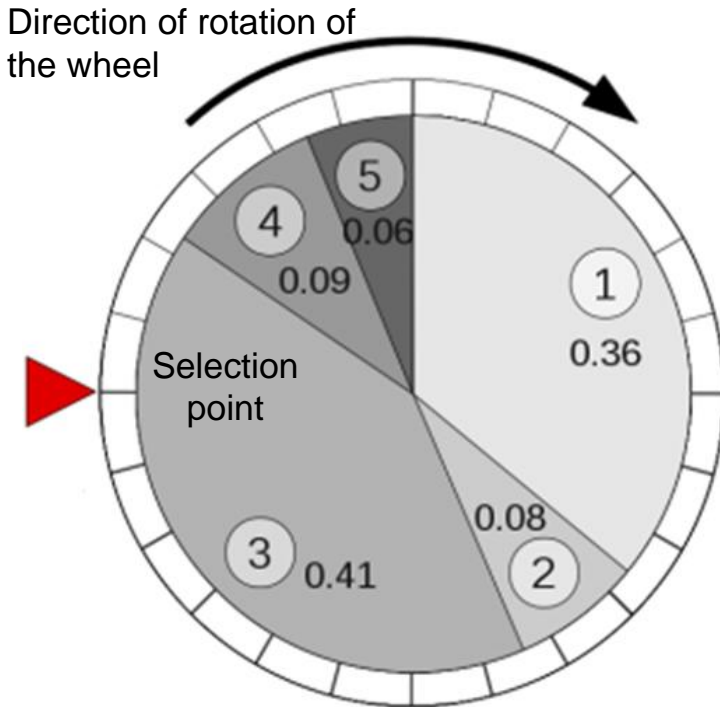


Figure 7. Roulette wheel in genetic algorithm (Stankiewicz et al., 2011)

Butterfly-Based Particle Swarm Optimization (BBPSO)

Particle swarm optimization, which is the basis of metaheuristic algorithms used today and is frequently used with other algorithms, is developed and used on a butterfly basis. PSO consists of certain stages. The flow diagram of the PSO is given in Figure 8.

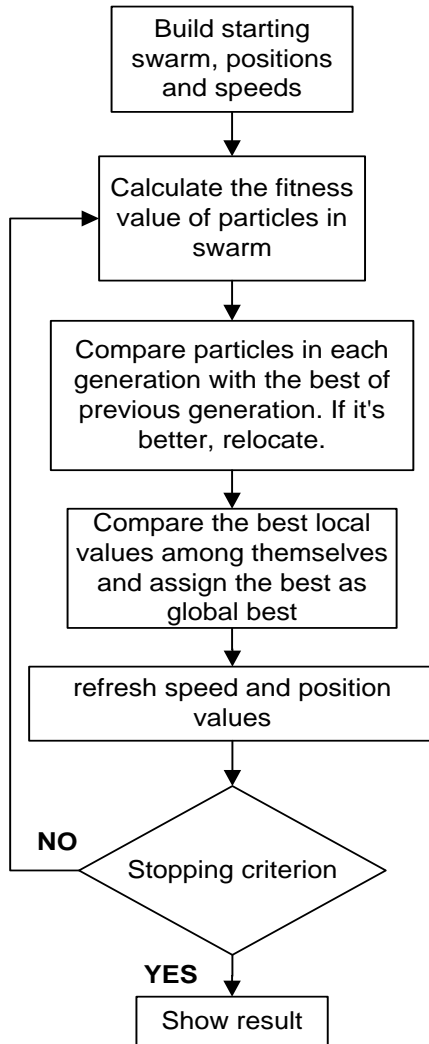


Figure 8. Particle swarm optimization flow chart (Özsağlam et al., 2008)

PSO phases begin by randomly placing each particle in the swarm. An objective function is then calculated for each part, comparing whether the calculated objective value is lower than the particle's personal best. If it is not lower, no action is taken, if lower,

personal best position value is assigned as current position of the particle with the lowest objective value. After these actions, personal best position is updated by overwriting the global best position. Next; the velocity of each particle is calculated, and position of each particle is updated using the calculated velocity. Finally, it is questioned whether the obtained values are sufficient to stop the loop. Particle swarm optimization is written as a function in Matlab/Simulink. While writing the function, the lower bound-upper bound for the particles, the cognitive and social coefficients, the number of particles and swarm size, and finally the inertia coefficient is determined. The mathematical expressions of the PSO for velocity and position are equations.

$$\begin{aligned}
 v_{k+1} = & w * v_k + c_1 r_1 (pbest_k \\
 & - currentposition) \\
 & + c_2 r_2 (gbest_k \\
 & - currentposition)
 \end{aligned} \tag{4}$$

$$x_{(k+1)} = x_k + V_{k+1} \tag{5}$$

In equation 2, the coefficient of inertia w is two random numbers between r_1 and r_2 (0, 1). c_1 and c_2 are cognitive and social scaling parameters. However, to achieve butterfly-based particle swarm optimization, it is necessary to place butterfly optimization equations in particle swarm optimization loop. The velocity equation of particle swarm optimization is rewritten according to butterfly optimization. Velocity equation for butterfly-based particle swarm optimization is given in Eq. 6.

$$\begin{aligned}
v_{k+1} = w * v_k + S_k(1 - P_k)c_1r_1(pb_{best_k} \\
- currentposition) \\
+ p_kc_2r_2(gbest_k \\
- currentposition)
\end{aligned} \tag{6}$$

In equation 6, S_k stands for sensitivity and P_k stands for probability. The equations of S_k and P_k are given in equations (Bohre A K et. al., 2015).

$$s_k = exp - (Iter_{max} - Iter_k)/Iter_{max} \tag{7}$$

$$P_k = FIT_{gbest,k}/-(FIT_{lbest,k}) \tag{8}$$

Cuckoo Algorithm

The cuckoo algorithm is based on the swarm behavior of cuckoos. While the cuckoo lives in nature unlike other birds, it does not build a nest itself. It uses nests made by other birds. If the bird, the original owner of the nest, recognizes the eggs laid by the cuckoo, it either discards them or leaves nest and builds the new nest. In this respect, it is defined as a brood parasite in the literature (Rajabioun, 2011; Al-Abaji et al., 2020; Mareli et al., 2018; Joshi et al., 2018). The flowchart of the cuckoo algorithm is given in Figure 9.

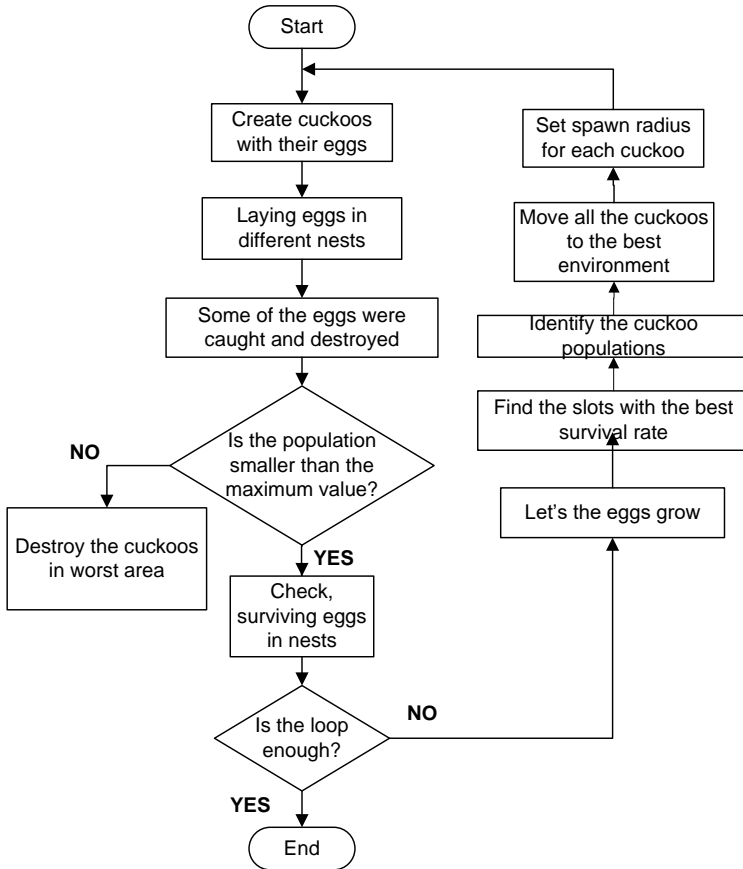


Figure 9. Cuckoo algorithm flowchart (Shadkam E et. al., 2018).

To create the cuckoo algorithm, whose flow diagram is given in Figure 8, a cuckoo habitat is created in the virtual environment. The equation of the habitat created in Eq. 9 is given.

$$Habitat = [X_1 \ X_2 \ X_3 \ \dots \ \dots \ X_{Nvar}] \quad (9)$$

The created habitat consists of a 1*Nvar-sized array. The profit function of the suitability of this habitat is evaluated in Eq. 10.

$$profit = f_b(habitat) = f_b(X_1 X_2 X_3 \dots \dots X_{Nvar}) \quad (10)$$

To start the cycle of cuckoos in the virtual environment, the first habitat matrix of size $N_{pop} * N_{var}$ is introduced to the system. For the first cuckoo habitat here, eggs are randomly produced. Cuckoos have a spawning radius in their environment. The mathematical expression of the spawning radius is given in Eq. 11.

$$\frac{\text{Number of cuckoo eggs available}}{\text{Total number of eggs}} * (var_{hi} - var_{lo}) \quad (11)$$

var_{hi} and var_{lo} in Eq. 11 are the lower and upper bounds for the variables, respectively.

Control Methods

PID Controller

PID controller can be expressed as proportional integral derivative controller. The PID controller, which is still used in today's systems, is a very old control method. In Figure 10, the drawing of the PID controller in a feedback system is given.

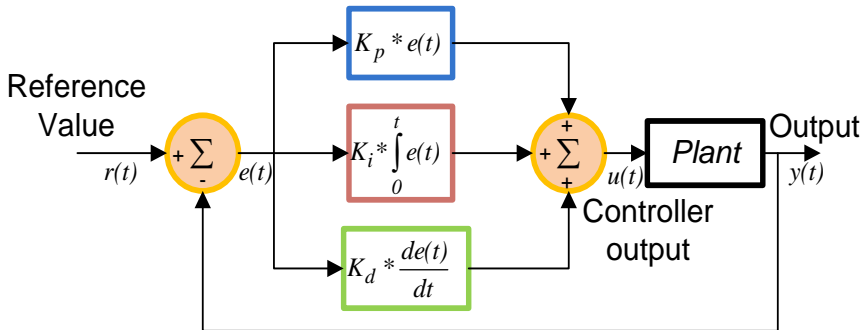


Figure 10. PID controller-feedback system (Borase et al., 2018; Wang, 2018).

If we want to find the controller coefficients Kp , Ki and Kd of PID controller for the control of any system, there are different methods. These can be trial and error method, Nichols-Ziegler, relay tuning method and Cohen-Coon method (Borase et al., 2021). In Equation 12, the general mathematical equation of the PID controller is given.

$$PID(t) = Kp * e(t) + Ki * \int_0^t e(t) + Kd * d \frac{e(t)}{dt} \quad (12)$$

The coefficients of the PID controller can be found by these methods as well as by metaheuristic methods (Joseph et al., 2022)

I-PD Controller

The I-PD controller is a modified version of PID controller. This controller also has a design difference. Figure 11 shows the Matlab/Simulink drawing of the I-PD controller.

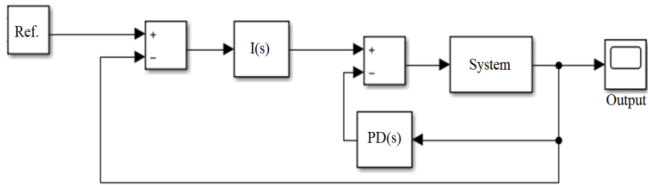


Figure 11. I-PD controller simulink model (Sain D 2016)

Unlike PID controller, I-PD controller is written using a different mathematical equation in the feedback function. The feedback function of the I-PD controller is given in equation. 13 (Saha et al., 2016)

$$1 + G_p(s)(G_I(s) - G_{PD}(s)) = 0 \quad (13)$$

Fuzzy Logic Based I-PD Controller

Fuzzy logic control is a control method with a long history. With this control method, systems that are difficult to control are controlled. Today, it has a structure that includes membership functions based on fuzzy logic control method, which has types such as Mamdani, Takagi-Sugeno, and singleton type. A Mamdani-based the fuzzy logic controller created for the twin engine multi input multi output systems in the Matlab program is given in Figure 12 (Nguyen et al., 2019).

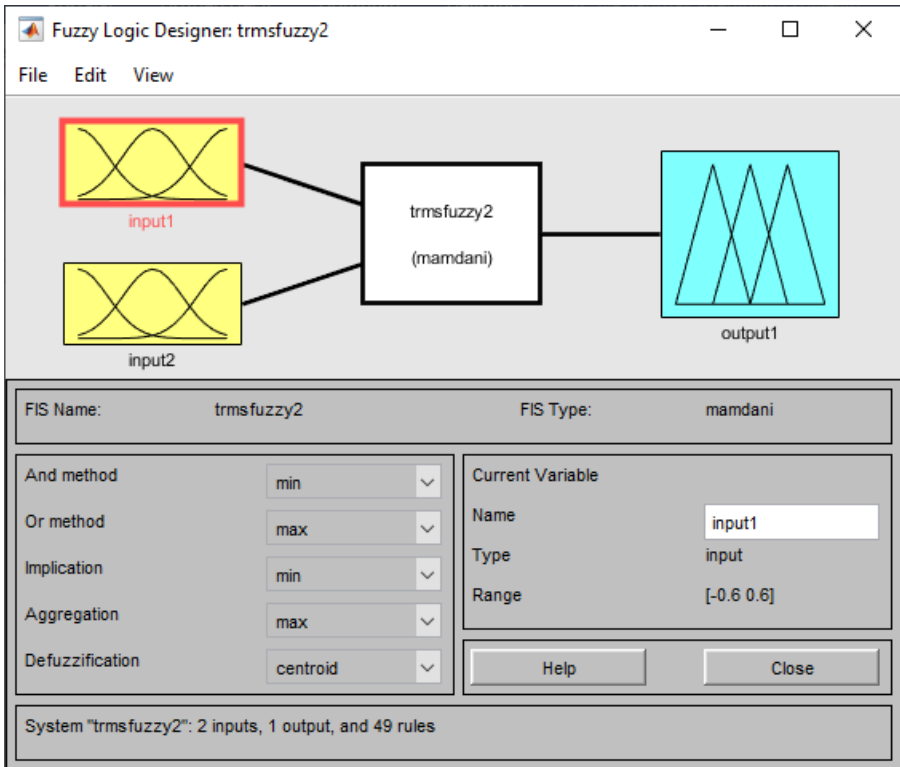


Figure 12. Fuzzy logic structure of the twin engine multi input multi output system

In fuzzy logic system structure given in Figure 11, there are 2 inputs and 1 output to control the system, including the

instantaneous error of the system and the derivative of the error, for the twin engine multi input multi output systems. The rule base was created to control the fuzzy logic system for the generated inputs and outputs. 49 rules were written in this rule base. The rule base is given in Table 1 (Hashim et al., 2015).

Table 1. The rule base of fuzzy logic controller

$\Delta e/e$	NL	NM	NS	Z	PS	PM	PL
NL	NVL	NVL	NL	NM	NS	NS	Z
N	NVL	NL	NM	NM	NS	Z	PS
NS	NL	NM	NS	NS	Z	PS	PM
Z	NM	NS	NS	Z	PS	PS	PM
PS	NM	NS	Z	PS	PS	PM	PL
P	NS	Z	PS	PM	PM	PL	PVL
PL	Z	PS	PS	PM	PL	PVL	PVL

In membership functions, the type of membership functions is chosen as trimf. While the input membership function ranges were chosen as [-0.6 0.6], the output membership function ranges were determined as [-0.2 0.2]. While creating the rule table, optimum results were tried to be obtained by connecting the membership functions with each other and with logic expressions.

A drawing with 2 inputs and 1 output was created in Matlab/Simulink within the framework of the membership function and rules were created for fuzzy logic (Housny et al., 2015). The Matlab/Simulink block design of the fuzzy logic based I-PD controller is given in Figure 13.

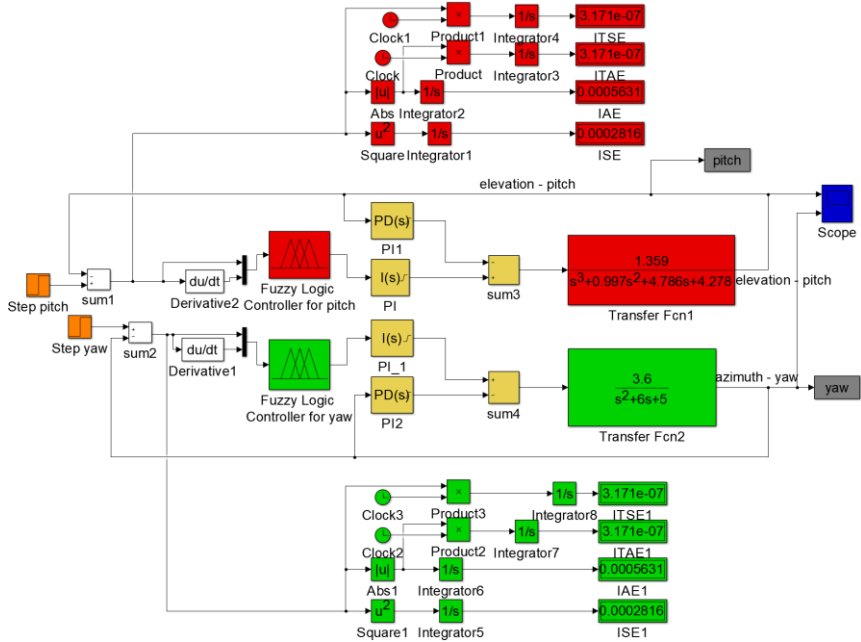


Figure 13. Fuzzy logic based I-PD controller Matlab/Simulink design

Cost Function

In metaheuristic optimization methods, objective functions are the functions used to minimize the error. Objective functions are divided into two as unit-model and multi-model (Zhan et al., 2009). The mathematical expression of the unimodal cost function used in this study is given in Eq. 14.

$$\begin{aligned}
 & \text{cost}_{function}(t) \\
 = & \frac{\sum_0^t (\theta_{pitch}(t) * (\theta_{pitch_{error}}(t)^2) + \theta_{yaw}(t) * (\theta_{yaw_{error}}(t)^2))}{(\theta_{pitch}(t) + \theta_{yaw}(t))} \quad (14)
 \end{aligned}$$

Cost functions that are allow the metaheuristic optimization method to minimize the error. It is one of the factors affecting the

success of metaheuristic optimization. The more the cost function used in metaheuristic optimization minimizes the error, the easier it is to reach the reference value.

Finding Coefficients of Different Controllers

In this section, the coefficients determined for four different algorithms and controllers are given in detail in Table 2.

Table 2. Coefficients produced by different controllers

Algorithms	Controller	Angle	Kp	Ki	Kd
Cuckoo	PID	Pitch	5.7219	33.0657	32.9486
Cuckoo	PID	Yaw	7.4627	18.4596	9.6691
Genetic	PID	Pitch	0.1687	0.70026	0.24
Genetic	PID	Yaw	2.0104	3.5137	2.6699
BBPSO	PID	Pitch	0.1074	2.123	0.44955
BBPSO	PID	Yaw	2.2159	2.3052	1.4698
Dragonfly	PID	Pitch	0.12789	1.701	0.45839
Dragonfly	PID	Yaw	3.8191	5.9085	4.0016
Cuckoo	I-PD	Pitch	6.62	1.3048	15.3869
Cuckoo	I-PD	Yaw	7.7689	10.03	13.7494
Genetic	I-PD	Pitch	0.6748	0.7756	1.8148
Genetic	I-PD	Yaw	2.3244	2.3158	1.5706
BBPSO	I-PD	Pitch	4.5546	4.7176	12.1918
BBPSO	I-PD	Yaw	8.1896	3.6244	1.3599
Dragonfly	I-PD	Pitch	2.4765	0.7334	4.3108
Dragonfly	I-PD	Yaw	4.4226	2.8617	1.3348
Cuckoo	Fuzzy Logic I-PD	Pitch	4.4331	7.06	9.19
Cuckoo	Fuzzy Logic I-PD	Yaw	6.79	52.9513	9.07
Genetic	Fuzzy Logic I-PD	Pitch	0.25907	3.9453	0.19077
Genetic	Fuzzy Logic I-PD	Yaw	0.4892	1.4721	3.3039
BBPSO	Fuzzy Logic I-PD	Pitch	1.8057	6.8036	20.9692
BBPSO	Fuzzy Logic I-PD	Yaw	2.6413	3.6141	6.632
Dragonfly	Fuzzy Logic I-PD	Pitch	1.6143	5.8473	4.7666
Dragonfly	Fuzzy Logic I-PD	Yaw	4.2126	9.512	7.8185

RESULTS

IAE, ISE, ITAE and ITSE Error Analysis

Specific tests are carried out to examine the fault performance of TRMS. These tests are integral absolute error (IAE), integral squared error (ISE), integral time absolute error (ITAE), and integral time squared error (ITSE). Mathematical expressions of error performance criteria are given as equations (Yusoff W A W et. al., 2009; Faisal R F et. al., 2009).

$$ISE = \int_0^{\infty} e^2(t)dt \quad (15)$$

$$ITSE = \int_0^{\infty} e^2(t)t dt \quad (16)$$

$$IAE = \int_0^{\infty} |e(t)|dt \quad (17)$$

$$ITAE = \int_0^{\infty} t|e(t)|dt \quad (18)$$

The error performances of dragonfly, genetic, butterfly-based particle swarm, and cuckoo algorithms, whose drawings are given in Matlab/Simulink in Figure 12, are given in detail in Table 3.

Table 3. Controller error performance analysis of different algorithms

Algorithms	Controller	Angle	ISE	IAE	ITAE	ITSE
Cuckoo	PID	Pitch	0.3868	2.087	14.52	0.03
Cuckoo	PID	Yaw	0.0099	0.1452	0.2857	0.0106
Genetic	PID	Pitch	0.6646	2.361	11.62	8.127
Genetic	PID	Yaw	0.048	0.3961	0.8569	0.045
BBPSO	PID	Pitch	0.3162	1.089	3.678	0.3296
BBPSO	PID	Yaw	0.0664	0.3798	0.4838	0.1096
Dragonfly	PID	Pitch	0.3551	1.265	5.548	0.7391
Dragonfly	PID	Yaw	0.0244	0.2382	0.426	0.0374
Cuckoo	I-PD	Pitch	1.179	3.746	20.81	20.81
Cuckoo	I-PD	Yaw	0.3256	1.444	7.73	3.943
Genetic	I-PD	Pitch	0.7959	2.47	8.872	8.702
Genetic	I-PD	Yaw	0.3152	0.9462	1.368	0.5866
BBPSO	I-PD	Pitch	0.4652	1.663	6.139	0.5413
BBPSO	I-PD	Yaw	0.3712	1.321	3.075	3.075
Dragonfly	I-PD	Pitch	1.135	3.833	24.02	24.02
Dragonfly	I-PD	Yaw	0.3213	1.015	1.538	1.538
Cuckoo	Fuzzy Logic I-PD	Pitch	0.9092	2.883	13.86	8.696
Cuckoo	Fuzzy Logic I-PD	Yaw	0.2877	0.9534	3.763	1.806
Genetic	Fuzzy Logic I-PD	Pitch	1.698	5.631	49.74	49.58
Genetic	Fuzzy Logic I-PD	Yaw	0.4634	1.49	5.445	0.0912
BBPSO	Fuzzy Logic I-PD	Pitch	1.048	3.469	23.08	2.1
BBPSO	Fuzzy Logic I-PD	Yaw	0.977	2.999	14.2	9.106
Dragonfly	Fuzzy Logic I-PD	Pitch	0.7667	2.373	10.01	4.034
Dragonfly	Fuzzy Logic I-PD	Yaw	0.6198	1.903	7.102	1.409

Performance Analysis of Controllers

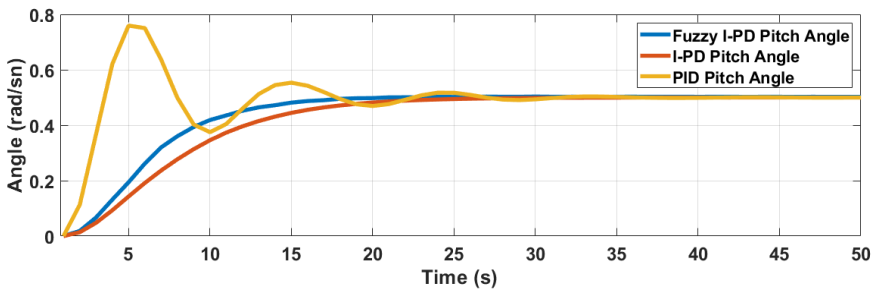
The performances of the controller and metaheuristic algorithms used are related to the rise time, settling time and overshoot they perform in reaching the reference value. These times are compared with different controllers and different algorithms one by one and detailed in Table 4.

Table 4. Controller performance analysis of different algorithm

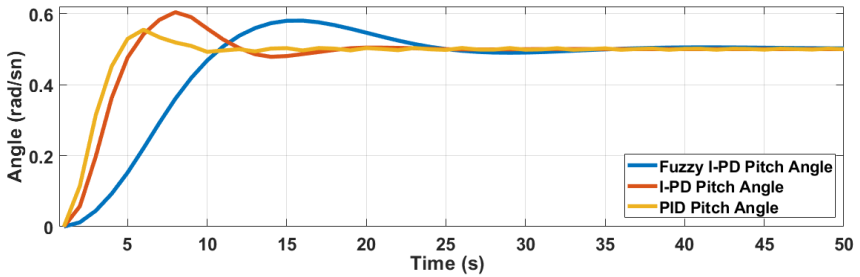
Algorithms	Controller	Angle	Rise Time	Settling Time	Overshoot(%)
Cuckoo	PID	Pitch	1.8835	25.9001	51.8677
Cuckoo	PID	Yaw	0.8796	4.8275	4.4207
Genetic	PID	Pitch	8.5908	24.0852	0.6116
Genetic	PID	Yaw	1.7173	6.7128	8.1873
BBPSO	PID	Pitch	2.5453	8.9956	11.1375
BBPSO	PID	Yaw	1.8614	6.4670	3.0692
Dragonfly	PID	Pitch	3.2136	18.0164	7.1740
Dragonfly	PID	Yaw	1.2283	5.7297	5.4784
Cuckoo	I-PD	Pitch	12.4506	22.5368	0
Cuckoo	I-PD	Yaw	3.1560	21.4948	0
Genetic	I-PD	Pitch	7.9296	14.6272	0.12
Genetic	I-PD	Yaw	2.5253	7.8613	5.6477
BBPSO	I-PD	Pitch	2.8971	16.6892	20.7852
BBPSO	I-PD	Yaw	5.2816	10.3811	0
Dragonfly	I-PD	Pitch	13.8852	25.9156	0.0012
Dragonfly	I-PD	Yaw	3.5314	6.9715	0
Cuckoo	Fuzzy Logic I-PD	Pitch	9.3478	17.4099	0.1867
Cuckoo	Fuzzy Logic I-PD	Yaw	2.8534	5.5716	0.1543
Genetic	Fuzzy Logic I-PD	Pitch	20.9584	36.8308	0
Genetic	Fuzzy Logic I-PD	Yaw	4.5536	9.2596	0.0717

BBPSO	Fuzzy Logic I-PD	Pitch	6.5560	31.1422	15.5935
BBPSO	Fuzzy Logic I-PD	Yaw	9.2021	16.4757	0.1808
Dragonfly	Fuzzy Logic I-PD	Pitch	7.1208	13.1491	0.4509
Dragonfly	Fuzzy Logic I-PD	Yaw	5.4283	9.7816	0.5316

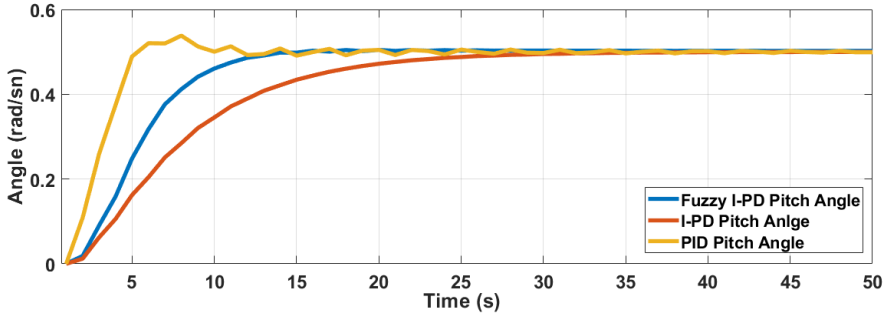
Pitch angle responses for Fuzzy I-PD, I-PD and PID controllers are given for different types of metaheuristic algorithms in Figure 14.



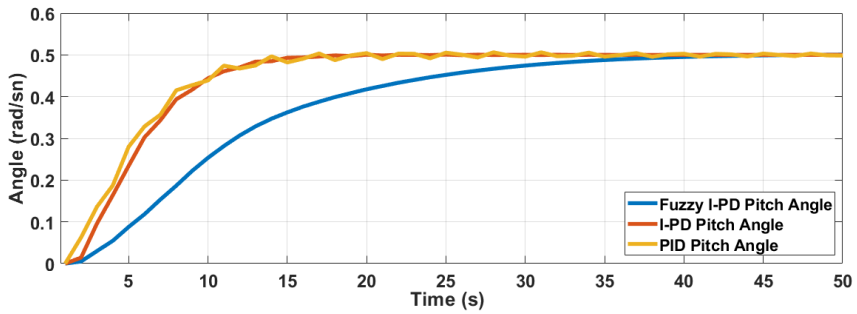
a)



b)



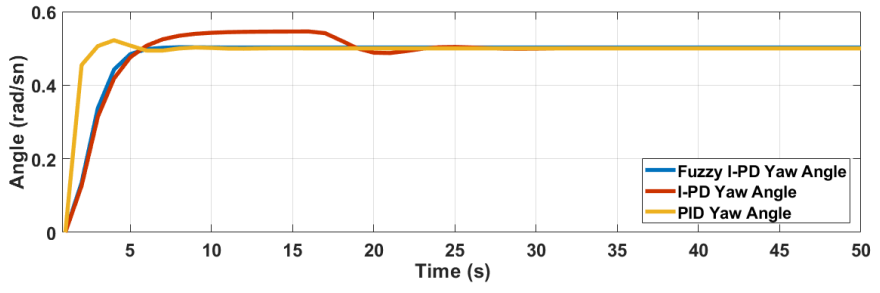
c)



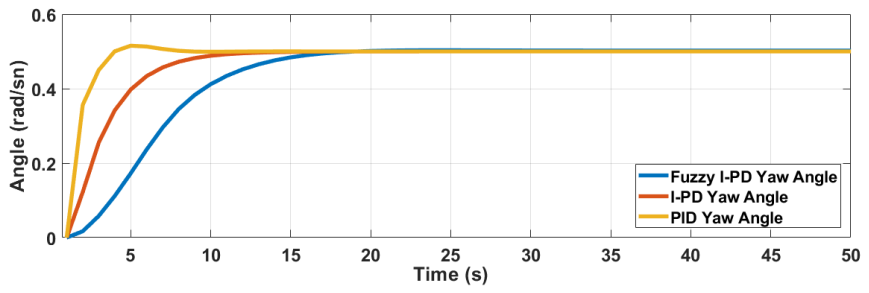
d)

Figure 14. Pitch angle controller algorithms; (a) Cuckoo algorithm; (b) BBPSO algorithm; (c) Dragonfly algorithm; (d) Genetic algorithm

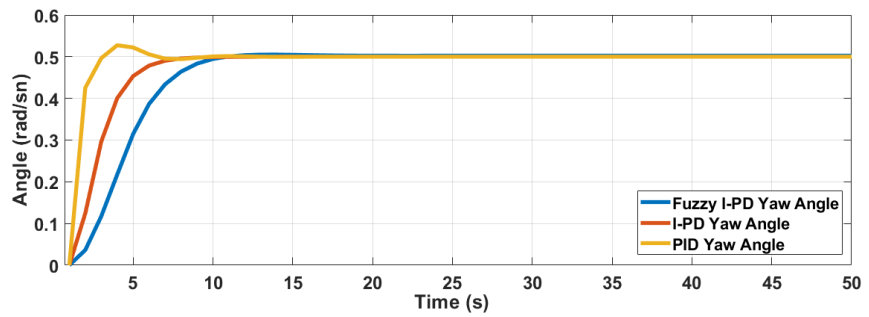
Yaw angle responses for Fuzzy I-PD, I-PD and PID controllers are given for different types of metaheuristic algorithms in Figure 15.



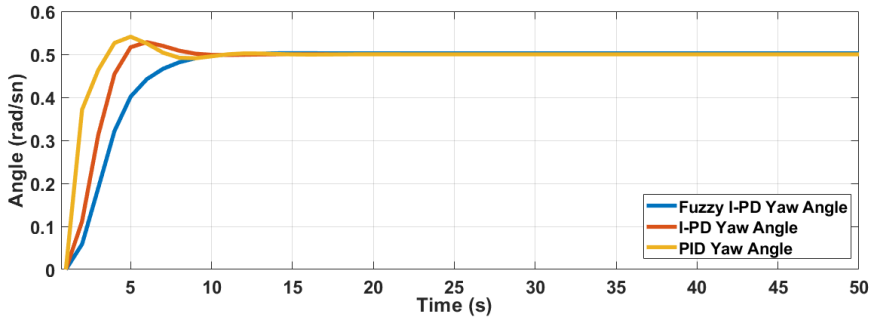
a)



b)



c)



d)

Figure 15. Yaw angle controller algorithms; (a) Cuckoo algorithm; (b) BBPSO algorithm; (c) Dragonfly algorithm; (d) Genetic algorithm

CONCLUSION

In this study, the performances of yaw and pitch angles are the most important outputs of the system. According to this, in Figure 14a, Fuzzy I-PD controller has a smoother output response than I-PD and PID controllers. It also gave a faster output response compared to the I-PD controller. But, fast response and high overshoot are achieved in the PID controller. In In In Figure 14b, although the Fuzzy I-PD controller exceeded the reference value, the chattering did not occur as in the PID controller. In an overall comparison, the Fuzzy I-PD controller gave a better output response. In Figure 14c, the PID controller performs a lot of overshoot and chattering, while the best output response is achieved with the Fuzzy I-PD controller. According to Figure 14d, while the PID controller performs too much overshoot and chattering, the best output response is obtained with I-PD controller. Here, Fuzzy Logic I-PD controller has the slower output response than the I-PD controller.

When yaw angles are analyzed, it is seen in Figure 15a that PID controller and I-PD controllers overshoot, while Fuzzy Logic I-PD controller gives a smooth and no overshoot output response. In Figure 15b, it is seen that the PID controller overshoots with a fast

response, I-PD controller and Fuzzy Logic I-PD controller responds without overshoot and I-PD controller is faster than Fuzzy Logic I-PD controller. In Figure 15c, it is seen that PID controller overshoots by responding quickly, the I-PD and Fuzzy I-PD controllers respond without overshoot, and I-PD controller is faster than Fuzzy Logic I-PD controller. In Figure 15d, it is seen that PID and I-PD controllers respond quickly, and Fuzzy Logic I-PD controller does not cause overshoot and chattering. PID, I-PD and Fuzzy Logic I-PD controller methods; compared with different types of algorithms, when settling time, overshoot, and chattering criteria are evaluated, it has been seen that Fuzzy Logic I-PD controller stands out more than other control methods and is a more preferable method.

References

Abdel-Basset M Abdel-Fatah L and Sangaiah A K 2018 Chapter 10-metaheuristic algorithms: a comprehensive review. Computational intelligence for multimedia big data on the cloud with engineering applications.

Al-Abaji M A 2020 A literature review of cuckoo search algorithm. Journal of Education and Practice, 11(8): 1-8. <https://doi.org/10.7176/JEP/11-8-01>

Allouani F Boukhetala D and Boudjema F 2011 Ant colony optimization based fuzzy sliding mode controller for the twin rotor MIMO system. International Journal on Sciences and Techniques of Automatic Control and Computer Engineering, 5(2): 1604-1615.

Alshinwan M Abualigah L Shehab M Elaziz M A Khasawneh A M Alabool H and Hamad H A 2021 Dragonfly algorithm: a comprehensive survey of its results, variants, and applications. Multimedia Tools and Applications, 80: 14979-15016. <https://doi.org/10.1007/s11042-020-10255-3>

Azar A T Sayed A S Shahin A S Elkholy H A and Ammar H 2020 PID controller for 2-DOFs twin rotor MIMO system tuned with particle swarm optimization. In Proceedings of the International Conference on Advanced Intelligent Systems and Informatics 2019, 229-242. Springer International Publishing. https://doi.org/10.1007/978-3-030-31129-2_22

Bohre A K Agnihotri G and Dubey M 2015 The butterfly-particle swarm optimization (Butterfly-PSO/BF-PSO) technique and its variables. International Journal of Soft Computing, Mathematics and Control (IJSCMC), 4(3). <http://dx.doi.org/10.2139/ssrn.3529113>

Borase R P Maghade D K Sondkar S Y and Pawar S N 2021 A review of PID control, tuning methods and applications. International Journal of Dynamics and Control, 9: 818-827. <https://doi.org/10.1007/s40435-020-00665-4>

Castillo O Kutlu F and Atan Ö 2020 Intuitionistic fuzzy control of twin rotor multiple input multiple output systems. *Journal of Intelligent & Fuzzy Systems*, 38(1): 821-833. <https://doi.org/10.3233/JIFS-179451>

Chalupa P Příkryl J and Novák J 2015 Modelling of twin rotor MIMO system. *Procedia Engineering*, 100: 249-258. <https://doi.org/10.1016/j.proeng.2015.01.365>

Chaudhary S and Kumar A 2019 Control of twin rotor MIMO system using PID and LQR controller. *Journal of Aircraft and Spacecraft Technology*, 3(1): 211-220. <https://doi.org/10.3844/jastsp.2019.211.220>

Eröz E and Tanyildizi E 2019 Çok amaçlı metasezgisel optimizasyon algoritmalarının performans karşılaştırması. In 2019 International Artificial Intelligence and Data Processing Symposium (IDAP), 1-11. IEEE. <https://doi.org/10.1109/IDAP.2019.8875955>

Faisal R F and Abdulwahhab O W 2021 Design of an adaptive linear quadratic regulator for a twin rotor aerodynamic system. *Journal of Control, Automation and Electrical Systems*, 32(2): 404-415. <https://doi.org/10.1007/s40313-020-00682-w>

Hammouri A I Mafarja M Al-Betar M A Awadallah M A and Abu-Doush I 2020 An improved dragonfly algorithm for feature selection. *Knowledge-Based Systems*, 203: 106131. <https://doi.org/10.1016/j.knosys.2020.106131>

Hashim H A and Abido M A 2015 Fuzzy controller design using evolutionary techniques for twin rotor MIMO system: a comparative study. *Computational intelligence and neuroscience*, 49-49. <https://doi.org/10.1155/2015/704301>

Housny H and El Fadil H 2019 Fuzzy PID control tuning design using particle swarm optimization algorithm for a quadrotor. In 2019 5th International Conference on Optimization and

Applications (ICOA), 1-6. IEEE.
<https://doi.org/10.1109/ICOA.2019.8727702>

Huu T D and Ismail I B 2016 Modelling of twin rotor MIMO system. In 2016 2nd IEEE International Symposium on Robotics and Manufacturing Automation (ROMA), 1-6. IEEE. <https://doi.org/10.1109/ROMA.2016.7847803>

Jain A Sheel S and Kuchhal P 2018 Fuzzy logic-based real-time control for a twin-rotor MIMO system using GA-based optimization. *World Journal of Engineering*, 15(2): 192-204. <https://doi.org/10.1108/WJE-03-2017-0075>

Joseph S B Dada E G Abidemi A Oyewola D O and Khammas B M 2022 Metaheuristic algorithms for PID controller parameters tuning: Review, approaches and open problems. *Heliyon*, e09399. <https://doi.org/10.1016/j.heliyon.2022.e09399>

Joshi A S Kulkarni O Kakandikar G M and Nandedkar V M 2017 Cuckoo search optimization-a review. *Materials Today: Proceedings*, 4(8): 7262-7269. <https://doi.org/10.1016/j.matpr.2017.07.055>

Karaköse E 2022 A Genetic Algorithm Based Approach for Mission Sharing of Swarm Unmanned Aerial Vehicles. *Firat University Journal of Engineering Sciences*, 34(1): 351-360. <https://doi.org/10.35234/fumbd.1026653>

Katoch S Chauhan S S and Kumar V 2021 A review on genetic algorithm: past, present, and future. *Multimedia Tools and Applications*, 80: 8091-8126. <https://doi.org/10.1007/s11042-020-10139-6>

Khalaf O I Abdulsahib G M and Sabbar B M 2020 Optimization of wireless sensor network coverage using the Bee Algorithm. *J. Inf. Sci. Eng.*, 36(2): 377-386. [https://doi.org/10.6688/JISE.202003_36\(2\).0015](https://doi.org/10.6688/JISE.202003_36(2).0015)

Kumar R 2021 Control of dynamical aerial system by grey wolf optimization tuned TID and I-TD controllers. Available at SSRN 3880114. <https://doi.org/10.30780/specialissue-ICAASET021/004>

Lambora A Gupta K and Chopra K 2019 Genetic algorithm-A literature review. In 2019 international conference on machine learning, big data, cloud and parallel computing (COMITCon), 380-384. IEEE. <https://doi.org/10.1109/COMITCon.2019.8862255>

Mareli M and Twala B 2018 An adaptive Cuckoo search algorithm for optimisation. Applied computing and informatics, 14(2): 107-115. <https://doi.org/10.1016/j.aci.2017.09.001>

Meraihi Y Ramdane-Cherif A Acheli D and Mahseur M 2020 Dragonfly algorithm: a comprehensive review and applications. Neural Computing and Applications, 32(21): 16625-16646. <https://doi.org/10.1007/s00521-020-04866-y>

Mihaly V Şuşcă M and Dulf E H 2021 μ -Synthesis FO-PID for Twin Rotor Aerodynamic System. Mathematics, 9(19): 2504. <https://doi.org/10.3390/math9192504>

Mirjalili S 2016 Dragonfly algorithm: a new meta-heuristic optimization technique for solving single-objective, discrete, and multi-objective problems. Neural computing and applications, 27: 1053-1073. <https://doi.org/10.1007/s00521-015-1920-1>

Nguyen A T Taniguchi T Eciolaza L Campos V Palhares R and Sugeno M 2019 Fuzzy control systems: Past, present and future. IEEE Computational Intelligence Magazine, 14(1): 56-68. <https://doi.org/10.1109/MCI.2018.2881644>

Norsahperi N M H and Danapalasingam K A 2020 Particle swarm-based and neuro-based FOPID controllers for a Twin Rotor System with improved tracking performance and energy reduction. ISA transactions, 102: 230-244. <https://doi.org/10.1016/j.isatra.2020.03.001>

Özsağlam M Y and Çunkaş M 2008 Particle swarm optimization algorithm for solving optimization problems. Journal of Polytechnic, 11(4): 299-305.

Rahman C M Rashid T A Alsadoon A Bacanin N Fattah P and Mirjalili S 2021 A survey on dragonfly algorithm and its applications in engineering. Evolutionary Intelligence, 1-21. <https://doi.org/10.1007/s12065-021-00659-x>

Rajabi Moshtaghi H Toloie Eshlaghy A and Motadel M R 2021 A comprehensive review on meta-heuristic algorithms and their classification with novel approach. Journal of Applied Research on Industrial Engineering, 8(1): 63-89. <https://doi.org/10.22105/jarie.2021.238926.1180>

Rajabioun R 2011 Cuckoo optimization algorithm. Applied soft computing, 11(8): 5508-5518. <https://doi.org/10.1016/j.asoc.2011.05.008>

Rezoug A Achour Z and Hamerlain M 2014 Ant colony optimization of type-2 fuzzy helicopter controller. In 2014 IEEE International Conference on Robotics and Biomimetics (ROBIO 2014), 1548-1553. IEEE. <https://doi.org/10.1109/ROBIO.2014.7090554>

Saha A and Chakraborty S 2016 Genetic algorithm based I-PD controller design for Twin Rotor MIMO system. In 2016 2nd International Conference on Control, Instrumentation, Energy & Communication (CIEC), 15-19. IEEE. <https://doi.org/10.1109/CIEC.2016.7513826>

Sain D 2016 PID, I-PD and PD-PI controller design for the ball and beam system: A comparative study. Proceedings of International Science Press, 9: 9-14.

Shadkam E and Bijari M 2014 Evaluation the efficiency of cuckoo optimization algorithm. arXiv preprint arXiv:1405.2168. <https://doi.org/10.48550/arXiv.1405.2168>

Sohail A 2021 Genetic algorithms in the fields of artificial intelligence and data sciences. *Annals of Data Science*, 1-12. <https://doi.org/10.1007/s40745-021-00354-9>

Stankiewicz W Roszak R and Morzyński M 2011 Genetic algorithm-based calibration of reduced order Galerkin models. *Mathematical Modelling and Analysis*, 16(2): 233-247. <https://doi.org/10.3846/13926292.2011.579187>

Tiwalkar R G Vanamane S S Karvekar S S and Velhal S B 2017 Model predictive controller for position control of twin rotor MIMO system. In 2017 IEEE International Conference on Power, Control, Signals and Instrumentation Engineering (ICPCSI), 952-957. IEEE. <https://doi.org/10.1109/ICPCSI.2017.8391852>

Wang L 2020 Basics of PID Control.1: 1-30. <https://doi.org/10.1002/9781119469414.ch1>

Yusoff W A W Yahya N M and Senawi A 2006 Tuning of Optimum PID Controller Parameter Using Particle Swarm Optimization Algorithm Approach. *Fakulti Kejuruteraan Mekanikal Universiti Malaysia Pahang*.

Zeglache S Benyettou L Djerioui A and Ghellab M Z 2020 Twin rotor MIMO system experimental validation of robust adaptive fuzzy control against wind effects. *IEEE Systems Journal*. <https://doi.org/10.1109/JSYST.2020.3034993>

Zhan Z H Zhang J Li Y and Chung H S H 2009 Adaptive particle swarm optimization. *IEEE Transactions on Systems, Man, and Cybernetics, Part B (Cybernetics)*, 39(6): 1362-1381. <https://doi.org/10.1109/TSMCB.2009.2015956>

CHAPTER IX

Real-time Measurement of CO Gas Released During Laser Cutting of Wood using MQ-7 Sensor

Çağatay ERSİN¹
Mehmet GÜNEŞ²

Introduction

Wood is a natural, environmentally friendly, renewable, aesthetic, reusable, sustainable, waste-free, and, with all these, truly an engineering material. At the same time, wood is a material whose raw materials are easy to find, light, highly durable, and easy to shape by process (Çolak and Değirmentepe, 2020).

Wood has been an indispensable material for humanity since the past. From the first people making simple tools to today's modern

¹ Lecturer, Department of Electronics and Automation, Cankiri Karatekin University, cagatayersin@karatekin.edu.tr

² Dr. Lecturer, Desing Department, Cankiri Karatekin University, mehmetgunes@karatekin.edu.tr

architecture, wood has stood out with its sustainability, workability and aesthetic properties. Different methods and technologies have been developed for shaping and processing wood in today's industry. One of these technological methods is CO₂ laser cutting (Islam, 2023).

Laser cutting is the preferred method for achieving precise, fast, clean cuts. Especially in cases where complex patterns and detailed workmanship are required, laser cutting is much more advantageous than other traditional methods. However, in addition to these advantages, laser cutting also has some difficulties and risks. During this process, various gases are emitted from the wood due to high temperatures. One of these gases is carbon monoxide (CO) gas, which is formed especially during combustion (Munoz, 2023).

This method, which constitutes an important turning point in technology, is used in various methods and on different materials in all leading areas of the industry. These materials include wood, polymer, nickel alloys, steel, chrome alloys, titanium alloys, stainless steel, aluminum, and their alloys (Dorukan et al., 2014).

When wood material burns, two main polluting gases, CO and NO_x, and harmful substances such as benzene, aldehydes, respirable particulate matter, and other free radicals are released. The life-threatening conditions in fires mostly occur not from the touch of flames but from exposure to smoke, toxic gases or oxygen depletion (Yaşar and Atar, 2017).

Since their development, lasers have greatly impacted the advancement of today's technology by making our lives easier. The manufacturing industry has taken the largest share from laser technology and it has become a preferred technology in many manufacturing applications. Almost all types of materials can be processed with laser cutting and are widely used in the industry's marking, engraving, and cutting processes. With the laser method, brittle and soft material types that are not easy to cut can be processed quickly, with high precision, without contact (Köle, 2022).

Many different types of materials, small and large in thickness, can be cut close to the exact size using a laser. Thanks to the use of laser on computer-aided machines, hole drilling can be performed in cases where the dimensions and position accuracy on the part are important. In addition, the distances between holes can be adjusted accurately and precisely in multiple-hole drilling. Engraving and engraving techniques are also commonly used in laser manufacturing processes. In this way, a channel can be opened on the part or a partial material reduction can be made by creating a thin path (Köle, 2022).

While wooden materials are processed with a CO₂ laser cutting device, they release carbon monoxide (CO) gas into the environment. Intense and long-term exposure to this gas is very important for human health. This study measured the CO gas released from cutting 3 different wooden materials with a CO₂ laser machine. In the study, the amount of CO was measured with the MQ-7 carbon monoxide gas sensor connected to the suction line of the laser cutting machine and the Arduino Uno microcontroller development board. With the code written in C language on the microcontroller development card, 10-bit data was read instantly via the analog pin (A0). Instant data obtained with the MQ-7 carbon monoxide gas sensor was saved in real time to Excel via serial port with the Datastreamer plug-in.

Materials and Methods

It is important to know the machinability properties of any material so that it can be evaluated in the best way. Knowing its characteristic features is even more important when it comes to wood material. Because wood material has a more complex and anisotropic structure than other main engineering materials. The principle of laser cutting is based on increasing the burning effect of the force by collecting the light force applied to any object in a small area through stimulated radiation emission. In other words, a sharp blade in mechanical cutting represents a fully concentrated (diluted) laser beam in laser cutting. Likewise, like mechanical cutting, laser

cutting is based on the principle of destroying (burning) the structure between the fibers by weakening them. Laser cutting is more similar to saw cutting in mechanical cutting (Açık and Tutuş, 2023). Carbon monoxide (CO) gas, which is dangerous and highly toxic, is produced by burning wooden materials and is one of the most important causes of poisoning. It is very difficult to detect and perceive with human senses due to its odourless, colorless and tasteless properties (Kök, 2020). This study measured the carbon monoxide gas change resulting from burning 3 different wooden materials (MDF, Beech, Pine) with a CO₂ laser cutting machine.

Carbon Monoxide Gas and Limit Values

Carbon monoxide (CO) is a colorless, odorless, and tasteless gas. Because of these properties, it is difficult to detect by humans, making it particularly dangerous. CO prevents oxygen from binding to the blood in the human body. The haemoglobin molecule binds CO approximately 200 times faster than oxygen, which reduces the oxygen-carrying capacity of the blood (Smith and Ernst, 2011). As a result, when inhaled in high concentrations, CO can cause poisoning, leading to headaches, dizziness, weakness, nausea, vomiting, and even death (Raub oath Benignus, 2002).

CO is dangerous is that it binds haemoglobin in the blood much faster than oxygen. This reduces the oxygen-carrying capacity of the blood and may result in insufficient oxygen reaching the tissues. This can lead to headache, dizziness, weakness, shortness of breath, nausea, and even loss of consciousness. Prolonged exposure or exposure to high concentrations may cause permanent brain damage or death. It is vital to take the necessary precautions to prevent the CO concentration from exceeding these limit values, especially in closed areas. This is especially true for workshops, garages or industrial facilities where combustion devices or equipment are used (Khatak, 2022).

In 1971, the U.S. Environmental Protection Agency established the National Ambient Air Quality Standard for CO,

which established a time-weighted average exposure limit of 9 ppm for 8 hours and 35 ppm for 1 hour in outdoor environments. There are currently no regulations regarding indoor CO levels. However, some US agencies have established guidelines for upper exposure limits (Aiha, 2015). For example, the Occupational Safety and Health Administration recommends limiting CO exposure to 50 ppm for 8 hours; The National Institute for Occupational Safety and Health recommends a time-weighted limit of 35 ppm for 8 hours with an upper ceiling of 200 ppm, and the American Conference of Governmental Industrial Hygienists recommends limiting CO exposure to 25 ppm for 8 hours. (Levy, 2022). Conversely, exposure to an environment containing CO at concentrations exceeding 200 ppm readily produces overt symptoms of toxicity, and inhalation of > 800 ppm CO results in COHb levels exceeding 60% and can rapidly result in death. (Baker, 1988). CO concentration and the situations people encounter accordingly are given in Table 1.

Table 1. CO Concentration limit values (OSHA, 2019)

CO Concentration (ppm)	Situation	Explanation
0-9	Trustworthy	Generally considered safe for 8 hours of exposure.
10-24	Attention	Prolonged exposure may cause headaches and fatigue.
25-34	Dangerous	The maximum limit for 1 hour exposure. Dizziness, nausea, and other symptoms may occur.
35-49	Very dangerous	Even short-term exposure can cause health problems.
50-99	Critical	Serious health risk. Ventilation should be done immediately.
100 and above	Life Danger	Rapid loss of consciousness, risk of death. Immediate intervention is required.

CO gas is released during wood cutting with CO₂ laser cutting in wood workshops. This can pose a serious hazard, especially when working in confined and poorly ventilated areas. Therefore, continuous monitoring and control of CO gas concentration is critical for worker health and safety. Especially in wood workshops, measuring the CO gas released from CO₂ laser cutting is important to protect worker health and minimize potential risks (Hampson and Weaver, 2010).

Laser Cutting Machine

CO₂ lasers have become an extremely effective and popular tool for cutting wood. This technology is ideal for precise cuts and detailed workmanship requirements. However, research on the effects and consequences of this cutting method on wood helps us better understand the interaction of this technology with wood (Rezaei, 2022). High voltage electric current is passed through the CO₂ gas, thus obtaining a high-intensity light beam. This light beam occurs in the part called the resonator. This light beam is reflected on the cutting head via optical mirrors. To assist in cutting, high-pressure gas is sprayed according to the type of material being cut (Köle, 2022). The CO₂ laser cutting machine used in the study is shown in Figure 1.



Figure 1. CO₂ laser cutting device

Use of CO₂ Laser in Wood Cutting

CO₂ lasers are a technology in which high-energy beams are focused on the wood surface and these beams rapidly evaporate the wood and perform cutting. The use of CO₂ lasers in wood cutting brings many advantages:

Precision Cutting: CO₂ lasers can make cuts with precision well below a millimeter. This allows complex designs and details to be cut easily.

Non-contact Process: Laser cutting occurs without physical contact with the wood. This prevents the material from becoming displaced or damaged.

Low Heat Effect: CO₂ lasers vaporize wood, allowing even heat-sensitive materials to be cut without damage.

Flexibility: Lasers can work on different types and thicknesses of wood. This allows the user to use the same equipment for various projects.

Low Maintenance and Operating Cost: Laser cutting machines can operate for a long time with minimal maintenance requirements. It also produces less waste than traditional slaughtering methods.

However, cutting wood with a CO₂ laser also has some difficulties. For example, wood can have different densities and moisture levels because it is a natural material. This may change the effect of the laser on the wood. Additionally, smoke and gas emissions may occur from wood during laser cutting. These emissions can pose a potential hazard to worker health and safety.

Performing Carbon Monoxide Gas Measurement

In this study, the measurement of carbon monoxide gas resulting from the processing of wood material was carried out using a mechanism consisting of an Arduino Uno microcontroller development board and an MQ-7 carbon monoxide gas sensor. Since Arduino Uno analog pins are 10 bits, it is possible to read data up to a maximum of 1024. The analog pin of the MQ-7 carbon monoxide sensor was connected to the ADC (Analog Digital Converter) pin of the controller, and data was read every 1 second (1000 milliseconds) with the C code written to the controller. Before the cutting process started, the CO value in the environment was measured, and after the cutting process was completed, the measurement continued until the CO amount returned to this value.

Arduino Uno and MQ-7 Gas Sensor

Arduino Uno is an open-source microcontroller platform. This card, which has an Atmega328P microcontroller, is supported by a large community. Arduino Uno has digital and analogue input/output pins. These pins can easily interact with various sensors, LEDs, motor drivers and other components. The image of the Arduino Uno microcontroller development board used is given in Figure 2.

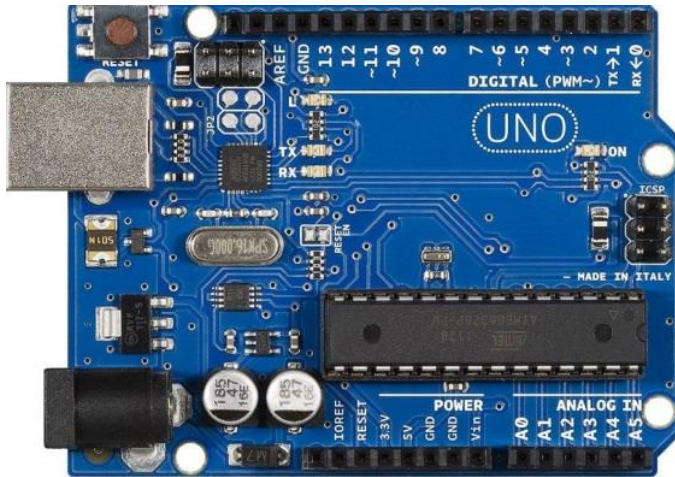


Figure 2. Arduino Uno microcontroller development board

MQ-7 used in the study is a gas sensor used to measure carbon monoxide gas. It works on the principle of an electrochemical reaction. The sensor can measure CO gas within a certain ppm range. One of the biggest advantages of the MQ-7 is its low cost and easy availability. This sensor works well with controllers. The image of the carbon monoxide gas sensor used for measurement in the study is given in Figure 3.



Figure 3. MQ-7 carbon monoxide gas sensor

By combining Arduino Uno and MQ-7 gas sensors, we can create an effective CO gas measurement system. First, the VCC and GND pins of the MQ-7 gas sensor are connected to the corresponding pins of the Arduino Uno. The sensor's analog output is connected to an analog input pin of the Arduino. The image of the device used in the study is given in Figure 4.

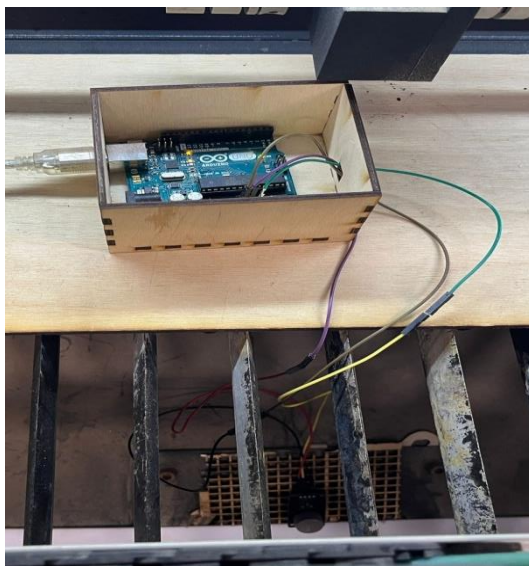


Figure 4. The experimental setup

Research Findings

MDF (fibreboard), beech, and pine trees were cut continuously for 3 minutes on a 150-watt CO₂ laser machine by entering the parameters at 15mm/min speed and 40%-Watt power. For the gas sensor to accurately measure the amount of CO in the environment, the environment was measured and calibrated for 48 hours before cutting in the workshop environment. Then, the MDF sheet was processed with the entered parameters and gas measurement was made. The appearance of MDF material during cutting is shown in Figure 5.



Figure 5. Processing of MDF plate with CO₂ laser cutting device

The carbon monoxide change of the processed MDF plate was measured with a device made with a controller, and instantaneous data was transferred to Excel with the Datastreamer plug-in. The graph of the data received in Excel is shown in Figure 6.

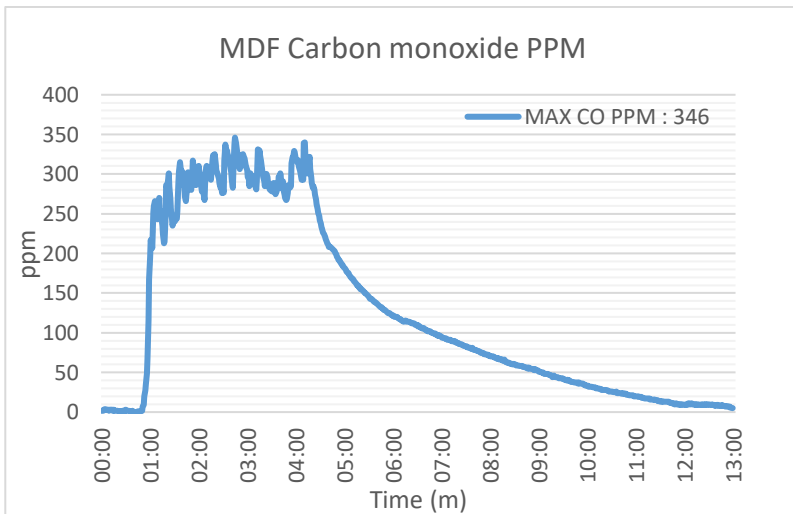


Figure 6. CO values resulting from the processing of MDF plate

Then, the beech wood material was cut with a laser machine under the same conditions and in the same environment. The image of the cut beech material is shown in Figure 7.

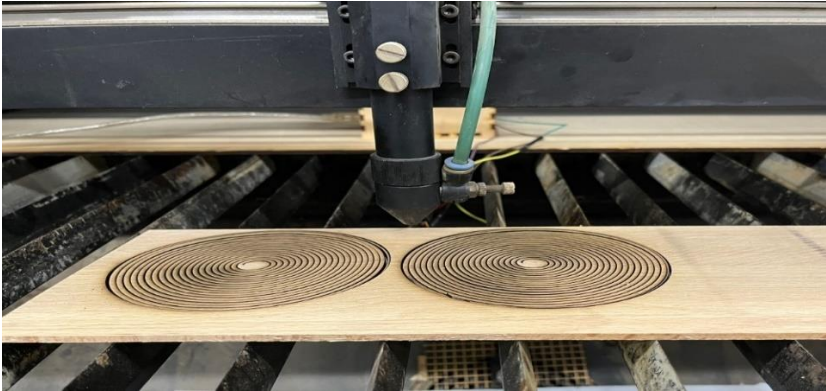


Figure 7. Processing of beech wood material with CO₂ laser cutting device

The CO data of the processed beech material converted into a graph in Excel is shown in Figure 8.

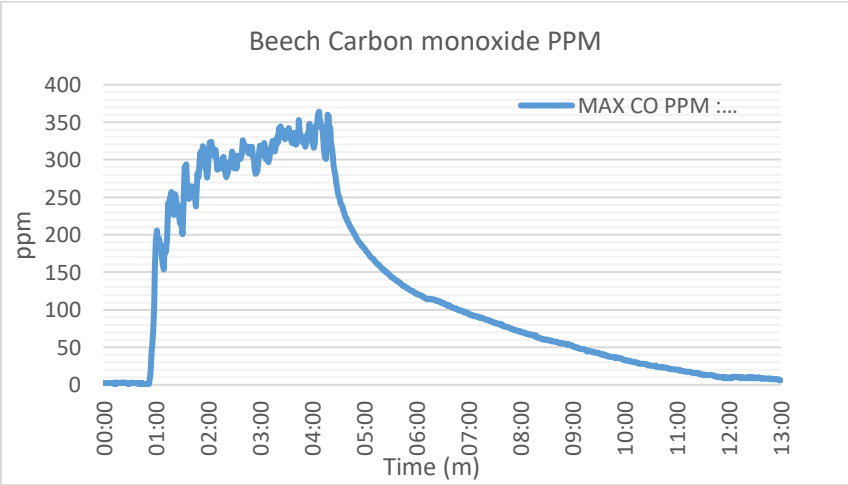


Figure 8. CO values resulting from the processing of beech material

Finally, the pine wood material was placed in the CO₂ laser-cutting device and processed with the same parameters. The appearance of the material during processing is given in Figure 9.

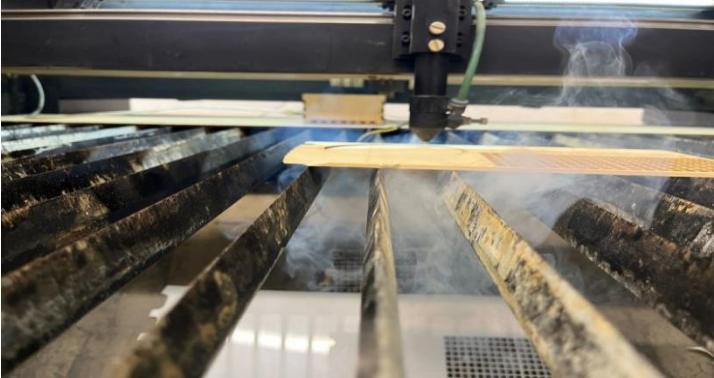


Figure 9. Processing of pine wood material with CO₂ laser cutting device

The CO values of the processed pine wood material are given graphically in Figure 10.

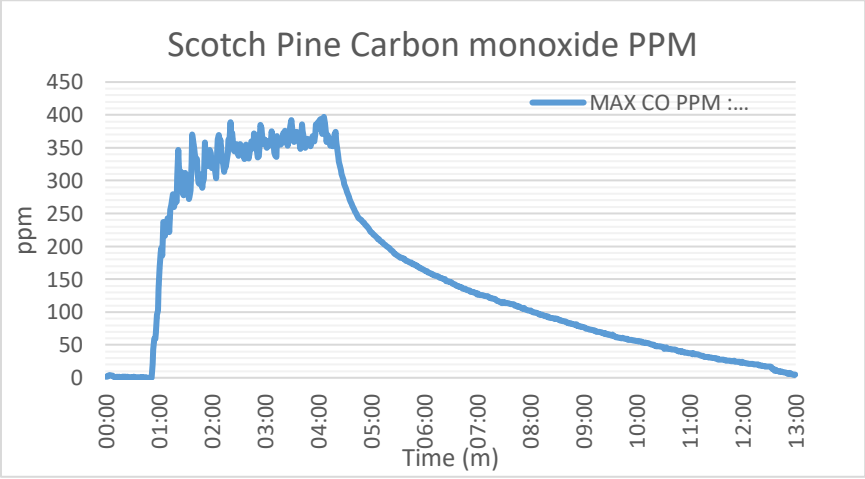


Figure 10. CO values resulting from the processing of pine material

Conclusion

In this study, carbon monoxide gas values resulting from cutting 3 different materials with a CO₂ laser cutting device were measured and compared in ppm. Among the materials cut with the CO₂ same thickness and the same parameters, 346 ppm was measured in MDF board, 364 ppm in beech wood and 397 ppm in pine wood, respectively. In the study, it is understood that as a result of processing these 3 different materials simultaneously and with the same parameters, the wood material that reaches the highest carbon monoxide value is pine, and the lowest is MDF board. When the materials are cut, these values are measured on the gas suction line. When CO concentration limit values are taken as reference (OSHA, 2019), it poses a life-threatening risk at values above 100 ppm, rapidly causing loss of consciousness and risk of death. In such cases, urgent medical intervention is required. Never opening the machine's top cover during the cutting process and stopping the process in case of a possible malfunction in the vacuum motor in the gas discharge will minimize possible work accidents. In further studies, sensors measuring more detailed gas emissions and different wooden materials used in the industry can be used.

References

Açık, C., Tutuş, A. (2023). Endüstriyel ürün imalatında kullanılan bazı ahşap türlerinin CNC lazerle işlenebilme performanslarının araştırılması. *Gazi Üniversitesi Mühendislik Mimarlık Fakültesi Dergisi*, 38(1), 461-470.

American Industrial Hygiene Association (AIHA). (2015). Threshold Limit Values for Chemical Substances in the Work Environment. *AIHA Journal*, 76(1), 16-23.

Baker, M. D., Henretig, F. M., Ludwig, S. (1988). Carboxyhemoglobin levels in children with nonspecific flu-like symptoms. *The Journal of pediatrics*, 113(3), 501-504.

Çolak, M., Değirmen-tepe, S. (2020). İç ve dış mekânlarda ahşap malzemelerin mobilya ve yapı malzemesi olarak kullanımı. *Türk Doğa ve Fen Dergisi*, 9(Özel Sayı), 190-199.

Durukan, Z., Motorcu, A., Güllü, A. (2014). AISI 304 çeliğini farklı geometrilerde lazerle kesmede parametrelerin boyutsal doğruluk üzerine etkilerinin modellenmesi. *Gazi Üniversitesi Mühendislik Mimarlık Fakültesi Dergisi*, 29(3).

Hampson, N.B., Weaver, L.K. (2010). Carbon Monoxide Poisoning: A New Incidence for an Old Disease. *Undersea & Hyperbaric Medicine*, 37(3), 163-168.

Islam, M.N., Das, A.K., Billah, M.M. et al. (2023). Multifaceted Laser Applications for Wood - A Review from Properties Analysis to Advanced Products Manufacturing. *Lasers Manuf. Mater. Process.* 10, 225–250.

Khatak, P. (2022). Laser cutting technique: A literature review. *Materials Today: Proceedings*, 56, 2484-2489.

Kök, F. (2020). Yangında açığa çıkan gazların, insan sağlığına vereceği zararın engellenmesi. *Ulusal Çevre Bilimleri Araştırma Dergisi*, 3(2), 83-94.

Köle, A., Ayan, Y., Kahraman, N. (2022). Markalama ve Kesme İşlemleri İçin Karbondioksit (CO₂) Lazer Makinesi Tasarımı, Üretimi ve Test Çalışmaları. *Politeknik Dergisi*, 1-1.

Levy, R. J. (2022). Anesthesia-Related Carbon Monoxide Exposure. *Carbon Monoxide in Drug Discovery: Basics, Pharmacology, and Therapeutic Potential*, 286-301.

Munoz, A., Schmidt, J., Suffet, I. M., & Tsai, C. S. J. (2023). Characterization of Emissions from Carbon Dioxide Laser Cutting Acrylic Plastics. *ACS Chemical Health & Safety*. 30(4), 182-192.

Occupational Safety and Health Administration (OSHA). (2019). Carbon Monoxide Exposure Limits. *OSHA Technical Manual, Section III*, Chapter 2.

Raub, J.A. and Benignus, V.A. (2002). Carbon monoxide and the nervous system. *Neuroscience & Biobehavioral Reviews*, 26(8), 925-940.

Rezaei, F., Wimmer, R., Gaff, M., Gusenbauer, C., Frömel-Frybort, S., Kumar Sethy, A., Niemz, P. (2022). Anatomical and morphological characteristics of beech wood after CO₂-laser cutting. *Wood Material Science & Engineering*, 17(6), 459-468.

Smith, R.P. and Ernst, E. (2011). Carbon Monoxide Poisoning: Pathogenesis, Management, and Future Directions of Therapy. *American Journal of Respiratory and Critical Care Medicine*, 183(5), 598-604.

Yaşar, Ş., Atar, M. (2017). Ahşap koruyucularla muamele edilmiş bazı ağaç malzemelerin yanmasıyla ortaya çıkan gaz emisyon miktarları. *İleri Teknoloji Bilimleri Dergisi*, 6(3): 503-514.

CHAPTER X

Design of Servo Motor Positioning Application for Android Phone with Arduino Nano 33 IoT on Simulink

Erdem İLTEN¹
Metin DEMİRTAS²
Haris CALGAN³

Introduction

Servo motors, specifically RC servo motors or hobby servo motors, are essential components widely used in various applications such as robotics, automation, modeling, and electronics. These compact and versatile devices play a crucial role in providing accurate and precise control over rotational or linear motion (Wada et al., 2009). A servo motor consists of several key components,

¹ Asst. Prof. Dr., Balikesir University Electrical-Electronics Engineering, erdemilten@balikesir.edu.tr

² Prof. Dr, Balikesir University Electrical-Electronics Engineering, mdtas@balikesir.edu.tr

³ Dr, Balikesir University Electrical-Electronics Engineering, haris.calgan@balikesir.edu.tr

including a DC motor, a gearbox, a control circuit, and a feedback system (Sustek *et al.*, 2017). The DC motor generates the mechanical power required for motion, while the gearbox amplifies torque and reduces the motor's rotational speed. The control circuit, often embedded within the servo motor, interprets signals and commands from an external source to regulate the motor's position, speed, and acceleration. The feedback system, typically based on a potentiometer or an optical encoder, provides positional information to the control circuit, allowing for closed-loop control (Haidar *et al.*, 2013). One of the distinguishing features of servo motors is their ability to achieve precise and repeatable positioning. By utilizing a closed-loop control system, servo motors can actively monitor their position and adjust accordingly to reach and maintain a desired angle or position. This makes them ideal for applications that require accurate control, such as robotic arm movements, camera gimbal stabilization, or steering mechanisms in remote-controlled vehicles (Firoozian, 2014). RC servo motors or hobby servo motors, as the name suggests, are commonly used in the field of radio control models and hobbies. They are compatible with standard radio control systems, making them easily controllable with remote transmitters. Hobby servo motors come in various sizes and power ratings, catering to different requirements and scales of model vehicles, airplanes, boats, and other related projects.

In today's fast-paced, interconnected world, microcontrollers are the unsung heroes that power a wide array of electronic devices we encounter in our daily lives. From smartphones and home appliances to automotive systems and industrial machinery, microcontrollers play a pivotal role in controlling and managing these technologies. In essence, a microcontroller is a compact, self-contained computer designed for specific tasks, making them indispensable for various applications across diverse industries (Gridling and Weiss, 2007). At their core, microcontrollers are miniature computing systems with processing capabilities, memory, and input/output interfaces, all integrated onto a single microchip. Unlike general-purpose computers, microcontrollers are optimized

for efficiency and are typically programmed to execute a specific set of tasks, known as embedded systems. This specialization allows them to excel in tasks that demand real-time control, precision, and low power consumption (Hintz and Tabak, 1992). Over the decades, microcontrollers have evolved dramatically, becoming more powerful, energy-efficient, and affordable. They have enabled groundbreaking innovations, ranging from the Internet of Things (IoT) and robotics to medical devices and consumer electronics. Understanding how microcontrollers work and how to program them has become an essential skill for engineers, hobbyists, and innovators looking to bring their ideas to life in today's technology-driven world.

Here is a list of some popular microcontroller families:

1. **Arduino:** Arduino is a highly popular open-source hardware and software platform known for its user-friendly development environment. It is based on various microcontroller chips, including the ATmega series from Microchip Technology (Küçükdermenci, 2023a, 2023b; McRoberts, 2013).
2. **Raspberry Pi:** While not a traditional microcontroller, the Raspberry Pi is a single-board computer that can be used for a wide range of projects and is often used in embedded systems and IoT applications (Küçükdermenci, 2023c, 2023d, 2023e).
3. **PIC Microcontrollers:** Developed by Microchip Technology, the PIC (Peripheral Interface Controller) microcontroller family is widely used in industrial and consumer electronics (Ilten and Demirtas, 2016; Küçükdermenci, 2023f, 2023g).
4. **STM32:** STM32 microcontrollers, produced by STMicroelectronics, are known for their high performance and extensive peripheral options. They are commonly used in industrial and automotive applications (Ilten, 2022a).
5. **AVR Microcontrollers:** Another Microchip Technology product, AVR microcontrollers are known for their simplicity

and are commonly used in educational and hobbyist projects (Kunikowski *et al.*, 2015).

6. **ARM Cortex-M Series:** ARM-based microcontrollers, such as the Cortex-M0, M3, and M4, are widely used in various applications due to their scalability and performance. Manufacturers like NXP, Texas Instruments, and STMicroelectronics produce ARM-based microcontrollers (Hemanthkumar *et al.*, 2022).

In this study, Arduino Nano 33 IoT is preferred. Arduino Nano 33 IoT is a compact and versatile development board that combines the power of the Arduino ecosystem with the capabilities of Internet of Things (IoT) technology. It is designed to enable the creation of smart, connected projects and is suitable for a wide range of applications, including home automation, sensor networks, IoT devices, and wearable technology. Arduino Nano 33 IoT board is based on the Atmel SAMD21 microcontroller, which provides a powerful processing core and a rich set of features. It offers 256KB of Flash memory and 32KB of SRAM, allowing for the execution of complex tasks and the storage of data (Arduino, 2023). Additionally, it includes built-in Wi-Fi and Bluetooth connectivity, enabling seamless integration with the internet and other wireless devices. One of the key advantages of the Arduino Nano 33 IoT is its small form factor, which makes it ideal for projects with space constraints or those requiring portability. The board is only 45mm x 18mm in size, allowing it to be easily integrated into compact enclosures or wearable devices. Despite its size, it offers a wide range of I/O pins, including digital and analog inputs and outputs, pulse width modulation (PWM) outputs, UART, SPI, and I2C interfaces, enabling the connection of various sensors, actuators, and external modules. With Arduino Nano 33 IoT, users can create interactive and intelligent projects that can communicate with the internet and other devices (Kurniawan, 2020). It can collect data from sensors, process it locally, and send it to the cloud for further analysis or control. The board can also receive commands from the cloud or other devices, allowing for remote control and monitoring.

In the era of smartphones and smart devices, Android phone applications have revolutionized the way we interact with the world around us. One exciting and practical application of this technology is using Android phone applications for remote control purposes (Arvindan and Keerthika, 2016). With the right app and compatible devices, users can transform their Android phones into powerful remote-control devices to manage a wide range of electronic devices and systems. Android phone applications for remote control offer an intuitive and convenient way to control various devices remotely. From home entertainment systems, such as televisions, media players, and sound systems, to home automation systems, including lights, thermostats, and security systems, these applications provide a centralized control interface right at your fingertips. By connecting your Android phone to compatible devices via Wi-Fi, Bluetooth, infrared, or other wireless protocols, you can effortlessly navigate menus, adjust settings, and execute commands with ease. The versatility of Android phone applications for remote control extends beyond home electronics. Many applications also support controlling drones, robotic devices, and even vehicles (Moon *et al.*, 2011). Whether you want to pilot a drone, operate a robotic arm, or control your car's multimedia system, these apps offer a seamless and immersive experience, enabling you to interact with your devices in innovative and exciting ways.

Simulink, developed by MathWorks, is a graphical modeling and simulation environment widely used in various industries for designing, simulating, and analyzing complex dynamic systems. Simulink enables engineers to create system models using a block diagram approach, where different blocks represent components or functions of the system, and the connections between blocks define the flow of data and signals (Ilten, 2022b). This visual representation simplifies the design process and facilitates the understanding and communication of system behavior. Simulink Embedded Coder, is a powerful tool within the Simulink environment that allows engineers and developers to generate efficient and optimized embedded code from their Simulink models (Ilten, 2023a). It bridges the gap

between model-based design and embedded systems development by automatically translating high-level system designs into executable and deployable code for embedded hardware platforms (Ilten, 2023b). The generated embedded code can be compiled and deployed onto target hardware platforms, such as microcontrollers, digital signal processors (DSPs), field-programmable gate arrays (FPGAs), or application-specific integrated circuits (ASICs) (Ilten, 2022c). This enables the execution of the designed system directly on the embedded hardware, bringing the model to life in a real-world environment.

In this study, angular positions of 3 servo motor are controlled by an Android phone via Arduino Nano 33 IoT over Wi-Fi. Servo motors are supplied from an external 5 V_{dc} source. Simulink Embedded Coder is used for development and implementation both Arduino Nano 33 IoT and Android phone application. *Simulink Support Package for Arduino Hardware* is used for Arduino. For the Android phone application, *Simulink Support Package for Android Devices* is used. A separate Simulink model is created for each. The development processes of these designs are explained in detail in the following sections.

This chapter is organized as follows: Servo motor control system is explained in section 2, Android application design is given in section 3, Experimental results are demonstrated in section 4, and Conclusion is presented in section 5.

Servo Motor Control System

Block diagram of the servo motor position control system is presented in Figure 1 and the experimental setup is given in Figure 2. In this system, servo motors are powered by an external 5 V_{dc} power supply. Control pins of the servo motors are controlled by Arduino Nano 33 IoT with 3 separate PWM signals which are 50 Hz and period between 1-2 ms. Android phone and Arduino Nano 33 IoT communicate on Wi-Fi access point.

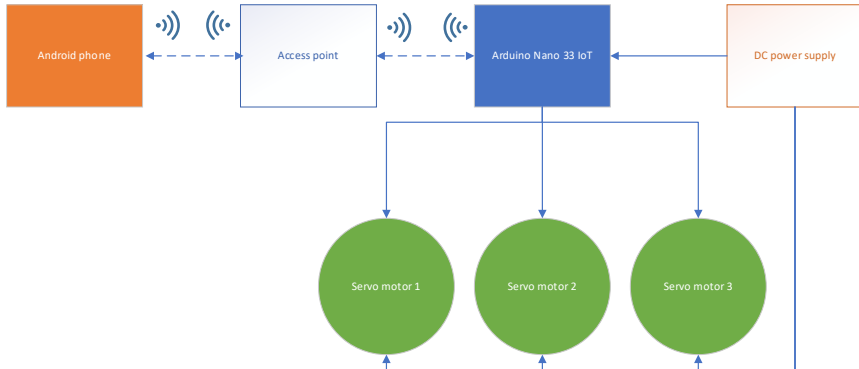


Figure 1. Block diagram of the system.

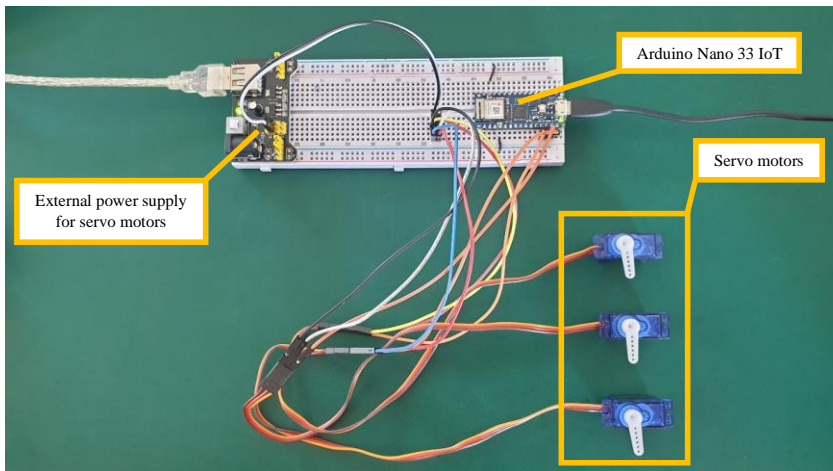


Figure 2. Experimental setup.

In Figure 2, Tower Pro Micro Servo 9g SG90 servo motors are used. This servo motor can be seen in Figure 3. In Figure 3, red cable is Vcc, brown cable is Ground and orange cable is control signal input (PWM signal). Servo motor positions for various control signals are demonstrated in Figure 4 (Bakker, 2020). Arduino Nano 33 IoT pins are presented in Figure 5 (Arduino, 2023).



Figure 3. Tower Pro Micro Servo 9g SG90.

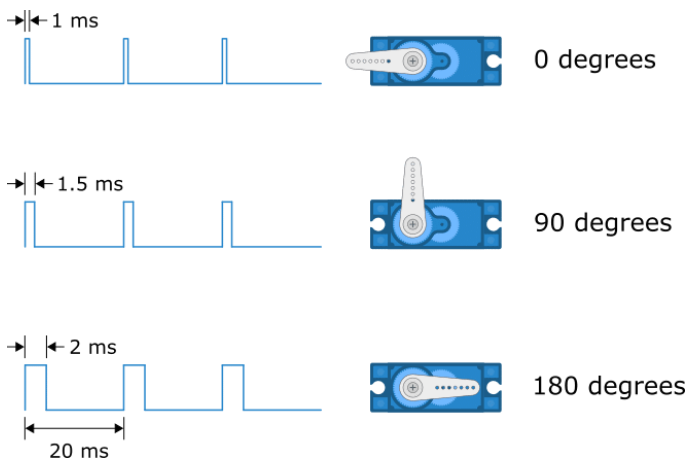


Figure 4. Servo motor positions for various control signals.

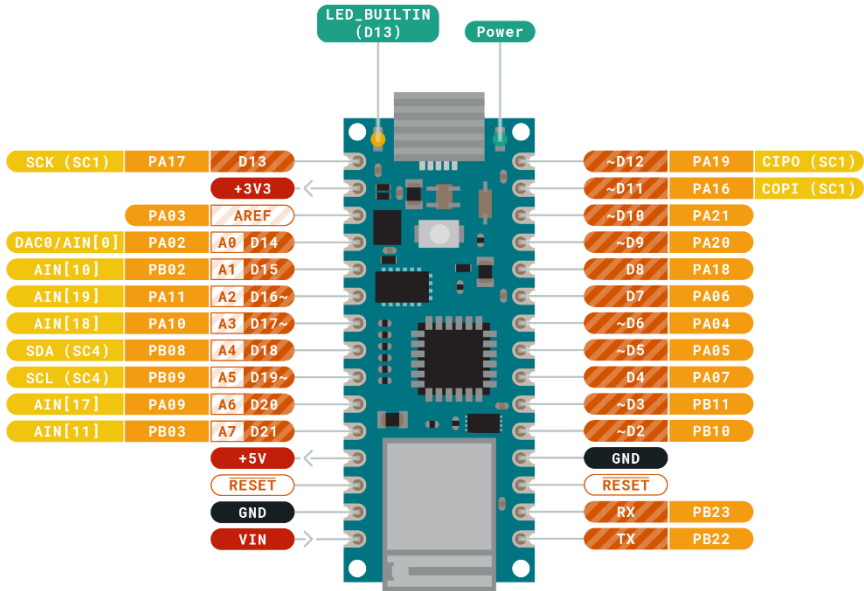


Figure 5. Arduino Nano 33 IoT pins.

Servo motor control algorithm is prepared on Simulink environment by using *Simulink Support Package for Arduino Hardware* tool of Matlab. Simulink block diagram for Arduino model is illustrated in Figure 6. An LED is connected to Pin-13, the LED is turned on at a frequency of 1Hz to check whether the system is working properly. Pin-9, Pin-10 and Pin-11 are set as servo motor control terminals. Servo motor position information is sent by Wi-Fi via Android phone and read by Arduino's Wi-Fi module. The position information coming as a package is parsed with the demux block and sent to the relevant servo motor blocks.

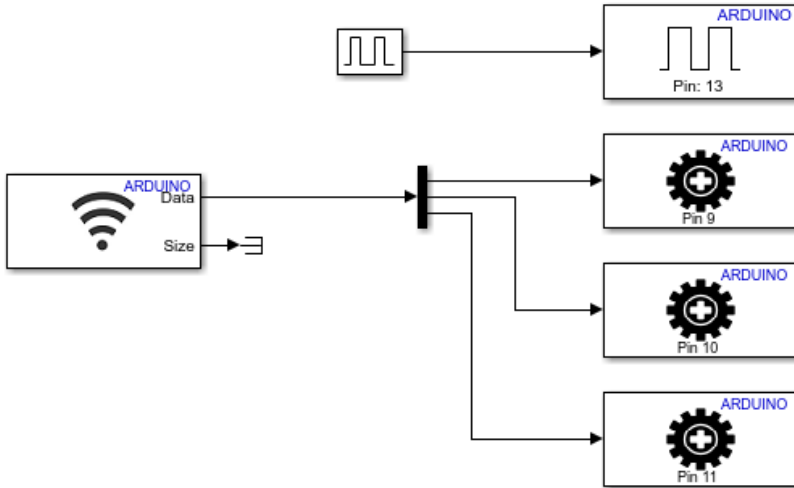


Figure 6. Simulink block diagram for Arduino model.

Android Application Design

Android phone algorithm is prepared on Simulink environment by using *Simulink Support Package for Android Devices* tool of Matlab. Simulink block diagram for Android model is illustrated in Figure 7. For adjusting servo motor positions, 3 slider blocks are used. These sliders are limited between 0 and 180 values. Slider outputs are converted to double and merged with mux block. Merged data is sent over Wi-Fi via “UDP Sent to Arduino” block. Android phone screen for this application is presented in Figure 8.

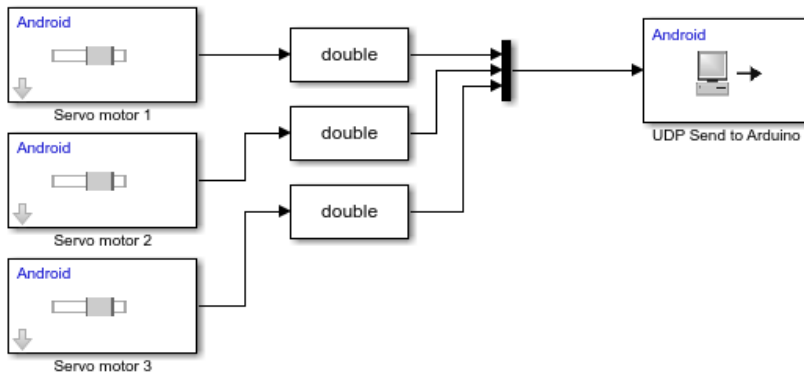


Figure 7. Simulink block diagram for Android model.



Figure 8. Screen of Android application.

Figure 8 shows separate sliders for each servo motor. The servo motor position information that needs to be changed can be easily adjusted on the touch screen of the Android phone.

Experimental Results

Written algorithms for Arduino Nano 33 IoT and Android phone are tested experimentally. In experimental tests, Samsung Note 9 smart phone is used. 3 tests are done for different positions

for each motor. Test results are demonstrated in Figure 9, 10 and 11. In test 1, servo motor positions are sent as 142, 85 and 29. In test 2, positions are 24, 151 and 2-91. Finally in test 3, positions are 59, 20 and 167.

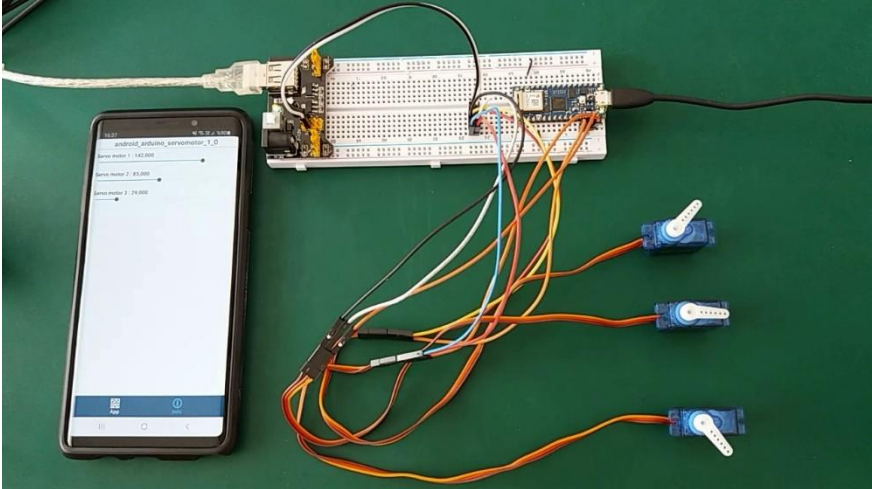


Figure 9. System test 1.

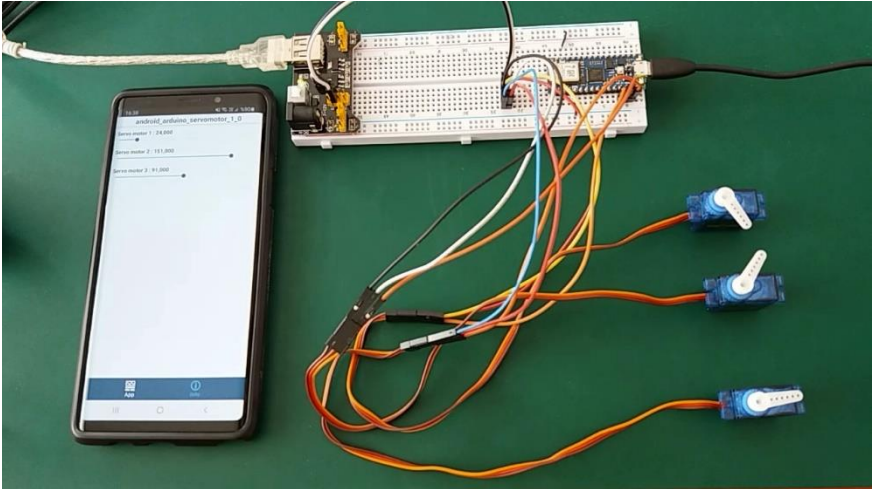


Figure 10. System test 2.

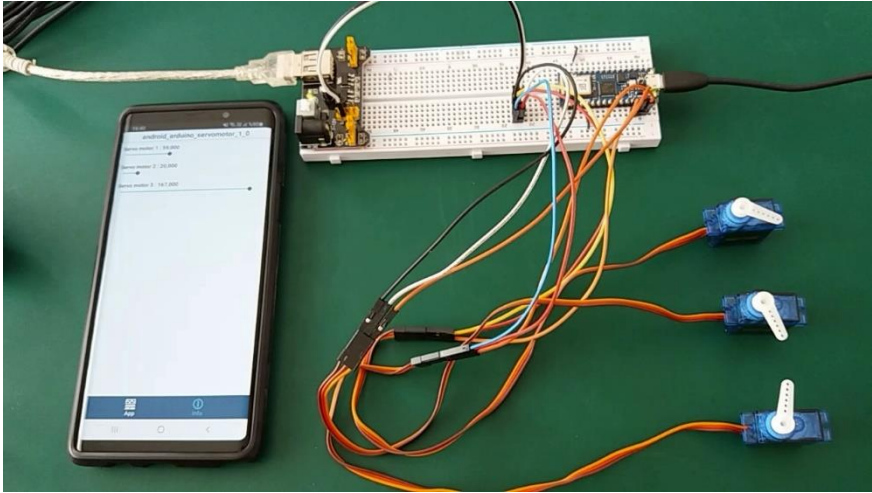


Figure 11. System test 3.

When Figures 9, 10 and 11 are examined, it is clearly seen that the servo motor position information sent by the Android phone is read correctly by Arduino Nano 33 IoT and applied to the motors. When the Android phone application is closed or out of range, the servo motors are brought to the 0 position by Arduino Nano 33 IoT.

Conclusion

This paper presents a Wi-Fi application between Arduino and Android phone. According to the information sent by the Android phone over Wi-Fi, the positions of 3 servo motors are adjusted with Arduino Nano 33 IoT. For programming of Arduino and Android phone Simulink Embedded Coder is used. Simulink Support Package for Arduino Hardware and Simulink Support Package for Android Devices tools of Matlab are used in algorithm designing process for Arduino Nano 33 IoT and Android phone, respectively. The system is tested experimentally, and the results are presented. When the results are examined, the aimed operations have been carried out successfully.

References

Arduino. (2023), “Arduino Nano 33 IoT”, available at: <https://docs.arduino.cc/hardware/nano-33-iot>.

Arvindan, A.N. and Keerthika, D. (2016), “Experimental investigation of remote control via Android smart phone of arduino-based automated irrigation system using moisture sensor”, *2016 3rd International Conference on Electrical Energy Systems (ICEES)*, IEEE, pp. 168–175.

Bakker, B. de. (2020), “How to control servo motors with Arduino”, available at: <https://www.makerguides.com/servo-arduino-tutorial/>.

Firoozian, R. (2014), *Servo Motors and Industrial Control Theory*, Springer.

Gridling, G. and Weiss, B. (2007), “Introduction to microcontrollers”, *Vienna University of Technology Institute of Computer Engineering Embedded Computing Systems Group*, p. 25.

Haidar, A.M., Benachaiba, C. and Zahir, M. (2013), “Software interfacing of servo motor with microcontroller”.

Hemanthkumar, P.B., Anireddy, S.R., Josh, F.T. and Venkatesan, R. (2022), “Introduction to ARM processors & its types and Overview to Cortex M series with deep explanation of each of the processors in this Family”, *2022 International Conference on Computer Communication and Informatics (ICCCI)*, IEEE, pp. 1–8.

Hintz, K. and Tabak, D. (1992), *Microcontrollers: Architecture, Implementation, and Programming*, McGraw-Hill, Inc.

Ilten, E. (2022a), “Conformable Fractional Order Controller Design and Implementation for Per-Phase Voltage Regulation of Three-Phase SEIG Under Unbalanced Load”, *Electric Power Components and Systems*, Taylor & Francis, Vol. 50 No. 11–12, pp. 636–648.

Ilten, E. (2022b), “Conformable fractional order controller design and optimization for sensorless control of induction motor”, *COMPEL-The International Journal for Computation and Mathematics in Electrical and Electronic Engineering*, Emerald Publishing Limited, Vol. 41 No. 5, pp. 1528–1541.

Ilten, E. (2022c), “Induction Motor Speed Controller Interface Design Via Simulink External Mode”, *II. International Joint Conference on Engineering, Science and Artificial Intelligence*, pp. 59–63.

Ilten, E. (2023a), “Permanent Magnet Synchronous Motor Control Interface Design and Implementation with TI F28335 DSP on Simulink External Mode”, *International Conference on Applied Engineering and Natural Sciences*, Vol. 1, pp. 67–70.

Ilten, E. (2023b), “DC motor position control with Raspberry Pi on Simulink wireless external mode”, *International Conference on Pioneer and Innovative Studies*, Vol. 1, pp. 228–231.

Ilten, E. and Demirtas, M. (2016), “Off-line tuning of fractional order PI λ Controller by using response surface method for induction motor speed control”, *Journal of Control Engineering and Applied Informatics*, Vol. 18 No. 2, pp. 20–27.

Küçükdermenci, S. (2023a), “Engelli Bireyler İçin Braille Yöntemine Yönelik Yardımcı Teknolojiler”, *Mühendislik Alanında Uluslararası Teori, Araştırma ve Derlemeler Cilt 2*, Serüven Yayınevi / Serüven Publishing, pp. 15–28.

Küçükdermenci, S. (2023b), “İşaret Dili İçin Akıllı Eldiven Tasarımları”, *Mühendislik Alanında Uluslararası Teori, Araştırma ve Derlemeler Cilt 1*, Serüven Yayınevi / Serüven Publishing, pp. 85–101.

Küçükdermenci, S. (2023c), “Raspberry Pi based braille keyboard design with audio output for the visually challenged”, *1st International Conference on Modern and Advanced Research ICMAR 2023*, All Sciences Academy, pp. 334–339.

Küçükdermenci, S. (2023d), “Sign language voice convertor design using Raspberry pi for impaired individuals”, *Proceeding Book of 1st International Conference on Recent and Innovative Results in Engineering and Technology ICRIRET 2023*, All Sciences Academy, pp. 160–166.

Küçükdermenci, S. (2023e), “Smart Wheelchair Design for Elderly and Disabled People”, *International Conference on Innovative Academic Studies*, All Sciences Academy, available at:<https://doi.org/10.59287/icias.1592>.

Küçükdermenci, S. (2023f), “Yaşlı ve Engelli Bireylere Yönelik Akıllı Tekerlekli Sandalye Tasarımları”, *Mühendislikte Güncel Yaklaşımlar*, Duvar Yayınları, pp. 419–440.

Küçükdermenci, S. (2023g), “Su Kalitesi Akıllı Ölçüm Sistemleri”, *Mühendislikte Güncel Yaklaşımlar*, Duvar Yayınları, pp. 441–458.

Kunikowski, W., Czerwiński, E., Olejnik, P. and Awrejcewicz, J. (2015), “An overview of ATmega AVR microcontrollers used in scientific research and industrial applications”, *Pomiary Automatyka Robotyka*, Sieć Badawcza Łukasiewicz-Przemysłowy Instytut Automatyki i Pomiarów, Vol. 19 No. 1, pp. 15–19.

Kurniawan, A. (2020), *Beginning Arduino Nano 33 IoT: Step-By-Step Internet of Things Projects*, Apress Media LLC.

McRoberts, M. (2013), *Beginning Arduino*, Apress.

Moon, S.W., Kim, Y.J., Myeong, H.J., Kim, C.S., Cha, N.J. and Kim, D.H. (2011), “Implementation of smartphone environment remote control and monitoring system for Android operating system-based robot platform”, *2011 8th International Conference on Ubiquitous Robots and Ambient Intelligence (URAI)*, IEEE, pp. 211–214.

Šustek, M., Marčaník, M., Tomášek, P. and Úředníček, Z. (2017), “DC motors and servo-motors controlled by Raspberry Pi 2B”, *MATEC Web of Conferences*, EDP Sciences.

Wada, T., Ishikawa, M., Kitayoshi, R., Maruta, I. and Sugie, T. (2009), “Practical modeling and system identification of R/C servo motors”, *2009 IEEE Control Applications, (CCA) & Intelligent Control, (ISIC)*, IEEE, pp. 1378–1383.

CHAPTER XI

Design of Robotics Educational Material For Teaching English Color Concepts in Preschool

Mehmet GÜNEŞ¹
Çağatay ERSİN²

Intruction

Nowadays, robotics and coding studies are becoming increasingly important. Robotics applications are widely used in education as well as in all areas of life.

Early childhood is the phase in which the child undergoes the fastest change and development, both cognitively and physically. The child tends to continue his actions through play during this period of rapid development; For this reason, toys used in vehicle games are also important for child development (Soyupak and Soyupak). Pre-school education; It is a preparation phase for the

¹ Dr, Çankırı Karatekin University

² Dr, Çankırı Karatekin University

child's normal education period, and the correct education and development guidance the child receives at this stage has a key role that will affect the child's entire life (Soydan et al., 2014). Preschool education covers the years from the day the child is born to the day he starts basic education and plays an important role in the later lives of children; It is defined as the development and education process in which physical, motor, social-emotional, mental and language development is largely completed and shaped by the education given (Mutlu et al., 2012). Preschool education is an educational process that supports all developmental areas of children aged 0-6. During this period, children gain basic knowledge and skills that will support what they will learn in later periods. Therefore, the quality of the education to be provided to children in the pre-school period is of great importance in terms of raising mentally, physically and spiritually healthy generations. Aiming to ensure the active participation of the child in pre-school education, the basic feature of the child's learning by doing and experiencing, gaining different experiences, taking into consideration family participation and individual differences and interests among children has been adopted as a basic feature. It is possible for the child to gain different experiences in educational activities and to learn by doing and experiencing by diversifying the educational materials. Today's technological developments cause children to grow up in touch with technology and therefore make it inevitable to use computers as educational materials (Şahin et al., 2015). Children in the pre-school period; Because they are curious, extremely willing to research, and have strong imagination; Supporting children's development in this direction is possible in educational environments where they can research and question, use their curiosity, establish cause and effect relationships, and make predictions (Özkubat, 2013).

Preschool education is a critical period in laying the foundation for children's social, emotional and cognitive development. During this period, children learn many basic concepts and skills. Colors are an important element that helps children understand the world and also contributes to language development.

Nowadays, with the rapid development of technology, the use of technological tools in education is increasing. Programmable microcontrollers such as Arduino have great potential for creating interactive and instructional materials in education.

In recent years, studies have been conducted on how Arduino can be an effective tool in pre-school education. For example, one study stated that Arduino can be used to teach coding to children (Tiryaki and Balaman, 2021). Another study showed that Arduino can be used to design educational toys (Wen, 2020). Additionally, it has been proven that Arduino-based educational robots contribute to children's skill development and knowledge acquisition (Chou, 2018).

This study examines how effective an educational material designed using Arduino is in introducing colors to preschool children aloud and in English. This material aims to help children recognize colors and at the same time improve their English language skills. In the study, TCS230 color detection sensor, Arduino Uno microcontroller development board for controlling the material, 3 watt 5 ohm speaker for sound output, and SD card module for recording audio files in which the colors are voiced in English were used.

Material and Method

Preschool education requires a stimulating environment that will maximize learning. Preparation of children, classroom environment, teaching methods, assessments and teaching aids influence the teaching and learning process to provide an effective educational environment. Depending on a variety of factors, teaching aids have a direct impact on both teaching and learning. Instructional materials play an important role in the success of the teaching-learning process. For teachers, Instructional materials are important to assist teachers in teaching lessons effectively. Effective use of these materials by teachers allows students to understand the subject better. According to Piaget, instructional materials alone do

not guarantee effective teaching; instructional materials must be appropriately selected and used to make teaching and participation effective (Abayan et al., 2021). In this study, an educational material was designed and implemented to be used in preschool education. The designed educational material is made of birch plywood material, which is healthy for children. First, the design was drawn in Autocad software and cut and produced on a CO₂ laser cutting device. The production of the design on the CO₂ laser cutting device is shown in Figure 1.

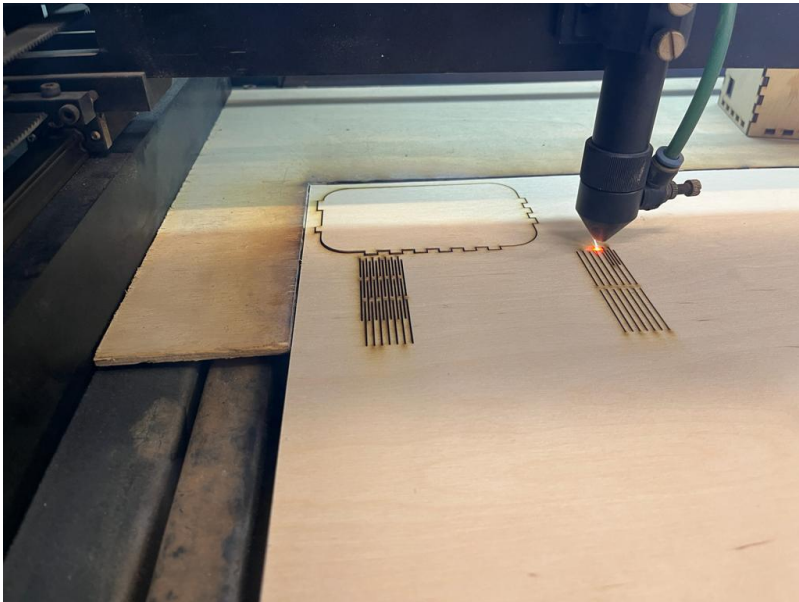


Figure 1. Production of the design on a CO₂ laser cutting device

The produced design has been created to be interconnected and has been adjusted to be put into circuit. Then, in order to recognize the colors in the material, cubes were created from birch plywood and painted with natural materials in primary colors. Color cubes created with the CO₂ laser cutting device are shown in Figure 2.

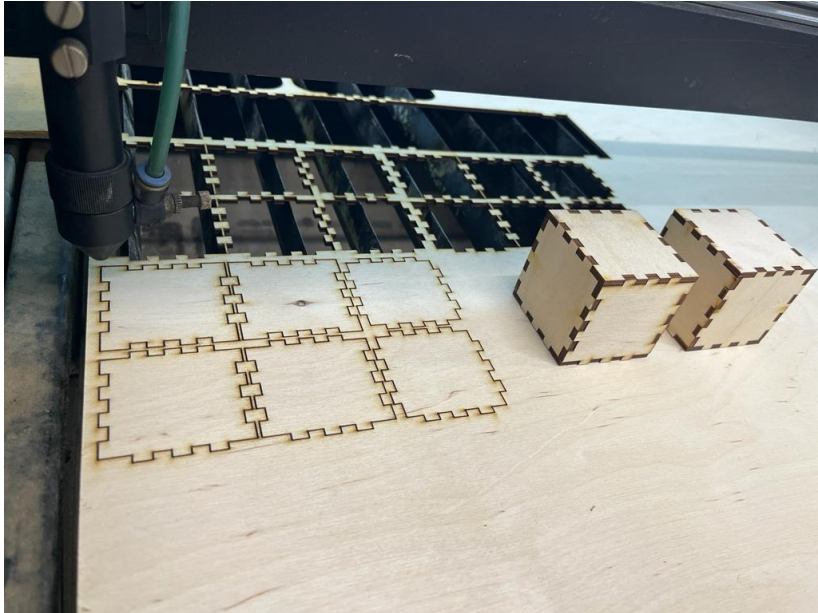


Figure 2. Creation of color cubes used in the design

After the external design of the system was realized, the TCS230 color sensor was used to recognize the color cubes, the Arduino Uno microcontroller development board, which is widely used today, was used to control the system, and the SD card module and speakers were used to read the audio files.

TCS3200 Color Sensor

The TCS3200 Color Sensor Module used in the training material is a color detector including 4 white LEDs. It is used in applications such as test strip reading, color sorting, ambient light detection, calibration and color matching. This sensor contains 4 different filters. In this way, it can detect colors. There are a number of sensors in its internal structure. The output frequency range varies between 2Hz and 500 kHz. The block diagram of the TCS230 color detection sensor is shown in Figure 3.

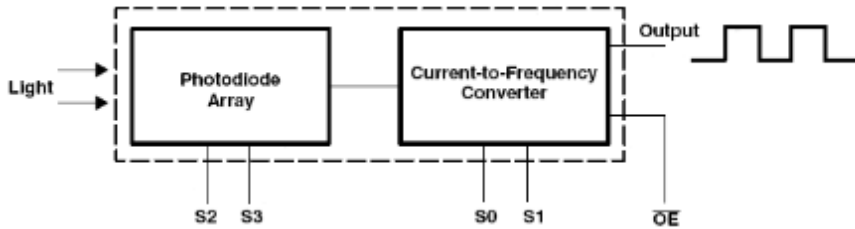


Figure 3. Block diagram of the color sensor used in the design (Altun,)

Arduino Uno Microcontroller Development Board

Arduino is a controller board developed as an open source code, containing an Atmel AVR microcontroller as a processor and various peripheral units. There has been a great increase in its use in recent years due to reasons such as being open source, having libraries that provide ease of use, and having a lot of resource opportunities. Processing/wiring language and Arduino IDE environment are used for programming. Arduino Uno R3 board is an Atmega328 microprocessor based controller board. There are a total of 20 pins on the card to be used as input and output. Of these, 6 can be used as analog inputs and 14 as digital input-outputs. There are many peripheral units on the card required for the microcontroller to operate. Arduino Uno R3 board has hardware features such as 16 Mhz crystal oscillator, 32 KB flash memory, 2 KB SRAM, 1 KB EEPROM (Özdemirci et al., 2017; Üçgün and Kaplan, 2017; Yildirim et al., 2018; Erdoğan et al., 2022; Kumar et al., 2016; Arduino, 2015). The pin connection status of the Arduino Uno microcontroller development board is shown in Figure 4.

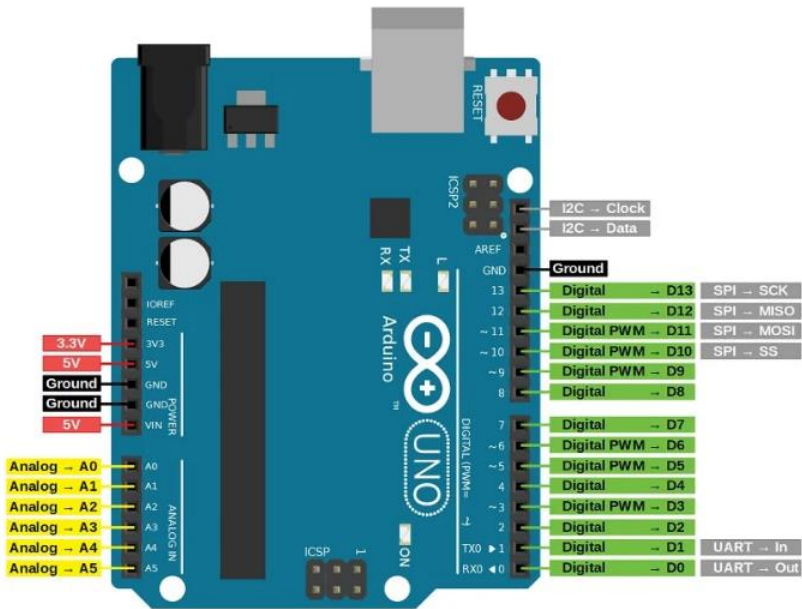


Figure 4. Arduino Uno R3 microcontroller development board used in the training material [16]

SD card Module

Generally, data entry to the SD Card module via the Arduino device is convenient and easy, so this external memory card is used for data entry in many projects. The SD card module consists of two main components: The standard microSD card has an operating voltage of 3.3 V. As a result, we cannot connect it directly to circuits that use 5V logic; In fact, any voltage above 3.6V can permanently damage the microSD card. Therefore, the module has a built-in ultra-low voltage regulator that can regulate the voltage down to 3.3V [Nasriddinovich and Narimanovich, 2023].

Electronic Circuit of Educational Material

In the study, an educational material was developed for preschool students that can recognize primary colors with a color

sensor and speak English out loud. Colors were detected with the system, whose exterior design was made of birch plywood, using the TCS230 color sensor and the software written on the Arduino Uno microcontroller development board. The English primary colors were recorded in the system via a microphone and converted to “wav” file format. An SD card module was connected to the Arduino Uno microcontroller development board and the SD card on which the sound files were recorded was inserted into this module. When the student brings the color cubes close to the color sensor of the created system, the sensor will detect the colors and read the audio file via the SD card. When the student scans the color cubes into the system, he/she will speak the commands "red", "blue", "green" through the speaker. The image of the electronic part of the training material is shown in Figure 5.

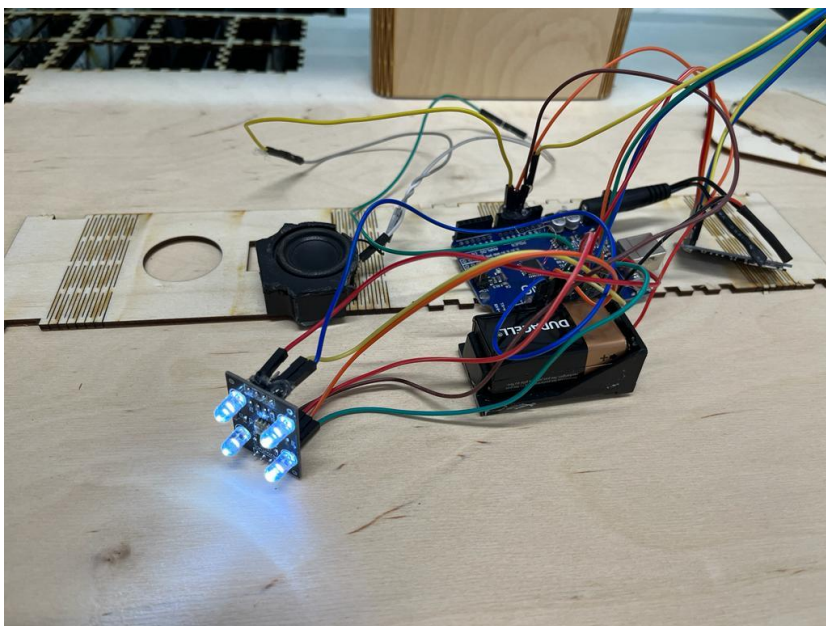


Figure 5. Electronic part of the training material

The educational material in this study was tested on students and it was observed that the system worked stably. The educational

material, made of healthy material, is aimed to be used in teaching primary colors to students. The image of the educational material in the study is shown in Figure 6.

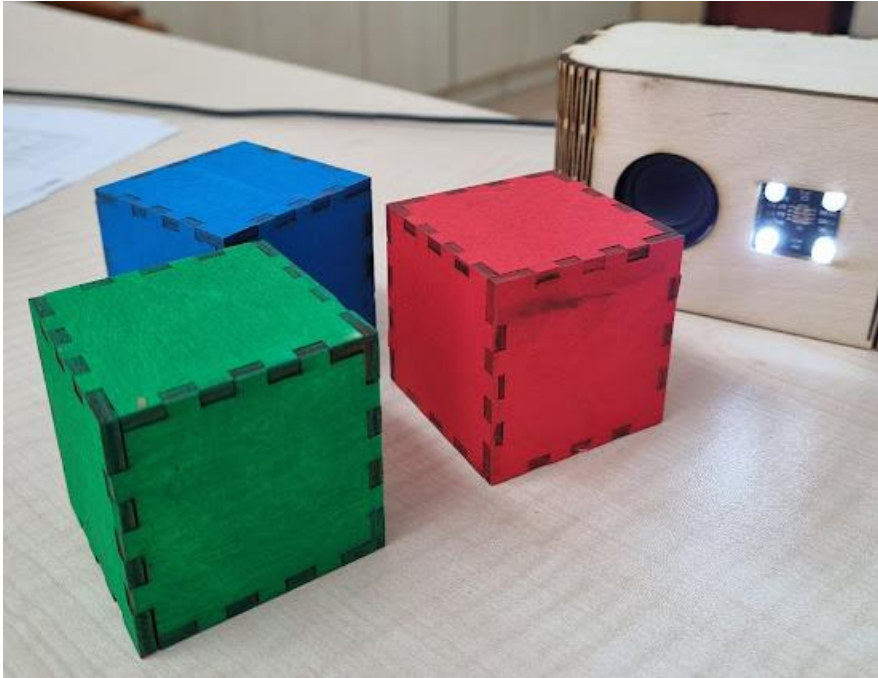


Figure 6. Training material

Conclusion

Educational materials are educational supports that can be used at every stage of education and provide students with the opportunity to learn by experiencing and provide permanent learning. In this study, birch plywood educational material was designed to teach English colors to preschool students. The design was created with a CO₂ laser cutting device, then color cubes were cut from the same material. In order for the training material to recognize the primary colors and to provide audio output in English, the audio files previously recorded on the SD card were read with the SD card module. When the sound sensor detected the color

cubes, the relevant sound file was called with the Arduino software and sound output was obtained from the speaker. With this study, students will be involved in the education process and achieve permanent learning while learning the English of colors. The work can then be diversified with different colors and color cubes can be designed in different geometric shapes to contribute to the development of children's psychomotor skills.

References

Abayan, M. R. A., Placigo, M. R., & Las Johansen, B. C. (2021). Evaluating the Kindergarten Instructional Materials: Inputs for Materials Production. *Evaluating the Kindergarten Instructional Materials: Inputs for Materials Production*, 69(1), 8-8.

Altun, M. Y. H. Renk Sentezleyici Tasarlayarak Renk Oluřturulması Ve Taos Tcs 0 Programlanabilir Renk Sensörü Kullanılarak Renk Tanıma Uygulaması.

Arduino, B. (2015). Arduino Uno.

Chou, P. N. (2018). Skill development and knowledge acquisition cultivated by maker education: Evidence from Arduino-based educational robotics. *EURASIA Journal of Mathematics, Science and Technology Education*, 14(10), em1600.

Erdoğan, M. Ö., Okatan, A., Umut, U. Z., Yılmaz, F., & Çetinkaya, A. (2022). Production, and Analysis of a Two-Axis Food Liquid Pouring Machine. *International Journal of Engineering Technologies IJET*, 8(1), 1-7.

Kumar, N. S., Vuayalakshmi, B., Prarthana, R. J., & Shankar, A. (2016, November). IOT based smart garbage alert system using Arduino UNO. In *2016 IEEE region 10 conference (TENCON)* (pp. 1028-1034). IEEE.

Mutlu, B., Ergiři, A., Ayhan, A. B., & Neriman, A. R. A. L. (2012). Okul öncesi dönemde Montessori eğitimi. *Ankara Sağlık Bilimleri Dergisi*, 1(3), 113-128.

Nasriddinovich, Z. H., & Narimanovich, R. O. (2023). Arduino Qurılmasında Sd Card Modulu Va At24c256 Serial Eeprom Modulu İshlatılıř Usulları Va Tahlılı. *Conferencea*, 122-129.

Özdemirci, E., Ersin, Ç., & Canal, M. R. (2017). Arduino UNO uygulama setinin gerçekteřtirilmesi. Mehmet Akif Ersoy Üniversitesi Fen Bilimleri Enstitüsü Dergisi, 8(Özel (Special) 1), 127-133.

Özkubat, S. (2013). Okul öncesi kurumlarında eğitim ortamlarının düzenlenmesi ve donanım. *Adnan Menderes Üniversitesi Eğitim Fakültesi Eğitim Bilimleri Dergisi*, 4(2), 58-66.

Soydan, O., Benliay, A., & Bensus, C. Ü. C. E. (2014). Okul Öncesi Eğitim Kurumlarında Dış Mekân Peyzaj Tasarımının 5-6 Yaş Çocuk Grubu Algısı Üzerindeki Etkisi. *Niğde Ömer Halisdemir Üniversitesi Mühendislik Bilimleri Dergisi*, 3(1), 37-47.

Soyupak, O., & Soyupak, İ. Erken Çocukluk Dönemine Yönelik Ahşap Oyuncak Tasarımı Ve Nitelikleri.

Şahin, M. C., İşııl, T. A. Ş., Oğul, İ. G., Çilingir, E., & Keleş, O. (2015). Tablet Bilgisayarların Okul Öncesi Eğitimde Destek Materyali Olarak Kullanılmasının İncelenmesi. *Abant İzzet Baysal Üniversitesi Eğitim Fakültesi Dergisi*, 15(2), 335-348.

Tiryaki, S. H., & Balaman, F. (2021). The Opinions of Students about Scratch, Arduino and Python Using from Open Source Code Softwares. *Journal of Computer and Education Research Year*, 9(18), 831-852.

Üçgün, H., & Kaplan, Z. K. (2017, October). Arduino based weather forecasting station. In *2017 International Conference on Computer Science and Engineering (UBMK)* (pp. 972-977). IEEE.

Wen, Z. (2020). Infant learning platform using Arduino (project 3).

Yildirim, M. S., Selvi, A. O., & Dandil, E. (2018, October). Web based animal tracker system. In *2018 2nd International Symposium on Multidisciplinary Studies and Innovative Technologies (ISMSIT)* (pp. 1-5). IEEE.

CHAPTER XII

Single Phase Inverter Square Wave Inverter and PWM Control Circuit

Metin DEMİRTAS¹

Introduction

Inverters are power electronics devices that find a wide range of uses in industrial applications. It is also one of the electronic converters. In terms of working principles, they are flexible devices because they can produce voltage at the desired amplitude and frequency. This flexible structure has an important place in many areas, especially in control and automation systems. The inverters are also known as DC-AC converters. They convert DC voltage to AC voltage at the desired output voltage and frequency (Guo et al., 2020). Today, inverters are produced as single-phase and three-phase. They are used in many industrial areas such as electric

¹ Balıkesir University, Dept. of Electrical-Electronics Engineering, Balıkesir, Turkey, mdtas@balikesir.edu.tr

vehicles, solar energy, communication systems, and uninterruptible power supplies. The basic principle in inverter operation is to switch power electronics semiconductor switching elements such as IGBT, MOSFET, GTO, BJT in the appropriate order and time to obtain the output voltage at desired amplitude and frequency. These switches are operated in the cut-off and saturation region.

The voltage with known amplitude and frequency at the inverter output is not pure sinusoidal, it is in the form of a square wave. In other words, the inverter output voltage contains harmonic components at different frequencies and amplitudes other than the desired frequency when the output voltage is a square wave. Inverters are divided into two groups, current-fed or voltage-fed, according to their feeding characteristics in the application. In voltage source inverters (VSI), the output voltage waveform is determined by input direct voltage and the switching method. The load cannot affect this waveform (Ahmed, 1998; Gülgün, 1999).

In current source inverters, the source that feeds the inverter has the feature of a constant current source. Connecting a very large inductance in series with the rectifier output is a common practice in power electronics to smooth out the current drawn by the inverter from the source. This inductor is often referred to as a "smoothing inductor" or "filter inductor." The purpose of this inductor is to reduce the ripple in the current waveform, making the current more constant and continuous. The schematic representation of the inverter is given in Figure 1.



Figure 1. Inverter general structure

Voltage control in single-phase inverters is illustrated in Figure 1, where the DC supply to the inverter is provided by the

battery or rectifier. The inverter is used to control the fundamental voltage magnitude and the frequency of the AC output voltage. AC loads may require constant or adjustable voltage at their input terminals when such loads are fed by inverters. The output voltage of the inverters must be controlled to fulfill the requirement of the loads.

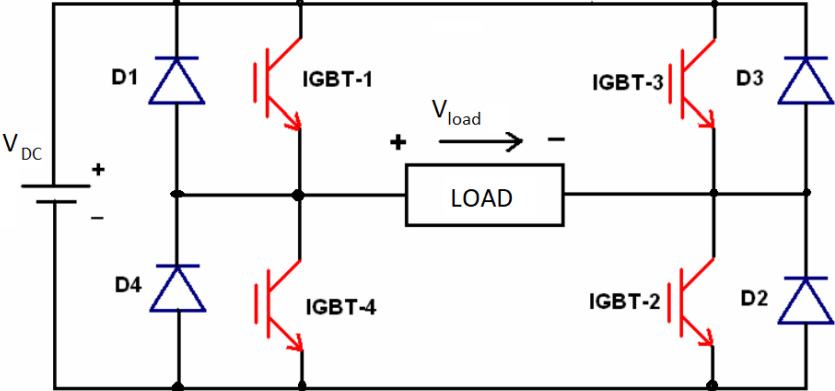


Figure 2. A single-phase full-bridge inverter circuit

A single-phase full-bridge inverter circuit is shown in Figure 2. Diodes D1, D2, D3 and D4 are freewheeling diodes. In the one-phase full-bridge inverter circuit shown in Figure 2, IGBT-1 and IGBT-2 devices work in conjunction with IGBT-3 and IGBT-4 devices. As seen in the circuit diagram, when the same pairs conduct at the same time, the DC source becomes short-circuited and the elements burn out.

In inverter design, the amplitude of the main harmonic component of the output voltage and in addition to adjusting the frequency to the desired value, minimizing harmonic components is very important issue.

There are three basic single-phase inverter structures: half bridge, full bridge, and push-pull. This chapter focuses on the full-bridge topology since it provides double the output voltage compared to the half-bridge topology. There are different models of

inverters depending on the type of signal produced. They are square wave inverters, modified sine wave inverters, and pure sine wave inverters.

In the literature, inverter is designed to control its frequency and output voltage by using Microcontroller. This circuit generates 40-50Hz sin waves to supply AC load (Shangguan, 2018). The authors proposed an inverter to produce sine wave alternative voltage at the output in the frequency range of 0-50 Hz. PI controller is applied to control the inverter in MATLAB/Simulink (Yalçın et al., 2020). The paper proposed the analysis and development of single-phase and three-phase inverter to design with MOSFET and IGBT by sinusoidal pulse width modulation (SPWM) technique using MATLAB/Simulink. The hardware is designed using the SG3524 microcontroller (Alam et al., 2023).

On the other hand, Raspberry Pi has gained immense popularity due to its low cost, making it an attractive option for educational institutions, DIY enthusiasts, and anyone interested in learning about computing (Küçükdermenci, 2023b). The platform encourages hands-on experimentation and creative exploration, allowing users to delve into programming, electronics, and the world of digital making (Ilten & Demirtas, 2023). Thanks to MATLAB/Simulink program, Raspberry Pi toolbox offers graphical coding environment to the users (Shah et al., 2016). Therefore Raspberry Pi finds application in various fields such as biomedical (Küçükdermenci, 2023c), light transmission (Küçükdermenci, 2023a) or liquid level control (Ilten et al., 2023).

In this chapter, a single-phase wave inverter is designed and driven by PWM technique. Raspberry Pi is used as a microcontroller to produce the PWM signals. The Simulink model is downloaded to Raspberry Pi. Raspberry Pi produces the PWM signals to drive SKYPER 32 PRO. The electronics card is designed to trigger the IGBTs over the SKYPER. It is possible to prepare PWM signals to be generated at the desired duty cycle in a period and upload them to the Raspberry Pi processor without compiling.

Pulse width modulation

PWM, which stands for Pulse Width Modulation, is a method used to encode information in a pulsing signal. It is commonly employed in various applications, ranging from controlling the speed of motors to regulating the brightness of LEDs. The basic idea behind PWM is to modulate the width of pulses in a periodic signal while keeping the frequency constant.

PWM involves the modulation of the duty cycle of a square wave signal. The duty cycle is the ratio of the pulse width to the total period of the waveform. A high-duty cycle means the signal is on for a longer duration, while a low-duty cycle indicates a shorter on-time.

Sinusoidal-pulse width modulation (SPWM)

Sinusoidal Pulse Width Modulation (SPWM) is a modulation technique used in power electronics and inverters to generate a sinusoidal waveform from a DC voltage source. The primary goal of SPWM is to produce an AC output voltage that closely resembles a pure sinusoidal waveform. This is achieved by modulating the width of the pulses in the inverter's output. Here's a basic explanation of how Sinusoidal Pulse Width Modulation works:

Reference sinusoidal wave: A reference sinusoidal waveform, usually the desired output waveform, is generated. This waveform represents the AC voltage that the inverter aims to produce.

Carrier Signal: A high-frequency triangular waveform, known as the carrier signal, is generated. The frequency of the carrier signal is typically much higher than the frequency of the desired sinusoidal waveform.

Comparison: The amplitude of the reference sinusoidal waveform is compared with the carrier signal. The instantaneous amplitude of the sinusoidal waveform determines the width of the pulses.

Pulse Width Modulation: During each cycle of the carrier signal, the width of the pulses is modulated based on the instantaneous amplitude of the reference sinusoidal waveform. As the amplitude increases, the pulse width increases, and as it decreases, the pulse width decreases.

Output Generation: The modulated pulses are used to switch the power electronic devices (such as IGBTs or MOSFETs) in the inverter. This switching action generates an AC output waveform that approximates the shape of the reference sinusoidal waveform.

Filtering (Optional): In some applications, a low-pass filter may be used to further smooth the output waveform and reduce harmonic content.

Advantages of sinusoidal pulse width modulation

Low Harmonic Distortion: SPWM results in an output waveform with low harmonic distortion, making it suitable for applications where a clean sinusoidal waveform is required.

Reduced Electromagnetic Interference (EMI): The low harmonic content contributes to reduced electromagnetic interference, which is beneficial in applications where EMI must be minimized.

Improved Power Quality: SPWM provides better power quality by closely approximating a sinusoidal waveform, making it suitable for sensitive loads.

Smooth Motor Operation: In motor control applications, SPWM is often preferred for its ability to provide smooth and efficient motor operation.

However, it's worth noting that the implementation of SPWM can be more complex than other modulation techniques, and it may require higher computational resources. Despite this, SPWM is widely used in applications where high-quality AC waveforms are

essential, such as in uninterruptible power supplies (UPS), variable frequency drives (VFDs), and other power electronics systems.

PWM applications

Pulse Width Modulation (PWM) is a technique used in electronic systems to control the average voltage or power delivered to a load by varying the width of the pulses in a pulse train. PWM has several advantages in various applications:

Reduced Power Losses: PWM allows for more efficient control of power delivery by adjusting the duty cycle of the pulses. This results in less power dissipation as compared to continuous operation at full power.

Precise Voltage Regulation: PWM provides precise control over the average voltage delivered to a load. By adjusting the duty cycle, the output voltage can be finely tuned to match the desired level.

Current Limiting: PWM can be used to implement current limiting. By monitoring the load current and adjusting the duty cycle, the current flowing through the load can be controlled to prevent overcurrent conditions.

Smooth Motor Operation: In motor control applications, PWM is commonly used to regulate the speed of motors. The smooth and precise control offered by PWM allows for accurate speed control without significant power losses.

Reduced Heating: PWM minimizes power dissipation in electronic components, reducing the overall heat generated in a system. This is particularly important for energy-efficient systems where minimizing energy losses is crucial.

Compatibility with Digital Systems: PWM is easily generated and controlled using digital systems, making it well-suited for integration into digital control circuits and microcontrollers.

LED Brightness Control: In lighting applications, PWM is commonly used for LED dimming. By adjusting the duty cycle of the PWM signal, the brightness of the LEDs can be controlled without significant loss of efficiency.

Audio Signal Processing: PWM is employed in some audio amplifiers to convert analog audio signals into digital PWM signals. This digital signal can then be efficiently amplified.

Efficient Power Conversion: PWM is widely used in switching power supplies to efficiently convert DC power to different voltage levels. It allows for the rapid switching of transistors, minimizing energy loss during the conversion process.

Digital Communication Modulation: PWM is used as a modulation technique in digital communication systems, converting digital signals into analog waveforms for transmission.

In summary, Pulse Width Modulation provides a versatile and efficient method for controlling power in various electronic systems, offering advantages in terms of energy efficiency, precision, and compatibility with digital control.

Single-phase inverter topology

Single-phase square wave type voltage source inverter produces a square-shaped output voltage for a single-phase load. A lot of inverters have very simple control logic and the power switches must operate at much lower power. First-generation inverters using thyristors as switches were almost always square wave inverters. Because thyristor switches could only be turned on and off a few hundred times per second. In contrast, today's switches such as IGBTs are much faster and use switching frequencies of a few kHz. IGBT transistors are an important technological development widely used in power electronic circuits (Calgan, 2023). These transistors combine MOSFET and BJT features and are very suitable for high-power applications. IGBTs were used as switching elements in the inverter study.

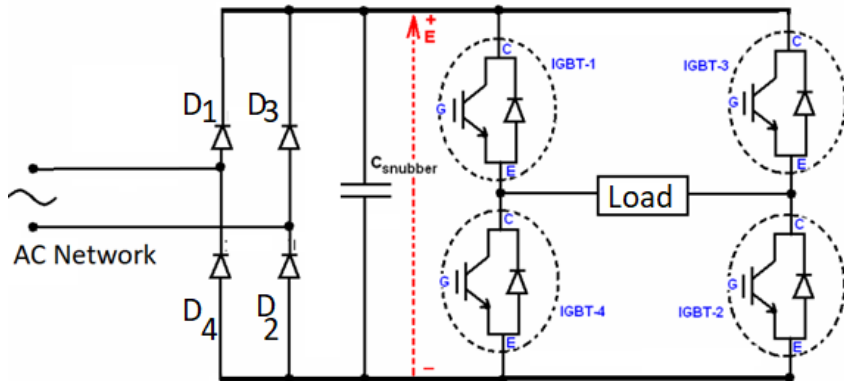


Figure 3. Single phase-full wave square wave inverter Working Principle:

Rectification: If the input source is not already DC, a rectifier is used to convert AC to DC. This is common in scenarios where the inverter is connected to a solar panel or a battery.

DC to AC Conversion: The DC power is then fed into the inverter circuit, which consists of switches. By switching these devices on and off in a specific sequence, the inverter creates an AC waveform. For a single-phase inverter, this waveform is typically a sine wave.

Pulse Width Modulation (PWM): In many modern inverters, pulse width modulation is used to control the switches. By varying the width of the pulses in the waveform, the inverter can control the average voltage and frequency of the AC output.

Filtering: The output may go through a filter to smooth out the waveform and reduce harmonic distortion, resulting in a cleaner AC signal.

Output: The final output is a single-phase AC waveform that can be used to power various electrical devices and appliances.

Inverter output voltage

Single-phase square wave inverter generates an output voltage that, as the name suggests, resembles a square wave. Unlike pure sine wave inverters that produce a smooth sinusoidal waveform, square wave inverters produce an output that alternates between two voltage levels: a positive maximum voltage and a zero voltage. The transition between these voltage levels is abrupt, resulting in a waveform that looks like a square. The output waveform is a square wave, which means it has sharp transitions between the two voltage levels. The voltage remains at the positive maximum level for a portion of the cycle and then drops abruptly to zero. The positive maximum voltage level of the square wave represents the peak voltage, and it is the highest voltage value during each cycle. The other level is zero volts, representing the absence of voltage. The frequency of the square wave is determined by the inverter's design and application. Common frequencies include 60 Hz or 50 Hz, depending on regional standards. Square wave inverters have a high harmonic content, meaning they produce significant harmonic frequencies beyond the fundamental frequency. The abrupt transitions in the waveform introduce harmonics that can affect the performance of connected devices. Square wave inverters are less common today due to their high harmonic content and potential issues with compatibility with certain types of equipment. They are often used in applications where the specific characteristics of a square wave are acceptable, such as powering simple resistive loads like incandescent lights or certain heating elements. The high harmonic content and sharp transitions make square wave inverters unsuitable for many modern electronic devices. Devices that are sensitive to the quality of the AC waveform may not operate efficiently or could be damaged when powered by a square wave inverter. While square wave inverters are simple and cost-effective, they are not as versatile as sine wave inverters, which are more commonly used in applications requiring a high-quality AC waveform. Pure sine wave inverters are preferred for powering sensitive electronic equipment, motors, and other devices that

demand a stable and clean AC power supply. A symmetrical square waveform is given in Figure 4.

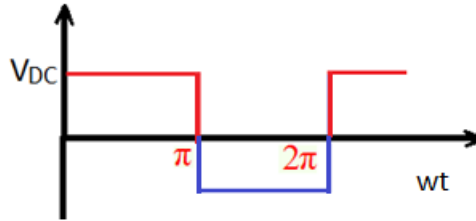


Figure 4. Symmetrical square waveform

Output voltage of single-phase full bridge inverter can be written as below,

$$V_0 = \sum_{n=1,3,5}^{\infty} \frac{4V_{DC}}{n\pi} \sin(nwt) \quad (1)$$

RMS value of the fundamental component is given follows,

$$v_{01} = \frac{4V_{DC}}{\sqrt{2\pi}} \quad (2)$$

For a square waveform, the RMS value of the voltage is equal to the magnitude of DC source. It is given in Equation (3).

$$v_0 = V_{DC} \quad (3)$$

Inverter applications

Solar Power Systems: Single-phase inverters are commonly used in residential solar power systems to convert DC power generated by solar panels into AC power for household use

Uninterruptible Power Supplies (UPS): Single-phase inverters are also used in UPS systems to provide backup power during electrical outages

Small-scale Wind Power Systems: Inverters can be used to convert the variable DC power generated by wind turbines into stable AC power

SKYPER applications of single square wave inverter

To enhance inverter efficiency up to 400 kW, circuit topologies tailored for specific applications have been developed. However, circuit configurations such as interleaved, multilevel, and parallel circuits, designed to improve IGBT efficiency, impose higher demands on signal performance. The newly introduced drive unit, SKYPER, harmonizes the advantages of digital signal consistency while preserving full functionality. SKYPER is a dual-channel IGBT driver unit compatible with 600, 1200, and 1700 V IGBT modules. It effectively manages IGBT modules up to 1000 A, delivering an output current of 80 mA and achieving a maximum switching frequency of 100 kHz.

Despite its outstanding performance, the SKYPER prioritizes maximum security. Features such as Soft Off and over-voltage recognition ensure a secure shutdown of any current. The separate transmission of switching and error signals enables swift error feedback, particularly beneficial in three-level applications. With adjustable error management, both the integrated protection circuit and the primary controller can promptly respond to system errors. Utilizing square-wave signals for isolated information transfer enhances robustness compared to traditional inductive transfer methods. Consequently, the driver unit adeptly handles interfering voltages up to 4 kV on the signal wires. The SKYPER is capable of operating external circuits monitoring excess temperature or voltage without requiring a separate power supply, facilitating the separate transmission of error signals to the control unit. The SKYPER 32 PRO is illustrated in Figure 5.



Figure 5. SKYPER 32 PRO board

Half bridge switches consisting of two IGBTs are demonstrated in Figure 6.

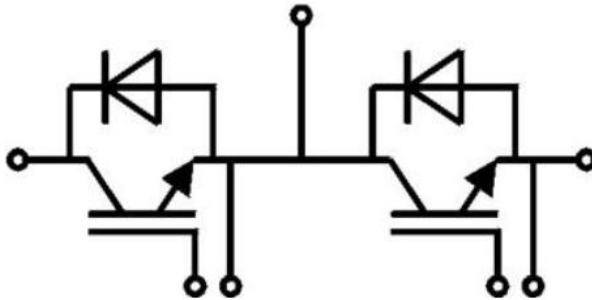


Figure 6. Half bridge switches

Single-phase square wave inverter hardware is given in Figure 7.

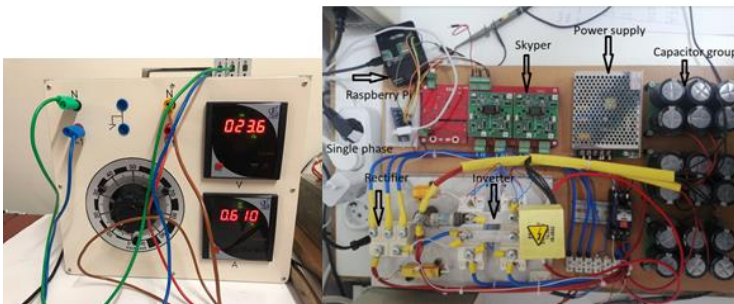


Figure 7. Hardware structure of the inverter

As shown in Figure 7, the Simulink model is used to produce the PWM signal to drive the inverter. The Simulink model is directly downloaded to the Raspberry Pi to control SKYPER. Here is no need to know any program like assembly language to run inverter driver. Raspberry Pi electronics card is widely applied to drive electrical machines and control systems (Ilten, 2023).

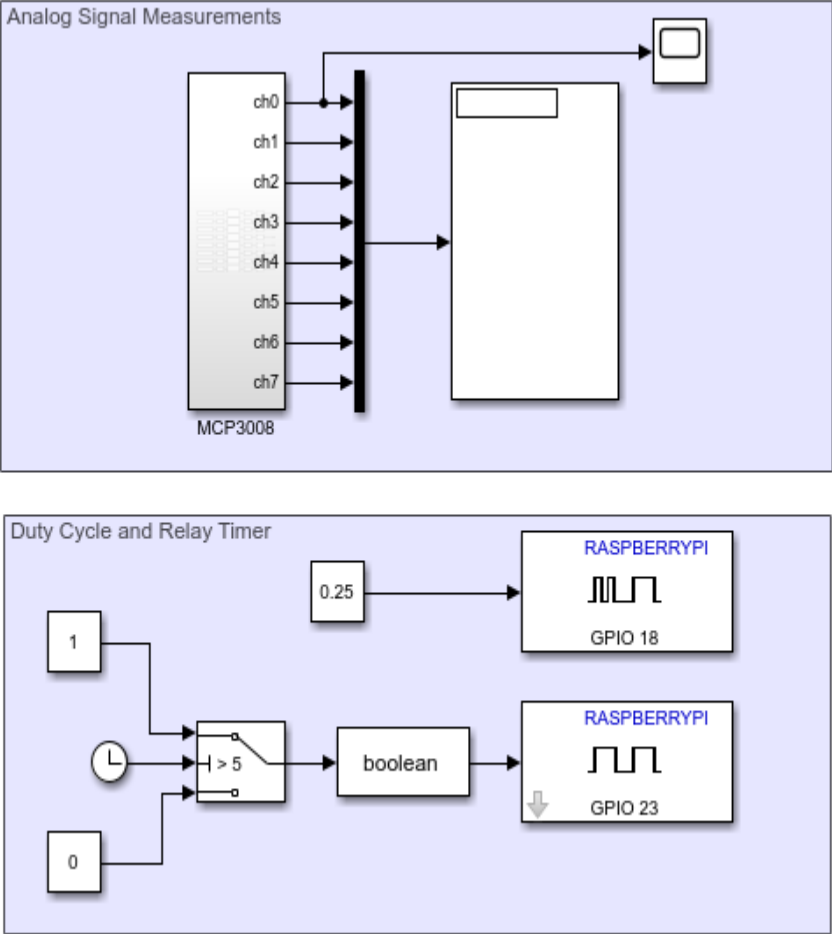
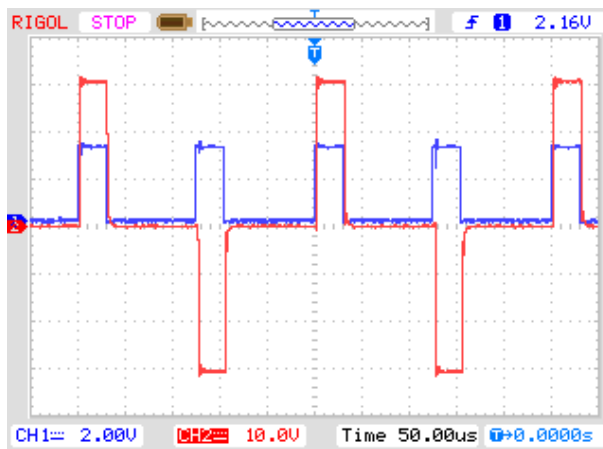


Figure 8. Simulink PWM generator blocks

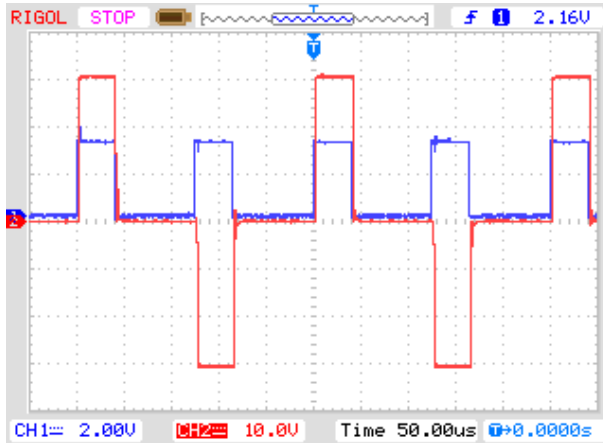
The blocks designed in MATLAB/Simulink to generate PWM signals are given in Figure 9.

Results and discussion

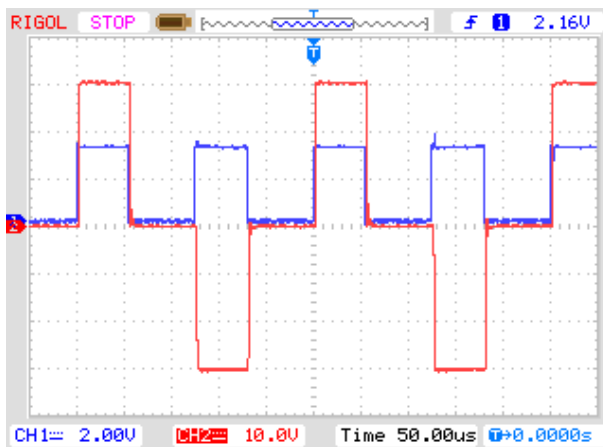
To provide specific results and discussions for a single-phase inverter, more details about the inverter structure and experiments can be made. However, I can outline a general structure for presenting results and conducting discussions in the context of a single-phase inverter study. Let's consider the study as an experiment conducted in the laboratory. The output voltage waveform of the inverter is measured and presented in Figure 9. The screen of the oscilloscope for the magnitude and frequency of the generated AC voltage is shown for different duty cycles. The blue line is a PWM signal and the red line is the output voltage. The duty cycle is changed using a PC. Changing the duty cycles on the computer and uploading them directly to the Raspberry Pi provides great convenience to the user.



a. Duty cycle=25%



b. Duty cycle=35%



c. Duty cycle=45%

Figure 9. PWM signals and output voltage

Conclusion

In conclusion, single-phase square wave full bridge inverters are electronic devices that convert direct current into single-phase square wave alternating current. Inverters have a wide range of applications, from small renewable energy sources to large power

plants. However, a quality inverter design is important for the device to be healthy and long-lasting. In this inverter, four IGBTs are used for switching devices. The Simulink program is downloaded to the Raspberry Pi to control IGBTs over SKYPER and the designed electronics card. The electronics card increases the voltage to drive IGBTs and produces a triggering signal for the upper and lower legs. Programming with Simulink provides expediency to the user as it does not require the user to know any language. Today, semiconductor technology allows the use of very fast switching elements that can withstand high currents and voltages. In recent years, devices consisting of silicon carbide (SiC) and gallium arsenide (GaN) components enable inverters to operate more efficiently.

References

Ahmed, A. (1998). Power electronics for technology. *Prentice Hall Inc.*, 100–200.

Alam, A., Monem, M. A., & Islam, K. K. (2023). Optimized Design and Analysis of Single-Phase and Three-Phase Inverters for Efficient Power Conversion: A Comparative Study. *Journal of Computer and Communications*, 11(8), 71–95.

Calgan, H. (2023). Optimal C-type Filter Design for Wireless Power Transfer System by using Support Vector Machines. *An International Journal of Optimization and Control: Theories & Applications (IJOCTA)*, 13(2). <https://doi.org/10.11121/ijocta.2023.1354>

Gülgün, R. (1999). *Güç elektroniği, Yıldız Teknik Üniversitesi Basım-Yayın Evi, 2. baskı*. İstanbul.

Guo, B., Su, M., Sun, Y., Wang, H., Liu, B., Zhang, X., Pou, J., Yang, Y., & Davari, P. (2020). Optimization design and control of single-stage single-phase PV inverters for MPPT improvement. *IEEE Transactions on Power Electronics*, 35(12), 13000–13016.

Ilten, E. (2023). DC motor position control with Raspberry Pi on Simulink wireless external mode. *International Conference on Pioneer and Innovative Studies*, 1, 228–231.

Ilten, E., Calgan, H., & Demirtas, M. (2023). Fuzzy Logic Level Control of a Coupled Tank System with Raspberry Pi Application. *2nd International Conference on Contemporary Academic Research*, 1(2), 61–65.

Ilten, E., & Demirtas, M. (2023). Liquid Level Control Interface Design on Simulink External Mode with Raspberry Pi. *Int. Conf. Mod. Adv. Res.*, 85–88.

Küçükdermenci, S. (2023a). Effects of Magnetic Fluid Concentration and Cell Size on Magneto-Optical Light

Transmission. *1st International Conference on Recent and Innovative Results in Engineering and Technology*.

Küçükdermenci, S. (2023b). Sign language voice convertor design using Raspberry pi for impaired individuals. *1st International Conference on Recent and Innovative Results in Engineering and Technology*, 160–166.

Küçükdermenci, S. (2023c). Smart Wheelchair Design for Elderly and Disabled People. *3rd International Conference on Innovative Academic Studies*.

Shah, A. A., Zaidi, Z. A., Chowdhry, B. S., & Daudpoto, J. (2016). Real time face detection/monitor using raspberry pi and MATLAB. *2016 IEEE 10th International Conference on Application of Information and Communication Technologies (AICT)*, 1–4.

Shangguan, S. J. (2018). Single-Phase Sine Wave Frequency Inverter Power Supply. *Journal of Physics: Conference Series*, 1087(4), 42004.

Yalçın, F., Arifoğlu, U., & Yazıcı, İ. (2020). A new single phase inverter based on buck converter. *Sakarya University Journal of Science*, 24(3), 480–486.

CHAPTER XIII

A Two-Port MIMO Patch Antenna at 28 GHz for mm-Wave Communication

Cem GÜLER¹
Sena Esen BAYER KESKİN²

Introduction

Communication technologies play a critical role in ensuring fast and efficient communication, optimizing data transfer, and providing easy access to information (Kishore & Senapati, 2022). These technologies enhance the efficiency of operations by offering advantages such as cost savings, global accessibility, and flexibility. They find diverse applications across sectors, including supporting distance learning in education, facilitating treatment and diagnosis in health, and enabling automation in industry (Barate et al., 2017.,

¹ Research Assistant, Department of Lüleburgaz Faculty of Aeronautics and Astronautics, Kırklareli University, e-mail: cemguler@klu.edu.tr

² Assistant Professor, Department of Electrical and Electronics Engineering, Kırklareli University e-mail: senakeskin@klu.edu.tr

Kun et al., 2021., Sabban, 2020., Mahmood et al., 2020., Cheng et al., 2018). Additionally, technologies like mobile communication, social media, and digital entertainment platforms are integrated into our daily lives (Caruso et al., 2019). The continual expansion of application domains and the number of devices necessitate the adoption of new technologies in wireless communication systems. 5G technology in particular further strengthens this important role in communication technologies. Its features, such as high data rates, low latency and large connection capacity, bring various advantages to applications in many sectors (Dahiya, 2017). 5G communication technology distinguishes itself from previous generations by providing features such as higher data rates, dependable connectivity, and nearly simultaneous latency of less than 1 ms (Albreem, 2015). 5G technology aims to take communication systems to a level that will operate more efficiently by classifying them in three different ways: mobile broadband communication (eMBB), ultra-reliable low latency communication (uRLLC) and massive machine-to-machine communication (mMTC), developed to meet different needs (Zhu et al., 2022). The frequency spectrum allocated for 5G communication technologies, ranging from 3 GHz to 300 GHz, enables the utilization of millimeter waves to support high data rates and capacity (IMT.,2015). In addition to the numerous benefits of millimeter waves, external factors, including atmospheric conditions and path loss attenuation, exert a significant influence on the millimeter wave spectrum. To mitigate these adverse effects, antennas need to be MIMO capabilities (Sharma et al., 2022). In MIMO antenna systems, antennas serve dual roles as both transmitters and receivers. The utilization of MIMO antennas facilitates the realization of the high data transmission rates anticipated with 5G technology through spatial multiplexing (Chen et al., 2020). To meet the requirements of the 5G system, antennas play an important role as physical hardware. Among the preferred antenna types for 5G applications, patch antennas are widely employed. Microstrip patch antennas, in particular, exhibit robust performance characteristics, a compact structure, ease of fabrication,

and design flexibility. However, many parameters (size, bandwidth, efficiency, gain) of microstrip antennas need to be improved (Mohammed et al., 2019). There are many two-port MIMO patch antenna designs in the literature for use in 5G communication Technologies (Kaur et al., 2023a., Sheshaprasad et al., 2022., Kumar et al., 2023., Hasan & Seo, 2018., Kaur et al., 2023b., Mishra et al., 2022). The most commonly used method to influence the performance parameters in patch antenna design is to change the shape of the radiating patch. Numerous studies in the literature focusing on different patch shapes with diverse designs, particularly operating at millimeter-wave frequencies. In 2023, Kaur et al. presented a patch antenna with dimensions of $9 \times 12 \times 1.575 \text{ mm}^3$ on an RT/duroid 5880 substrate. The antenna featured a two-port circular patch and circular slot, operating at a center frequency of 28 GHz. The designed antenna exhibited a bandwidth of 3 GHz (26.6-29.6 GHz), with a directivity gain ranging from 4.77 to 4.93 dBi. Additional performance metrics included an ECC < 0.06 , diversity gain exceeding 9.9, and port isolation of 13 dB (Kaur et al., 2023a.). Another study in 2022 presents an antenna design with dimensions of $26 \times 25.6 \times 1.6 \text{ mm}^3$ on FR-4 material. The two-port MIMO antenna design, which has a bandwidth of 5 GHz between 25 - 31.73GHz, offers a directivity gain of 4.168 dBi at the center resonant frequency and an isolation value of -25 dB between ports (Sheshaprasad et al., 2022). Kumar et al. achieved 1.62 GHz bandwidth between 27.3 - 28.92 GHz frequencies, 7 dB antenna gain and 22 dB isolation between ports with their 2-port MIMO antenna design on RT/duroid 5880 with dimensions of $12 \times 8.5 \times 0.8 \text{ mm}$ (Kumar et al., 2023). A two-port MIMO antenna design with dimensions of $10 \times 12 \times 0.38 \text{ mm}^3$ at 28 GHz center frequency is presented with a bandwidth of 2.5 GHz between 28.2-30.7 GHz and an ECC of < 0.001 (Hasan & Seo, 2018.,). Another study in 2023 presents a two-port MIMO antenna design on RT/duroid 5880 material with dimensions of $12 \times 12 \times 0.254 \text{ mm}^3$. The proposed antenna offers a bandwidth of 500 MHz between 27.7-28.2 GHz, an antenna gain of 10 dBi, an ECC of < 0.013 , a diversity gain of 9.999

dB and an isolation of >20 dB between ports (Kaur et al., 2023b.). Mishra et al. presented a two-port MIMO antenna design operating at 28 GHz center frequency consisting of an AMC structure consisting of 5x4 unit cells and two interconnected I-shaped slots. The dimensions of the proposed antenna are 25×40×40×3.7 mm³ with an antenna gain of 9.25 dBi, bandwidth of 1.9 GHz and port isolation greater than 18 dB (Mishra et al., 2022). Two-port antennas documented in the literature often face challenges related to bandwidth, directivity gain, or large size. To overcome these limitations, this paper introduces a microstrip patch antenna designed for 5G applications at a center frequency of 28 GHz. The proposed antenna is characterized by its low profile and easy fabrication. The antenna designed by mathematical calculations offers an isolation value of -20.2 dB and a bandwidth of 900 MHz. The introduction explains the significance of both 5G technology and antenna design, accompanied by a comprehensive literature review. In the rest of the paper, the length dimensions and stages of the antenna design are detailed, the parametric results of the designed antenna obtained with the simulation program are presented and compared with similar studies in the literature. The conclusion presents the evaluation of the work carried out.

Antenna design

In this investigation, a rectangular patch operating at a center frequency of 28 GHz is constructed on a Rogers RT-5880 substrate with a dielectric coefficient of 2.2 and a height of 0.787 mm. The dimensions of the patch, dielectric substrate, and microstrip line are subsequently determined utilizing the following mathematical equations, numbered Eq. 1- Eq. 6:

Width of the rectangular patch W is obtained by:

$$W = \frac{1}{2f_r \sqrt{\mu_0 \epsilon_0}} \sqrt{\frac{2}{\epsilon_r + 1}} = \frac{c}{2f_r} \sqrt{\frac{2}{\epsilon_r + 1}} \quad (4)$$

Here, c is the speed of light, f_r is the resonance frequency, ϵ_0 is the dielectric constant of the cavity, μ_0 is the magnetic permeability of the cavity. The actual length of the rectangular patch, denoted as L , is determined by the equation given below:

$$L = \frac{c}{2f_r\sqrt{\epsilon_{eff}}} - 2\Delta L \quad (5)$$

Here, ϵ_{eff} is the effective dielectric constant. In Equation (3), the value for ϵ_{eff} , and in Equation (4), the value for ΔL are provided, respectively.

$$\epsilon_{eff} = \frac{\epsilon_r + 1}{2} + \frac{\epsilon_r - 1}{2} \left[1 + 12 \frac{h}{W} \right]^{-1/2} \quad (6)$$

$$\Delta L = 0.412h \frac{(\epsilon_{eff} + 0.3) \left(\frac{W}{h} + 0.264 \right)}{(\epsilon_{eff} - 0.258) \left(\frac{W}{h} + 0.8 \right)} \quad (7)$$

The dimensions of the dielectric material are given in Equations (5) and (6).

$$W_m = 6h + W \quad (8)$$

$$L_m = 6h + L \quad (9)$$

Using Equation 1 and Equation 2, the dimensions of the radiating antenna patch are computed, resulting in the creation of the square patch depicted in Figure 1a. To enhance the S_{11} parameter, a quadrature slot is introduced to the square patch, as illustrated in Figure 2a. Consequently, the antenna functions within the frequency range of 28.84-30.36 GHz at <-10 dB. For the square patch depicted in Figure 1c, an additional square patch is integrated and connected to the outer square patch, enabling the antenna to operate at the desired frequency.

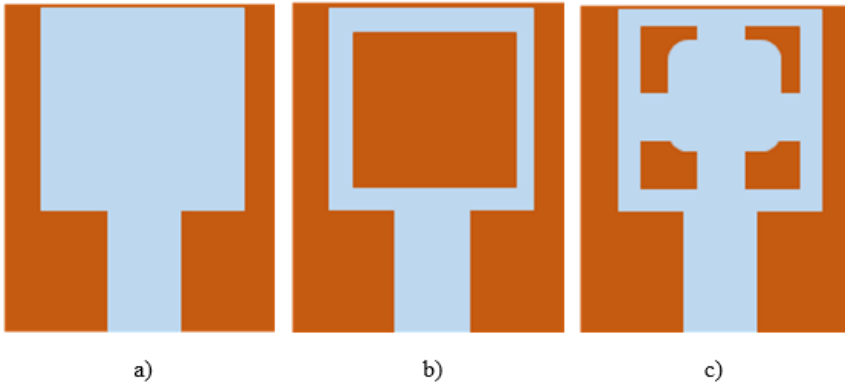


Figure 1. Design steps of the single antenna, a) Step I, b) Step II, and c) Final Design.

The front side of the final design is depicted in Figure 2a, while Figure 2b displays the parametric dimensions on the back side of the antenna.

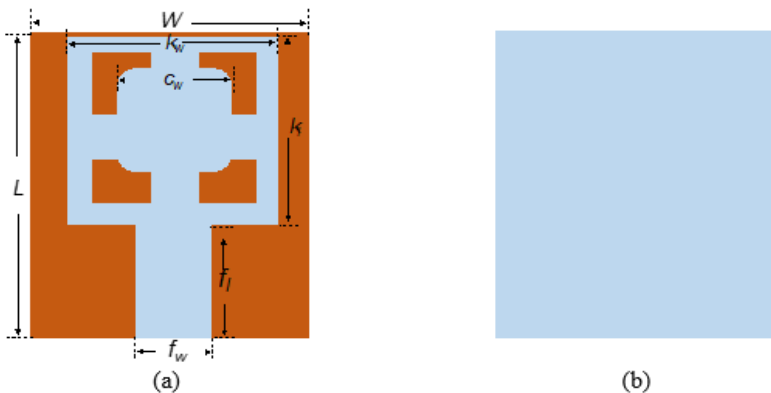


Figure 2. The length parameters of the final antenna design, a) Front view, b) Back view.

The length parameters of the designed antenna are given in Table 1.

Table 1. The length parameters of the proposed antenna

Parameter	Dimension (mm)	Parameter	Dimension (mm)
D_w	9.04	d_l	10.91
f_w	2.45	f_l	4.03
$k_w=k_l$	6.78	$s_w=s_l$	1.51
c	3.21	$L=W$	10.9

Figure 3 illustrates the S_{11} parameters across various design steps. In the final antenna design, it is evident that the radiation aligns with the desired frequency. The antenna, centered at 28 GHz, exhibits a bandwidth of 470 MHz, spanning from 27.64 to 28.38 GHz, with a bandwidth of 2.6%.

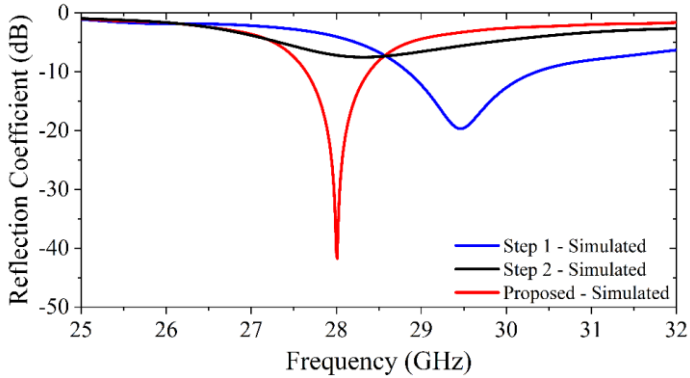


Figure 3. S_{11} parameters at various design steps of the presented antenna

Figure 4 shows the three-dimensional radiation pattern of the designed antenna, with a directivity gain of 6.9 dBi at the central resonant frequency of 28 GHz.

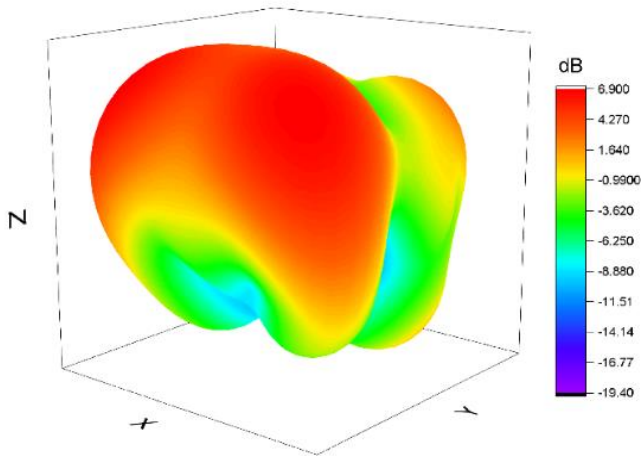


Figure 4. 3D gain of the proposed antenna.

In Figure 5, the red plot represents the E-plane for $\Phi=0^\circ$, while the blue plot corresponds to the H-plane for $\Phi=90^\circ$ at 28 GHz. The half-power beamwidth (HPBW) measures 164.7° for $\Phi=0^\circ$ and 52.5° for $\Phi=90^\circ$.

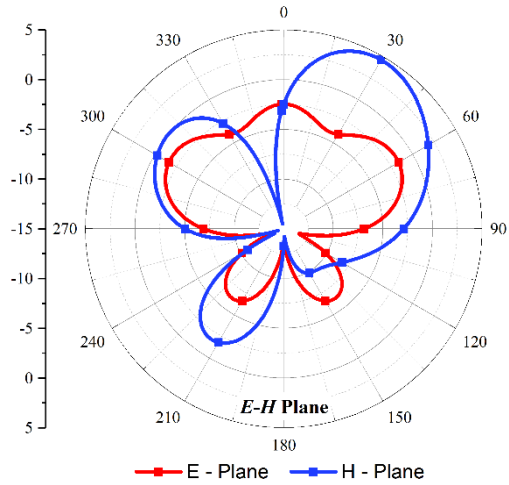


Figure 5. E and H radiation pattern plots (2D) of the proposed antenna.

The maximum surface current amplitude of the designed antenna reaches 48 dB (A/m) at the resonant frequency of 28 GHz. At this frequency, the surface currents exhibit concentration along the edges of the patch and at the junction of the feed line and the patch, as visually depicted in Figure 6.

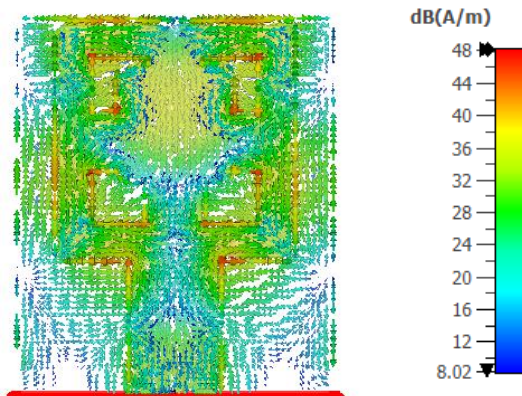


Figure 6. Surface current distribution of the proposed antenna.

Figure 7 illustrates the Frequency Standing Wave Ratio (VSWR) of the proposed antenna. At the center frequency, the proposed antenna achieves an exceptional VSWR value of 1.0002, corresponding to the point where the return loss is maximized.

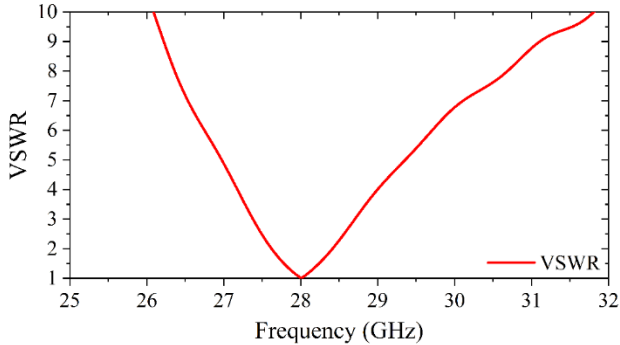


Figure 7. VSWR plot of the proposed antenna.

Figure 8 (a-b) shows the placement of the designed single antenna to provide the two-port Multiple In Multiple Out (MIMO) feature. The d_w length of the antenna is 21.09 mm, and the d_l length is 10.91 mm.

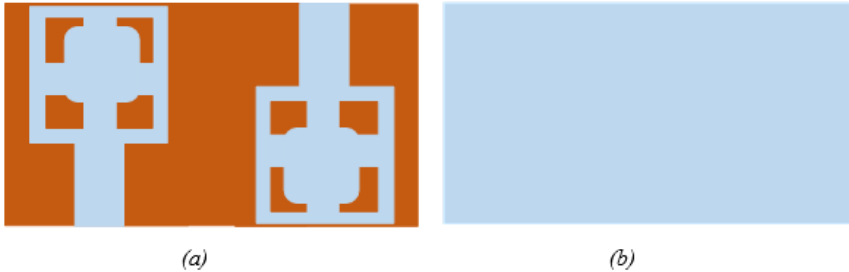


Figure 8. 2-port MIMO Antenna, (a) Front view, (b) Back view.

In order to evaluate the performance of the proposed two-port MIMO antenna design, simulation results of the variations of S_{11} and S_{22} parameters on four different dielectric layers are shown in Figure 9. The tests performed on RT Duroid 5880 ($\epsilon_r=2.2$), FR-4 ($\epsilon_r=4.4$), Arlon AD 600 ($\epsilon_r=6.15$) and RT6010 ($\epsilon_r=10.2$) dielectric

materials shows the effect of each material on the antenna performance. Notably, the simulation results reveal that the antenna constructed with RT Duroid 5880 material surpasses others in terms of overall performance. This underscores the significance of RT Duroid 5880, characterized by low dielectric loss and a high dielectric constant, as a preferred dielectric material in MIMO antenna design.

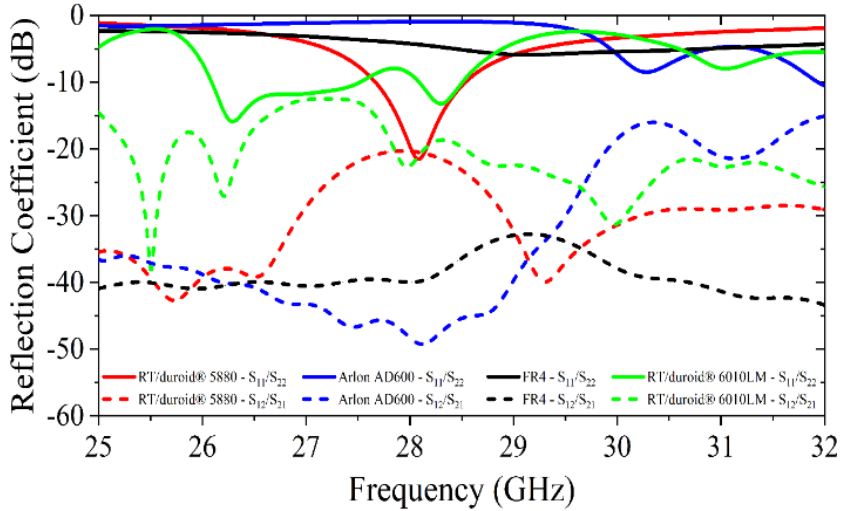


Figure 9. Performance analysis of the proposed two-port MIMO antenna across various dielectric layers.

Figure 10 shows the 3D radiation pattern of the antenna whose design has been completed. The antenna has a directivity gain of 6.3 dBi at the 28 GHz center resonance frequency.

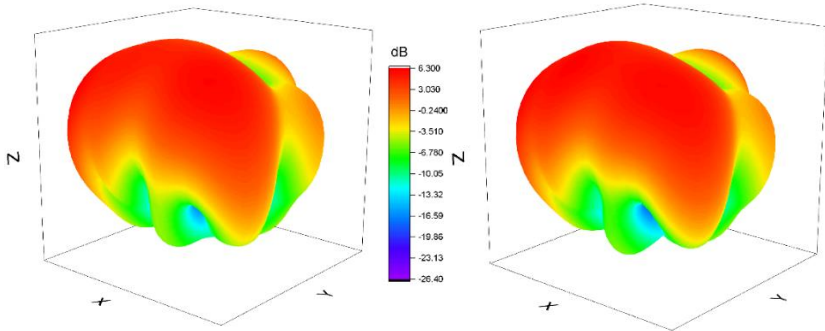


Figure 10. 3D gain of the proposed two-port MIMO antenna.

Figure 11 depicts the E-plane at $\Phi=0$ and H-plane at $\Phi=90$ for both ports at a frequency of 28 GHz. In Port 1, the half-power beamwidth (HPBW) measures 60.3° at $\Phi=0$ and 47.2° at $\Phi=90$. For Port 2, the half-power beamwidth (HPBW) is 55.9° at $\Phi=0$ and 46.6° at $\Phi=90$.

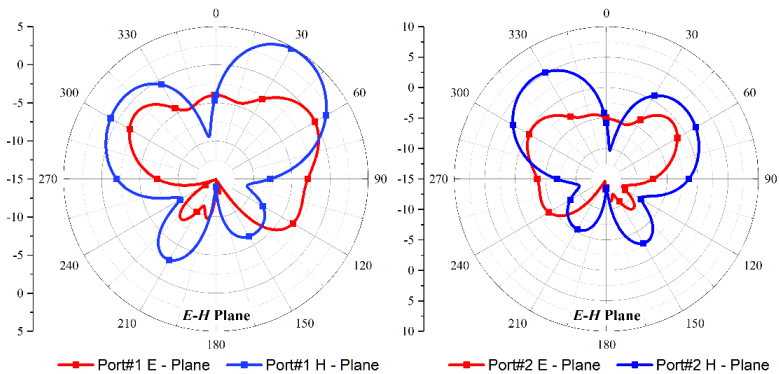


Figure 11. 2D Gain Plots (E-plane and H-plane) for the Proposed Two-Port MIMO Antenna.

The maximum surface current amplitude of the designed antenna is obtained as 48.5 dB (A/m) at the 28 GHz resonant frequency, as depicted in Figure 12a for Port1 and Figure 12b for Port2.

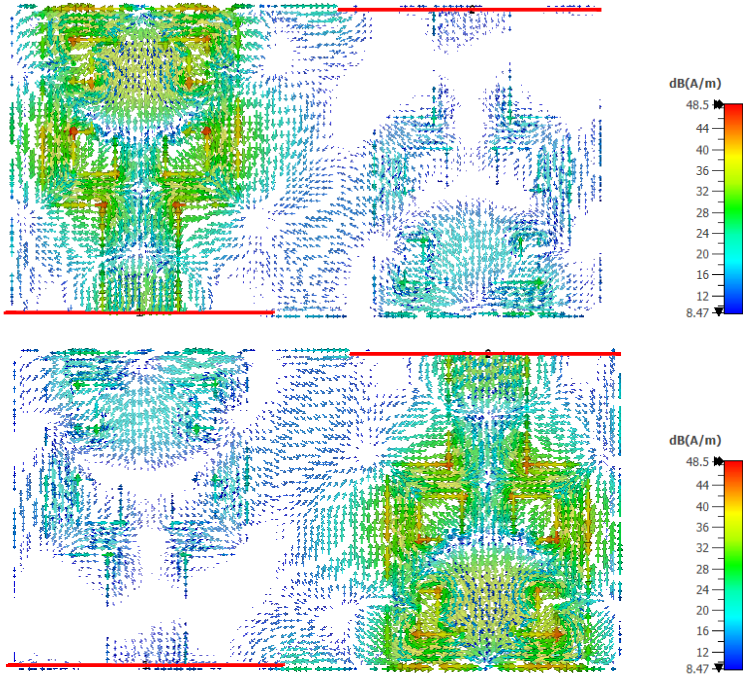


Figure 12. Surface current distribution plot of the proposed 2-port MIMO antenna a) Port 1, b) Port 2.

The envelope correlation coefficient (ECC) is an important component to examine whether the MIMO characteristics of the antenna are sufficient. Theoretically, in the ideal case, the ECC value should be zero. However, due to various losses, $ECC < 0.5$ is accepted in practice. For any MIMO antenna system, the ECC can be expressed in terms of S parameters given by Equation (7) (Blanch et al., 2003). The ECC values obtained for the MIMO antenna designed using Equation (7) are shown in Figure 13. The ECC value obtained is less than < 0.0005 .

$$\text{ECC} = \frac{|S_{11}^* S_{12} + S_{21}^* S_{22}|^2}{(1 - |S_{11}|^2 - |S_{21}|^2)(1 - |S_{22}|^2 - |S_{12}|^2)} \quad (7)$$

Diversity gain (DG) is another key component to examine whether the MIMO characteristics of the antenna are sufficient. In wireless systems, the diversity gain should be close to 10 dB. The diversity gain of a MIMO antenna is derived from the ECC using Equation (7). The simulated diversity gain value is shown in Figure 13.

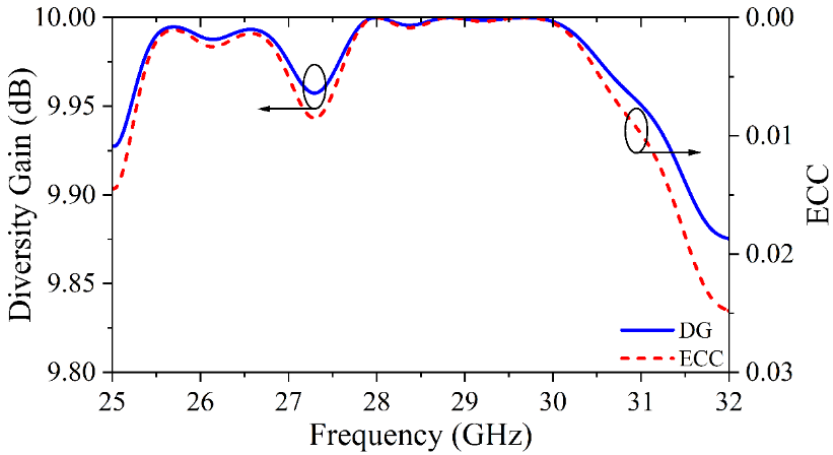


Figure 13. ECC and DG graph for the proposed two-port MIMO antenna.

The frequency-Standing Wave Ratio (VSWR) of the proposed MIMO is given in Figure 14. It shows that the proposed antenna has the desired low VSWR values in a wide frequency range.

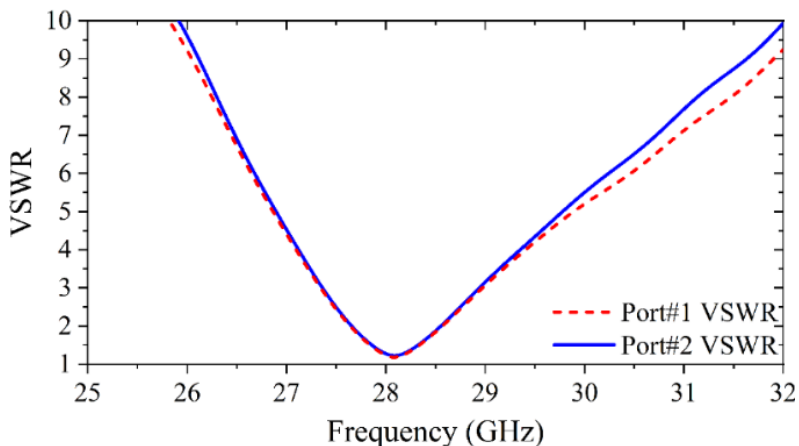


Figure 14. VSWR plot of the proposed two-port MIMO antenna.

Comparison with existing mm-wave antennas in Table 2 indicates that the proposed reference antenna outperforms other studies in the literature in terms of size, bandwidth, gain, isolation, ECC, and return loss within the scope of 5G communication technologies.

Table 2 Comparative Analysis of Reference Antennas in Relation to Existing Literature

Referans	Antenna dimension (mm)	Bandwidth	Min. Isolation	Directivity Gain	ECC
(Kaur et al., 2023a)	9×12×1.575	3 GHz	13	4.93	<0.06
(Sheshaprasad et al., 2022)	26×25.6×1.6	5 GHz	25	4.168	
(Hasan & Seo 2018)	10×12×0.38	2.5 GHz	-	-	<0.001
(Kaur et al., 2023b)	12×12×0.254	500 MHz	>21	10	<0.013
This Work	10.91×21.09×0.787	900 MHz	>20.2	7.15	<0.0005

Conclusion

In this paper, a novel antenna design for fifth generation wireless communication applications at millimeter wave frequencies is presented. The two-port Multiple-Input Multiple-Output (MIMO) microstrip patch antenna has a simple and compact geometrical structure that provides high bandwidth. Among the antenna parameters determined by modeling and simulations using CST Microwave Studio software, it is observed that the antenna built on RT Duroid 5880 material exhibits the best performance. The antenna built on RT Duroid 5880 material has dimensions of $10.9 \times 21 \times 0.787$ mm³ and a bandwidth of 900 MHz between 27.6 GHz and 28.5 GHz frequencies. It offers a gain of 6.22 dB at center frequency, a directivity gain of 7.15 dBi and an inter-port isolation of -20.2 dB. It offers a successful solution for fifth generation wireless communication applications, achieving <0.005 ECC and <9.995 DG values, supporting that it is a low-cost, compact and suitable candidate for 5G applications.

References

Albreem, M. A. M. (2015). 5G wireless communication systems: Vision and challenges. 2015 International Conference on Computer, Communications, and Control Technology (I4CT). IEEE.

Baratè, A., Haus, G., Ludovico, L. A., Pagani, E., & Scarabottolo, N. (2017). 5g technology and its applications to music education. Proceedings of the International Conference on E-Learning 2019. IADIS Press.

Blanch, S., Romeu, J., & Corbella, I. (2003). Exact representation of antenna system diversity performance from input parameter description. *Electronics Letters*, 39(9), 705. doi:10.1049/el:20030495

Caruso, G., Nucci, F., Gordo, O. P., Rizou, S., Magen, J., Agapiou, G., & Trakadas, P. (2019). Embedding 5G solutions enabling new business scenarios in Media and Entertainment Industry. 2019 IEEE 2nd 5G World Forum (5GWF). IEEE.

Chen, S., Sun, S., Xu, G., Su, X., & Cai, Y. (2020). Beam-space multiplexing: Practice, theory, and trends, from 4G TD-LTE, 5G, to 6G and beyond. *IEEE Wireless Communications*, 27(2), 162-172.

Cheng, J., Chen, W., Tao, F., & Lin, C.-L. (2018). Industrial IoT in 5G environment towards smart manufacturing. *Journal of Industrial Information Integration*, 10, 10–19. doi:10.1016/j.jii.2018.04.001

Dahiya, M. (2017). Need and advantages of 5G wireless communication systems. *International Journal*, (6).

Hasan, M. N., & Seo, M. (2018). Compact omnidirectional 28 GHz 2×2 MIMO antenna array for 5G communications. In 2018 international symposium on antennas and propagation (ISAP) (pp. 1–2). IEEE.

IMT Vision: Framework and overall objectives of the future development of IMT for 2020 and beyond. (2015). In Recommendation ITU-R M.

Kaur, P., Malhotra, S., & Sharma, M. (2023). Tilted Pentagon with Rectangular Slotted Patch Two-Port MIMO Antenna for 28GHz 5G mm-wave band Applications. In 2023 First International Conference on Microwave, Antenna and Communication (MAC) (pp. 1–6). IEEE.

Kaur, P., Sharma, M., & Gill, R. (2023). Circular Patch with Circular Slots Two-Port-MIMO Antenna for 28 GHz (n-257) 5G-Millimeter-Wave Band Applications. In 2023 IEEE Renewable Energy and Sustainable E-Mobility Conference (RESEM) (pp. 1–6). IEEE.

Kishore, N., & Senapati, A. (2022). 5G smart antenna for IoT application: A review. *International Journal of Communication Systems*, 35(13). doi:10.1002/dac.5241

Kumar, S., Tiwari, N., Dwivedi, A. K., & Singh, V. (2023). MIMO Antenna with Low Mutual Coupling and High Gain for n257-Band 5G mm-Wave. In 2023 13th International Symposium on Advanced Topics in Electrical Engineering (ATEE) (pp. 1–5). IEEE.

Kun, G., Kovacs, R., Meszaros, K., Wuhrl, T., Gyanyi, S., Nadai, L., & Varga, P. J. (2021). Introduction of 5G in education. 2021 IEEE 4th International Conference and Workshop Óbuda on Electrical and Power Engineering (CANDO-EPE). IEEE.

Mahmood, S. N., Ishak, A. J., Saeidi, T., Alsariera, H., Alani, S., Ismail, A., & Soh, A. C. (2020). Recent advances in wearable antenna technologies: A review. *Progress in Electromagnetics Research B*. Pier B, 89, 1–27. doi:10.2528/pierb20071803

Mishra, P., Jain, P., Singh, M. P., & Ghosh, S. (2022). Artificial magnetic conductor backed printed monopole MIMO

antenna for millimeter-wave 5G WBAN applications. 2022 URSI Regional Conference on Radio Science (USRI-RCRS). IEEE.

Mohammed, A. S., Kamal, S., Ain, M. F., Ahmad, Z. A., Ullah, U., Othman, M., & Rahman. (2019). Microstrip patch antenna: A review and the current state of the art. *Journal of Advanced Research in Dynamical and Control Systems*, 11(7), 510–524.

Sabban, A. (2020). *Advanced Radio Frequency Antennas for Modern Communication and Medical Systems*.

Sharma, P., Tiwari, R. N., Singh, P., Kumar, P., & Kanaujia, B. K. (2022). MIMO antennas: Design approaches, techniques and applications. *Sensors* (Basel, Switzerland), 22(20), 7813. doi:10.3390/s22207813

Sheshaprasad, N., Kiran, K. N., & Sumathi, A. (2022). A 28 GHz 5G High Gain MIMO Antenna Array System for Human Body Communication. *International Journal of Creative Research*, 10.

Zhu, Z., Li, X., & Chu, Z. (2022). Three major operating scenarios of 5G: eMBB, mMTC, URLLC. In *Intelligent Sensing and Communications for Internet of Everything* (pp. 15–76). Elsevier.

